Universitat Autònoma de Barcelona

High energy emission from recurrent novae

Laura Delgado

High energy emission from recurrent novae

Laura Delgado
Institut de Ciències de l'Espai (ICE, CSIC/IEEC)

Advisor: Margarita Hernanz
Tutor: Lluís Font

Universitat Autònoma de Barcelona
Departament de Física

A thesis submitted for the degree of

Doctor of Philosophy in Physics

Bellaterra, July 2017

A mis abuelos a los que siempre echaré de menos.

Hujus generis sunt stellæ fixæ, quæ subito apparent, & sub initio quam maxime splendent, & subinde paulatim evanescuant

— I. Newton (Principia Mathematica)

ACKNOWLEDGMENTS

Primero de todo quería dar las gracias a Margarita Hernanz por haberme dado la oportunidad de hacer realidad el sueño de dedicarme a la astrofísica, además de por su tiempo y dedicación ya que sin tu ayuda no habría sido posible la realización de esta tesis.

Gracias a Jordi Isern, a Aldo Serenelli y al resto del grupo de evolución estelar, con mención especial a Martin Henze, por ayudarme a avanzar y a perder parte de mis miedos a lo largo de estos 4 años en las reuniones de los viernes. Gracias a Josep Gerrero por la paciencia que ha tenido conmigo y por recordarme que los ordenadores no suelen explotar. También al personal de administración por ayudarme siempre que lo he necesitado.

I would like to thank Mike Bode and Tim O'Brien for giving me the opportunity to do work with them and for the enjoyable discussions, lunches and dinners together

Gracias a mis compañeros de doctorado por esos días en el cyber que nos unieron tanto y por disfrutar de tantos ratos fuera y dentro del instituto que han hecho que el doctorado sea menos duro. Gracias al despacho de la sinceridad, a las estrellitas y a mi gemela de doctorado, sabéis que un trocito de este doctorado es vuestro. También quería darle las gracias a mi "familia de Barcelona" por soportarme en casa y escucharme practicar charlas de las cuales no entendían ni el título.

Finalmente quería darle las gracias a mi familia y amigos por aguantarme cuando las cosas no iban bien y sobre todo por celebrar las cosas buenas. Gracias a mis padres por darme siempre su apoyo incondicional, a mi hermana y a Fran por hacerme tía de las dos personitas más bonitas del mundo y GRACIAS a Hugo por que sin ti todo esto no tiene sentido.

CONTENTS

LIST OF FIGURES

LIST OF TABLES

ACRONYMS

AAVSO American Association of Variable Star Observers

ACIS Advanced CCD Imaging Spectrometer

APEC Astrophysical Plasma Emission Code

ARF Auxiliary Response File

ASM All Sky Monitor

BAT Burst Alert Telescope

CCD Charge-Coupled Device

CN Classical Nova

CV Cataclysmic Variable

EM emission measure

EPIC European Photon Imaging Camera

EVN European VLBI Network

FTOOLs FITS-based software Tools developed at Goddard Space Flight Center

FOV Field of view

FWHM Full Width at Half Maximum

FWZI Full Width at Zero Intensity

GMRT Giant Metrewave Radio Telescope

GRB Gamma-Ray Burst

GBM Gamma-ray Burst Monitor

GTI Good Time Interval

HEASoft High Energy Astrophysics Software

HEG High Energy Grating

HETG High Energy Transmission Grating

HEW Half Energy Width

HEXTE High-Energy X-ray Timing Experiment

HRC High Resolution Camera

HRMA High Resolution Mirror Assembly

IM Imaging Mode

IR Infra Red

ISM interstellar medium

IUE International Ultraviolet Explorer

LAT Large Area Telescope

LETG Low Energy Transmission Grating

LTE Local Thermodynamic Equilibrium

MEG Medium Energy Grating

MERLIN Multi-Element Radio-Linked Interferometer Network

MOS Metal Oxide Semiconductor

OCRA-p One-Centimetre Radio Array

ODF Observation Data File

OGLE Optical Gravitational Lensing Experiment

OM Optical/UV Monitor

PC Photon-Counting

PCA Proportional Counter Array

PSF Point Spread Function

RG Red Giant

RGA Reflection Grating Assembly

RGS Reflection Grating Spectrometer

RMF Redistribution Matrix File

RN Recurrent Nova

RXTE Rossi X-ray Timing Explorer

SAS Standard Analysis System

SED Spectral Energy Distribution

SN Supernova

SNR Supernova Remnant

SMARTS Small and Moderate Aperture Research Telescope System

SSS Super Soft Source

tbabs Tuebingen-Boulder absorption model

TNR thermonuclear runaway

UVOT UV/Optical Telescope

VLA Karl G. Jansky Very Large Array

VLBA Very Long Baseline Array

VLBI Very Long Baseline Interferometry

XRT X-Ray Telescope

XSPEC X-Ray Spectral Analysis Package

WD white dwarf

WT Windowed Timing

1

INTRODUCTION

The origin of the term 'nova' comes from the latin *stella nova* and it refers to a new star appearing in the sky where before there was only darkness. The first time this term was used in the literature was in *Naturæ historia* by C. Plinius Secundus, written around AD 75 (Plinius, 1855). Nowadays we know that a nova is not actually a new star, it is more appropriate to say that it is a star whose luminosity suddenly increases more than ∼10 mag. In the 17$^{\rm th}$ century, Newton explained in his famous *Principia Mathematica* that a nova is a temporary star that suddenly increases its luminosity and then vanishes, and also introduced the basis for the thermonuclear runaway (TNR) concept (José, 2016, Chapter 4). Until the 20$^{\rm th}$ century, novae and supernovae were not distinguished from each other because of the little knowledge about Supernova Remnants (SNRs) and their absolute magnitudes. In the early 20$^{\rm th}$ century, some novae were discovered in spiral nebulae by G.W Ritchey, H.D. Curtis, H. Shapley, K. Lundmark and others, and they found that these extragalactic objects have much a larger intrinsic brightness than the galactic ones (Bode & Evans, 2008, and references therein). The Nova S Andromedae (S And), discovered by E. Hartwig in 1885, and the new determination of the Hubble scale distance, supposed that Andromeda was outside the Milky Way, and therefore, S And's intrinsic luminosity was exceptionally large. Thereafter, they started to call these two types of objects with different names. The first person to mention *giant novae* was Lundmark (1920), and in 1934, Baade & Zwicky denominated this class of high luminous objects *supernovae* (Baade & Zwicky, 1934).

On average a bright nova (m_v=3) can be seen per decade with the naked eye during some nights. However, its magnitude will decrease in the following days. Most of the first discoveries of novae were made in the Far East, by the imperial Chinese court around 200 BC, by the Korean around the time of Christ and by the Japanese in the 6$^{\rm th}$ century AD (Stephenson & Green, 2002). However, it was not until the end of the 19$^{\rm th}$ century that a large number of novae were discovered thanks to the Harvard College Observatory and later followed by other observatories in Germany and Russia. First, 'stellar patterns' were checked with binoculars. Around 1970, some regions were monitored with photographic plates and later with Charge-Coupled Devices (CCDs). Since the 1980s, most of the novae are discovered by amateurs, who are called 'nova hunters'. Around 50 novae explode every year in our galaxy, but only around 9 are discovered (Shafter, 2017). With the new robotic optical surveys on the ground, and the networks of amateurs around the world as the American Association of Variable Star Observers (AAVSO), we live a new era in the discovery of novae.

Thanks to launch of *XMM-Newton* and *Chandra*, and more specifically the *Swift* satellite, novae have been detected in hard X-rays (E: $1-50$ keV) the first hours/days after

the outburst in the last years. Previously, this emission had been detected with *ROSAT* and *RXTE*. These satellites allow to have the evolution of the shocked plasma from the early stages thanks to the fast action and their high resolution, improving the knowledge of the thermal plasma parameters. This hard X-ray emission detected in novae are due to the shock wave running into the circumstellar material. The shock heats the material and it emits as an optically thin plasma, mainly as a thermal bremsstrahlung continuum with lines excited by electron collisions. In the early stages of the explosion particle acceleration (p and e^-) may also occur. The high-energy γ-ray emission is a consequence of π^0 decay (hadronic process) and/or Inverse Compton (leptonic process). This emission can be detected by satellites as Fermi, launched in 2008, that detects photons at GeV energy range (Hernanz & Tatischeff, 2012).

Nowadays novae are routinely detected at E>100 MeV by the *Fermi* satellite, demonstrating that the particles are accelerated to relativistic energies due to strong shocks in the ejecta. This emission is still one of the least known and least understood in novae. In recent years, eight classical and two symbiotic recurrent novae have been detected. In most cases, a high energy emission has been observed early after the explosion, around the optical maximum, and for a short period of time (Abdo et al., 2010; Cheung et al., 2016b). In particular, this work is focused on the study of the symbiotic recurrent novae RS Oph and V745 Sco. RS Ophiuchi (2006) was the first nova for which particle acceleration was predicted (Tatischeff & Hernanz, 2007). This prediction stated that the blast wave decelerated faster than expected as a consequence of acceleration of particles in the shock. The last outburst of V745 Sco was detected by *Fermi* but only a marginal detection was obtained because of its distance ($\sim$8 kpc).

The aim of our thesis is to study the evolution of the symbiotic recurrent novae the first days after the outburst through a multiwavelength study, mainly X-ray emission, and its relation with the acceleration of particles. The present thesis work has been aimed to perform a comprehensive multiwavelength study of the last outburst of RS Oph and V745 Sco.

In this framework, our research deals the reduction and analysis of the several early X-ray observations from RS Oph and V745 Sco to obtain the evolution of the shocked plasma. Moreover, Infra Red (IR) and radio emission are also studied in this thesis. We therefore carry out a multiwavelength study that will allow in the future to understand better the γ-ray emission in novae. This thesis is organised according to the outline detailed below:

- **Chapter 2** presents a brief overview of past and current X-ray observations of novae. Moreover, a summary of the characteristics and the observations of the novae detected by Fermi is presented. Some of the concepts that will be employed in the subsequent analyses are presented, as the different scenarios of novae or the characteristics of the shock wave evolution in a SNR.

- **Chapter 3** presents the multiwavelength study performed for RS Oph. This multiwavelength campaign was carried out in the last outburst of RS Oph in 2006. The early X-ray observations by *XMM-Newton* are the main focus of our

study. The analysis is completed with *RXTE*, *Swift* and *Chandra* observations. A compilation of the early radio and IR emissions is carried out. The properties of the shocked plasma and the Red Giant (RG) wind are determined and compared with the results obtained by Tatischeff & Hernanz (2007).

- **Chapter 4** shows the early observations of the last outburst of V745 Sco in 2014. The reduction and the analysis of *Swift* and *Chandra* observations is described together with the *NuStar* observations. Moreover, a compilation of the early radio and IR emission is presented as in RS Oph. With this information and the marginal detection of *Fermi*, a study of the characteristics and the evolution of the shocked plasma and the RG wind, and its relation with the particle acceleration is carried out.

- **Chapter 5** describes the differences and the similarities of these two novae in the different wavelengths, from radio to high energy γ-rays, showing possible common features for all the symbiotic systems.

In the last chapter the conclusions of the study of both novae are presented, and also important ideas to take into account in future observational campaigns to understand the nature of the γ-ray emission.

2

THE HIGH ENERGY ERA OF NOVAE

2.1 DEFINITION AND SCENARIOS OF NOVAE

Nowadays, we know that a nova is a hydrogen TNR on an accreting white dwarf (WD) in a close binary system. A WD is the final stage of the evolution of stars with masses smaller than 10 $M_\odot$ and it is made of electron-degenerate matter. Its chemical composition can be He, CO or ONe. Its typical mass is 0.6 $M_\odot$, being CO WDs ($M_{WD} \leq$1.1 $M_\odot$) less massive than ONe WDs ($M_{WD} \geq$1.1 $M_\odot$). The maximum mass that a WD can reach is the Chandrasekhar mass $\sim$1.4 $M_\odot$. When a WD is isolated, it cools down to invisibility (L$\sim$ $10^{-4.5}$ $L_\odot$), but when it is in a binary system, it can eventually explode as a nova.

Novae can have a main sequence star companion. In this case, the companion fills its Roche lobe and the material is transferred onto the WD via an accretion disc. However, if the companion is a RG or a subgiant, the WD also captures the material from the stellar wind of the companion. The accreting matter forms a layer on top of the WD and the material is progressively compressed and heated by the strong surface gravity of the WD. When the companion star has transferred $\sim 10^{-4} - 10^{-5}$ $M_\odot$ to the WD, hydrogen ignition takes place in semi-degenerate conditions. The temperature increases in the layer below the accreting matter to 10^8 K, leading to the TNR (José & Hernanz, 1998; Bode & Evans, 2008, and references therein). Nova explosions do not destroy completely the WD in contrast to type Ia supernovae. As the explosion only affects the external hydrogen-rich layers, the outburst is expected to recur.

The explosion ejects outer layers into the circumstellar medium which causes the expulsion of a fraction of the accreted envelope. This in turn enriches the interstellar medium (ISM) with some elements. The ejecta is often enriched in C, N and O, and also heavier elements like Ne, Mg or S. The global heavy element abundances in nova ejecta are well above solar abundances. High abundances can not be only due to the TNR, because the temperatures in the explosion are not high enough. Therefore, the more accepted explanation is that there is some mixing between accreted matter and the underlying CO or ONe core.

There are two nova scenarios, cataclysmic variable and symbiotic binary system, with different properties.

Cataclysmic Variables (CVs) are close binary systems composed of a WD and a main-sequence star companion. The main sequence star fills its Roche lobe and mass is transferred onto the WD via an accretion disc. Typical orbital periods are between hours and days, and their orbital separations are around 10^{10} cm. The nova explosion occurs as the result of a TNR on the WD accreting H-rich matter from the main sequence companion. These nova explosions are called classical novae (CNe) and have long recurrence periods ($P_{rec} \sim 10^{4-5}$ yr). Therefore, only one outburst has been recorded. Their kinetic energy is 10^{45} erg, $M_{ejected}$ $10^{-6} - 10^{-3}$ $M_\odot$, L=10^5 $L_\odot$ and v_{ejec} $10^2 - 10^3$ km/s.

Symbiotic binaries are close binary systems in which the secondary star is a RG or an Asymptotic Giant Branch (AGB) star. In this case, the WD captures matter from the stellar wind of the RG companion. Moreover, the matter can be transferred via an accretion disc, as in CNe. They have an orbital period of around 100 days that is longer than the typical CV period, and their orbital separation is $10^{13} - 10^{14}$ cm. The type of symbiotic systems studied in this thesis are the recurrent novae (RNe) (Anupama & Mikolajewska, 1999). This type of novae have a short recurrence period ($P_{rec} < 100$ yr) because of a highly massive WD, probably close to the Chandrasekhar limit, together with a high accretion rate ($\sim 10^{-8} - 10^{-7}$ $M_\odot yr^{-1}$). For this reason, this type of novae is a possible scenario for SNe Ia. CN ejecta show overabundances compared to the Sun, which indicates some mixing between the core and the accreted mass. However, no large overabundances are observed in RNe because they only need a very small quantity of accreted mass to explode, and therefore, not much mixing occurs between the accreted envelope and the WD core.

Nowadays, and thanks to galactic and extragalactic surveys, we know a large number of recurrent novae (Anupama, 2008; Schaefer, 2010; Shafter et al., 2015). However, the *historical galactic recurrent novae* are a small and heterogeneous group of 10 members (T CrB, RS Oph, V3890 Sgr, V745 Sco, U Sco, V394 CrA, T Pyx, Cl Aql, V2487 Oph and IM Nor)(Anupama, 2008; Schaefer, 2010). Using the orbital period as a criterion, they are divided in two types: the long period and the short period ones.

- The *long period RNe* are RS Oph, T CrB, V3890 Sgr and V745 Sco. They have an orbital period of the order of 100 days as RS Oph ($P_{orb} \sim 456$ days) or as T CrB (P_{orb} ~228 days). The binary systems are composed of a hot WD and a giant, and their properties are similar for all the members of the group.
- The *short period RNe* are U Sco, V394 CrA, T Pyx, Cl Aql and IM Nor. Their orbital period is between 1.2 days (U Sco) and 0.07 days (T Pyx). These systems are composed of a WD and a main sequence star or a subgiant. Therefore, they are similar to classical novae but the nature of the recurrence makes them different. This group is very heterogeneous. However, their outbursts are very similar.

2.2 X-RAY EMISSION FROM NOVAE

X-ray observations of novae are a very powerful tool for their study, providing many fundamental and sometimes totally unexpected results. However, it is a recent source

of knowledge. X-ray observations allow to have a global view of the nova outburst, and to study the hot WD and shocks, deriving physical parameters such as the temperature, the emission measure (EM) or the duration of the H-burning on top of the WD. There are three mechanisms that produce X-rays in novae: hard X-ray emission originated by the shock (E > 1 keV), the soft X-ray emission due to the hot WD photosphere (E < 1 keV), and the re-establishment of accretion that occurs during quiescence because the disc is destroyed in the eruption (Patterson & Raymond, 1985a,b). In this work, we will focus on the two first mechanisms.

Nova observations before *Swift*, *XMM-Newton* and *Chandra*

The first nova detected in X-rays was GQ Mus 1983 by *EXOSAT* 460 days after the outburst at 0.04-2 keV (Ögelman et al., 1984), but the *EXOSAT* instruments did not have the necessary spectral resolution to determine the type of X-ray emission. In this case, the emission was interpreted as a WD emitting as a black body. The **soft X-ray emission** reveals the hot WD photosphere because of the remaining nuclear burning shell on top of the WD after its nova explosion. This emission becomes visible, when the ejecta becomes optically thin to soft X-rays. The depletion of the mass on top of the WD induces a decrease in the photosphere radius, and consequently, an increase in the effective temperature (T_{eff}) of the WD, reaching values up to 10^5 K. The duration of this emission is directly related to the amount of H-rich matter on top of the WD after the nova explosion. Not all novae are detected in soft X-rays and one of the reasons can be that the residual nuclear burning shell switched off before the ejecta became optically thin to soft X-rays. *EXOSAT* also observed other novae: PW Vul 1984, QU Vul 1984 and RS Oph in its 1985 outburst (Mason et al., 1987).

With the launch of *ROSAT* in 1990, there was the possibility to have spectral information about novae. It had a high sensitivity in the range of very soft X-rays and a modest spectral resolution with the Position Sensitive Proportional Counter (PSPC) instrument. During 10 years, 108 different classical and recurrent novae in outburst and in quiescence have been observed with *ROSAT* during the ROSAT All Sky Survey and in pointed observations (Orio et al., 2001a). GQ Mus 1983 was also observed five more times during its Super Soft Source (SSS) phase by *ROSAT*, which turned off 9 years after the nova outburst (Ögelman et al., 1993; Shanley et al., 1995). In theory, the soft X-ray spectra show ionization absorption edges and a continuum, but because of the resolution of *ROSAT* only the continuum was detected. Ögelman et al. (1993); Shanley et al. (1995) used a black body as a first order approximation to fit the soft X-ray emission of GQ Mus 1983. However, this emission can also be modelled by a hot atmosphere model. For instance, Balman & Krautter (2001) used MacDonald & Vennes (1991)'s atmosphere models to analyse the same observations (Figure 1).

ROSAT only detected two more novae during their SSS phase: V1974 Cyg 1992 and LMC 1995. The whole evolution of V1974 Cyg 1992 was observed, whose SSS phase was analysed using black body models (Krautter et al., 1996), and the MacDonald's atmosphere model (Balman et al., 1998). A hard X-ray tail was detected in all *ROSAT* observations of V1974 Cyg 1992. Its temporal evolution of the hard compon-

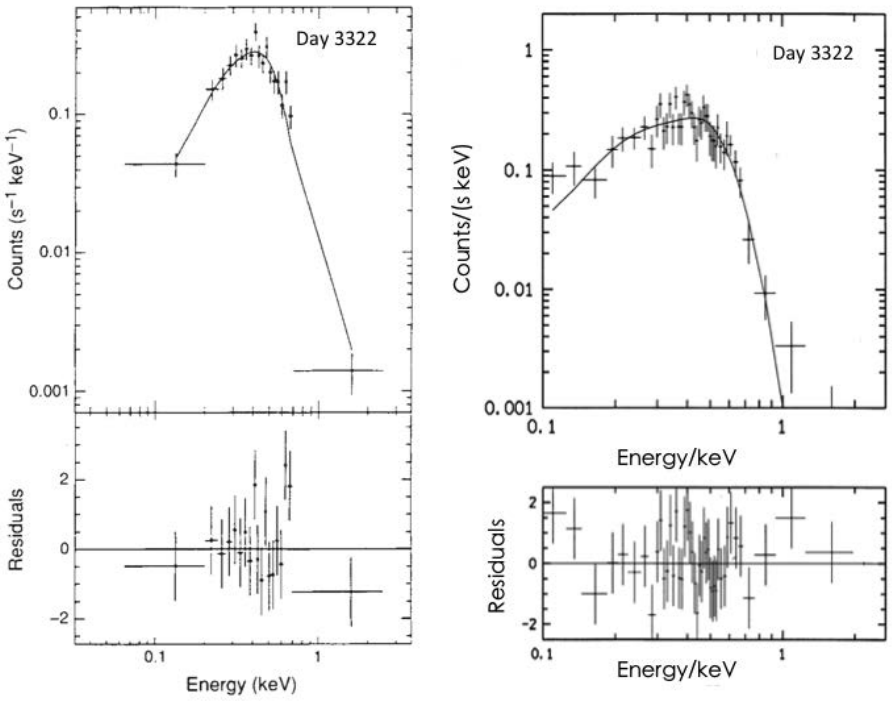

Figure 1: SSS emission of GQ Mus 1983 observed by *ROSAT*. Left panel: Spectrum fitted with a black body (adapted from Ögelman et al., 1993). Right panel: Spectrum fitted with an atmosphere model (adapted from Balman & Krautter, 2001).

ent was also analysed by Balman et al. (1998), using thermal plasma emission models (Raymond & Smith, 1977). LMC 1995 was observed several occasions during its SSS phase, which allowed to see the evolution of its SSS phase. It lasted almost 8 years and was analysed using a Local Thermodynamic Equilibrium (LTE) CO atmosphere model (Orio et al., 1997; Orio & Greiner, 1999).

The first nova whose early hard component was observed only 5 days after the outburst was V838 Her 1991 with *ROSAT* (Lloyd et al., 1992). This early **hard X-ray emission** is originated in the internal shocks in the ejecta, and/or in external shocks between the ejecta and the circumstellar medium, but we can not distinguish one from the other. When the shock heats the plasma, the observed X-ray emission corresponds to an optically thin collisional plasma whose most important processes are the continuum, mainly as a thermal bremsstrahlung continuum, and lines excited by electron collisions. The hard component of Nova Pup 1991 was also detected with *ROSAT*, but 16 months after the outburst (Orio et al., 1996). Its hard X-ray emission was interpreted as shocks in the ejecta shell or the re-establishment of accretion.

At this time there were other X-ray satellites that also detected some novae, for example *RXTE*, that was designed to observe the time variation of astronomical X-ray sources (see Appendix A), *Beppo-Sax*, which was the first X-ray mission capable to observe simultaneously between 0.1 and 300 keV, and *ASCA*, which was the first telescope with CCDs. The most important novae detected with them was V382 Vel 1999 (Figure 2). The first observation of *RXTE* was 5 days after the outburst, but no

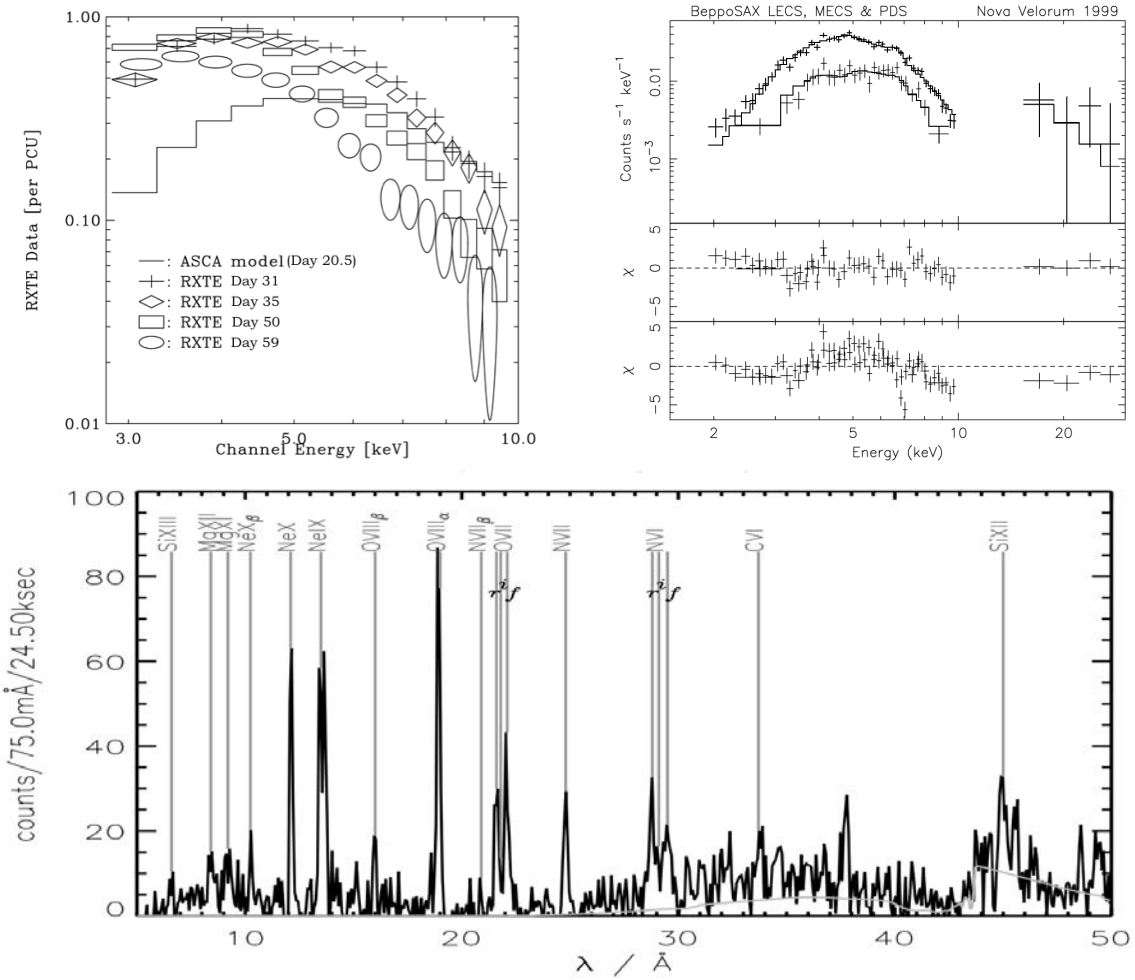

Figure 2: Hard X-ray emission of V382 Vel 1999 observed with *RXTE* and *ASCA* (adapted from Mukai & Ishida, 2001) (top left panel), and with *BeppoSAX* (from Orio et al., 2001b) (top right panel). Soft X-ray emission of V382 Vel 1999 observed by *Chandra* (from Ness et al., 2005)

significant results were obtained. However, 20 days after the outburst V382 Vel 1999 was detected with *ASCA*, and the temperature obtained in its analysis was kT∼10 keV. Similar results were obtained with *Beppo-Sax* 15 days after the outburst (Orio et al., 2001b). The subsequent *RXTE* observations allow to observe the evolution of the hard component, showing that the temperature decreased over time (Mukai & Ishida, 2001) (Left panel Figure 2). Moreover, 184 days after the outburst its super soft emission was detected for the first time with *Beppo-Sax*. This day both X-ray components, hard and soft, were observed (Orio et al., 2001b, 2002).

Swift, *XMM-Newton* and *Chandra* nova observations

The biggest step came at the end of the 20$^{\text{th}}$ century with the launch of *Chandra* and *XMM-Newton*, which improved the sensitivity and energetic resolution with their grating spectrometers (see Appendix A). For the first time, it was possible to obtain high resolution spectra in the X-ray range. These satellites, together with *Swift*, provide a high density of monitoring campaigns. *Swift* allows to know the X-ray evolution of novae with a good temporal coverage in different ranges of X-rays, and assists and facilitates the *XMM-Newton* and *Chandra* observations. Ness et al. (2007a) and Schwarz et al. (2011) summarized all the X-ray observations obtained with *Swift* until that moment. They obtained that, for instance, half of all novae detected by *Swift* show pre-SSS hard X-ray emission.

Several novae were observed with these satellites in the last years. This is the case of V382 Vel 1999. Its soft component was observed for the first time with high spectral resolution with *Chandra* around 250 days after the outburst (Starrfield et al., 2000; Burwitz et al., 2002; Ness et al., 2005). It was the first time that a spectrum showed emission lines dominating over an atmospheric emission (Figure 2). They stated that the emission lines were formed in a collisionally ionized and excited expanding shell. Its SSS phase lasted 8 months. LMC 1995 was also observed by *XMM-Newton* with the European Photon Imaging Camera (EPIC) during its SSS phase 6 years after the outburst. It was still a bright SSS and was analysed by Orio et al. (2003) using Non-LTE atmosphere models (Rauch, 1997). However, the SSS phase had already faded 8 years after the outburst as was seen in a *XMM-Newton* observation.

XMM-Newton and *Chandra* have made us notice that novae are highly variable sources, both on long time-scales and short time-scales during its SSS phase. In the SSS light curve of V1494 Aql 1999 obtained with *Chandra* observations both a short time-scale X-ray 'burst' and oscillations was found for the first time (Drake et al., 2003). In addition, stronger variations were seen in the SSS light curve of V4743 Sgr 2002 obtained also with *Chandra* observations, showing large-amplitude oscillations with a period of 22 minutes (Ness et al., 2003). *XMM-Newton* and *Chandra* grating X-ray spectra during the SSS phase were also analysed by Rauch et al. (2010) using Non-LTE model atmospheres.

V723 Cas 1995 had the longest SSS phase, which lasted 12 years. It was observed by *Swift* in 2006-2007 but these observations did not conclusively demonstrate the ex-

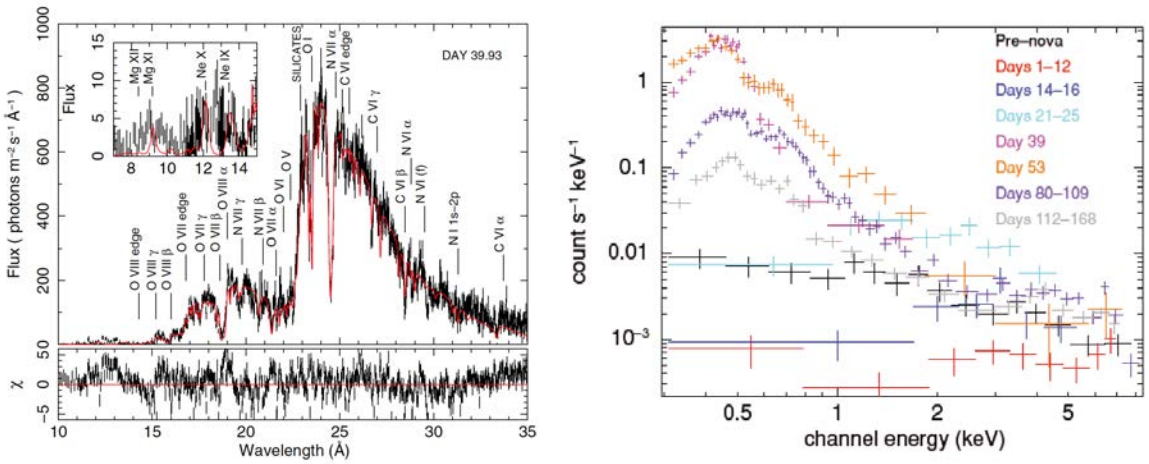

Figure 3: SSS emission of V2491 Cyg observed by *XMM-Newton* (from Pinto et al., 2012) (left panel), and by *Swift* (from Page et al., 2010) (right panel).

istence of this phase. Nevertheless, in 2010 it was detected by *XMM-Newton* which confirmed the presence of the super soft emission (Ness et al., 2008). V5115 Sgr 2005a and V5116 Sgr 2005b were detected with *XMM-Newton* and *Chandra* during their SSS phase. V5116 Sgr 2005b shows an abrupt increase and decrease of its flux (Sala et al., 2007, 2008, 2017). During the low-flux periods, the spectrum was dominated by an atmosphere, but during the high-flux period, several emission features were superimposed over the atmosphere. These emission lines are well modelled with an optically thin plasma in collisional equilibrium. They suggested a partial eclipse produced by an asymmetric disk. Its turn-off was between 2 and 3 years after the outburst.

RS Oph in its last outburst in 2006 was very well observed in X-rays during all its evolution, showing an early hard X-ray emission since the RG wind is swept-up by the fast nova ejecta, and also showing variations in the SSS phase. In this thesis we have studied in detail the early hard X-ray observations of this emblematic nova and its possible acceleration of particles suggested by Tatischeff & Hernanz (2007) (Chapter 3). The fast nova V2491 Cyg 2008 was detected by *Suzaku* 9 and 29 days after the outburst between 1 and 70 keV (Takei et al., 2009). They argue a non thermal origin for this emission, suggesting the presence of accelerated charged particles in the nova explosion. It was also monitored with *Swift* (Figure 3), whose SSS phase spectra were fitted to a simple black body model (Page et al., 2010). Two additional high resolution observations with *XMM-Newton* were studied by Ness et al. (2011) and Pinto et al. (2012) using hydrodynamic atmosphere models (van Rossum & Ness, 2010). V2491 Cyg 2008 has great similarities with RS Oph in the SSS phase (Ness et al., 2011). However, their early hard X-ray emission was very different between them, because in V2491 Cyg 2008, that is a CN, the hard X-ray emission was due to internal shocks in the ejecta.

Other recurrent novae were observed in X-rays in their last outburst. U Sco was detected with *XMM-Newton* (Ness et al., 2012b) and *Chandra* (Orio et al., 2013) in its last outburst in 2010. *XMM-Newton* observations 23 and 35 days after the outburst showed two full passages of the companion in front of the nova ejecta and the reform-

ation of the accretion disk. Both *Chandra* and *XMM-Newton* observations showed evidences for Thompson scattering of the photospheric emission from the WD. In the last outburst of T Pyx in 2011, it was detected with the *Chandra* and *XMM-Newton* gratings (Tofflemire et al., 2013), and with *Swift* and *Suzaku* (Chomiuk et al., 2014b). The emission lines obtained with the grating data are consistent with a high-density plasma in collisional ionization equilibrium (Tofflemire et al., 2013). During the SSS phase a partial obscuration of the WD was showed suggesting a non-spherical ejecta. The hard X-ray emission was attributed to internal shocks into the 2011 nova ejecta, because of a dual-phase ejection (Chomiuk et al., 2014b). Finally, in 2014 the recurrent nova V745 Sco was observed with *Swift*, *NuStar* and *Chandra*. It was observed with *Swift* only 4 hours after the optical discovery and also had the fastest SSS phase. We will see more details in Chapter 4.

XMM-Newton and *Chandra* with the help of *Swift* have carried out a dedicated monitoring of M31 novae in X-rays during their SSS phase (Henze et al., 2010, 2011, 2014). Thanks to this monitoring of M31, the nova with the shortest recurrent period (1 year) has been detected (M31N 2008-12a, Darnley et al., 2016, and references therein), whose SSS phase appeared 6 days after the outburst and switched off 16 days later.

Finally, it is worth mentioning that thanks to the *XMM-Newton* observations, the re-establishment of accretion in a nova was found for the first time, observing V2487 Oph 1998 between 2.7 - 8.8 years after its discovery (Hernanz & Sala, 2002a). It was also observed with *ROSAT* in 1990, being the first novae seen in X-rays before and long after the explosion (Hernanz & Sala, 2002a). Two more novae, V4633 Sgr 1998 (Hernanz & Sala, 2002b) and V2491 Cyg 2008 (Ibarra et al., 2009; Takei et al., 2011), were detected in this phase.

An important point to consider is that the presence of hard X-ray emission requires a fast ejecta to produce the shock with a preexisting slower material. The detection of some novae in very high energy γ-rays with *Fermi*, implies that the shocks in novae are also capable of accelerating particles, increasing our interest in the ejecta physics.

2.3 FERMI NOVAE

In the last 10 years novae have been detected at GeV energies by the *Fermi* satellite, suggesting that particles are accelerated to relativistic energies by strong shocks in the ejecta. The *Fermi* satellite was launched in 2008, having two instruments on board, the Large Area Telescope (LAT) which performs an all-sky survey covering an energy range between 30 MeV and 300 GeV, and the Gamma-ray Burst Monitor (GBM) (see Appendix A).

RS Ophiuchi was the first nova for which particle acceleration was predicted (see Chapter 3). This prediction showed that the blast wave decelerated faster than expected as a consequence of the acceleration of particles in the shock (Tatischeff & Hernanz, 2007). The first nova detected by *Fermi* at high-energy γ-rays was V407 Cyg in 2010

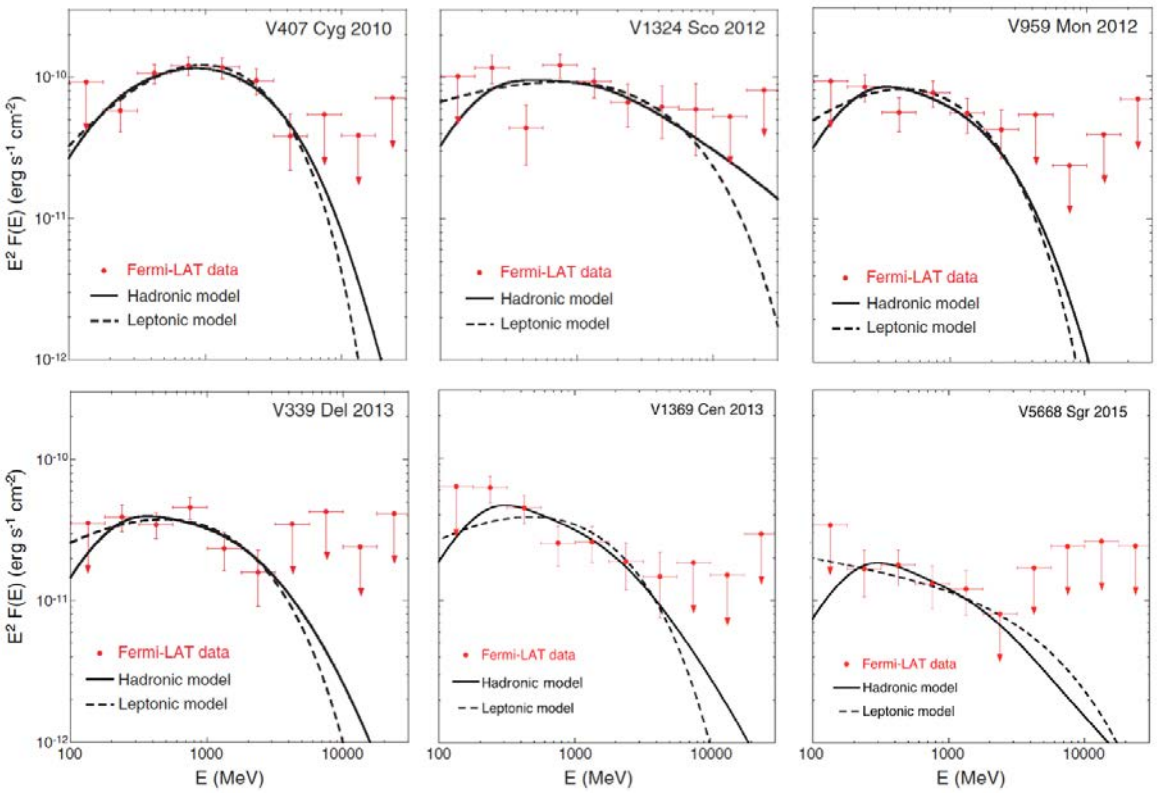

Figure 4: Best-fit hadronic (solid lines) and leptonic (dashed lines) models and *Fermi*-LAT data (red dots) for E> 100 MeV of the six first novae detected by *Fermi*-LAT (adapted from Ackermann et al., 2014; Cheung et al., 2016b).

(Abdo et al., 2010). V407 Cyg is a symbiotic recurrent novae with a Mira companion. Three outbursts have been recorded, in 1936, 1998, and the last one in 2010. Its distance was estimated between 1.9 kpc (Kolotilov et al., 1998) and 2.7 kpc (Munari et al., 1990). The detection by *Fermi* was on 2010 March 10, the same day as the discovery of the optical outburst. Thanks to this detection it was demonstrated that novae can produce GeV photons. Up to now, 10 novae have been detected by *Fermi*/LAT, eight classical novae: V1324 Sco, V959 Mon, V339 Del, V1369 Cen, V5668 Sgr, Nova Lup, V5855 Sgr and ASASSN-16ma, and two recurrent novae: V407 Cyg and V745 Sco. They are listed in Table 1.

The γ-ray light curves show that the γ-ray emission starts (with a slight delay) at the same time as the optical maximum (Figure 2 of Ackermann et al., 2014) and (Figure 1 of Cheung et al., 2016b). V1369 Cen and V5668 Sgr have a peculiarity with respect to the other novae detected by *Fermi*, because they had multiple maxima in the optical associated to different shocks in the ejecta or different outbursts from the WD surface. These different maxima were observed during 40 and 60 days respectively, probably associated to their long γ-ray emission duration (Cheung et al., 2016b). These two novae had low values of total energies and total number of emitted photons. A larger number of novae detected by *Fermi* would be needed to know if these low values are related to the physics of the outburst.

Table 1: Summary of the novae detected by *Fermi*

System	RS Oph[1]	V407 Cyg[2,3,8]	V1324 Sco[4,8]	V959 Mon[5,8]	V339 Del[6,8]	V1369 Cen[7,12]	V745 Sco[9]	V5668 Sgr[10,12]	Nova Lup[11]	V5855 Sgr[13]	ASASSN[11] −16ma
year	(2006)	2010	2012	2012	2013	2013	2014	2015	2016	2016	2016
Distance (kpc)	1.6	2.7	4.5	3.6	4.2	2.5	8	2	?	?	?
Nova class	RN	RN	CN	CN	CN	CN	RN	CN	CN	CN	CN
γ-ray emission											
Fermi/LAT detection	X	√	√	√	√	√	upper limits	√	√	√	√
Days after optical maximum	-	0	-4	?	0	1.5	1	1.5	1	0	13
γ-ray duration (days)	-	22	17	22	27	40	1	60	3	4	9
γ-ray flux $\times 10^{-7}$ph cm^{-2}s^{-1}	predicted	14	13	14	4	5.7	3	1.4	1.8	2.6	9.7
X-ray Observations											
Telescope (Days after discovery)	RXTE(3)[15] Swi.(3)[16] Chan.(13)[17,18,19] XMM(13)[18,19]	Swi.(3)[20] Suz.(29)[20]	-	Swi.(58)[21] Suz.(95)[22] Chan.(82)[23]	Swi.(41)[24] Chan.(88)[25] XMM(99)[26]	Swi.(85)[27]	Swi.(0.16)[28] NuS.(10)[29] Chan.(16)[30]	Swi.(90)[31]	Swi.(150)	NuS.	Swi.(120)

1.Tatischeff & Hernanz (2007), 2. Cheung et al. (2010), 3.Abdo et al. (2010), 4.Cheung et al. (2012a), 5.Cheung et al. (2012b),6.Cheung et al. (2013a), 7.Cheung et al. (2013b), 8.Ackermann et al. (2014), 9.Cheung et al. (2014), 10.Cheung et al. (2015), 11.Cheung et al. (2016a), 12.Cheung et al. (2016b), 13.Li & Chomiuk (2016), 14.Li et al. (2016), 15.Sokoloski et al. (2006), 16.Bode et al. (2006), 17.Drake et al. (2009), 18.Nelson et al. (2008), 19.Ness et al. (2009), 20.Nelson et al. (2012a), 21.Page et al. (2013), 22.Mukai et al. (2014), 23.Orio & Pa (2012), 24.Page & Beardmore (2013), 25.Nelson et al. (2013), 26.Ness et al. (2013), 27.Page et al. (2014), 28.Page et al. (2015b), 29.Orio et al. (2015), 30.Drake et al. (2016), 31.Page et al. (2015a).

*Swi.(Swift), Chan.(Chandra), XMM(XMM-Newton), Suz.(Suzaku) and NuS.(NuSTAR).

Figure 4 shows the spectra of six of the novae detected with *Fermi*/LAT with two possible fits: hadronic model (solid line) and leptonic model (dashed line):

- **The Inverse Compton** (leptonic case) involves the scattering of photons to high energies by ultra-relativistic electrons. The photons gain energy, opposite to the Compton effect (Longair, 1999).
- In **the decay of neutral pions** (hadronic case), the neutral pions are created by the interactions between relativistic protons and nuclei of atoms and ions of the surrounding gas ($p + p \rightarrow \pi^+, \pi^-, \pi^0$). π^0 decays into a pair of very high-energy γ-rays with E>100 MeV ($\pi^0 \rightarrow \gamma + \gamma$), whereas, π^+ and π^- decay into muons and neutrinos (Longair, 1999).

Both models fit the data correctly but there are differences at around 100 MeV where in all cases only upper limits were obtained observationally. In all the spectra detected by *Fermi*, it is not possible to distinguish between the hadronic or the leptonic scenario. All γ-ray detected novae are remarkably similar, with a soft spectra and emission detected up to few GeV. This suggests a possible common γ-ray emission mechanism involving interactions of the accelerated high-energy protons (hadronic scenario) and/or electrons (leptonic scenario) within the ejecta. The problem is that their underlying binary systems are very different, so the γ-ray emission mechanism was probably distinct.

V745 Sco is the only nova detected with *Fermi* whose hard X-ray emission was observed the first hours after the outburst (see Chapter 4). V407 Cyg was observed in X-rays by *Swift* and *Suzaku* whose observations took place 28.9 days after the outburst (Nelson et al., 2012a). They found that the X-ray evolution is consistent with the shock wave running into the dense wind of the Mira companion. V959 Mon 2012, unlike the other novae, was first detected in γ-rays, even before in optical or X-rays. When discovered by *Fermi*, it was too close to the Sun for follow-up observations from optical to X-rays. Finally, V959 Mon 2012 was monitored by *Swift* 58 days after the outburst (Nelson et al., 2012b; Page et al., 2013), and was also observed with *Suzaku* and *Chandra*. These observations are consistent with two systems of ejecta whose collision resulted in a shock (Mukai et al., 2014; Orio & Pa, 2012; Ness et al., 2012a). No X-ray detection was obtained in the case of V1324 Sco 2012. Fermi novae X-ray observations are listed in Table 1. An interesting case is T Pyx (distance ∼5 kpc). This nova was not detected with Fermi in its last outburst in 2011. However its hard X-ray emission was attributed to internal shocks into the nova ejecta. Chomiuk et al. (2014b) suggested a dual-phase ejection with a delay between both phases. This dual ejection was also consistent with radio and optical observations of T Pyx (Nelson et al., 2014; Surina et al., 2014).

Early radio observations play a crucial role in the interpretation of particle acceleration in novae. The location of the γ-ray production was observed for the first time in a nova, thanks to the high-resolution images of V959 Mon with the Very Long Baseline Interferometry (VLBI). It is the first CN whose synchrotron emission due to the outburst has been observed (Chomiuk et al., 2014a). The radio images were interpreted as a gas that was expelled rapidly along the poles, while a dense equatorial material was

propelled by orbital motion. In most of the novae the radio emission is dominated by the thermal bremsstrahlung (free-free emission). However, in some cases, as in V959 Mon or V745 Sco, synchrotron (non-thermal emission) is also observed the first days after the outburst. In order to have synchrotron emission, a significant population of relativistic electrons which have been accelerated in the shocks is needed in addition to a magnetic field. The study of the radio emission is a powerful tool to understand the γ-ray emission at very high energies.

Another type of long-studied γ-ray emission is that produced by radioactive nuclei. These radioactive nuclei are produced in novae in their thermonuclear explosion, which produce γ-rays in the MeV range when they decay (José & Hernanz, 1998; Hernanz, 2015, and references therein). ^{7}Be and ^{22}Na decays produce a long-lasting γ-ray emission that can be observed during 2 months and 3 years respectively. These emissions produce lines at 478 keV, in the case of CO WD novae, and at 1275 keV, in the ONe WD novae respectively. Some attempts to detect ^{7}Be and ^{22}Na in novae were made with the COMPTEL instrument on board the Compton Gamma-Ray Observatory (CGRO) satellite, and with the GRS instrument on board the Solar Maximum Mission (SMM) satellite, but only upper limits have been obtained (Harris et al., 1991; Iyudin et al., 1995). Nowadays these γ-ray emissions can be observed with *INTEGRAL*. V5668 Sgr was by chance in the field of view of *INTEGRAL* before and after its optical maximum. No detection has been obtained up to now, because the exposure time was shorter than needed. However, in near UV ^{7}Be was detected for the first time in V339 Del with *Subaru* 8.2 m (Tajitsu et al., 2015; Hernanz, 2015). ^{7}Be detection was confirmed in V5668 Sgr with *Subaru* 8.2 m and *VLT* (Tajitsu et al., 2016; Molaro et al., 2016). This discovery was possible thanks to the excellent spectral resolution of the instruments. Another important improvement was the discovery of ^{7}Li, that is the daughter of ^{7}Be, in novae. It was detected in V1369 Cen in optical (Izzo et al., 2015), but other identifications can also be possible.

2.4 CHARACTERISTICS OF THE SHOCK WAVE EVOLUTION

In general, a shock wave is produced by a supersonic compressive perturbation, which propagates faster than the local sound velocity and produces irreversible changes in the state of the fluid, increasing its entropy (Shull & Draine, 1987). We shall show a simple set of equations that describe a shock and agree on a basic coordinate system that will be employed in the remainder of this thesis.

Figure 5 shows the picture of the shock from the point of view of the observer (left panel) and in its own rest frame (right panel). A fluid flows into front from the right with a velocity u_1 out, to the left with velocity u_2. At $x = 0$ the flow velocity changes abruptly from u_1 to a slower velocity u_2 and then continues to the infinity. In this section we adhere to the convention that the subindex 1 refer to quantities measured

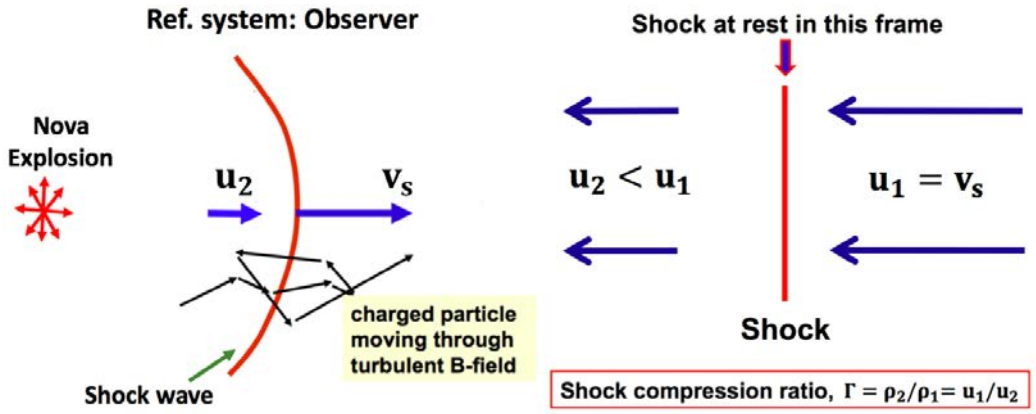

Figure 5: Diagram of the principle of diffusive acceleration in a shock wave which propagates with a shock velocity v_s into a medium with density ρ_1, temperature T_1 and pressure P_1. The ejected material has a velocity u_2 with density ρ_2, temperature T_2 and pressure P_2. In the reference system of the shock front the upstream material flows towards the shock with velocity $u_1 = v_s$ and the downstream material moves away with velocity $u_2 = v_s/\Gamma$ where Γ is the shock compression ratio (adapted from Ellison, 2013).

upstream and 2 to those measured downstream (Jones & Ellison, 1991).

The relation between u_1, ρ_1, T_1, P_1, and u_2, ρ_2, T_2 and P_2 can be derived for a steady-state, plane-parallel shock, where velocity is perpendicular to the shock front and the properties depend only on the distance to the front. The Rankine-Hugoniot jump conditions for a plane-parallel steady state shock are

$$\text{Conservation of mass: } \rho_1 u_1 = \rho_2 u_2 \tag{1}$$

$$\text{Conservation of momentum: } P_1 + \rho_1 u_1^2 = P_2 + \rho_2 u_2^2 \tag{2}$$

$$\text{Conservation of energy: } \frac{1}{2}\rho_1 u_1^3 + \frac{\gamma}{\gamma-1} P_1 u_1 = \frac{1}{2}\rho_2 u_2^3 + \frac{\gamma}{\gamma-1} P_2 u_2 \tag{3}$$

where γ is the adiabatic index ($= 5/3$ for monoatomic gas). Using the Rankine-Hugoniot relations, the shock compression ratio is given by $\Gamma = \dfrac{\rho_2}{\rho_1} = \dfrac{u_1}{u_2} = \dfrac{(\gamma+1)M_S^2}{(\gamma-1)M_S^2+2}$ where M_S is the sonic Mach number ($M_S = v_s/c$).

$M_S \gg 1$ corresponds to a strong shock, then $\Gamma \approx \dfrac{\gamma+1}{\gamma-1} = 4$ for a monoatomic gas with $\gamma = 5/3$. According to Figure 5, the upstream material flows towards the shock with velocity $u_1 = v_s$ and the downstream material moves away with velocity $u_2 = v_s/\Gamma$. Using the ideal gas law, $P_2 = \rho_2 k T_2/(\mu m_H)$, and Equations 1 and 2, we obtain that for a strong shock

$$P_2 = \rho_1 u_1^2 - \rho_2 u_2^2 = \rho_1 u_1 (v_1 - u_2) = \rho_1 v_s^2 (\Gamma - 1)/\Gamma \tag{4}$$

where P_1 is considered negligible compared with $\rho_1 u_1^2$. From the ideal gas law and Equation 4, the relation for a test-particle strong shock is obtained

$$kT_2 = \frac{3}{16}\mu m_H v_s^2 \tag{5}$$

where k is the Boltzmann constant and μm_H is the mean particle mass.

In a spherical expansion with a uniform density, the simple velocity distribution is given by $u_1 = v_s = (R/t)$, where R is the outer boundary, and the ejected mass is $M_{eje} = (4/3)\pi\rho_1 R^3$. In this situation, the kinetic energy and the internal energy are

$$E_{kin} = \frac{1}{2}M_{ej}u_1^2 = \frac{2}{3}\pi\rho_1 u_1^2 R^3 = \frac{2}{3}\pi\rho_1\frac{R^5}{t^2} \tag{6}$$

$$E_{thermal} = \frac{3}{2}PV = \frac{3}{2}P_2\left(\frac{4\pi}{3}\right)R^3 = 2\pi\rho_1 V_s^2 R^3 = 2\pi\rho_1\frac{R^5}{t^2} \tag{7}$$

This suggests that the thermal energy is of the same order of the kinetic energy. Then for the total energy, which is a conserved quantity, we expect

$$E_{total} = E_{kin} + E_{thermal} \propto \rho_1\frac{R^5}{t^2} \tag{8}$$

In this thesis, we will take into account all these relations to understand the conditions of the shocks and the acceleration of particles in them.

2.4.1 *SNR Phases*

The supernova remnants go through different phases over time. These phases can last millions of years. For nova explosions, if these phases occur, they only last for short periods of time (Vink, 2012, and references therein). All the numerical details can be seen in Appendix E and are summarized in Table 2. We now describe the phases supernovae and novae go through.

Phase I: Free expansion ($M_{ej} \gg M_{sw}$). This phase is the irruption of the ejecta moving at constant velocity ($v_s \sim cont$) into the circumstellar medium (Woltjer, 1972). The ejecta dominates this phase because the ejected mass is larger than the swept-up matter (M_{sw}). The duration of this phase will depend on the amount of matter swept by the shock. When the swept matter is larger than the ejected mass, the remnant will move to the phase II. In supernovae, it can go on from a few weeks to several years. This phase can last from days to weeks in novae.

Phase I $\rightarrow$ II: Self-similar driven wave ($M_{ej} \geq M_{sw}$). This phase is an intermediate phase between the free expansion (Phase I) and the Sedov-Taylor phase (Phase II). It occurs when the shock starts to slow down, the expanding ejecta runs into the swept-up circumstellar medium and a reverse shock appears. In this intermediate phase the supernova remnant develops a characteristic structure from the center outwards: ejecta, reverse shock into the ejecta, shocked ejecta, contact discontinuity, shocked circumstellar medium and forward shock into the circumstellar medium. Under these conditions, the energy radiated away by the shocked material has no impact on the dynamics of the SNR. The expanding medium and the stationary circumstellar medium have a power law density profile ($\rho \propto r^{-n}$ and $\rho \propto r^{-s}$ respectively). As the density profiles are approximated with a power law, the evolution during this stage can be analytically

described by a self-similar driven wave solution (Chevalier, 1982b).

Different values of s and n describe the density profiles of Type I and Type II supernovae (Chevalier, 1982b). Type I supernovae expand with a density profile $\rho \propto r^{-n}$ with $n = 7$ (Colgate & McKee, 1969), into a uniform medium ($s = 0$) with $R \propto t^{4/7}$ (Chevalier, 1981). In Type II supernovae, unlike in Type I supernovae, the progenitor is surrounded by a circumstellar density distribution of matter ($s = 2$). Therefore, $R \propto t^{(n-3)/(n-2)}$ because n>5 (Chevalier, 1982c).

Phase II: Adiabatic phase or Sedov-Taylor phase ($M_{ej} \ll M_{sw}$). In this phase the swept-up mass dominates over the ejecta and the remnant forgets its early history. The total energy is about the same as the explosion energy because the radiative losses are negligible. According to Sedov (1959), this occurs when a large amount of energy is released into uniform ambient medium, creating a strong explosion characterized by a strong shock wave emanating from the point where the energy was released. The mass of the swept-up material is of the order of $M(t) \sim \rho R^3(t)$ and the velocity of the expanding ejecta, $v_s(t) \sim R/t$. In this situation, the motion of the shock tends to follow the law $R \propto (E/\rho)^{1/5} t^{2/5}$. However, if the circumstellar medium has a $\rho_W(R) \propto R^{-2}$ ($s = 2$), then R becomes proportional to $(E/\rho)^{1/3} t^{2/3}$. In supernova remnants, this phase lasts up to $\sim$ 1000 years after the outburst. In novae, it can last up to few months.

Phase III: Radiative snow-plow ($t > t_{rad}$) This phase is dominated by radiative losses. The radial expansion is governed by momentum conservation, $Mv = 4\pi/3 R^3 \rho \, dR/dt$. According to Truelove & McKee (1999, Appendix A), $\rho = M_{ej}/(4\pi/3) \; R^{(3-s)}$ in this phase. In this phase, the inner parts of the SNR are still expanding adiabatically and push the outer shell due to its pressure. At the time for which radiative losses become important, t_{rad}, the transition from the Sedov-Taylor phase to the radiative snow-plow phase occurs. At this time, the remnant will have a radius $R \propto t^{1/(4-s)}$, which is the observed radius. Thus, velocity will be $v \propto t^{(s-3)/(4-s)}$

Phase IV: Merging with the ISM. Finally, the shock wave slows, cools and becomes subsonic. The expansion velocity of the remnant becomes comparable to that of interstellar gas ($\sim$10 km/s). As a consequence of that, the shock wave loses its identity and merges into the interstellar medium (Woltjer, 1972).

Table 2: Summary of the different phases

Phase	n	s	$R \propto t^{\frac{(n-3)}{(n-s)}}$	$v \propto t^{\frac{(s-3)}{(n-s)}}$	Ref.
Supernova I (ρ_1 =const.)					
Phase I	-	-	$\propto t^{1}$	cte	Woltjer (1972)
Phase I$\rightarrow$ II	7	0	$\propto t^{4/7}$	$\propto t^{-3/7}$	Chevalier (1982b)
Phase II	5	0	$\propto t^{2/5}$	$\propto t^{-3/5}$	Sedov (1959)
Phase III	4	0	$\propto t^{1/4}$	$\propto t^{-3/4}$	Woltjer (1972)
Phase IV	-	-	cte	0	Woltjer (1972)
Supernova II ($\rho_1 \propto r^{-2}$)					
Phase I	-	-	$\propto t^{1}$	cte	Woltjer (1972)
Phase I$\rightarrow$ II	>5	2	$\propto t^{\frac{(n-3)}{(n-2)}}$	$\propto t^{\frac{(-1)}{(n-2)}}$	Chevalier (1982c)
Phase II	5	2	$\propto t^{2/3}$	$\propto t^{-1/3}$	Chevalier (1982a)
Phase III	4	2	$\propto t^{1/2}$	$\propto t^{-1/2}$	Truelove & McKee (1999)
Phase IV	-	-	cte	0	Woltjer (1972)

3

RS OPH

3.1 INTRODUCTION

RS Ophiuchi (RS Oph) is a symbiotic recurrent nova composed of a massive WD orbiting a RG companion whose mass is ∼0.5 $M_\odot$, and its estimated spectral type is M0/2III (Bohigas et al., 1989; Anupama & Mikolajewska, 1999). Its orbital period is 455.72±0.83 days (Fekel et al., 2000), if a low inclination (i∼40°) and a WD near the Chandrasekar limit are adopted (Shore et al., 1996; Dobrzycka & Kenyon, 1994; Ribeiro et al., 2009). It is believed that the RG underfills its Roche lobe, and therefore, the accretion process takes place through the RG wind and not through the Roche lobe overflow as in classical novae. However, both processes, stellar wind capture and Roche lobe overflow, can be considered as the mass transfer mechanisms in RS Oph (Wynn, 2008).

Its five previous recorded outbursts took place in 1898, 1933, 1958, 1967 and 1985 (Rosino, 1987; Rosino & Iijima, 1987). During the period between the 1898 and the 1933 outbursts, RS Oph was not considered a recurrent nova. An unobserved outburst might have taken place between these years. Schaefer (2004) suggested that RS Oph probably had an outburst in 1907 while it was hidden by the Sun. Besides, there are some evidences for another outburst in 1945 obtained studying the AAVSO visual data from 1920 to mid-1993 (Oppenheimer & Mattei, 1993). If we look at the time interval between outbursts, we see that the recurrence period of RS Oph is very irregular, between 9 and 26 years. An inter-outburst period as short as 9 years must be due to a combination of high-WD mass and a high accretion rate (Nomoto et al., 1984). Its accretion rate has been estimated by Snijders (1987) ($\dot{M}_{acc} \sim 5 \times 10^{-8}$ $M_\odot$ yr^{-1}) using UV observations in quiescence and by Worters et al. (2007) ($\dot{M}_{acc} \sim 10^{-10}$ to 10^{-9} $M_\odot$ yr^{-1}) based on V-band variability.

The distance to RS Oph has been widely discussed in the literature. There are estimated values from ≤540 pc to 4.2 kpc. Monnier et al. (2006), for instance, determined the distance to be ≤540 pc using infrared interferometry. This value is one of the lowest estimations. The same distance was also obtained by the Hachisu & Kato (2000, 2001) models. Hjellming et al. (1986) used Karl G. Jansky Very Large Array (VLA) radio observations and obtained that RS Oph is at a distance close to 1.6 kpc with an ISM absorption N_H=2.4×10^{21} cm^{-2}. However, Rupen et al. (2008) determined that the distance to RS Oph is 2.45 kpc comparing the angular size observed with VLBI with the radius inferred from optical, X-ray and IR observations. Finally, Schaefer (2010) obtained the farthest distance (4.2 kpc) using different methods to calculate the distance through the effective surface temperature. A summary of the different distances

Table 3: Observations of RS Oph

Days after discovery	Wavelength	Telescope	Reference
0	Optical		Hirosawa et al. (2006)
*	γ-rays		Tatischeff & Hernanz (2007)
3-21	X-rays	RXTE	Sokoloski et al. (2006)
3-820	X-rays	Swift/XRT	Bode et al. (2006); Osborne et al. (2011)
0-20	X-rays	Swift/BAT	Bode et al. (2006)
13-239	X-rays	XMM-Newton	Ness et al. (2007b, 2009); Nelson et al. (2008)
13-208	X-rays	Chandra	Ness et al. (2007b, 2009) Nelson et al. (2008); Drake et al. (2009)
1-47	IR	1.2m Mount Abu	Das et al. (2006); Banerjee et al. (2009)
4-65	IR	Keck	Monnier et al. (2006)
11-55	IR	UKIRT	Evans et al. (2007)
11-284	Radio	GMRT	Kantharia et al. (2007)
13-60	Radio	VLA	O'Brien et al. (2006); Rupen et al. (2008) Sokoloski et al. (2008); Eyres et al. (2009)
4-50	Radio	MERLIN	Eyres et al. (2009)
16-38	Radio	OCRA-p	Eyres et al. (2009)

* Particle acceleration was deduced by Tatischeff & Hernanz (2007)

is presented in Barry et al. (2008). They highlighted the importance of the escape of cosmic rays in the nova outbursts predicted by Tatischeff & Hernanz (2007) because it has important effects in the measurements of luminosity and can change the resulting distance. Finally, we adopt a distance of 1.6±0.3 kpc in this chapter, because this value has been determined by different methods (Hjellming et al., 1986; Bode & Kopal, 1987; Barry et al., 2008).

Since 1898, there have been detections of RS Oph at different wavelengths. The first observation of RS Oph in X-rays was 55 days after its 1985 outburst by *EXOSAT* and low-resolution spectra were obtained (Mason et al., 1987; O'Brien et al., 1992). In the last outburst in 2006, RS Oph was observed at practically all wavelengths and we can say that it is one of the best known novae. Its last outburst was first discovered on 2006 February 12.83 (Hirosawa et al., 2006) and it reached a magnitude of V=4.5 mag. We define this date as t=t_0 throghout the rest of the chapter. The optical light curve had a rapid decline, consistent with previous outbursts (Rosino, 1987). The interstellar absorption, $N_{H,ISM} = (2.4 \pm 0.6) \times 10^{21}$ cm^{-2}, has been determined from H_I 21 cm measurements (Hjellming et al., 1986). This value is consistent with the visual extinction (E(B-V)=0.73±0.1) determined from International Ultraviolet Explorer (IUE) observations in 1985 (Snijders, 1987). However, other authors adopt a value of the interstellar medium absorption of $N_{H,ISM} = 4 \times 10^{21}$ cm^{-2} (Sokoloski et al., 2006, and references therein). RS Oph was observed in radio (O'Brien et al., 2006; Rupen et al., 2008; Kantharia et al., 2007; Sokoloski et al., 2008; Eyres et al., 2009), visible, infrared

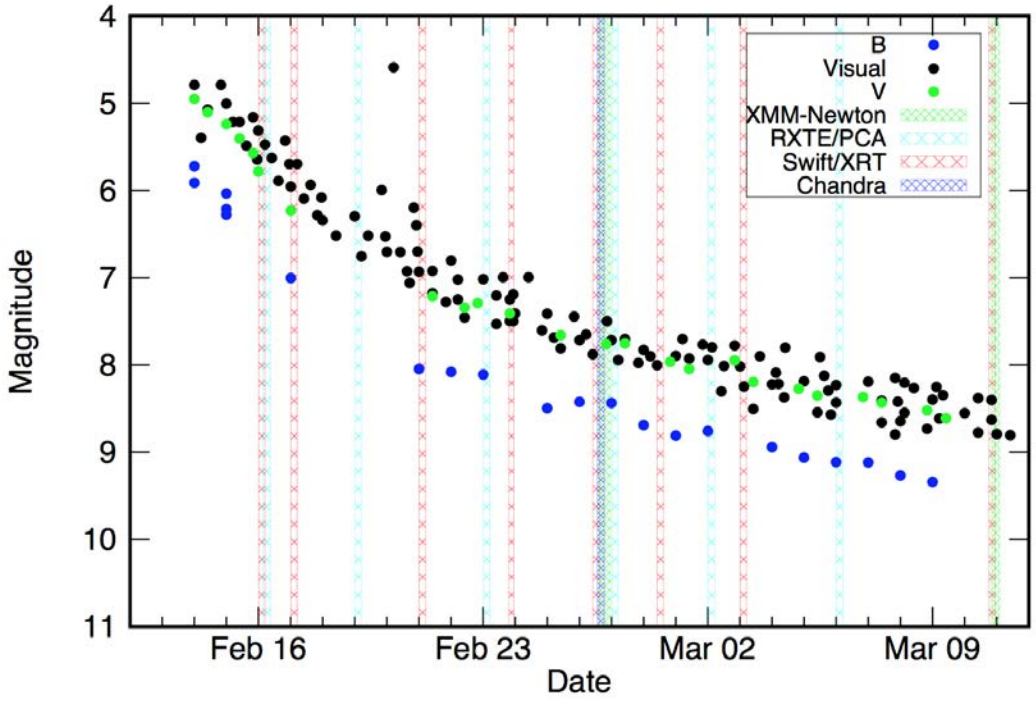

Figure 6: Optical light curve of RS Oph (AAVSO). The epochs of *XMM-Newton*, *RXTE*/PCA, *Swift*/XRT and *Chandra* observations discussed in this chapter are indicated by green, cyan, red and blue shaded regions respectively.

(Das et al., 2006; Monnier et al., 2006; Iijima, 2006; Buil, 2006; Evans et al., 2007) and X-rays (Sokoloski et al., 2006; Bode et al., 2006; Ness et al., 2007b; Nelson et al., 2008; Ness et al., 2009; Drake et al., 2009), but not in γ-rays (Table 3). Tatischeff & Hernanz (2007) showed that non-linear diffusive shock acceleration of particles at the blast wave and the subsequent escape of the highest energy protons from the shock region explain the observed early evolution of the nova; this acceleration can also account for the difference between shock velocities deduced from the X-rays and IR data. Accelerated particles should produce high energy γ-rays, as proven later by *Fermi* (Abdo et al., 2010).

3.2 OBSERVATIONS OF THE 2006 OUTBURST

3.2.1 *Early X-Ray Observations*

The first few weeks of the evolution of RS Oph were monitored by several X-ray instruments. The X-ray emitting shocked plasma was detected by *RXTE*/PCA (Sokoloski et al., 2006) and by the hard X-ray instrument on board of the *Swift* satellite, BAT (Bode et al., 2006). *Swift* and *RXTE* showed that the source was fading and cooling (Bode et al., 2006). Sokoloski et al. (2006) stated that this emission was produced by the shock within the blast wave from the nova explosion and the circumstellar material. The early hard X-ray emission was also observed with *Chandra* and *XMM-Newton* (Nelson et al.,

2008; Drake et al., 2009; Ness et al., 2009). We indicate the dates of the X-ray observations in the optical light curve from the AAVSO in Figure 6. During the first two weeks after the outburst, a hard spectrum was observed. However, on March 10^{th}, the situation changed and the SSS phase began. The observations during the SSS phase were studied in detail by Ness et al. (2007b); Nelson et al. (2008); Osborne et al. (2011).

In this section, we present a reanalysis of *RXTE* observations by Sokoloski et al. (2006). We show also the analysis of *Swift* observations carried out by Bode et al. (2006) and the study of *Chandra* and *XMM-Newton* observations made by Nelson et al. (2008); Drake et al. (2009); Ness et al. (2009). Besides, we complete all this information with the analysis of the *XMM-Newton* EPIC/MOS1 observations and a new analysis of the RGS observations on day 13.8 and 26.1 after the outburst. We show how a broad energy range and a good spectral resolution can provide a global picture of the early hard X-ray emission of RS Oph.

3.2.1.1 X-ray observations with RXTE

RS Oph was detected by the *RXTE* satellite with the Proportional Counter Array (PCA) instrument at energies between 2 and 25 keV (see Appendix A). It was the first time that the early hard X-ray evolution of RS Oph was observed, thanks to the fast monitoring of *RXTE* (Sokoloski et al., 2006). The spectra were fitted by Sokoloski et al. (2006), using an absorbed single-temperature thermal bremsstrahlung model and a gaussian to represent the Fe lines at 6.69 keV (Table 5). Figure 7 (left panel) shows the observed spectra with *RXTE*/PCA with the best-fit spectral model. The flux and the plasma temperature decreased faster than expected for an adiabatic shock (Sokoloski et al., 2006, Figure 2).

3.2.1.1.1 Reanalysis of the RXTE observations

We carry out a reanalysis of the *RXTE*/PCA observations between days 3 and 21 after the outburst. The log of the *RXTE* observations is shown in Table 4. We use the clean spectrum given in the standard products for each one of the observations.

We study the hard X-ray evolution observed with *RXTE*/PCA using XSPEC (version 12.8 (Arnaud et al., 2012)). An absorbed single-temperature thermal bremsstrahlung model was used. We fix the parameters given in Sokoloski et al. (2006) such as the temperature between days 3 and 17 and the absorption (N_H) on days 3 and between 10 and 21 (see Table 5). We use abundances from Anders & Grevesse (1989). Because of the modest PCA energy resolution, a single gaussian is used to fit the Fe K line complex at 6.69 keV. We fix the σ Fe line on days 6, 14 and 17 after the outburst to reproduce exactly the points included in the line observed in Figure 8 (left panel). Table 5 shows the results of the models used to fit the spectra compared to those obtained by Sokoloski et al. (2006). One of the known parameters is the unabsorbed flux. We can not fix this parameter in our model and when we calculate it, our unabsorbed flux is lower than the one obtained by Sokoloski et al. (2006). The reason is that the energy

Table 4: Log of RS Oph observation with *RXTE*/PCA

Observation Date	ID	Time after discovery	Exp.time (ks)	Count rate (count s^{-1})
2006 Feb 15	91441-01-01-00	3	1.4	161.4±0.3
2006 Feb 18	91441-01-02-00	6	2.0	425.3±0.4
2006 Feb 22	91441-01-03-00	10	1.5	56.9±0.2
2006 Feb 26	91441-01-04-00	14	3.2	24.0±0.1
2006 Mar 02	91441-01-05-00	17	1.0	11.4±0.1
2006 Mar 05	92406-01-01-00	21	1.7	6.13±0.09

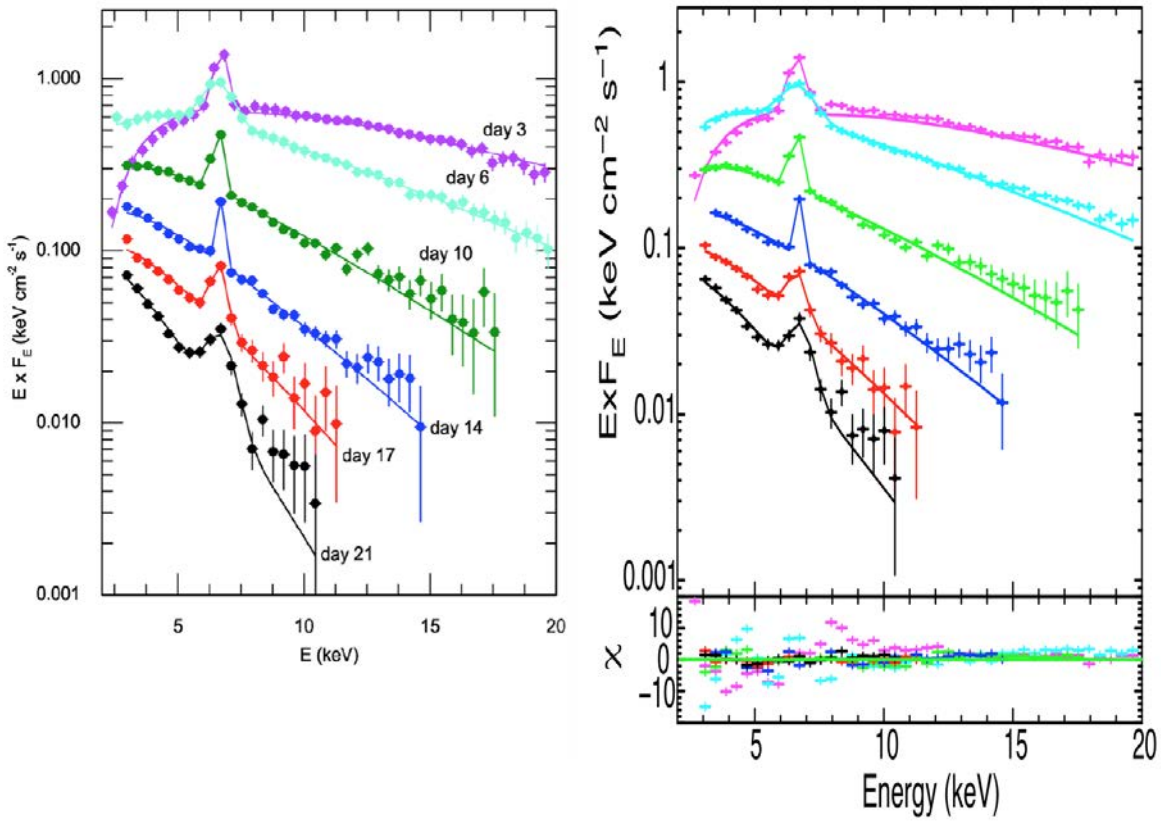

Figure 7: *RXTE*/PCA observed spectra and best-fit model for RS Oph by Sokoloski et al. (2006) (left) and this work (right) for days 3, 6, 10, 14, 17 and 21. The residuals from our fits are plotted in the bottom panel.

Table 5: Parameters of the RXTE Models of RS Oph

Day	N_H ($10^{22} cm^{-2}$)		kT 10^7 K		σ Fe line	EM $\times 10^{58}$cm^{-3}	F_{unabs} $\times 10^{-10}$erg cm^{-2}s^{-1}		χ^2/dof, χ^2_{red}
	Sokoloski et al. (2006)	This work	Sokoloski et al. (2006)*	This work			Sokoloski et al. (2006)* (c)	This work(d)	
3	5.5±1	5.5(a)	9.9±0.7	9.9(a)	0.27±0.02	5.36± 0.01	32±4	27.2±0.5	1163/48, 24.2
6	-	1.33±0.03	6.8±0.2	6.8(a)	0.64(b)	6.06± 0.01	27±5	23.2±0.5	1085/48, 22.6
10	0.4	0.4(a)	4.84±0.03	4.84(a)	0.14±0.05	3.33±0.01	13±3	9.5±0.4	78/35, 2.4
14	0.4	0.4(a)	3.65±0.04	3.65(a)	0.004(b)	2.12±0.01	7±2	4.5±0.2	77/27, 2.9
17	0.4	0.4(a)	2.9±0.1	2.9(a)	0.03(b)	1.41±0.01	4±1	2.5±0.3	18/19, 1.0
21	0.4	0.4(a)	-	2.0±0.1	0.4±0.1	1.5±0.01	-	1.6±0.2	21/14, 1.5

(a) Parameter is frozen as the central value given by Sokoloski et al. (2006).
(b) σ is frozen to the value given by Sokoloski et al. (2006).
(c) Unabsorbed flux between 0.5 and 20 keV.
(d) Unabsorbed flux between 1.5 and 20 keV.
∗The errors and the values have been obtained from Sokoloski et al. (2006) (Figure 2).

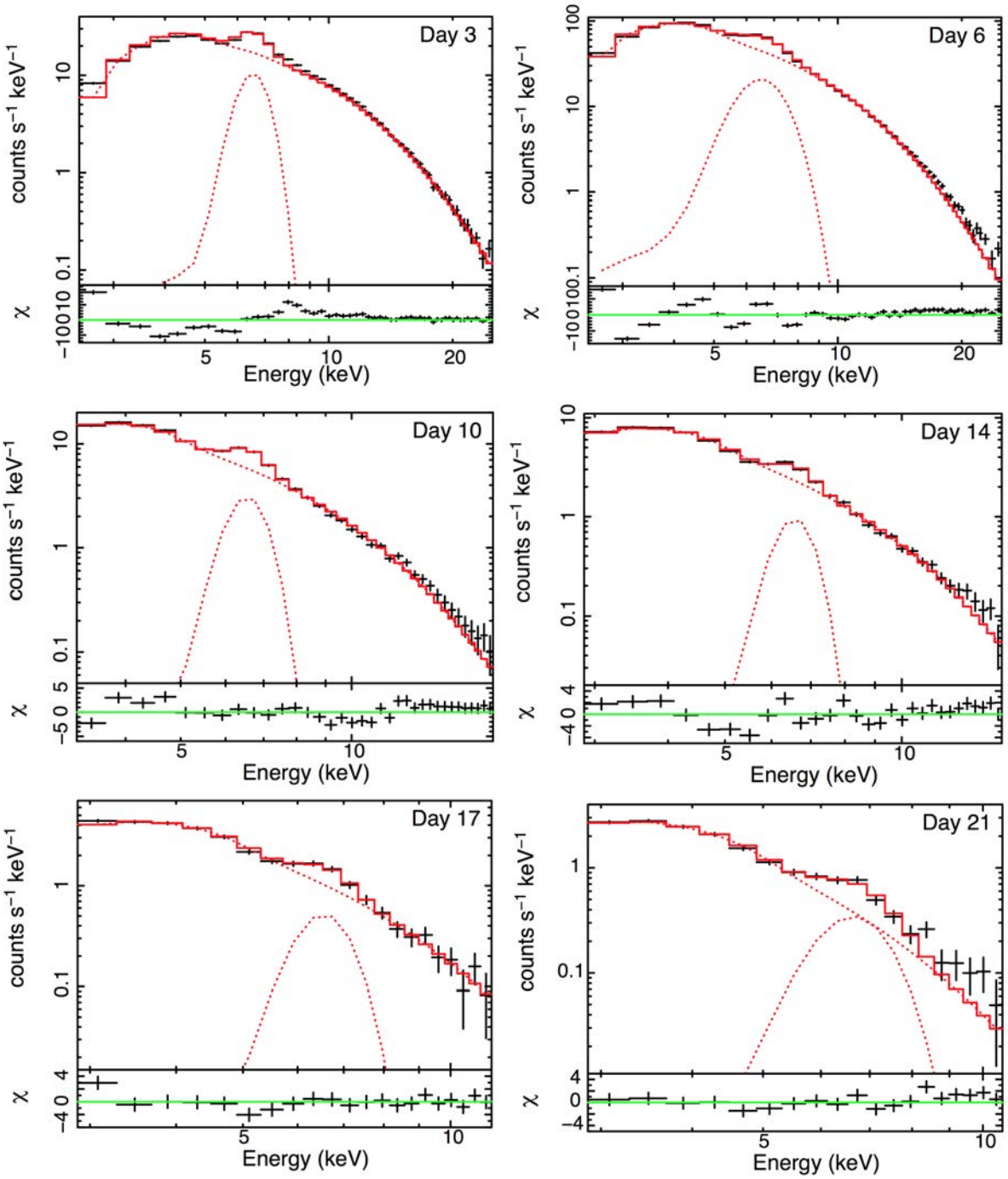

Figure 8: RS Oph *RXTE*/PCA observed spectra with best-fit models for days 3, 6, 10, 14, 17 and 21 and the residual plotted in the bottom panels.

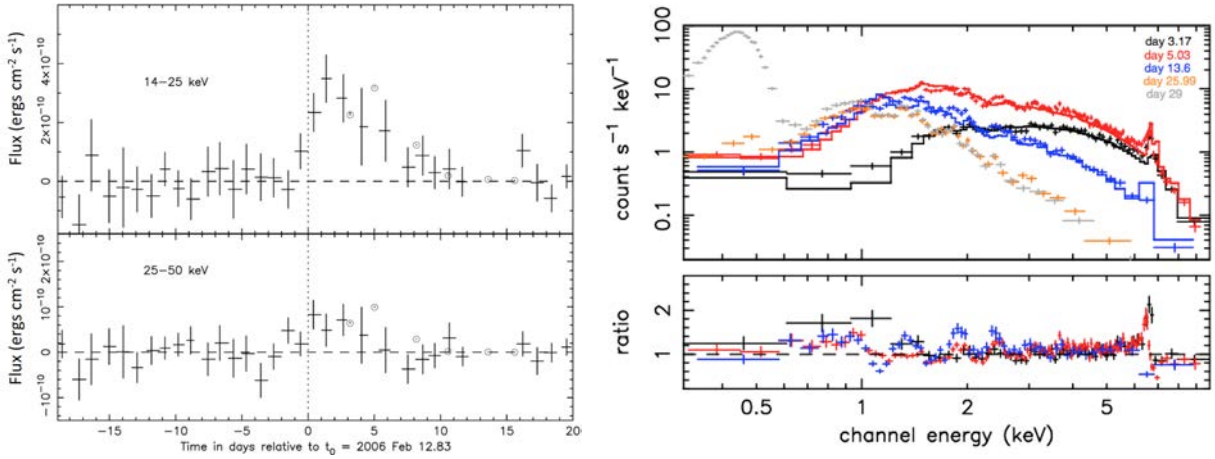

Figure 9: Left panel: Light curve by Swift/BAT of RS Oph the first days after outburst in the $14-25$ (top) and $25-50$ keV (bottom) bands (adapted from Bode et al., 2006). Right panel: RS Oph *Swift*/XRT observed spectra with best-fit models for days 3.17, 5.03, 13.6, 25.99 and 29. The residuals are plotted in the bottom panel (from Bode et al., 2006).

range of the response file given by the standard products (E: 1.5-20 keV) is smaller than that used by Sokoloski et al. (2006) (E: 0.5-20 keV). Figure 7 shows Figure 1 of Sokoloski et al. (2006) and our reanalysis with the χ^2 of the models. Our χ^2 is larger than the χ^2 obtained by them because of the fit of energies lower than 5 keV on days 3 and 6 after the outburst. We show all the details of the fit in Figure 8. Thanks to this reanalysis, we can know the values of the EM[1] of the *RXTE* observations and its evolution during the first 21 days after the explosion. Sokoloski et al. (2006) did not provide this parameter that, as we will see later (§ 3.2.4), is essential to know how much material was involved in the shock.

3.2.1.2 Swift observations

RS Oph was detected in hard X-rays with *Swift*/BAT from t =-20 to +20 days. *Swift*/BAT data was analysed by Bode et al. (2006), obtaining a clear detection of RS Oph in the $14-25$ keV band during the first 3 days after the outburst. The light curve showed a prompt increase in the flux the first days after the outburst (Figure 9). These fluxes are consistent with the fluxes obtained with XRT spectra at the same epoch. No spectral information was shown in their work.

RS Oph was also observed with *Swift*/XRT the first days after the outburst (Bode et al., 2006). The observations started on day 3.17, the same day as with *RXTE*. The spectra were dominated by hard X-ray emission, but they progressively softened until the emergence of a super soft component on day 26 after the outburst. A single temperature MEKAL model (Mewe et al., 1985) was used to fit the spectra with XSPEC. All the details of the fit were given in Bode et al. (2006) in Table 2. The absorption N_H adopted was the sum of the red giant wind column density ($(N_H)_W$) plus the interstellar one, $(N_H)_{ISM}=(2.4 \pm 0.6)\times 10^{21}$ cm^{-2} (Hjellming et al., 1986). Very high absorption was

1 Emission measure: EM=$\int_V n_i\ n_e\ dV$, where n_e and n_i are the electron and ion densities respectively.

found the first days after the outburst but it decreased very fast until day 26, when the SSS phase began. Solar abundances were used to fit the spectra. The only observed line was the Fe K α line around 6.7 keV, which is expected for the plasma temperatures obtained in the fits. However, on days 3 and 5, a discrepancy between the data and the model was shown (see right bottom panel in Figure 9). This excess could be characterized by an additional line at 6.4 keV. It can be caused by scattering in the red giant wind and its equivalent width is consistent with fluorescent emission by the surrounding gas. In the analysis of the evolution of the ejecta, Bode et al. (2006) obtained that after the end of the free expansion phase on day 6 after the outburst, v_s declines over time, following a power law as $v_s \propto t^{-0.6}$ more similar to the radiative phase index than the expected index for the adiabatic phase (see §2.4.1). Moreover, F_{unabs} decreased as expected for radiative cooling. They concluded that Phase I may have ended on day 6 after the outburst and the remnant moved quickly into Phase III, skipping Phase II.

3.2.1.3 Previous studies of XMM-Newton and Chandra observations

RS Oph was also observed with *XMM-Newton* and *Chandra* two weeks after the outburst. These X-ray satellites have a better spectral resolution than *RXTE*/PCA and *Swift*/BAT, but with a softer energy range (E:0.2-10 keV). Nelson et al. (2008) and Ness et al. (2009) studied the same spectra between 13.8 and 239.7 days after the outburst, analysing the evolution of RS Oph during the first 9 months.

RS Oph was observed with *Chandra* on day 13.8 with the MEG and the HEG instruments (see Appendix A). These observations were analysed by Drake et al. (2009). They used the `PINTofALE` software for `IDL` that allows to identify spectral lines, measure fluxes, and obtain a detailed modelling of the properties of the individual lines (Kashyap & Drake, 2000). For this models, CHIANTI line emissivities (Dere et al., 1997; Landi et al., 2006) and an absorbed collisional ionization plasma with solar abundances (Grevesse & Sauval, 1998) were assumed. The temperature and the EM of the most prominent lines are listed in Table 6. Drake et al. (2009) also found that most of the lines were blueshifted, covering a large range of plasma temperatures (see later in Figure 14).

The *XMM-Newton*/RGS and the *Chandra*/HETG spectra of RS Oph on day 13.8 after the outburst were studied by Nelson et al. (2008) and Ness et al. (2009). Nelson et al. (2008) used an APEC model with four different temperatures, but did not provide the χ^2. On the other hand, Ness et al. (2009) found a good fit with χ^2=0.67, using an VAPEC model with three different temperatures. APEC (Smith et al., 2001) models allow to calculate both the lines and the continuum for optically thin collisional plasmas modifying not only temperatures and emissivities, but also abundances of several elements (VAPEC) and velocity broadening (BVAPEC) (see Appendix C.2). The *XMM-Newton*/RGS spectrum on day 26.1 was also studied by Nelson et al. (2008) and Ness et al. (2009). For this day Nelson et al. (2008) obtained, using atmospheric models, that the temperature of the WD was $\sim 8 \times 10^5$ K, suggesting that $M_{WD} \geq 1.18$

Table 6: X-Ray Emission Lines of RS Oph (Drake et al., 2009)

line	T(10^7 K)	EM (10^{57} cm^3)
O VIII	0.3 ±0.1	5±1
Fe XVII	0.6±0.2	1.1±0.2
Ne X	0.6±0.2	7±1
Mg XI	0.6±0.2	15±1
Si XIII	1±0.3	16±1
Mg XII	1±0.3	26±1
Si XIV	1.6±0.6	17±1
Si XV	1.6±0.6	19±1
S XVI	2.5±0.9	11±2
Fe XXV	6±3	17±2

Table 7: Parameters of the fit models by Nelson et al. (2008) and Ness et al. (2009)

	Day 13.8				Day 26.1	
	Nelson et al. (2008)		Ness et al. (2009)		Ness et al. (2009)	
	T keV	EM 10^{57} cm^3	T keV	EM 10^{57} cm^3	T keV	EM 10^{57} cm^3
	16.84	∼1	4.2±0.1	10.5±0.1	1.91±0.07	3.0±0.1
	2.31		0.74±0.01	5.7±0.1	0.74±0.01	4.9±0.1
	0.92		0.3±0.01	2.9±0.1	0.38±0.02	4.0±0.1
	0.64					
N_H(10^{21} cm^{-2})	12		6.9±0.3		5.6±0.1	

$M_\odot$. On the other hand, Ness et al. (2009) also used an VAPEC model with three different temperatures and the same abundances as for day 13.8, finding a fit with χ^2=1.7 for the energy range between 0.6 and 10 keV. The temperatures, EMs and N_H of Nelson et al. (2008) and Ness et al. (2009) analyses are listed in Table 7. When the SSS phase switched off 75 days after the outburst, the spectrum became dominated by the emission lines with a continuum, similar to the first observations but with lower temperatures.

Nelson et al. (2008) and Ness et al. (2009) also analysed individually the several lines observed in the spectra. Nelson et al. (2008) used `ISIS` package of CIAO and Ness et al. (2009) used the `PINTofALE` software as Drake et al. (2009). Nelson et al. (2008) suggested that there was a dependence between the velocity shifts and the ionization stage. Besides, they indicated that at this early stage the plasma was collisionally dominated with a G ratio ~ 1 (see Appendix C.3). Ness et al. (2009) found overabundances of N that can be due to the ejecta and/or the wind of the companion. Besides, Ness et al. (2009) observed that the flux decayed as expected for a radiative cooling ($\propto t^{-5/3}$) before day 70 after the outburst. However, after this day the flux decreased as $\propto t^{-8/3}$, which does not correspond to any given phase of the blast wave evolution. Two different peaks in the EM were observed that could represent two different circumstellar regions with different densities. One denser region in the equatorial plane and another less dense in the polar regions as expected for the radio and optical images obtained with the Very Long Baseline Array (VLBA) (O'Brien et al., 2006) and the Hubble Space Telescope (HST) (Bode et al., 2007), respectively. Ness et al. (2009) suggested that the cooler component observed 70 days after the outburst corresponded to the expanding ejecta, and the observations obtained before this day corresponded to the shocked material.

3.2.1.4 Study of the XMM-Newton observations the first days after the outburst

We present the analysis of RS Oph observations with the *XMM-Newton* satellite 13.8 and 26.1 days after the outburst (see Table 8). We analyse for the first time the observations with the EPIC-MOS1. Moreover, we carry out a new analysis of the combined spectrum obtained with the RGSs 1 and 2 that we compare with the previous studies of Nelson et al. (2008), Ness et al. (2009) and Drake et al. (2009). The log of the *XMM-Newton* observations is shown in Table 8.

3.2.1.4.1 Data reduction

We have focused on the data from the EPIC/MOS1 that were taken with the small window mode. The central CCD of the MOS2 camera was switched off during the observation in order to observe the secondary sources. Therefore, we do not have a RS Oph image taken with the EPIC/MOS2. Data were reduced with the *XMM-Newton* SAS (v 13.5.0) using the standard routine for the MOS spectra extraction for point-like sources. As RS Oph was very bright, the MOS observations had pile-up and we have needed to carry out some additional reduction steps. The pile-up is the arrival of more

Table 8: Log of RS Oph observations with *XMM-Newton*

Observation Date	ID	Time after discovery	Detector	Exp. Time (ksec)	Count rate (cts/s)
2006 Feb 26	0410180101	13.8	EPIC/MOS1	24	7.17±0.02
			RGS1		2.335±0.007
			RGS2		
2006 Mar 10	0410180201	26.1	EPIC/MOS1	12	4.97±0.03
			RGS1		2.70±0.01
			RGS2		

than one X-ray photon to one camera pixel or to adjacent pixels between two read outs. These photons are read as a single event with an energy that is the sum of the energies of the individual photons. Because of the pile-up, our spectra have more counts at high energies than they should have. Therefore, it is very important to carry out a good correction of the pile-up. See all the reduction steps in Appendix B.1.

In the case of the RGS observations, we have extracted the spectra using standard SAS routines. It is unusual that this instrument has pile-up but when the spectrum is very bright, as in the SSS phase, it is possible that the second order spectrum is due to pile-up in the first order photons. This is the case of RGS observations of RS Oph during the SSS phase of its last outburst (Ness et al., 2007b). The observations that we have studied took place the first days after the outburst. We have checked for pile-up of RGS as Ness et al. (2007b) and we confirm that these spectra do not have pile-up. Finally, we have combined the RGS source spectrum, the background spectrum and the response matrices. To combine correctly the spectra of the RGSs 1 and 2, we must use the same spectral order for both spectra. A more detailed description of the data reduction can be seen in Appendix B.1.

3.2.1.4.2 Data analysis

The spectra obtained with *XMM-Newton* the first days after the outburst are mainly in the range of hard X-rays (E>1 keV) and correspond to the shock between the ejecta and the red giant wind (Sokoloski et al., 2006; Bode et al., 2006).

We have analysed the *XMM-Newton* spectra using XSPEC (v.12.8, Arnaud et al., 2012). To model the X-ray emission, we have assumed an optically thin plasma in collisional ionization equilibrium. Specifically, we have used a multi-temperature APEC model (Smith et al., 2001). We have modified only the abundances of elements with emission lines in the spectra (Table 9) and have assumed solar abundances for the remaining elements (Anders & Grevesse, 1989). We have used the Tuebingen-Boulder

absorption model (tbabs) (Wilms et al., 2000) for all the spectra.

A thermal plasma model with a single-temperature is not good enough to fit the high spectral resolution spectra obtained with *XMM-Newton*. The analysis carried out by Nelson et al. (2008) and Ness et al. (2009) had four and three different temperatures, respectively. However, we have been able to simplify the problem by fitting these spectra with only two temperatures which correctly describe the temperature distribution in the spectra.

EPIC/MOS

EPIC/MOS1 spectra are characterized by a thermal bremsstrahlung continuum with superimposed H- and He- like emission lines, N VII (0.49 keV), O VII (0.57 keV), Ne IX (0.91 keV), Ne X (1.02 keV), Mg XI (1.35 keV), Mg XII (1.47 and 1.75 keV), Si XIII (1.86 keV), Si XIV (2.01 keV), S XV (2.46 and 2.88 keV), S XVI (2.62 and 3.13 keV) and Fe XXV (6.69 keV), and L-shell lines (Fe XVII-XXIV (0.72-0.92 keV)). On day 26.1 after the outburst, the N and O lines are not observed because they are hidden by the soft X-ray emission produced by the hot WD photosphere. We have also lost the Fe XXV line at 6.69 keV on day 26, because the pile-up corrections affect mainly the higher energies of the spectrum.

We test several APEC models trying to find a model that reproduces the data obtained with the MOS1 camera. The spectrum was not well fitted with an APEC model with two temperatures as a consequence of the Fe L-lines between 0.72-0.92 keV, giving χ^2=26 on day 13.8 and χ^2=125 on day 26.1. Therefore, we tried to reproduce the data with an VAPEC model with two temperatures modifying the abundances of the elements observed in the spectra, e.g., the Fe abundance. We obtained $\chi^2 = 1.9$ and $\chi^2 = 1.2$ for days 13.8 and 26.1 respectively. Finally, we improve even more the fit of day 13.8. We use a different model to fit properly both spectra. This is the BVAPEC model, which also includes velocity broadening of the lines. The velocity broadening obtained with the BVAPEC model is also compatible with the velocity broadening of the lines observed with RGS (Table 10).

As expected, the temperatures for day 13 are higher than the temperatures for day 26. Our T_{high} are compatible with the temperatures obtained by *Swift*, *RXTE* and the high temperature of Ness et al. (2009). These temperatures reproduce the continuum and the lines of the spectra at energies between $3 - 20$ keV. However, Nelson et al. (2008)'s high temperature on day 13 seems wrong, because it is larger than the temperatures obtained with *Swift* and *RXTE* the first days after the outburst (see later in Figure 18).

Since, *XMM-Newton* has better sensitivity than *Swift*/XRT and an energy range softer than *RXTE*/PCA, we can use a second temperature that allows us to know better the properties of the plasma. We compare our T_{low} with the temperatures obtained by Ness et al. (2009) and Nelson et al. (2008) for the RGS data. They used an additional temperature $<T_{low}$ to describe the RGS spectrum which shows the complexity

Table 9: Parameters of the fit models (BVAPEC/BVAPEC+BB) of RS Oph

Parameters	Day 13.8	Day 26.1
N_H ($\times 10^{21}$ cm^{-2})	5.8±0.5	$4.3^{+0.5}_{-0.4}$
kT_{high} (keV ($\times 10^7$ K))	4.3±0.3 (4.9±0.4)	$2.5^{+1}_{-0.5}$ ($3.0^{+1}_{-0.6}$)
EM_{high} [(a)] ($\times 10^{57}$ cm^{-3})	$7.8^{+1}_{-0.7}$	$2.1^{+1}_{-0.7}$
kT_{low} (keV ($\times 10^7$ K))	0.82±0.04 (0.95±0.5)	0.72±0.06 (0.85±0.07)
EM_{low} [(a)] ($\times 10^{57}$ cm^{-3})	$3.8^{+0.1}_{-0.2}$	$7.4^{+0.1}_{-0.2}$
v_{width} [(b)] (km/s)	<1200	<3000
kT_{bb} (keV)	-	0.034±0.003
L_{bb} [(c)] ($\times 10^{38}$erg s^{-1})	-	1.55 ± 0.05
$O/O_\odot$	$2.0^{+1.0}_{-0.8}$	-
$N/N_\odot$	40^{+20}_{-14}	-
$Ne/Ne_\odot$	$1.8^{+0.6}_{-0.4}$	0.8±0.2
$Mg/Mg_\odot$	$2.5^{+0.5}_{-0.4}$	1.1±0.2
$Si/Si_\odot$	$1.5^{+0.3}_{-0.2}$	0.5±0.1
$S/S_\odot$	$2.5^{+0.4}_{-0.3}$	0.7±0.2
$Fe/Fe_\odot$	$0.29^{+0.09}_{-0.06}$	0.1±0.2
$F_{abs\ 0.3\text{-}10.0\ keV}$($\times 10^{-10}$ erg cm^{-2}s^{-1})	$4.55^{+0.01}_{-0.07}$	1.50±0.01[(d)]
$F_{unabs\ 0.3\text{-}10.0\ keV}$($\times 10^{-10}$ erg cm^{-2}s^{-1})	$9.17^{+0.09}_{-0.03}$	$3.42^{+0.04}_{-0.02}$ [(d)]
$\chi^2_{v,r}$(χ^2_v/dof)	1.4 (1263/895)	1.1 (401/368)

(a) $norm_{BVAPEC}=10^{-14}EM/(4\pi D^2)$, where EM is the emission measure and D the distance in cm. We have adopted 1.6±0.3 kpc as the RS Oph distance.
(b) v_{width} is the gaussian broadening of the velocity in km/s.
(c) $norm_{bb}= L_{39}/D^2_{10}$, where L_{39} is the source luminosity in units of 10^{39} erg s^{-1} and D_{10} is the distance to the source in units of 10 kpc.
(d) Flux from 0.6-10.0 keV, ignoring super soft emission.

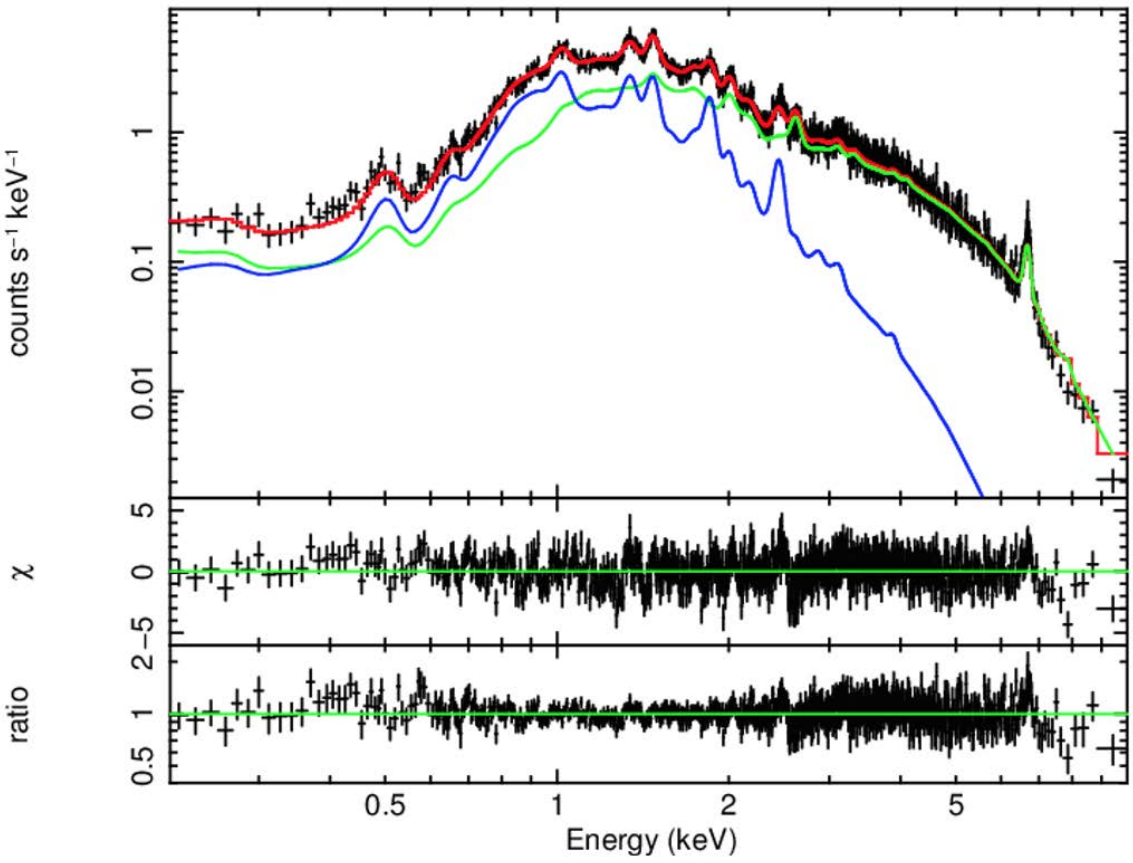

Figure 10: EPIC/MOS1 observed spectra and best-fit model for RS Oph at day 13.8 after the outburst. Residuals are plotted in the bottom panels. The global model and its two components (T_{high} and T_{low} BVAPEC) are shown with red, green and blue lines respectively.

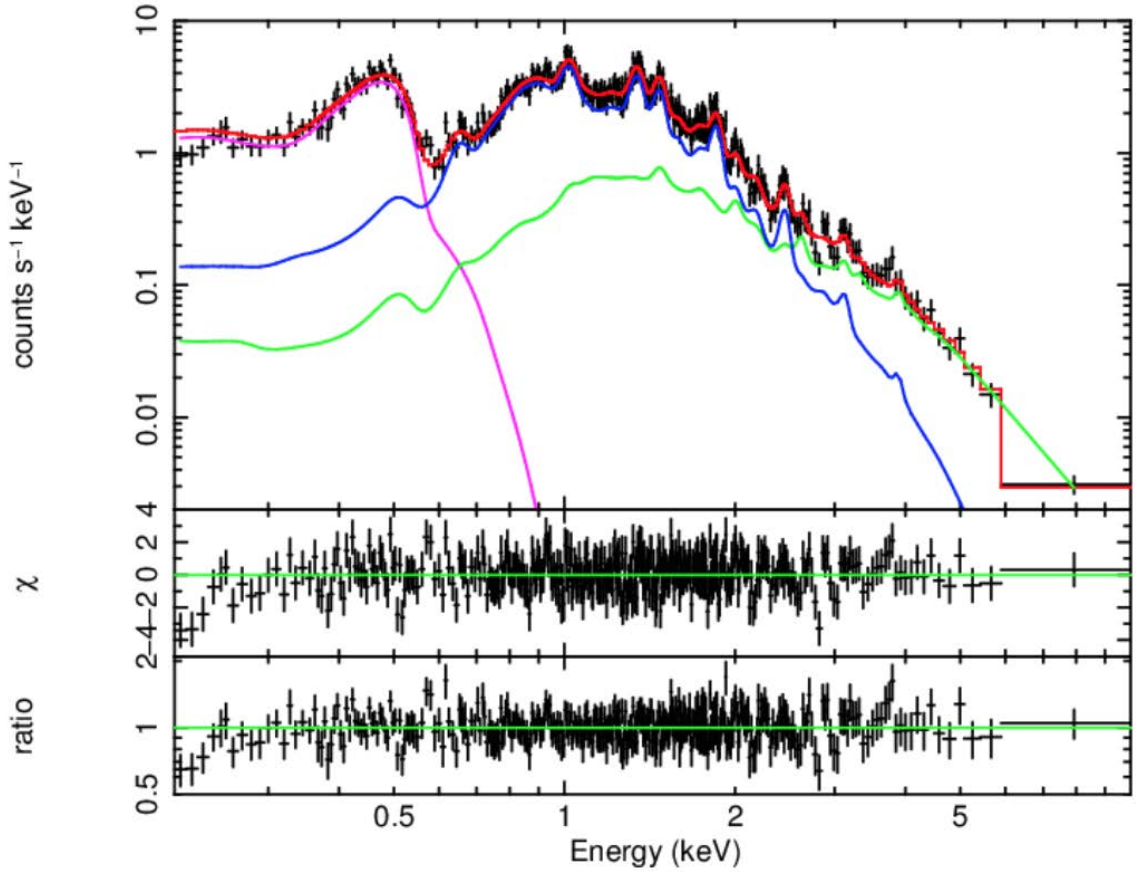

Figure 11: EPIC/MOS1 observed spectra and best-fit model for RS Oph at day 26.1 after the outburst. Residuals are plotted in the bottom panels. The global model and its three components (T_{high} and T_{low} BVAPEC and Black Body) are shown with red, green, blue and pink lines respectively.

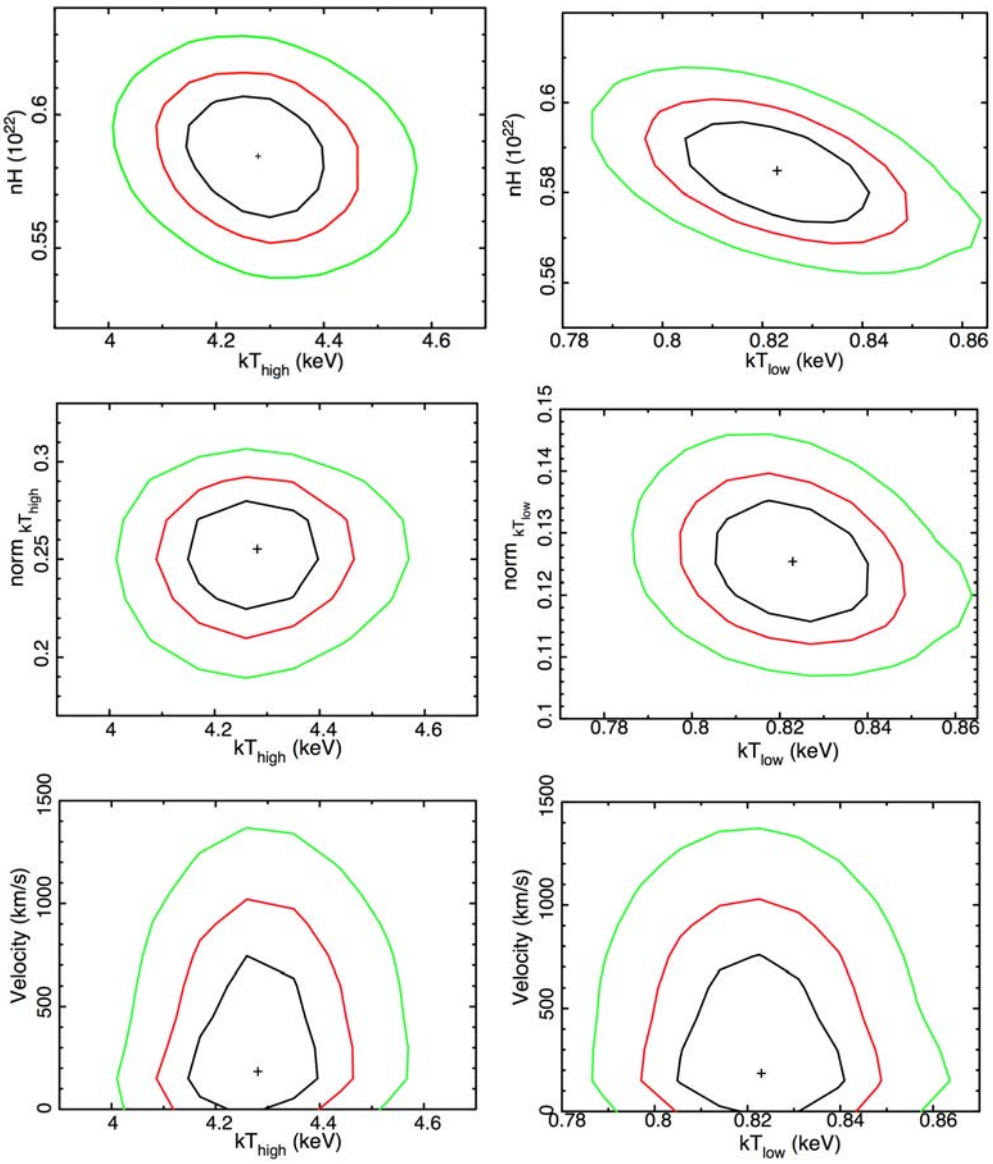

Figure 12: Confidence contours (1 (black line), 2 (red line), and 3 σ (green line)) of N_H-kT_{high} and -kT_{low} components, norm-kT_{high} and -kT_{low} components and kT_{high}- and kT_{low}- velocity broadening of BVAPEC model fitting the EPIC/MOS1 data 13.8 days after the outburst.

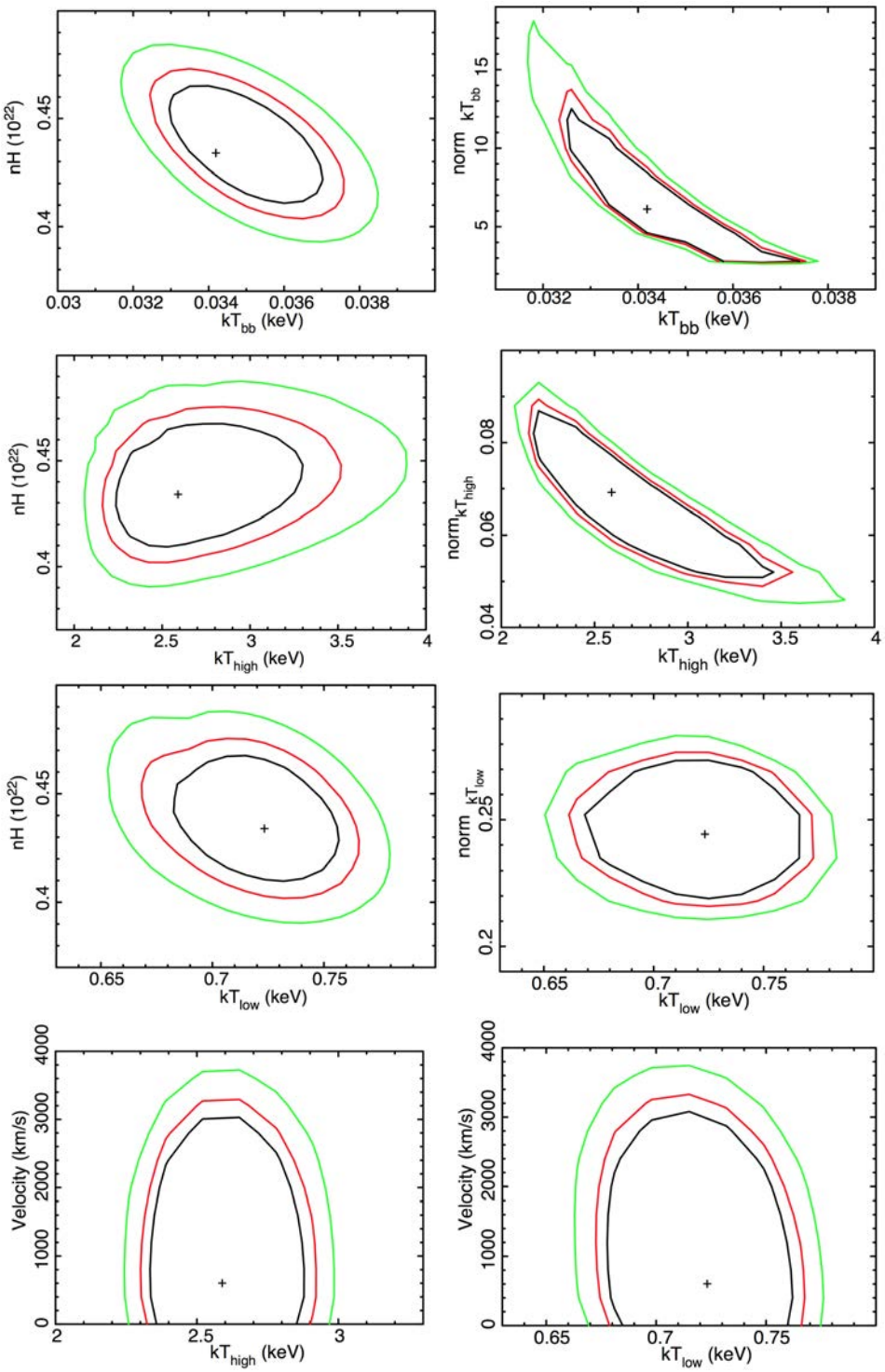

Figure 13: Same as Figure 12 but for day 26.1 after the outburst.

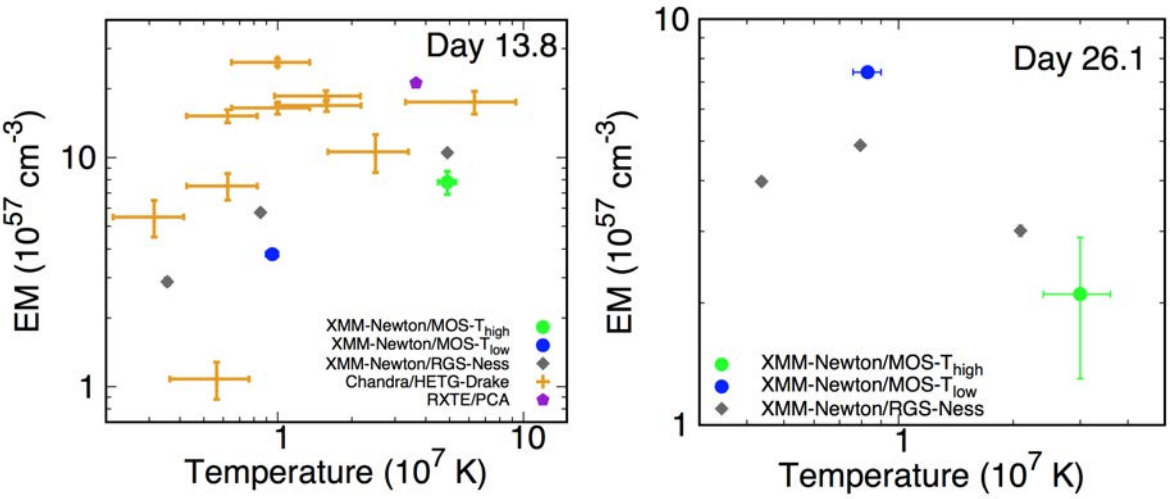

Figure 14: Plasma temperature and EM from the best-fit models for day 13 (left panel) and day 26 (right panel). Green and blue dots correspond to T_{high} and T_{low} of *XMM-Newton*/MOS1 respectively (§ 3.2.1.4), 3σ error bars. Purple pentagon, *RXTE*/PCA (§3.2.1.1), 1σ error bars. Gray diamond, *XMM-Newton*/RGS (Table 7), 2σ error bars. Orange cross, *Chandra*/HETG (Table 6).

of the plasma.

Our abundances on day 13.8 are slightly larger than the abundances obtained by Ness et al. (2009) for the RGS spectrum. These slight differences can be due to some lines being completely blended in EPIC/MOS1 because its spectral resolution is lower than in RGS. In general the abundances modified are slightly above to the solar abundances except for the Fe that is lower than the solar abundance. As we mentioned before, Ness et al. (2009) found also an overabundance of N and explained the possible causes of it. However, in EPIC/MOS1 spectrum part of the N overabundance observed, and the difference between Ness et al. (2009)'s study and ours, can be due the overabundance of other elements as S whose lines are blended with the N VII (0.49 keV) and broaden this line.

As we mentioned before, the SSS emission appeared on day 26.1 after the outburst. In the soft energy range, we did not see any absorption lines. We obtain a good fit using a black body. We use it to reproduce the SSS phase spectrum at energies below 0.5 keV, from which we obtain the temperature and the luminosity of the hot photosphere of the WD. The parameters of the BVAPEC and black body models are listed in Table 9. The corresponding observed and fitted spectra are shown in Figure 10 for day 13.8 and in Figure 11 for day 26.1. Confidence contours for the parameters of both spectra are shown in Figures 12 and 13, respectively.

To obtain more information about the plasma on these two days, we compare the temperature and EM obtained with the analysis of the observations with *RXTE*, *Chandra* and *XMM-Newton*. On day 13, Drake et al. (2009) obtained the EM as a function of

the temperature for several emission lines (see Table 6). As we have mentioned, they used the `PINTofALE` software for `IDL` (Kashyap & Drake, 2000). We compare this information with the information obtained using global models, with continuum and lines, to fit the *RXTE* (Sokoloski et al., 2006, and this work) and *XMM-Newton* (Ness et al., 2009, and this work) observations. Figure 14 shows the plasma temperature and the EM relationship in the shocked material. Except for the EM of the Fe XVII line (EM= 1×10^{57} cm^{-3}), the EM of the other lines is in the same range as the EM of the collisional ionization models (EM=$(3-30)\times10^{57}$ cm^{-3}). The temperatures of the lines and the models are similar, being all in the range $(0.2-10)\times10^{7}$ K (left panel Figure 14). On day 13, if we take into account only the EM of the global models, we can see that the EM at high temperatures tends to be larger than the EM at low temperatures. This means that most of the material is hot. On day 26, we only have information from the *XMM-Newton* observations. The temperatures and EMs obtained by Ness et al. (2009) are compared with those obtained by us. The EM at high temperatures decreases critically while the EM at low temperatures remains almost constant compared to the EM of day 13. In RS Oph, most of the material started being hot and ended up cooling down.

RGS

We fit the RGS spectra with the same best-fit models as the EPIC/MOS1 spectra (Table 9). We obtain that these models can not reproduce all the details of the spectra, giving a $\chi^2 \simeq 5$ (Schlegel et al., 2014). We see in the residual panels of Figure 15 that the model do not fit correctly the data of some of the lines appearing an excess in the lines. The line broadening is related with the thermal motion, therefore, we can obtain information about the several temperatures of the plasma studying the different line broadenings.

On day 26, unlike in the EPIC/MOS1, we see emission lines, mainly O and N, in the soft part of the spectrum (Figure 15). The model does not fit these lines in the RGS spectrum. As we have explained in §3.2.1.4.2, we have obtained a good fit of the MOS1 spectrum keeping these elements with solar abundances in the BVAPEC model. However, taking into account the results obtained on day 13 and that Ness et al. (2009) used the same abundances both days, we can expect that O and N abundances are above the solar values ($O/O_\odot=2.0^{+1.0}_{-0.8}$ and $N/N_\odot=40^{+20}_{-14}$ on day 13).

RGS line profiles and fluxes

In order to further characterize the plasma and to study the characteristics of the lines individually, we use RGS. With this instrument, we can identify the He-like triplets separately, resonance (r: $1s^2\ ^1S_0$ - 1s 2p $^1P_1$), intercombination (i: $1s^2\ ^1S_0$ - 1s 2p $^3P_{2,1}$), and forbidden (f: $1s^2\ ^1S_0$ - 1s 2s $^3S_1$) lines. The analysis of these lines and their ratios can provide the necessary measures to understand the physics and to model the details of the shock process in this type of objects. There are several emission lines that we can identify but we have only listed the best resolved ones (Figure 15). The strongest lines seen in the spectrum originate from H-like and He-like ions of Si XIV (6.18 Å) and

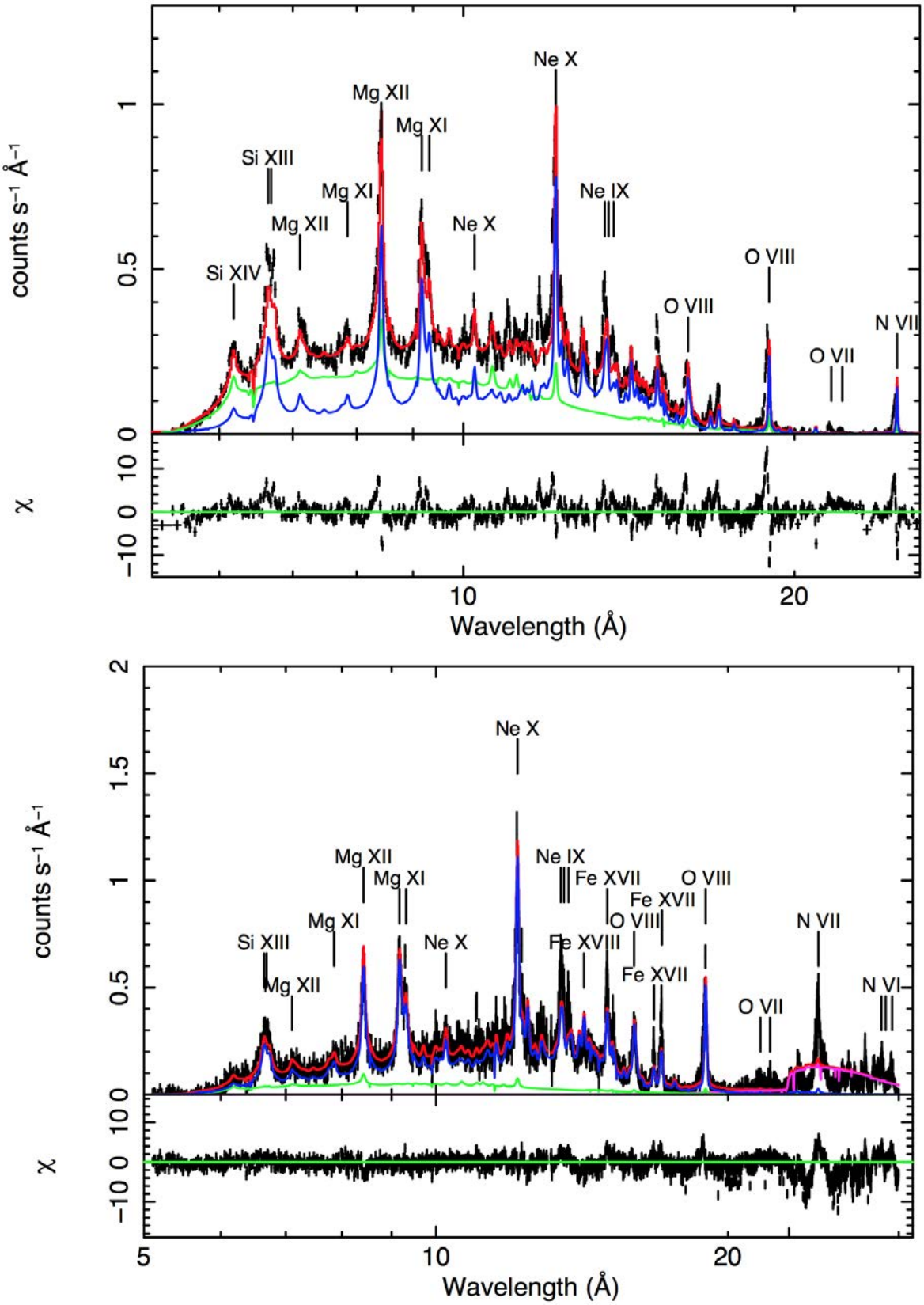

Figure 15: RGS observed spectra and best-fit model for RS Oph at day 13.8 (top) and at day 26.1 (bottom) after outburst. Residuals are plotted in the bottom panels. The global model and its three components (T_{high} and T_{low} BVAPEC and Black Body) are shown with red, green, blue and pink lines respectively.

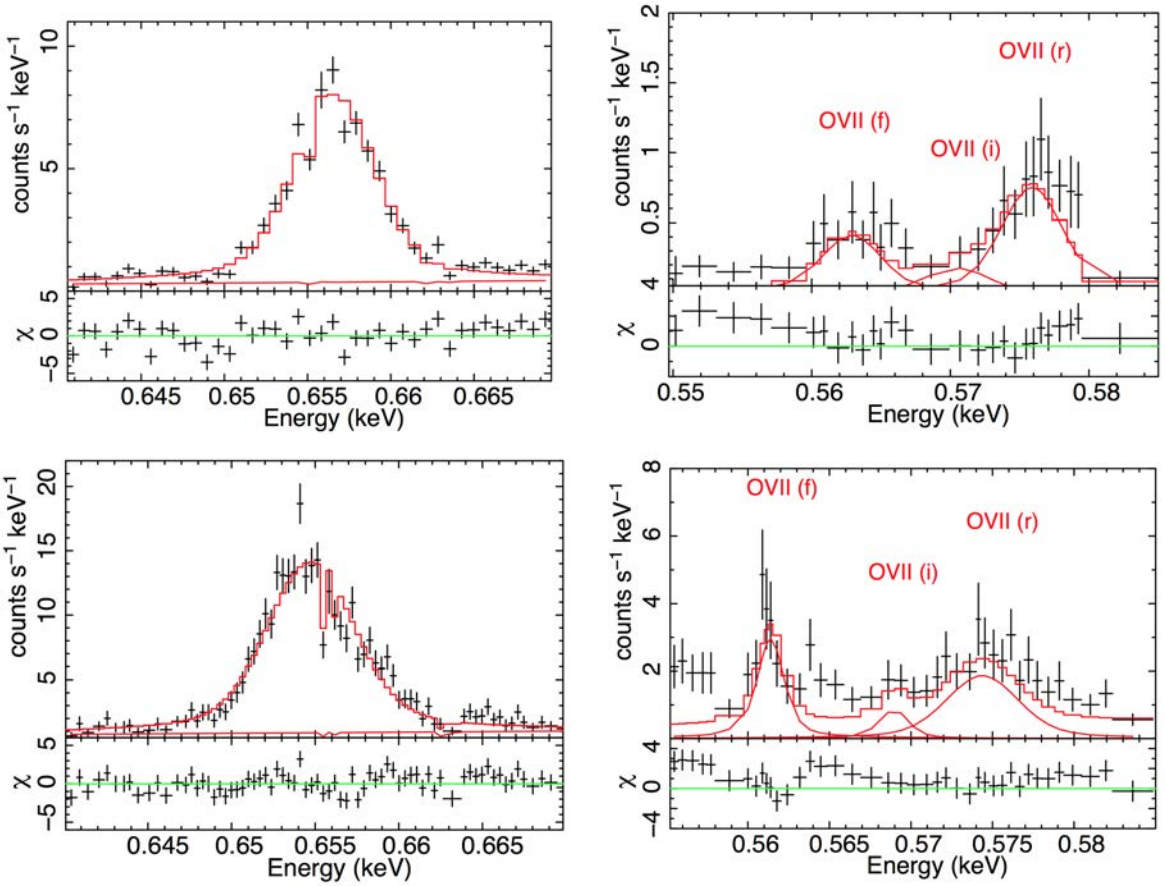

Figure 16: RGS observed lines (O VIII H-like (left) and O VII He-like (right)) and best-fit model for RS Oph at day 13.8 (top) and at day 26.1 (bottom) after the outburst.

Si XIII (6.65 Å), Mg XII (8.42 Å) and Mg XI (9.2 Å), Ne X (12.1 Å) and Ne IX (13.5 Å), and O VIII (18.97 Å) and O VII (21.6 Å) and N VII (24.78 Å) and N VI (29.1 Å). Some Fe lines are also present, Fe XVII (15.02, 16.78 and 17.1Å) and Fe XVIII (14.2 Å).

We fit the lines with a gaussian profile superimposed on a bremsstrahlung continuum. The bremsstrahlung temperature adopted is the same as that of the EPIC/MOS1 best-fit model. In the case of the He-like lines, we have fitted each of the three lines with a gaussian with the same line width and line shift (λ_{obs}-λ_{rest}), because we expect that these three lines come from the same ejecta material under the same physical conditions (Figure 16). The gaussian line width obtained in the gaussian profile model is converted to obtain its corresponding Doppler velocity (v_{width}). We have obtained the flux of the lines subtracting the flux of the bremsstrahlung continuum from the flux of the gaussian. The uncertainties in the measures correspond to a 90% confidence level (Table 10). Some lines are blends of other emission lines and may be present in the data contaminating our estimates from gaussian fitting. The uncertainties obtained with XSPEC are only statistical (see Appendix C). The errors represent the precision of the values but not the accuracy of them. The results for the best-fit of the He-like and H-like lines are listed in Table 10.

Table 10: X-Ray Emission Lines of RS Oph

			Day 13.8			Day 26.1		
Ion		λ_{rest} Å	λ_{obs} Å	v_{width} km/s	Flux 10^{-14} erg cm^2 s^{-1}	λ_{obs} Å	v_{width} km/s	Flux 10^{-14} erg cm^2 s^{-1}
Si XIV		6.19	6.18±0.06	1400±600	310±50	-	-	-
	r	6.65	6.62±0.05		420±20	-		
Si XIII	i	6.68	6.66±0.05	1300±300	230±30	-	-	-
	f	6.74	6.71±0.05		420±30	-		
Mg XII		8.42	8.39±0.02	900±100	640±20	8.41±0.06	1000±200	210±20
	r	9.17	9.22±0.04		560±10	9.23±0.04		310±10
Mg XI	i	9.23	9.29±0.04	900±100	430±10	9.30±0.04	500±200	190±10
	f	9.31	9.36±0.04		47±7	9.37±0.04		28±3
Ne X		12.13	12.11±0.03	900±100	330±10	12.13±0.05	300±100	370±20
	r	13.45	13.45±0.05		151±7	13.45±0.07		150±60
Ne IX	i	13.55	13.55±0.05	1100±100	73±3	13.55±0.07	600±100	40±10
	f	13.70	13.71±0.05		103±7	13.70±0.07		70±10
Fe XVII		15.02	-	-	-	15.00±0.04	500±100	151±7
O VIII		16.01	15.96±0.06	1500±100	98±4	15.99±0.08	1200±100	63±8
Fe XVII		16.78	16.74±0.06	700±200	28±2	16.78±0.07	300±100	24±7
O VIII		18.96	18.88±0.02	910±60	79±3	18.94±0.03	1000±40	180±10
	r	21.60	21.5±0.1		10±1	21.59±0.04		34±1
O VII	i	21.80	21.7±0.1	1000±100	2±1	21.79±0.04	1000±200	11±1
	f	22.10	22.0±0.1		4.8±0.8	22.09±0.04		23.6±0.8
N VII		24.78	24.67±0.09	1010±50	49±3	24.8±0.1	1700±100	243±8
	r	28.79	-		-	28.8±0.2		77±7
N VI	i	29.08	-	-	-	29.1±0.2	1200±70	29±4
	f	29.53	-			29.5±0.2		75±7

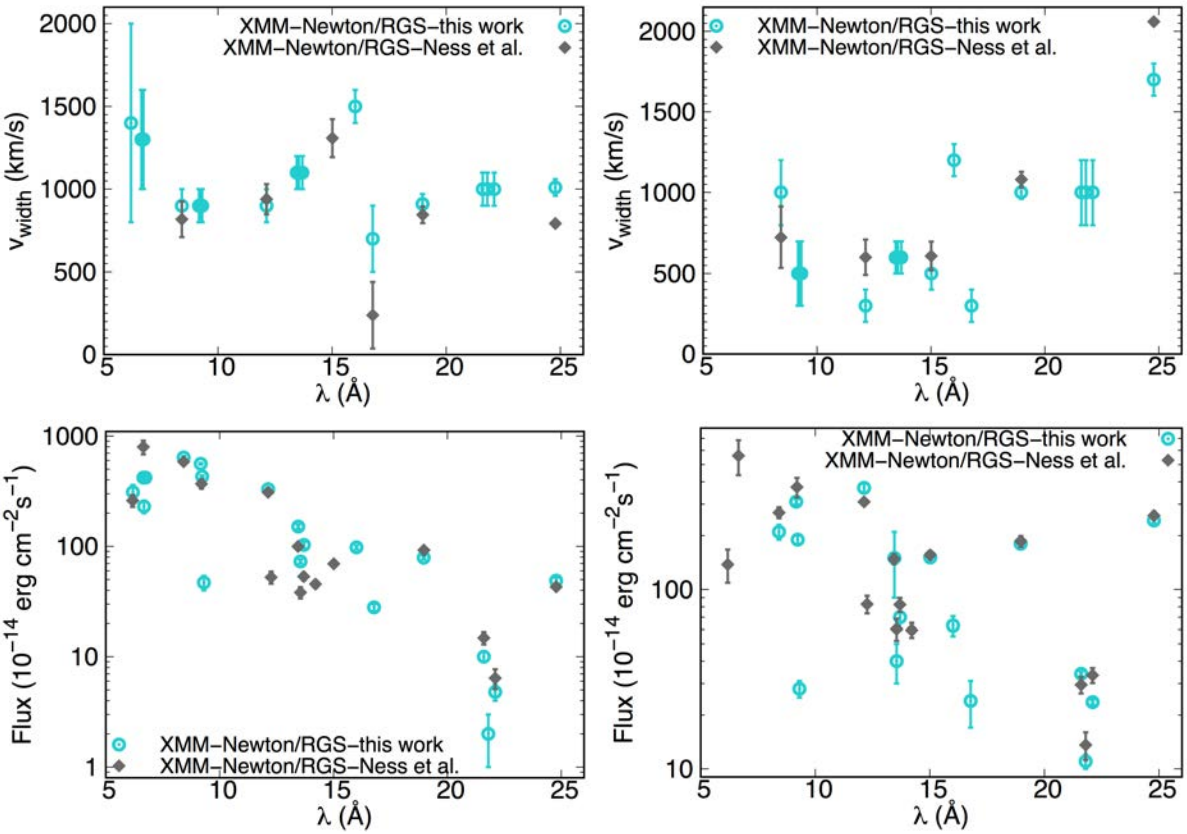

Figure 17: v_{width} (top) and flux (bottom) from RGS observed lines at day 13.8 (left) and at day 26.1 (right) after the outburst compared with Ness et al. (2009) results.

Table 11: Temperatures and densities derived from H- and He-like line ratios of RS Oph

Day 13.8						
	H- and He-like lines ratio		He-like lines ratios			
Ion	H/He	Temp. 10^7K	G *(f+i)/r*	Temp. 10^7K	R *f/i*	n_e 10^{10}cm^{-3}
Si	0.7± 0.1	1.33±0.03	1.5±0.1	0.55±0.03	1.8±0.1	1000±300
Mg	1.14± 0.01	0.99±0.03	0.85±0.02	0.54±0.01	0.11±0.02	20000±2000
Ne	2.18± 0.03	0.73±0.01	1.16±0.01	0.27±0.02	1.41±0.04	77±6
O	7.9± 0.4	0.64±0.01	0.68±0.1	0.3±0.03	2±1	1.6±0.9

Day 26.1						
	H- and He-like lines ratio		He-like lines ratios			
Ion	H/He	Temp. 10^7K	G *(f+i)/r*	Temp. 10^7K	R *f/i*	n_e 10^{10}cm^{-3}
Mg	0.67± 0.04	0.85±0.01	0.70±0.02	0.65±0.01	0.14±0.01	14700±300
Ne	2.4± 0.6	0.77±0.05	0.7±0.2	0.46±0.06	1.7±0.2	52±9
O	5.3± 0.1	0.55±0.03	1.01±0.03	0.18±0.01	2.1±0.1	2.0±0.3
N	-	-	1.35±0.03	0.09±0.01	2.6±0.1	0.47±0.05

In Table 10, we see that v_{width} of the RGS lines is compatible with those obtained in the fit of the EPIC/MOS1 spectra (Table 9). As in the case of the EPIC/MOS1 camera, the line broadening is related to the shocked plasma temperature (Beals, 1936). As the temperature on day 13 is higher than the temperature on day 26, it is expected that some of the lines on day 13 had a larger v_{width} than on day 26. However, there is not a large difference between both T_{low}, that is the dominant temperature in the RGS energy range (blue line in Figure 15). As a consequence of that, some lines have a similar v_{width}. These results are similar to those obtained by Nelson et al. (2008) and Ness et al. (2009). Figure 17 shows our results compared with the results of Ness et al. (2009). The differences can be due to the different temperatures that we assume to fit the continuum. With this study we demonstrate that it is possible to carry out a good study of the lines using XSPEC, obtaining similar results to the other authors that used specific softwares for the study of the individual lines as `ISIS` or `PINTofALE` (Nelson et al., 2008; Ness et al., 2009; Drake et al., 2009).

The flux of the H- and He-like lines of Si, Mg, Ne, O and N of days 13.8 and 26.1 is needed to diagnose the temperature and electron density of the emitting material (Porquet & Dubau, 2000; Mauche, 2002). The G ratio, $(f + i)/r$, is sensitive to the electron temperature and the ionization mechanism, where G $\sim$1 indicates a plasma in collisional ionization equilibrium. Larger values (G$>$ 4) indicate contributions from photoionization (Porquet & Dubau, 2000) (see Appendix C.3). Once we have the G ratios, it is possible to obtain the temperature of the Si XIII, Mg XI, Ne IX, O VII and N VI lines by using Figure 7 of Porquet & Dubau (2000) that relates the G ratio with the corresponding temperature. The obtained G ratios are around 1 for all the lines (Table 11). We conclude that we have a collisional plasma, reaffirming our choice of using the APEC model and the result of Nelson et al. (2008). The G ratio temperatures (Table 11) are smaller than T_{low} from EPIC/MOS1 but similar to the lowest temperature from RGS obtained by Ness et al. (2009) (0.3 keV).

We can alternatively obtain the temperature through the flux of the H-like and He-like recombination line ratios of Si, Mg, Ne, O and N using Figure 3 of Mauche (2002) that shows the temperature needed to obtain a certain value of the H/He ratio. Ness et al. (2009) used the theoretical predictions of the same ratios as a function of temperature extracted from an atomic database computed by the APEC, assuming that the plasma is at collisional equilibrium. The temperatures obtained with the H/He ratio (Table 11) are similar to T_{low} from EPIC/MOS1 and also to the values of Table 4 in Ness et al. (2009). The differences are due to the differences in the fluxes.

The R ratio, f/i, is related with the electron density and is a good diagnostic tool for collisional ionization equilibrium plasmas to measure electron densities if the electron density is in the range $10^8 - 10^{13}$ cm^{-3} (Vink, 2012). Once we have the R ratio, it is possible to obtain the electron density of the Si XIII, Mg XI, Ne IX, O VII and N VI lines by using Figure 9 of Porquet & Dubau (2000) that relates the R ratio with the corresponding electron density. However, the n_e obtained with this method are too large taking into account the densities that we will show in §3.2.4. We can use these densities as upper limits but not to prove the evolution of the density with the R ratio

(Ness et al., 2009). The results are summarized in Table 11.

By analysing the RGS and the MOS spectra together we obtain the global properties of the shocked plasma between 0.2 and 10 keV early after the explosion. Thanks to that we are able to fit the data with only two temperatures instead of the large number of temperatures employed by Nelson et al. (2008) and Ness et al. (2009), making the physical model simpler. Besides, with MOS and RGS we can determine the physical properties of the plasma more precisely than using only the RGS spectra, thus allowing for a better description of the nova evolution.

3.2.1.5 Evolution of the Shocked Plasma in X-rays

The study of the evolution of the plasma properties, such as temperature, absorption, flux, and emission measure, gives us a global view of the RS Oph shocked plasma. We compare the properties obtained with the study of the EPIC/MOS1 spectra with those obtained from *Swift*/XRT (Bode et al., 2006), *RXTE*/PCA observations (Sokoloski et al., 2006, and our reanalysis), and the previous studies of the *XMM-Newton*/RGS (Nelson et al., 2008; Ness et al., 2009). This study was performed for observations before the SSS phase.

The evolution of the temperature before the SSS phase is shown in Figure 18. The temperature is approximately constant the first days until day 8 after the outburst. Then it decreases with time faster than expected. This fast cooling is related to radiative loses. It has consequences in the study of the particle acceleration (Tatischeff & Hernanz, 2007) as we will see in §3.3. The several temperatures demonstrate the complexity of the plasma and the need for more than one temperature to describe the plasma. We affirm that the hottest temperature is the characteristic temperature of the shocked plasma.

The emission measure gives information about the amount of hot material that emits in X-rays. Figure 19 shows the evolution of the EM obtained from the study of *RXTE* and *XMM-Newton* observations. The emission measure is practically constant until day 6 and later decreases with time, reaffirming that the plasma is cooling. *RXTE* detects hotter material than *XMM-Newton*. Thus, on day 26 RS Oph could not be detected by *RXTE*.

We also study the evolution of the absorption N_H. In Figure 20, N_H decays until day 8, in which the absorption reached values similar to the interstellar medium absorption. Both our results and those of Ness et al. (2009) obtained with the satellite *XMM-Newton* give slightly larger values of N_H than those obtained with *RXTE*/PCA (Sokoloski et al., 2006) and *Swift*/XRT (Bode et al., 2006). The good resolution of *XMM-Newton* at low energies allows to determine N_H better than *RXTE*/PCA and *Swift*/XRT. Nelson et al. (2008)'s absorption on day 13 is larger than that obtained in the other studies. A good determination of N_H is crucial to estimate the mass-loss rate of the RG wind.

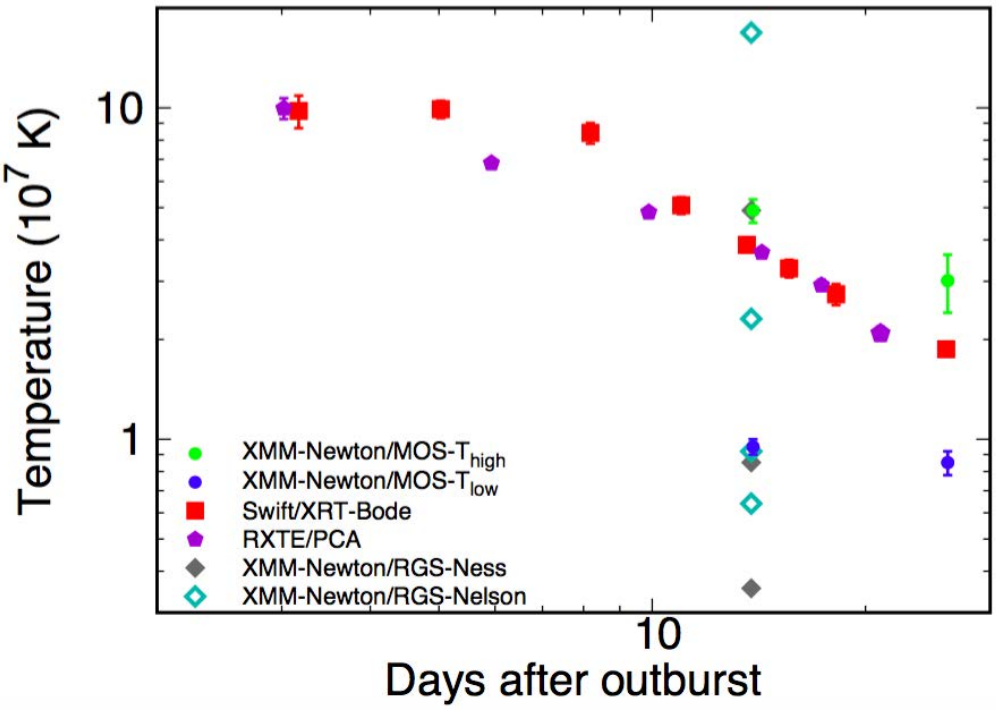

Figure 18: Plasma temperature evolution with time. Data from the studies of *XMM-Newton*/MOS1 (§ 3.2.1.4) with 3σ error bars, *Swift*/XRT (Bode et al., 2006) with 2σ error bars, *RXTE*/PCA (Sokoloski et al., 2006, and §3.2.1.1) with 1σ error bars, and *XMM-Newton*/RGS (Ness et al., 2009, 2σ error bars) and (Nelson et al., 2008).

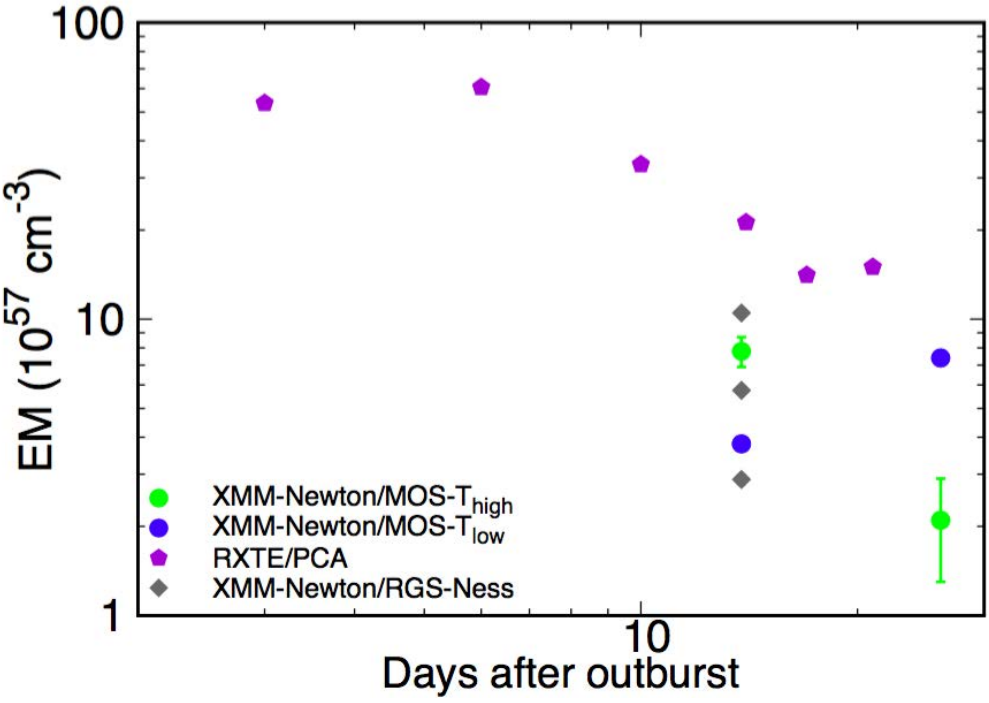

Figure 19: EM evolution with time. Data from the study of *XMM-Newton*/MOS1 (§ 3.2.1.4) with 3σ error bars, *RXTE*/PCA (§3.2.1.1) with 1σ error bars and *XMM-Newton*/RGS (Ness et al., 2009) with 2σ error bars.

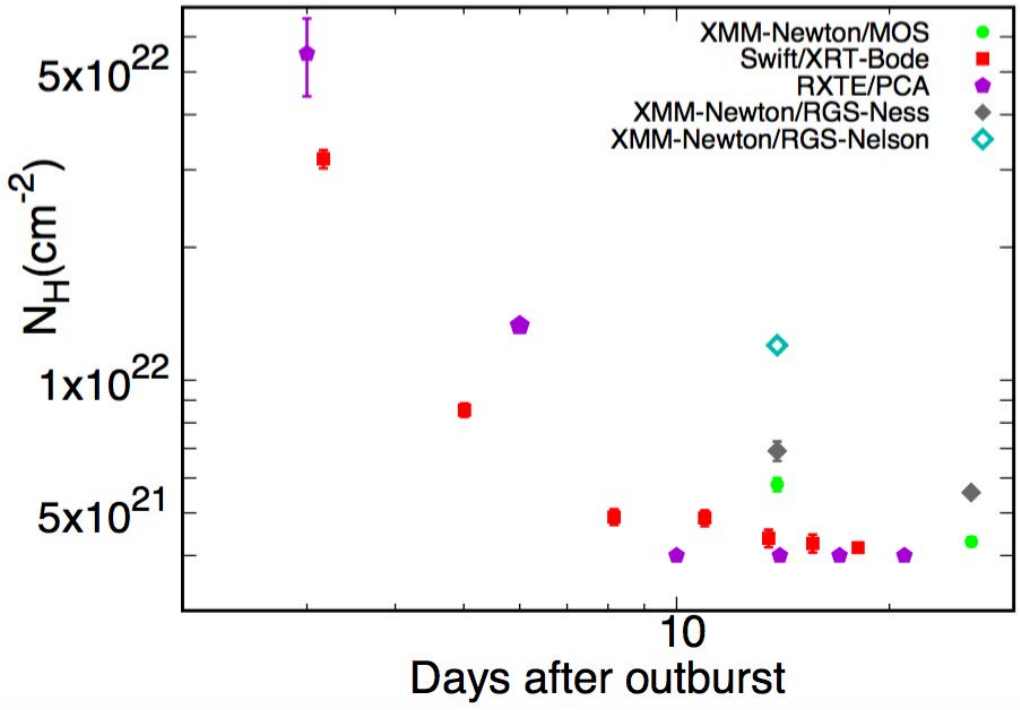

Figure 20: N_H evolution with time. Same data as Figure 18.

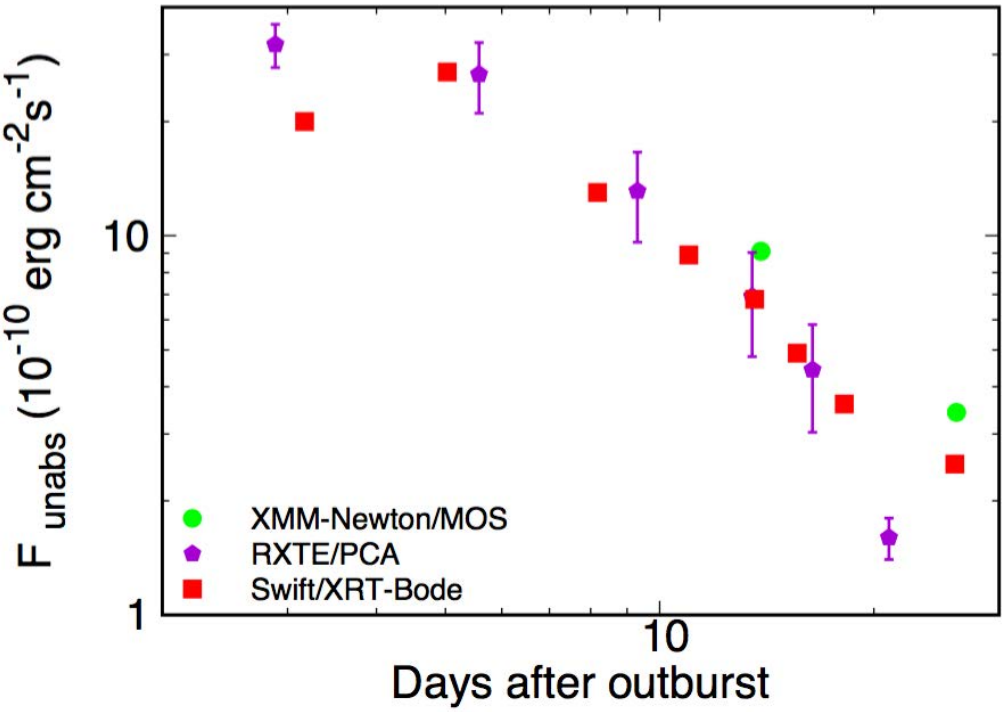

Figure 21: X-ray unabsorbed flux evolution over time. Data from the study of *XMM-Newton*/MOS1 (§ 3.2.1.4) with 2σ error bars, *Swift*/XRT (Bode et al., 2006) and *RXTE*/PCA (Sokoloski et al., 2006, and §3.2.1.1) with 1σ error bars.

Figure 21 shows the evolution of the unabsorbed flux of RS Oph. The unabsorbed flux is practically constant until day 5 after the outburst. However, after this day, the unabsorbed flux decreased very fast because of the cooling. This fact produced that *RXTE*/PCA, whose energy range is $3 - 20$ keV, detected less flux on day 21 after the outburst.

3.2.2 *Early Radio Emission*

In the last outburst, RS Oph was observed with several radio telescopes as Giant Metrewave Radio Telescope (GMRT), Multi-Element Radio-Linked Interferometer Network (MERLIN), VLA, One-Centimetre Radio Array (OCRA-p), European VLBI Network (EVN) and VLBA (O'Brien et al., 2006; Kantharia et al., 2007; O'Brien et al., 2008; Rupen et al., 2008; Sokoloski et al., 2008; Eyres et al., 2009). This emission was associated with the shock wave resulting from the outburst, which is the same material that we detect in hard X-rays. We will focus on the early radio emission of RS Oph, and specifically, on the observations of RS Oph the days 13 and 26 after the outburst to compare with the *XMM-Newton* observations and have a global view at all energies. The flux of the different detections between days 4 and 29 after the outburst are presented in Table 12.

The high angular resolution of the radio observations allows to have resolved observations of the shocked material (Figure 22). In the first epoch, RS Oph had approximately a circular structure at 1.7 GHz, and an annular shape at 5 GHz with a bright part on the eastern side. Its shape is similar to core collapse SNRs, which have an ambient medium with $\rho \propto R^{-2}$, as in the case of the symbiotic novae. The changes in the evolution of a Supernova (SN) II can last millions of years, while in a nova, we can study the different phases of its remnant in a short period of time.

In less than 10 days after the outburst, the structure grew quickly and a second component appeared to the east of the ring (Figure 22). This new component started to be observed because of a decrease in the column density absorption (Kantharia et al., 2007). Between day 20 and day 26, the eastern component did not show deceleration. Moreover, on day 26 after the outburst, the images are dominated by a ring which is much brighter to the east than to the west as on day 13. The asymmetry of the ring remains much more pronounced at 5 GHz than at 1.7 GHz. We could be seeing a non-spherical ejecta geometry as concluded from the radio observations of the 1985 outburst (Taylor et al., 1989; Lloyd et al., 1993). However, considering the 1.7 GHz observations, we can assume that spherical symmetry is a good approximation for the central source the first days after the outburst (Rupen et al., 2008).

The radio light curves of RS Oph the first days after the outburst (Figure 23) show an initial rapid rise detected at high frequencies, between 1.46 and 22.48 GHz. Eyres et al. (2009, Figure 1) divided the MERLIN observations on day 4 and 5 after the outburst into 30 min segments to follow the rapid rise. However, on day 7 after the outburst the flux was constant during all the observation. Two maxima took place on day 13

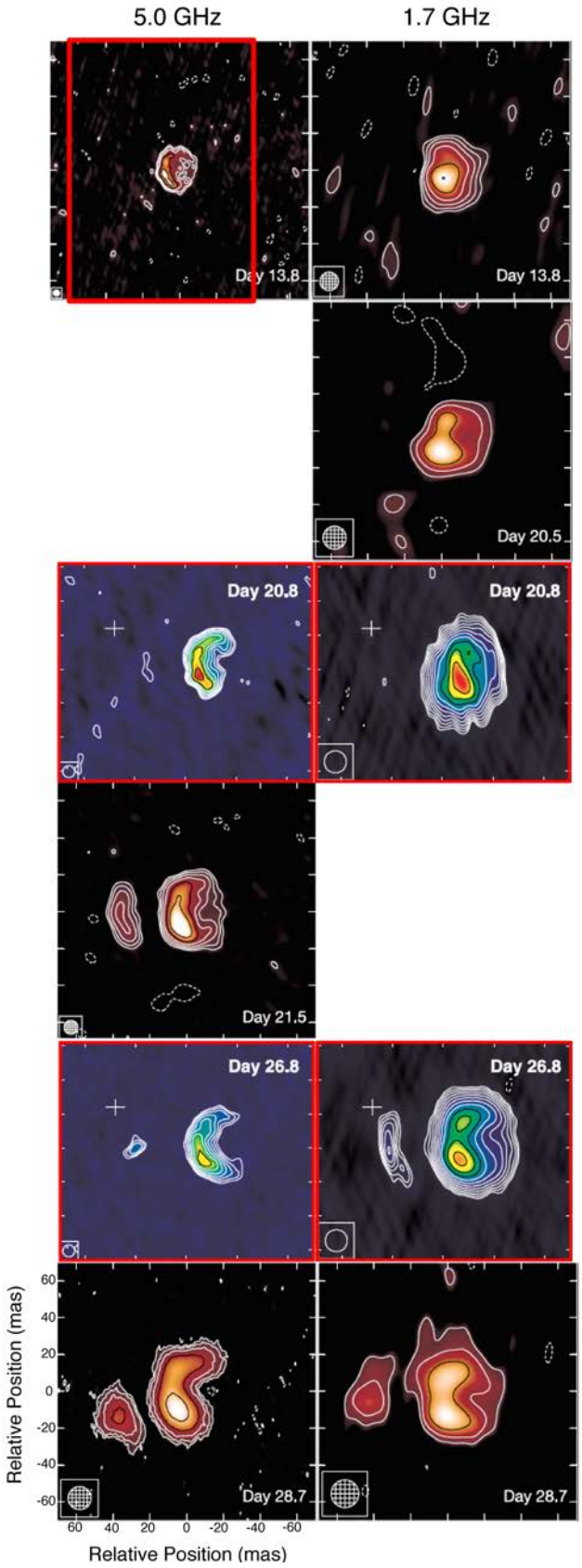

Figure 22: Radio image of RS Oph at 5.0 GHz (left column) and 1.7 GHz (right column) observed with the VLBA and EVN (adapted from O'Brien et al., 2006; Rupen et al., 2008). The synthesized beam is shown in the bottom left corner of each image. The images from O'Brien et al. (2006, warmer color scale) are taken in a larger area than those of Rupen et al. (2008), which is indicated in the top left panel with a red frame.

Table 12: Observed flux densities for RS Oph*

Days after outburst	0.61 GHz GMRT	1.06 GHz GMRT	1.28 GHz GMRT	1.39 GHz GMRT	1.46 GHz VLA	1.7 GHz VLBA	4.89 GHz VLA	5.0 GHz VLBA	6.0 GHz MERLIN	14.96 GHz VLA	22.48 GHz VLA	30.0 GHz OCRA-p
4.5	...	...	...	...	...	...	...	...	14±2.0	...	...	...
4.7	...	...	...	...	2.8±0.2	...	15.2±0.2	...	...	23.2±0.6	26.2±0.5	...
5.5	...	...	...	...	...	...	...	...	33±2.0	...	...	...
7.46	...	...	...	...	...	...	...	...	41.2±0.8	...	...	...
11.2	...	...	49.5±7.4	...	...	...	...	...	...	...	...	...
13.8	...	...	...	...	57.6±0.3	...	53.3±0.2	43±1	...	50.5±0.5	61.1±0.7	...
16.34	...	...	...	...	...	...	...	...	...	...	...	55±6.0
16.52	...	...	...	...	...	...	...	...	37.9±1.1	...	...	...
17.19	...	55.4±8.3	50±7.5	56.8±8.5	...	...	...	...	...	...	...	...
17.47	...	...	...	...	...	...	...	...	35.8±0.7	...	...	...
20.26	48.4±7.2	...	...	...	...	...	...	...	...	...	...	...
20.8	...	...	...	...	...	43.1±0.3	...	32.2±0.6	...	...	...	...
21.5	...	...	...	...	...	...	...	32±1	...	..	..	...
21.85	...	...	...	...	48.2±0.32	...	44.5±0.2	..	43±5.0	37.4±0.6	36.4±0.9	...
23.36	...	...	...	...	...	...	...	...	...	...	...	53±6.0
24.28	...	...	...	...	...	...	...	...	...	...	...	74±7.0
26.8	...	...	...	...	...	41.3±0.2	...	28.8±0.2	...	...	...	...
27.85	...	...	...	...	50.4±0.4	...	50.3±0.2	...	...	52.9±0.6	69.4±0.7	...
28.5	...	...	...	...	...	...	...	..	45±5.0	...	...	...
28.7	...	...	...	...	...	...	...	17.0±0.6	..	...	...	...

*Flux densities in mJy for RS Oph from GMRT (Kantharia et al., 2007), VLA (Eyres et al., 2009), VLBA O'Brien et al. (2006); Rupen et al. (2008); Sokoloski et al. (2008), MERLIN (Eyres et al., 2009) and OCRA-p (Eyres et al., 2009).

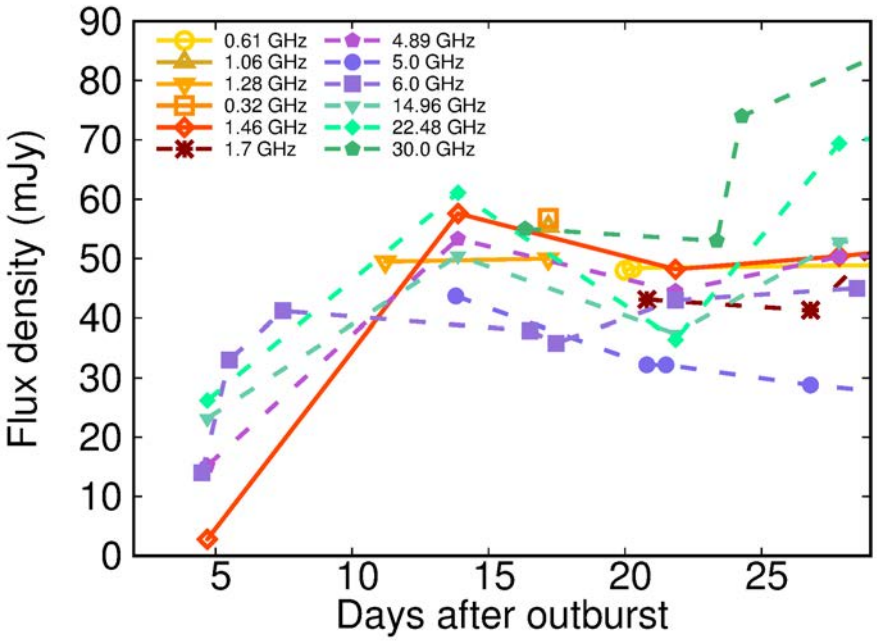

Figure 23: Radio light curve at low frequencies (warm colors) and high frequencies (cool colors) using the data of Eyres et al. (2009); Rupen et al. (2008); Sokoloski et al. (2008); O'Brien et al. (2006); Kantharia et al. (2007).

and 39 after the outburst, with a minimum between them on day 21. This early rise is due to the shock between the ejecta and the non-homogeneous RG wind. In the 1985 outburst only the second peak was observed with VLA (Taylor et al., 1989). The low frequencies (< 1.4 GHz) are dominated by a non-thermal emission component and the higher frequencies by a thermal component (Kantharia et al., 2007). Therefore, the first maximum is dominated by the thermal component while the second maximum is a mixture of both components (Figure 23). Actually, some nova radio light curves show an early bump and a second maximum in less than 100 days after the optical maximum (Vlasov et al., 2016). The second maximum and its flat spectrum, as in the case of RS Oph, were interpreted as a result from the shock interaction between the nova ejecta and a dense external shell.

To build the different spectra, we use information of different radio telescopes with different sensitivities. The first detection in radio was on day 4 after the outburst (Figure 24). These observations were simultaneous to *Swift* observations. We can say that this day the thermal emission dominated at all wavelengths including radio, and is consistent with the expansion of the ejecta in the dense parts of the circumstellar material. Moreover, this day RS Oph was only observed with radio telescopes sensitive to the thermal emission, VLA and MERLIN. At $\nu < 5$ GHz, there was a large increment of the flux with a power law index of $\alpha = 1.4$, this increment being smoother at $\nu > 5$ GHz with $\alpha = 0.3$. Taking into account Eyres et al. (2009, Table 3), the major axis of the deconvolved size on day 4 was larger than that on day 13 and equal to that of day 21. Therefore, this flux could correspond to contributions from other sources. They used a big beam for a small compact source and this made the flux of the source to be

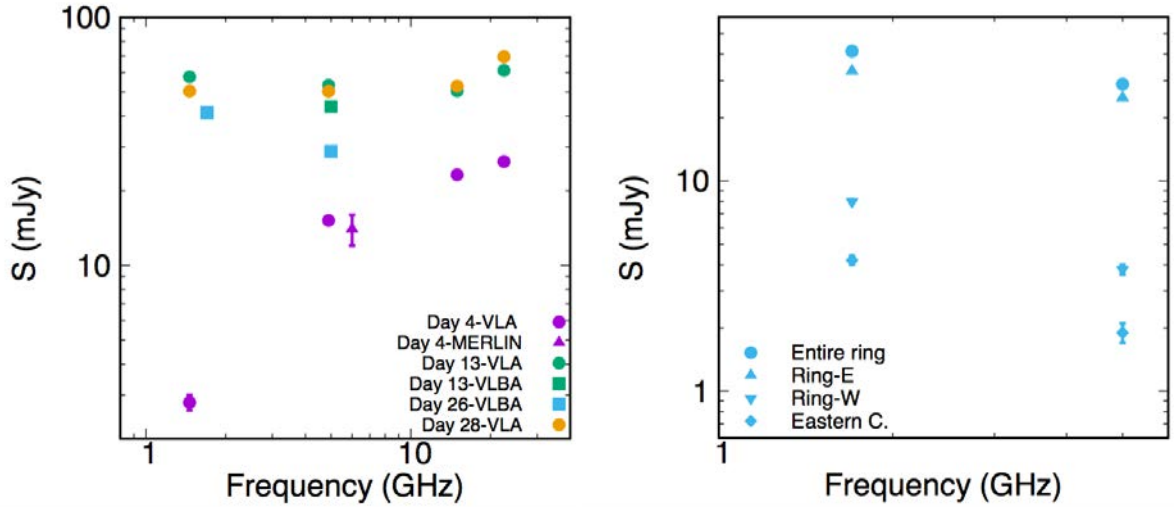

Figure 24: Left panel: RS Oph radio spectra evolution the first days after the outburst on day 4 (purple), 13 (green), day 26 (blue) and day 28 (orange) after the outburst. Dots correspond to the VLA observations, triangle to the MERLIN observations and squares to the VLBA observation (O'Brien et al., 2006; Rupen et al., 2008; Eyres et al., 2009). Right panel: Radio spectra of entire ring (dots), ring-E (inverse triangle), ring-W (triangle) and eastern component (diamond) of RS Oph by VLBA on day 26.8 (Rupen et al., 2008).

diluted in the flux of the surrounding medium.

On day 13 after the outburst, we see that the spectrum obtained with the VLA data is practically flat because it is a mix between non-thermal and thermal emission. There are minor differences ($\sim$ 1 mJy) between the flux detected by VLA and VLBA at 5 GHz (O'Brien et al., 2006, private communication). VLA observed the thermal component because it is sensitive to the extensive structure. However, there is a significant contribution from synchrotron emission, which we observe in the images obtained by the VLBA. This emission is related with the particles accelerated in the shock wave (O'Brien et al., 2006; Rupen et al., 2008). If we suppose that the VLBA measurement comes from non-thermal radiation, we see that the power law index for $\nu < 5$ GHz is $\alpha = -0.22$. However, for $\nu > 5$ GHz the power law index is practically 0.

Rupen et al. (2008) studied separately the different components of the image on day 26 and built the spectrum for each component. They measured the flux of the entire ring (Figure 24, left panel), but also the ring-east, the ring-west and the eastern component that appeared on day 21. Figure 24 (right) compares the fluxes of the different components, from which we conclude that all the spectra have a negative spectral index (Rupen et al., 2008, Table 1). The flux of the entire ring is 10 times higher than the flux of the eastern component. The spectral index of the ring ($\alpha = -0.33$) varies from -0.27 (bright part) to -0.67 (dim part) and the eastern component has a more pronounced spectral index (α = -0.71). Therefore, we conclude that the radiation detected by VLBA is dominated by the non-thermal emission which comes from the expanding shell. The nature of the eastern component is not clear but the fact that it was first observed on day 21 can be related to the density of the RG wind being lower than

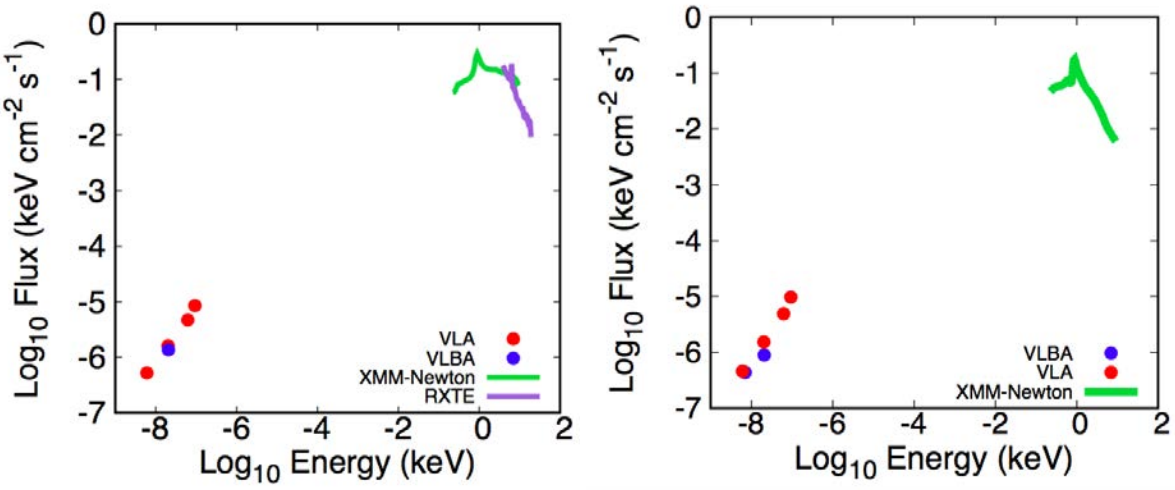

Figure 25: SED for RS Oph on 2006 February 26 (left) and 2006 March 10 (right), 13 and 26 days after the outburst respectively. Radio: VLBA data (blue dots) (O'Brien et al., 2006; Rupen et al., 2008) and VLA data (red dots) (Eyres et al., 2009). X-ray: *XMM-Newton* data (green line) and *RXTE* data (purple line) (Sokoloski et al., 2006).

in the previous days. Relativistic electrons and enhanced magnetic fields are needed for synchrotron emission produced in the shock between the ejecta and the circumstellar material. Rupen et al. (2008) obtained that the magnetic field in the ring and the eastern component is in the range of 0.03 and 0.1 G. However, Kantharia et al. (2007) obtained a B$\sim$3.5 G.

By analysing the spectrum measured by the VLA on day 28 (Figure 24), we see a mixture of thermal and non-thermal emission with a spectral index close to 0. The flux detected by VLA on day 13 and day 28 after the outburst is similar and is $\sim$10 mJy larger than the flux detected by VLBA on day 26 after the outburst. These differences are due to the different maxima in the light curve. Day 26 and day 28 observations took place during the second rise of the light curve, before reaching the second maximum on day 39. Therefore, the flux on day 26 must be lower than the flux on day 28. However, the flux on day 13 was similar to the flux on day 28, because the maximum on day 39 is higher than the maximum on day 13.

The radio observations demonstrated that thermal and non-thermal components took place the first weeks after the nova outburst. The early and fast rise the first days is consistent with a free expansion phase.

We build the Spectral Energy Distribution (SED) of the shocked material 13 and 26 days after the outburst (Figure 25). These days a multiwavelength campaign took place. There is radio emission information from VLBA data (O'Brien et al., 2006; Rupen et al., 2008) and VLA data (Eyres et al., 2009) that shows a mixture of thermal and non-thermal emission with similar fluxes. Besides, in X-rays we have information from *XMM-Newton* and *RXTE* that show a thermal bremsstrahlung continuum with emissions lines. There was probably a non-thermal bremsstrahlung emission related to the synchrotron

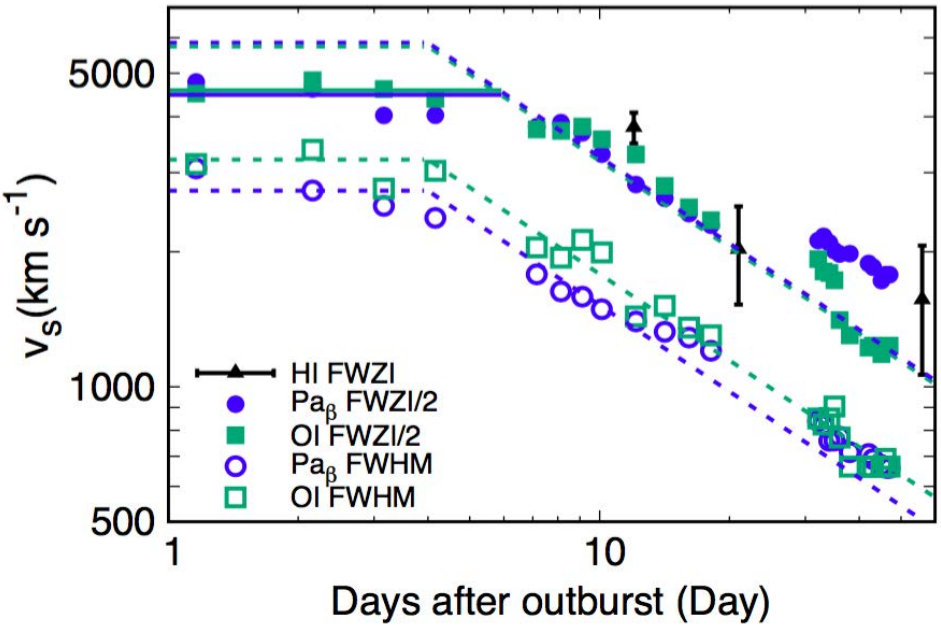

Figure 26: Temporal evolution of the broad gaussian line component FWHM (empty dots and squares) and FWZI/2 (solid dots and squares) of Paβ (blue dots) and O I (turquoise squares) (Das et al., 2006) and FWZI of H I (black triangles) (Evans et al., 2007) emission lines between 1 and 60 days after the outburst. The velocity is fitted to a $t^{-0.64}$ law (dashed line) representative of the radiative cooling phase.

emission detected in radio. However, without observations at higher energies (E>20 keV) the first days after the outburst, we only have the dominant thermal component. If *Swift*/BAT had obtained an spectrum, it could have shown the non-thermal component.

3.2.3 *IR observations*

RS Oph was detected in IR the first weeks after the 2006 outburst (Monnier et al., 2006; Das et al., 2006; Evans et al., 2007; Banerjee et al., 2009). This emission does not come from the same region as the X-rays because the lines observed in IR, as O I, can not be associated with a hot plasma. The near-IR emission is originated in the contact surface between the ejected material (hot compressed region) and the RG wind (cool uncompressed region). The IR lines are usually represented with two different gaussians, a narrow one that is related with the slow movement of wind material and is practically constant in time (Monnier et al., 2006; Evans et al., 2007), and a broad one that comes from a cool dense region with the same velocity of the shocked plasma (Das et al., 2006; Evans et al., 2007).

RS Oph was observed using JHK bands from the 1.2 m telescope at the Mount Abu Observatory (Das et al., 2006; Banerjee et al., 2009). The observations took place between 1.1 and 47 days after the outburst. In the J-band spectra, the most prominent lines are O I at 1.1287 μm and Paβ at 1.2818 μm. The fact that on day 47 after the

outburst, the lines were narrower than the lines on day 1.2 is associated with the deceleration of the shocked plasma (Banerjee et al., 2009, Figure 2 & 3). The kinematic broadening, Full Width at Half Maximum (FWHM) and Full Width at Zero Intensity (FWZI), are good indicators of the shock velocity. FWZI/2 can be used as a good measure of the expansion velocity.

Das et al. (2006) present the FWHM and FWZI/2 of the O I and Paβ lines without uncertainties in the measurements. They fitted the data using a simple power law ($v \sim t^{-\alpha}$) with α between 0.45 and 0.79 (α =0.64). Until day 4 after the outburst, a constant expansion velocity was obtained, corresponding to the free expansion phase. However, the power law index obtained after day 4 was closer to 0.5 (Phase III) than to 0.3 (Phase II) as we explained in §2.4.1. Either Phase II was very short or it did not take place. Figure 26 shows the FWZI/2 and the FWHM of the O I and Paβ fit with α =0.64, that is the spectral index obtained with the observations of *Swift*/XRT (Bode et al., 2006). The slope change of the FWHM data takes place on day 4 after the outburst, and on day 6 in the FWZI/2 as in *Swift*/XRT.

3.2.4 *Properties of the Shocked Plasma and the RG wind obtained with IR and X-ray information*

The combination of X-ray and IR data provide us with some of the properties of the shocked plasma and the RG wind. The first observations in IR and in X-rays were made 1 day after the outburst. IR observations were not simultaneous to X-ray observations. We interpolate the v_s corresponding to the *RXTE*/PCA and *XMM-Newton*/XRT observation times using the FWZI/2 of Paβ. With v_s at the X-rays and IR observation times, we calculate the radius of shocked material (R_s):

$$R_s(t) = \int_{t_0}^{t_f} v_s(t)dt \longrightarrow R_s(t_{i+1}) = R_s(t_i) + v_s(t_i)\Delta t \tag{9}$$

Figure 27 shows the shock radius as a function of time. The radius increases rapidly the first week. After day 6, with the decrease of the velocity, the increment in radius was reduced. There are different relevant radii in the geometry of the system: the separation between the WD and the RG ($\sim$ 1.5 AU ($\sim 2.4 \times 10^{13}$ cm), Fekel et al., 2000), and the outer radius of the RG wind. This last one is defined as the radius that reaches the RG wind moving out at velocities between 10 and 20 km s^{-1} between two consecutive outbursts, $r_{out} = u_{RG}\Delta t$ where $u_{RG} \cong 10 - 20$ km s^{-1} is the RG wind terminal velocity and Δt =21.04 yr is the time between the last two outbursts (1985 – 2006). We state that r_{out} was between 6.6×10^{14} cm and 1.3×10^{15} cm, and the ejecta reached it in $\sim 24 - 72$ days after the outburst, during the SSS phase. The minimum radius that we obtain is 5×10^{13} cm the 1st day after the outburst, being larger than the radius of the system separation. We can not know if the radius of the shocked plasma changed because of the system separation. On the other hand, the radius corresponding to the day when the super soft phase appeared and the lower r_{out} are the same. We see a change in the v_s slope around $R_s \sim 9 \times 10^{14}$ cm (day 30 after the outburst). However,

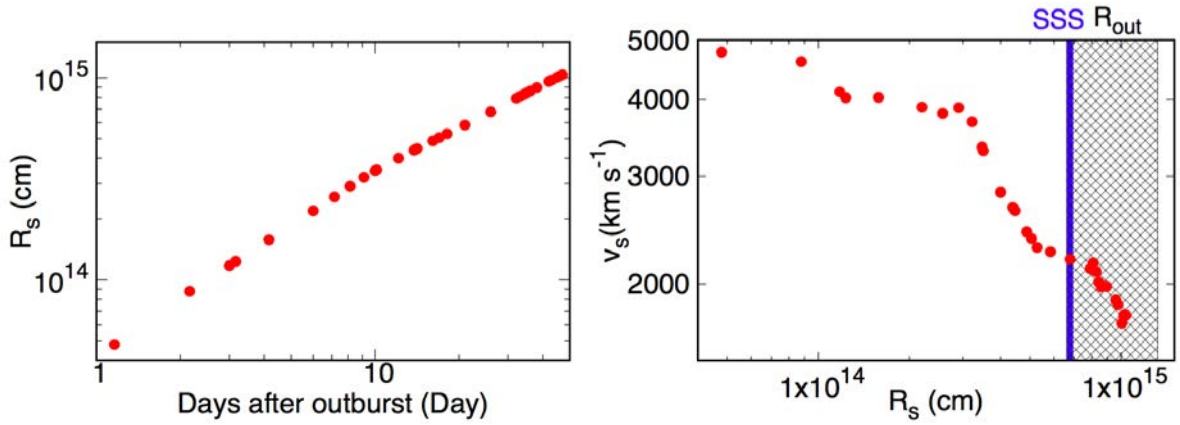

Figure 27: Left: Shock radius as a function of time. Right: FWZI/2 of Paβ line as a function of the shock radius.

the most dramatic change was on day 6 ($R_s \sim 4 \times 10^{14}$ cm).

In order to know the volume of the shocked plasma, we approximate the ejecta to an ideal spherical shell. We also consider that the RG wind has a spherically-symmetric density profile. With these simplifications, the volume of the shock material (Vol_s) is given by

$$\mathrm{Vol}_s(t) = \mathrm{Vol}_s(t_0) + \int_{t_0}^{t_f} 4\pi R_s^2(t) \cdot v_s(t) dt \longrightarrow \mathrm{Vol}_s(t_{i+1}) = \mathrm{Vol}_s(t_i) + 4\pi R_s^2(t_i) \cdot v_s(t_i) \Delta t \tag{10}$$

We use the Vol_s together with the EM (Figure 19) to obtain the electron density (n_e). There are different EMs for the same day. Thus, we use the EM corresponding to the most representative temperature of the shocked plasma for each day. The EM is only known from the X-ray detections. For this reason, we interpolate linearly the EM for the IR observation times. Figure 28 shows that n_e decreases faster after day 6 until it reaches a value of $\sim 10^6$ cm^{-3}, 50 days after the outburst. We assume that the main element of our plasma is hydrogen. The mass density of the shock plasma is given by $\rho_H = n_e \times \mu_e / N_a$ where N_a is the Avogadro constant and $\mu_e = 2/(X+1)$ where X is the fractional abundance of Hydrogen (by mass fraction). The mass density is directly proportional to the electron density, following the same behaviour.

We assume that the material that emits in X-rays is composed of the ejected mass (M_{ej}) and the swept-up material ($\mathrm{M}_{\mathrm{swept}}$) over time. We call the sum of these two masses shocked mass (M_s), which is defined as $\mathrm{M}_s = \rho \times \mathrm{Vol}_s$. Figure 28 shows how the shocked mass increases as a function of time because the RG wind is swept. The M_s the first day of the SSS phase 26 days after the outburst is similar to the M_{ej} obtained by Das et al. (2006) and Hachisu & Kato (2001) ($\sim 3 \times 10^{-6}$ $\mathrm{M}_\odot$).

The density of the RG wind (ρ_w) is given by

$$\rho_w(r) = \dot{\mathrm{M}}_{\mathrm{RG}} / 4\pi r^2 u_{\mathrm{RG}} \tag{11}$$

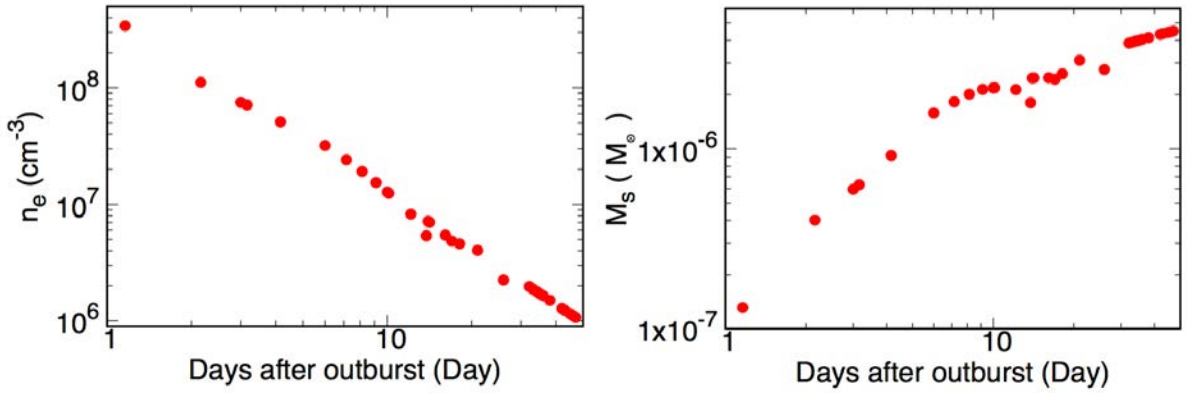

Figure 28: Evolution of the electron density and shocked plasma mass.

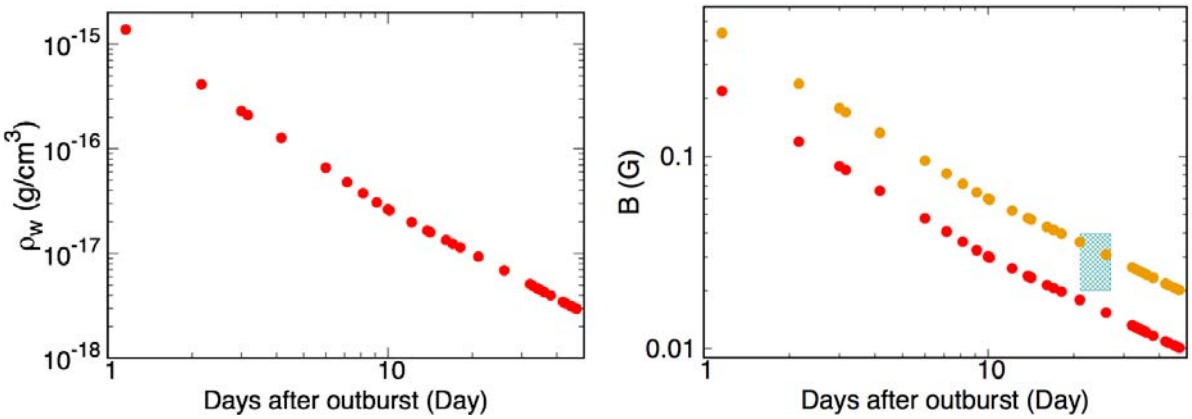

Figure 29: The density of the RG wind as a function of time (ρ_w) on the left, and the magnetic field of the RG wind as a function of time, B_w (red dots), the magnetic field of the shock, B_0 (orange dots) and the one detected by Rupen et al. (2008) (shaded area) on the right.

where $\dot{M}_{RG}$ is the RG mass-loss rate ($(\dot{M}/u)_{RG}$=4×10^{13} g cm^{-1}, Tatischeff & Hernanz, 2007) and r is R_s. This value is larger than $(\dot{M}/u)_{RG}$ obtained by O'Brien et al. (1992) for the 1985 outburst ($(\dot{M}/u)_{RG} = 5.2 - 7.44\times\ 10^{12}$ g cm^{-1}). Figure 29 shows that ρ_w decreases over time. If we compare ρ_w with ρ, we obtain that ρ_w is slightly larger than ρ.

In this type of systems, a relatively large magnetic field of stellar origin is expected to preexist in the RG wind. To obtain the RG wind magnetic field (B_w) it is assumed that the magnetic pressure (P_m=$B_w^2/8\pi$) is equal to the thermal pressure equipartition ($P_{th} = \rho_w k T_w/\mu m_H$). The B_w is given by

$$B_w = (8\pi\rho_w k T_w/\mu m_H)^{0.5} \tag{12}$$

where T_w=10^4 K is the wind temperature, which we assume uniform in the RG wind. The turbulent motions in the wind amplify the magnetic field close to the shock front because of the various interactions between the shock plasma and the accelerated particles (Figure 5). Thus, it is expected that B_w close to the shock front was $B_0 = \alpha_B B_w$ where α_B is the amplification factor (Lucek & Bell, 2000). Rupen et al. (2008) obtained a magnetic field of the shock of B_0=0.03 G at between 20 and 27 days after the outburst.

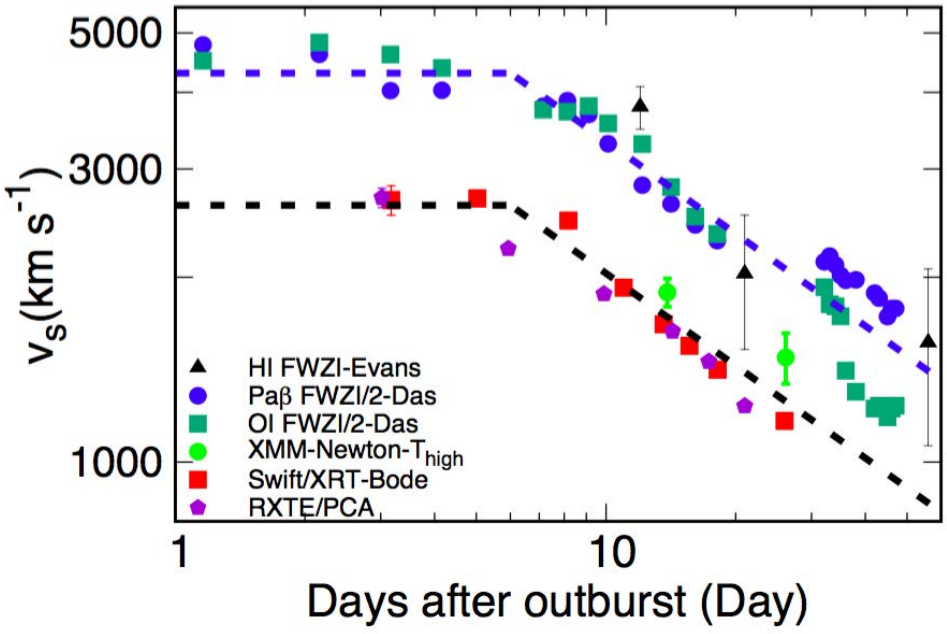

Figure 30: Comparison of the shock velocity as a function of time (adapted from Tatischeff & Hernanz, 2007). FWZI/2 of Paβ and O I (Das et al., 2006) and FWZI of H I (Evans et al., 2007) emission lines between 1 and 60 days after the outburst. Data from the studies of *XMM-Newton*/MOS1 (§ 3.2.1.4) with 3σ error bars, *Swift*/XRT (Bode et al., 2006) with 2σ error bars, *RXTE*/PCA (Sokoloski et al., 2006, and §3.2.1.1) with 1σ error bars

An amplification of the magnetic field is needed to reach this value. α_B =2 agrees with Rupen et al. (2008) value for the magnetic field and with the value of the amplification of the magnetic field by Tatischeff & Hernanz (2007). Figure 29 shows the RG wind magnetic field and the magnetic field of the shock compared with the value obtained by Rupen et al. (2008).

3.3 PARTICLE ACCELERATION IN RS OPH

The relation for a test-particle strong shock (§2.4) gives the velocity at which the shock expands into the RG wind (Zeldovich & Raizer, 1967; Longair, 1984; Landau & Lifshitz, 1987). However, this relationship is not valid when the shock is modified by the escape of cosmic rays. In this case the shock compression ratio ($\Gamma = (\gamma+1)/(\gamma-1)$, where γ is the adiabatic index) has no longer a value of $\Gamma = 4$, which corresponds to the ideal case without cosmic ray escape for a monoatomic gas, and acquires larger values ($\Gamma > 4$). In this case Equation 5 underestimates the shock velocities (Decourchelle et al., 2000; Ellison et al., 2007).

Tatischeff & Hernanz (2007) compared the shock velocities determined from the FWZI/2 of the IR data (Das et al., 2006; Evans et al., 2007) with the shock velocities obtained using the X-ray temperatures. A considerable difference between their values was found. They showed that the blast wave decelerated faster than expected as a consequence of

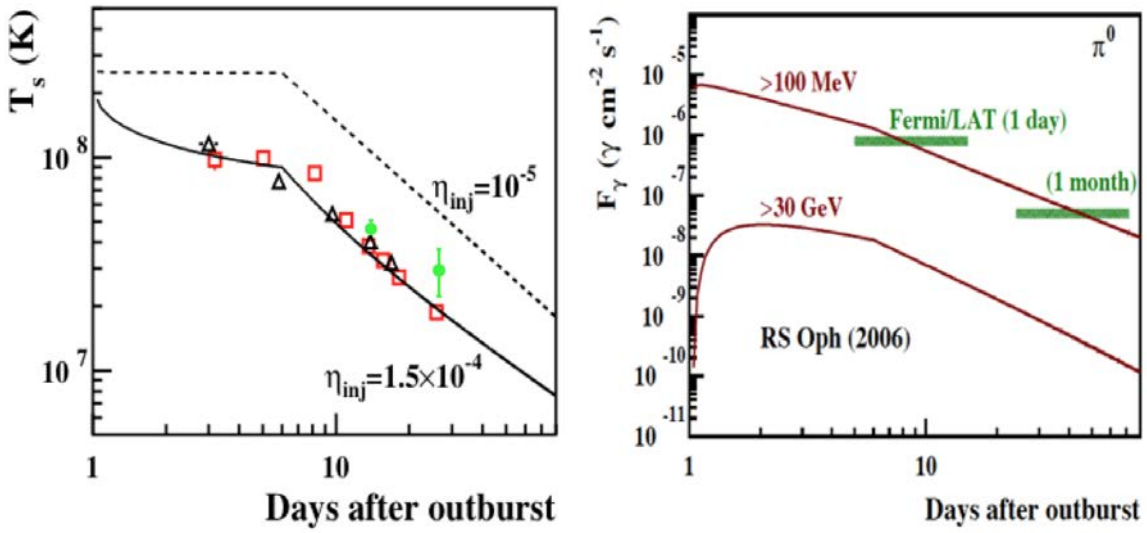

Figure 31: Left panel: Calculated postshock temperature for two values of η_{inj} compared to the RXTE, Swift and XMM Newton data (adapted from Tatischeff & Hernanz, 2008). Right panel: High energy γ-ray light curves expected for RS Oph (2006) compared with Fermi/LAT sensitivities for E> 100 MeV (from Hernanz & Tatischeff, 2012).

acceleration of particles in the shock. The reason is that the most energetic ions escaped from the shock region. Figure 30 shows that the IR and X-ray emissions have a constant velocity characteristic of the free expansion stage before day 6 after the outburst. After that the shocked material decayed as expected for a material which is cooled by radiative loses. The lack of the Sedov-Taylor phase or its short duration was also seen in both wavelength ranges. Figure 30 shows that our T_{high} obtained with the EPIC/MOS1 camera is consistent with the previous results, confirming the results of Tatischeff & Hernanz (2007) with a new test.

The production of non-thermal particles in the shock through the nonlinear diffusive shock acceleration process (Berezhko & Ellison, 1999), also called first-order Fermi shock acceleration, was deduced by Tatischeff & Hernanz (2007). This allowed to quantify the modification of the shock structure due to the energetic ions. With the results obtained with the study of the IR and X-rays data, they estimated an amplification factor of $\alpha_B = 2$ and a compression ratio of the shock of $\Gamma = 6.5 > 4$. The temperatures obtained with *RXTE*/PCA and *Swift*/XRT were reproduced with a proton injection rate η_{inj}=1.5×10^{-4} (Figure 31). In the case of the MOS1 data, a slightly larger injection of particles would be necessary to reproduce the obtained temperatures. With all these results, the thermodynamic properties of the shocked gas were obtained. These results reveal that the diffusive acceleration of particles can be efficient in collisionless shocks, and the pressure from the energetic ions can strongly modify the shock structure.

Finally, they estimated a F$\gamma \sim 3 \times 10^{-6}$ ph cm^{-2} s^{-1} for the first week after the outburst. Figure 31 shows the theoretical light curves for γ-ray energies E>100 MeV and E> 30 GeV compared to the Fermi/LAT sensitivities for 1 day and 1 month of

observations. The conclusion is that RS Oph would have been detected by Fermi/LAT in its last outburst.

3.4 SUMMARY

In this chapter, we present a new and detailed analysis of the early emission from RS Oph. It is based on X-ray, radio and IR observations, and takes into account the γ-ray prediction by Tatischeff & Hernanz (2007). This study simplifies and completes the description of the early X-ray emission and allows to obtain the evolution of the global properties of the shocked plasma the first weeks after the nova outburst. With respect to the previous X-ray works, we carry out a new analysis of the RXTE/PCA and the XMM-Newton/RGS observations. A double nature of the radio emission, thermal and non-thermal emission, was detected, suggesting the possible existence of a non-thermal X-ray emission, not yet observed in novae. Based on the X-ray and IR results, we have shown that the plasma suffered radiation losses, related with the acceleration of particles in the shock. Properties as the radii, the electron density, the shocked mass, the density of the RG wind and the amplification of the magnetic field were obtained. This has been derived from the comparison of the X-ray, IR and radio information. Finally, we compare our results with the study carried out by Tatischeff & Hernanz (2007), suggesting that a larger injection of particles would be necessary to explain the obtained temperatures with the MOS1 camera. In the next explosion in 2026 it will be possible to compare and check these theories with the new generation of telescopes as Athena, Astrogam or SKA.

4

V745 SCO

4.1 INTRODUCTION

V745 Sco is one of the nine recurrent novae known in our galaxy and has been detected three times. The first observation was in 1937. The nova was discovered in the 330 Franklin-Adams plates analysed in the Kapteyn Astronomical Laboratory at Groningen (Plaut, 1958). The second detection was in 1989 with IUE by Schaefer (2010). This same author suggested an additional unobserved outburst around 1963 between the two first detections and proposed a recurrence period of ∼25±1 years. This suggestion was confirmed 25 years later with a new outburst in 2014. This nova decreases very fast (t_3=7 days) and has a relatively faint peak (m_v=9 mag in the maximum). For these reasons, some outbursts might have been missed (Page et al., 2015b).

Regarding its composition, V745 Sco is a symbiotic binary system formed of a WD and a RG. The RG of the system is classified as an M-type star. Duerbeck (1989) used the TiO bands to conclude that the RG of the system is an M6 III, whereas, Harrison et al. (1993) used CO absorption features to conclude that it is an M4 III.

Anupama (2008) classified V745 Sco as a long period recurrent nova system like RS Oph, T CrB and V3890 Sgr based on its estimated orbital period. There are some discrepancies about it, but it is known that if the secondary is a red giant, the orbital period might be a few hundreds of days. The optical observations in quiescence taken at Cerro Tololo between 2004 and 2008 by Schaefer (2009, 2010) indicated a photometric periodicity of 255 ± 10 days. The systematic variations in the cycles of the light curve attributed to ellipsoidal modulations showed that the double of the photometric period is equal to the orbital period and therefore the expected orbital period is 510 days. However, Mróz et al. (2014) showed that there is no 255 days-periodicity or ellipsoidal effect, but instead they found semi-regular pulsations of the RG with sinusoidal variations at 136.5 days and 77.4 days. They used data from the Optical Gravitational Lensing Experiment (OGLE) from 2001 to 2014. Also, in the last outburst in 2014 a period of 77 and 155 days was observed with the Small and Moderate Aperture Research Telescope System (SMARTS) (F. Walter priv. comm.; see also Page et al., 2015b).

The distance to V745 Sco is not clear but Sekiguchi et al. (1990) suggested that this nova must be a member of the Galactic Bulge due to its position close to the Galactic Center. Therefore, its distance must be about 8 kpc. Using different methods to calculate the distance through the effective surface temperature, Schaefer (2010) found a distance of 7.8±1.8 kpc that is in agreement with the suggestion of Sekiguchi et al.

Table 13: Observations of V745 Sco

Days after discovery	Wavelength	Telescope	Detection	Reference
0	Optical		√	AAVSO[1]
1.3-15.3	Optical	2.3m Vainu Bappu	√	Anupama et al. (2014)
1.7-42	Optical	SMARTS	√	Page et al. (2015b)
1-2	γ-rays	*Fermi*	upper limits	Cheung et al. (2014, 2016b)
0.16-229.31	X-rays	*Swift*/XRT	√	Page et al. (2015b) Drake et al. (2016)
10	X-rays	*NuStar*	√	Orio et al. (2015)
16	X-rays	*Chandra*	√	Drake et al. (2016)
	X-rays	*Swift*/BAT	X	Page et al. (2015b)
1.3-15.3	IR	1.2m Mount Abu	√	Banerjee et al. (2014a)
1-217	Radio	GMRT	√	Kantharia et al. (2016)
2-3	Radio	VLA	√	Rupen et al. (2014)

(1990). We will adopt this value in this work.

The last outburst of V745 Sco was discovered on 2014 February 6.694 UT by Rob Stubbings (AAVSO Alert notice #380[1]; see also Waagen & Pearce, 2014) with $m_v \approx 9$ mag. For the purpose of this chapter, we define this as $t=t_0$. There was no evidence of the nova 24 hours before, with a $m_v \approx 13.0$ mag. This last eruption was detected from γ-rays to radio. V745 Sco is the first RS Oph-like nova detected in very high energies and the sixth nova detected with *Fermi*/LAT. This detection took place 1 and 2 days after the outburst (2014 February 6 and 7) with 2σ and 3σ γ-ray detections (F(E>100 MeV)$\sim$ $(3 \pm 1) \times 10^{-7}$ph cm^{-2} s^{-1}). Four days later, only upper limits ($< (2-3) \times 10^{-7}$ph cm^{-2} s^{-1}) were obtained (Cheung et al., 2014, 2016b). In near IR, Banerjee et al. (2014a) found broad lines with a narrow peak and expansion velocities around 4000 km s^{-1} (FWZI>9000 kms^{-1}) similar to the line profiles observed in the optical by Anupama et al. (2014). Radio emission was reported by Rupen et al. (2014) which detected a rising spectrum with VLA 2 days after the optical maximum, that can be consistent with a thermal emission or self-absorbed synchrotron emission, while Kantharia et al. (2016) detected synchrotron emission at 610 MHz and 235 MHz with GMRT 26 days after the eruption. These observations are shown in Table 13.

1 https://www.aavso.org/aavso-special-notice-380

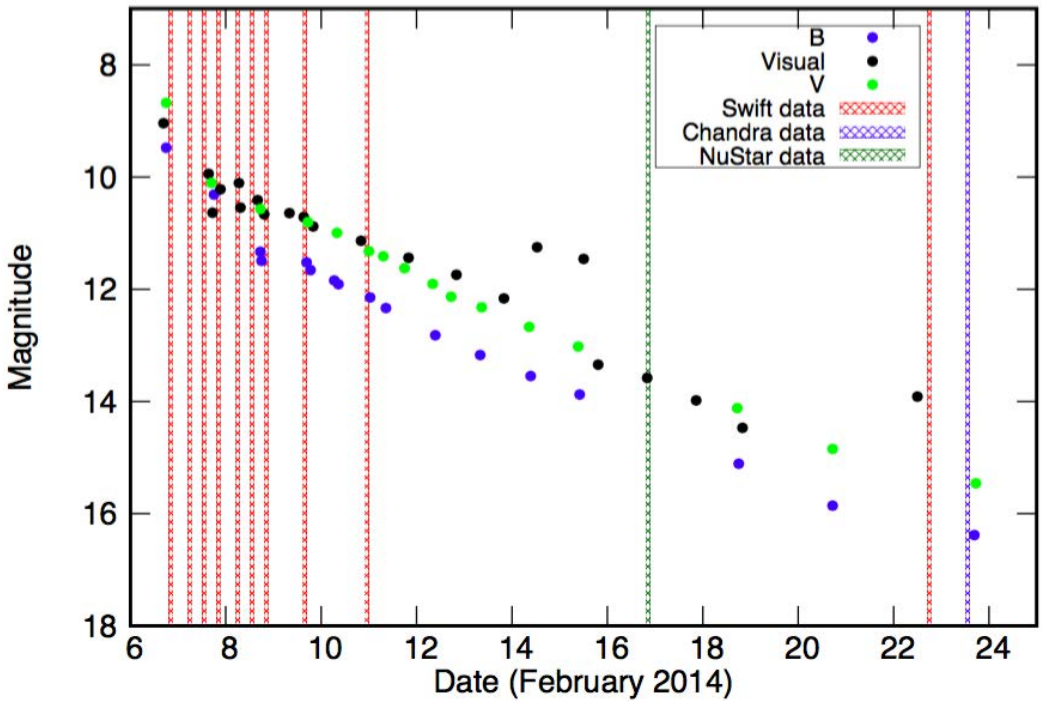

Figure 32: Optical light curve of V745 Sco by AAVSO. The epoch of *Swift*, *NuStar* and *Chandra* observations discussed in this chapter are indicated by red, green and blue shaded regions respectively.

4.2 OBSERVATIONS OF THE 2014 OUTBURST

4.2.1 *X-ray observations*

During its last outburst in 2014, V745 Sco was observed with several satellites in X-rays covering all the stages of the nova. The *Swift* satellite continuously monitored the source during seven months until V745 Sco was too weak (Table 13). The first days after the outburst, it was observed with *Swift*/XRT (see §4.2.1.2). However, on day 4 the SSS became visible. A detailed study of the SSS phase observed with *Swift*/XRT was presented by Page et al. (2015b). On the other hand, *Swift*/BAT did not find any detectable signal in the 15-50 keV energy range (H.A. Krimm, priv. comm.; see also Page et al., 2015b). V745 Sco was also detected with *NuStar* 10 days after the outburst in the energy range between 3-20 keV and only upper limits could be derived in the 20-70 keV range (Orio et al., 2015). Moreover, it was detected with *Chandra* (Drake et al., 2016) 16 days after its outburst, when the SSS phase had ended (see §4.2.1.3). There was also information in X-rays during the quiescence. Between the two last outbursts; V745 Sco was poorly detected with *XMM-Newton* in the energy range between 0.3-8 keV indicating the existence of a hot plasma (Luna et al., 2014). The dates of the X-ray observations that we use for our study are indicated in the optical light curve from the AAVSO (Figure 32).

4.2.1.1 Previous X-ray studies

Page et al. (2015b) showed a brief study of the pre-SSS phase. They studied the days between 0.16 and 3.23 after the outburst, using an absorbed single temperature VAPEC model. The iron abundance used was $Fe/Fe_{\odot}$=0.51 as found by Orio et al. (2015). However, they found a better fits with $Fe/Fe_{\odot}$ ∼6, suggesting that a distribution of temperatures could contributing to the shock emission. The temperatures obtained for these days were very high, T∼60 keV, and also the N_H, whose measure depends on the employed abundances. In this case Page et al. (2015b) used Wilms et al. (2000) abundances that correspond to the ISM (K. Page priv. comm.; see also Page et al., 2015b). All the details of the fits are given in Page et al. (2015b, Table 1).

Soft photons were already dominant 4 days after the outburst and remained dominant until day 12.5. Page et al. (2015b) carried out a detailed study of the super-soft emission of V745 Sco observed with *Swift*/XRT, suggesting that a combination of a very high velocity outflow and a low ejected mass induced an early SSS emission on V745 Sco. During this phase, the soft emission was very intense, and the hardness ratio ($2-10$ keV$/0.3-2$ keV) of the *Swift*/XRT spectra reached a minimum (0.01) on day 6 after the outburst (Page et al., 2015b, Figure 1). Unlike other novae, V745 Sco did not show a variable flux during this phase. The lack of this early variability can be due to a smoother density distribution of the ejecta or to the variability occurring when the ejecta was not yet transparent to the SSS emission. A black body model with five gaussians representing the O, Ne and Mg emission lines and two absorption edges corresponding to O were used to fit the observed soft emission. The existence of these emission lines showed that the WD of V745 Sco can be a ONe, and, therefore, V745 Sco is probably not a Type Ia supernova progenitor.

V745 Sco was observed with *NuSTAR* 10 days after the outburst (Orio et al., 2015). During this observation, the supersoft emission was dominant but not observable in the energy range of *NuSTAR* ($3-79$ keV). V745 Sco was detected by *NuSTAR* in the energy range between $3-20$ keV with a flux of $1.68\pm0.1\times10^{-11}$ erg cm^{-2} s^{-1}; above this energy, between 20-70 keV, only upper limits were obtained ($\sim10^{-13}$ erg cm^{-2} s^{-1}). Taking into account the very fast evolution of this nova, this observation was done too late to observe fluxes at energies larger than 20 keV. It was not possible to know the possible non-thermal emission related with the acceleration of particles. *NuSTAR* clearly detected the iron He-like triplet at 6.73 keV with an equivalent width of 1 keV. Orio et al. (2015) fitted the spectrum with a single temperature VAPEC model at kT=2.66 keV and $Fe/Fe_{\odot}$=0.51. However, they did not provide the error bar for the abundance. The velocities obtained by Banerjee et al. (2014a) were used to calculate the electron density of this observation ($n_e = [4.7\times10^6$ - $7.4\times10^7]$ cm^{-3}). The super soft component observed this day with *Swift* was fitted with two different methods: a stellar atmosphere at $\sim9.8\times10^5$K (Rauch et al., 2010), and a black body at $\sim10^5$K with an oxygen absorption edge at 0.87 keV, and superimposing oxygen emission lines at 0.65 keV and 0.57 keV. Orio et al. (2015) obtained a $N_H=(6.9\pm0.9)\times10^{21}$cm^{-2} for the *Swift* and *NuSTAR* spectrum. All the details of the fits are given in Orio et al. (2015, Table 2).

Finally, Drake et al. (2016) studied the spectra detected by *Chandra* 16 days after the outburst. They found that the *Chandra*/LETG observation had similar results to those of the *Chandra*/HETG observations but with larger uncertainties. To study the absorption, Drake et al. (2016) checked a partial covering model, but finally found best-fits using a single hydrogen column density. They tested APEC models with a single temperature, three temperatures and eight temperatures using in all cases solar abundances (Anders & Grevesse, 1989). An APEC model with 8 temperatures gives an idea about the temperature distribution in the plasma, while a single temperature gives the dominant temperature in this energy range. They also varied the abundances, the line broadening and the redshift of the model, obtaining abundances lower than solar abundances, and lines with a velocity broadening of approximately 510 km s^{-1} and with a blueshift corresponding to 165±10 km s^{-1}. Some of these results are shown in §4.2.1.3.

4.2.1.2 Early X-ray observations with Swift

V745 Sco was observed with *Swift*/XRT starting 3.7 hr after the optical discovery until 2014 March 06. This has allowed us to focus on the early observations made with *Swift*/XRT corresponding to the epoch of the expected particle acceleration in the shock (1 to 4 days after the outburst, Cheung et al., 2014). This fact enables us to obtain a global view of the plasma and the behaviour of the shock the first days after the outburst.

We present the analysis of V745 Sco XRT observations before the SSS phase, between day 0.16 and 4.23 after the eruption, and after the SSS phase, on day 16.03 after the eruption, contemporaneous with the *Chandra* observation (Drake et al., 2016). Most of the observations were made before the nova declined by 3 magnitudes (Figure 32), showing a harder spectrum than those produced by residual H burning on top of the WD. This emission is dominated by the hot ejected shell. The log of the *Swift*/XRT observations is shown in Table 14. These observations began 3.7 hours after the eruption and continued with a high cadence (6 hours) giving a very good temporal coverage, better than in the case of RS Oph in its 2006 outburst.

4.2.1.2.1 Data Reduction

Data were reduced using HEASoft (version 6.15). We used standard routines of FTOOLs for the extraction of spectra. The CCD detectors of the XRT instrument have three different modes: IM, WT mode and PC mode (see Appendix A). The first days, novae are very bright and usually their X-ray images have pile-up[2]. This effect causes the camera to read twice (or more) the real energy, and the highest energies of the spectra are contaminated. To reduce the pile-up in PC spectra, annular extraction regions around the source were used. On day 4.23, the SSS emission was detected using WT mode. The WT mode is the best mode to reduce the effects produced by the

2 pile-up is the arrival of more than one X-ray photon in one camera pixel or in adjacent pixels between two read outs.

Table 14: Observation log of V745 Sco with *Swift*/XRT

Observation Date	ID	Time after discovery	Exp.time (ks)	Count rate (count s^{-1})
2014 Feb 06	00033136001	0.16	0.98	0.28±0.01
2014 Feb 07	00033136002	0.56	0.98	0.35±0.01
2014 Feb 07	00033136003	0.89	0.91	0.37±0.02
2014 Feb 07	00033136004	1.16	1.77	0.40±0.01
2014 Feb 08	00033136005	1.51	0.89	0.46±0.02
2014 Feb 08	00033136006	1.89	0.96	0.58±0.02
2014 Feb 08	00033136007	2.17	0.98	0.49±0.02
2014 Feb 09	00033136012	2.96	0.97	0.54±0.02
2014 Feb 10	00033136017	4.23	1.03	10.6±0.1
2014 Feb 22[(a)]	00033136056	16.03	1.47	0.41±0.02

(a) After super soft emission.

pile-up because for this mode pile-up only appears for count rates higher than 30 count s^{-1}. More details of the data reduction are given in Appendix B.

4.2.1.2.2 Data Analysis

We study the early hard X-ray spectra obtained with *Swift*/XRT using XSPEC (version 12.8, Arnaud et al., 2012). V745 Sco is a system very similar to RS Oph and, as in this case, we expect the X-ray emission to be produced by the shock between the ejecta and the RG wind. The X-ray spectral evolution corresponding to the first days is shown in Figure 33.

We fit the XRT spectra with an absorbed single-temperature APEC model (Smith et al., 2001). APEC models calculate both line and continuum emissivities for an optically thin plasma in collisional ionization equilibrium. We use tbabs (Wilms et al., 2000) for all the spectra (see Appendix C). We know that a single-temperature model does not reproduce all the details of the spectrum but gives a global view of the properties of the plasma during the first days. The Fe K line complex at 6.69 keV is the only strong emission line visible in the spectra because of the low resolution of the data. Abundances from Anders & Grevesse (1989) are used, modifying only the abundance of Fe and assuming solar abundances for the remaining elements.

We obtain Fe abundance around 2 for the first days. It decreases to ~ 0.1 $Fe/Fe_{\odot}$ on day 16.03 after the outburst, a similar value to that from Drake et al. (2016). $Fe/Fe_{\odot}$ errors are calculated with 2σ. If we do not modify the Fe abundances, a discrepancy between the data and the model is seen at lower energies of the broad Fe K complex

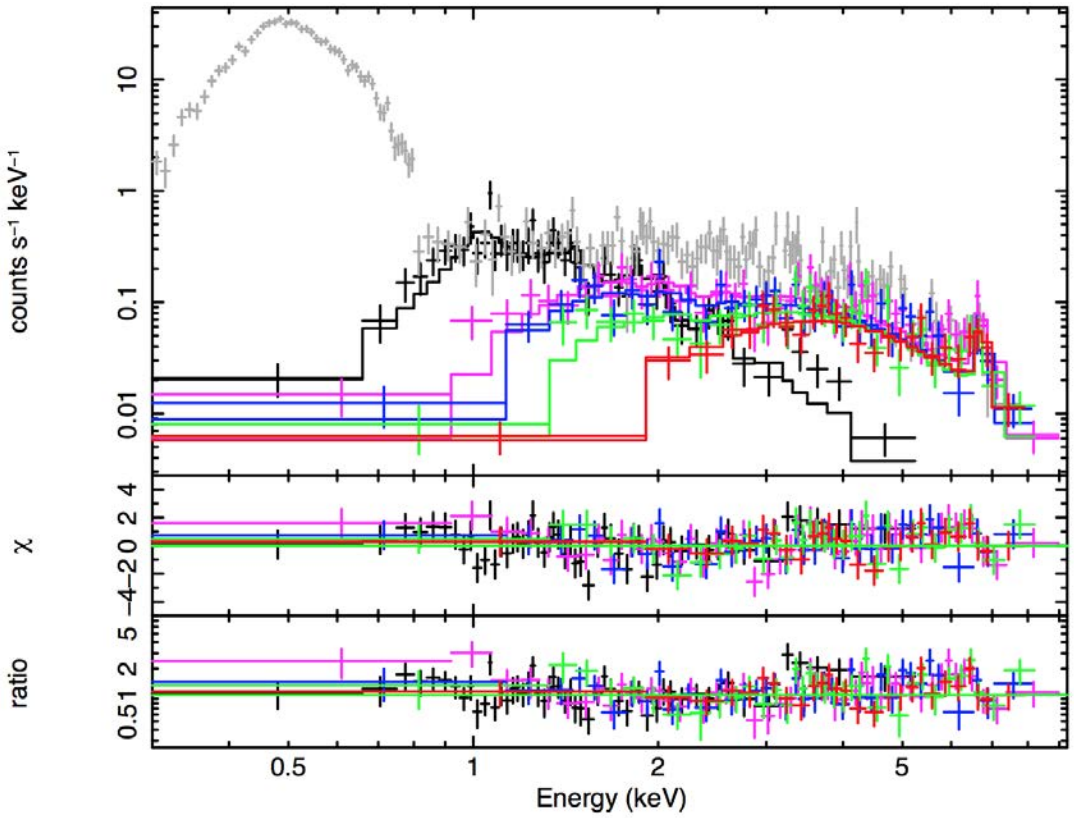

Figure 33: *Swift*/XRT observed spectra and best-fit models for V745 Sco at days 0.16 (red), 0.89 (green), 1.51 (blue), 1.89 (pink), 4.23 (gray) and 16.03 (black). Residuals are plotted in the bottom panels.

Table 15: Parameters of the VAPEC Models of V745 Sco

Day	$N_{H}{}^{(a)}$ $(10^{22} cm^{-2})$	kT (keV)			$Fe/Fe_{\odot}^{(b)}$	EM $^{(a,d)}$ $\times 10^{58}\mathrm{cm}^{-3}$	$F_{abs}^{(b,e)}$	$F_{unabs}^{(e)}$		χ^2/dof, χ^2_{red}
		(a)	(b)	(c)				(b)	(c)	
0.16	5^{+3}_{-2}	>5	10±5	[6 - 31]	2±1	4^{+3}_{-2}	$6^{+0.3}_{-1}$	$10.5^{+0.5}_{-1}$	[9 - 11]	18.7/23, 0.8
0.56	3±2	>6	12±3	[8 - 28]	2.2±0.6	4^{+6}_{-3}	7.13±0.05	$11.36^{+0.08}_{-0.07}$	[11.3 - 11.4]	49.5/29, 1.7
0.89	3^{+2}_{-1}	>5	9±3	[6 - 24]	1.8±0.8	5^{+4}_{-3}	8.27±0.04	$12.8^{+0.7}_{-0.6}$	[12 - 13]	43.9/32, 1.4
1.16	$2.0^{+0.8}_{-0.5}$	>7	12±3	[8 - 25]	2.5±0.9	4±2	$8.8^{+0.4}_{-0.9}$	$12.5^{+0.6}_{-1}$	[11 - 13]	83.1/67, 1.2
1.51	$1.7^{+0.9}_{-0.6}$	>5	12±3	[7 - 26]	1.7±0.8	4^{+3}_{-2}	$7.8^{+0.4}_{-0.5}$	10.8±0.6	[10 - 11]	37.1/35, 1.0
1.89	$1.7^{+0.7}_{-0.6}$	>6	10±2	[7 - 14]	2.7±0.8	3±2	7.7±0.3	10.5±0.4	[10 - 11]	59.8/51, 1.2
2.17	1.7±0.5	>6	9±2	[6 - 16]	2.8±0.9	4±2	9.7±0.4	13.3±0.6	[13 - 14]	52.8/44, 1.2
2.96	1.9±0.6	>8	13±2	[9 - 26]	2.8±0.9	4±2	$8.2^{+0.3}_{-0.5}$	$11.4^{+0.6}_{-0.5}$	[11 - 12]	86.8/47, 1.8
4.23 $^{(f)}$	$1.2^{+0.4}_{-0.5}$	>5	8±1	[7 - 12]	0.8±0.2	6±3	10.2±0.3	13.9±0.4	[13 - 14]	106.7/66, 1.6
16.03$^{(g)}$	0.5±0.2	$1^{+1}_{-0.2}$	1.23±0.06	[1.1 - 1.3]	0.14±0.04	3^{+1}_{-2}	2.3±0.1	$3.96^{+0.1}_{-0.2}$	[3.8 - 4.1]	66.6/49, 1.3

(a) Uncertainties correspond to 3σ.
(b) Uncertainties correspond to 1σ.
(c) Uncertainties correspond to 2σ.
(d) $\mathrm{norm}_{VAPEC}=10^{-14}\mathrm{EM}/(4\pi \mathrm{D}^2)$, where EM is the emission measure and D the distance in cm. We adopted a distance of 7.8±1.8 kpc ($(2.4\pm0.5)\times10^{22}$cm) (Banerjee et al., 2014a).
(e) 0.8-10.0 keV. Parameter units are $\times10^{-11}$erg cm^{-2}s^{-1}.
(f) Fits to 1.0-10 keV, ignoring super soft emission.
(g) After super soft emission.

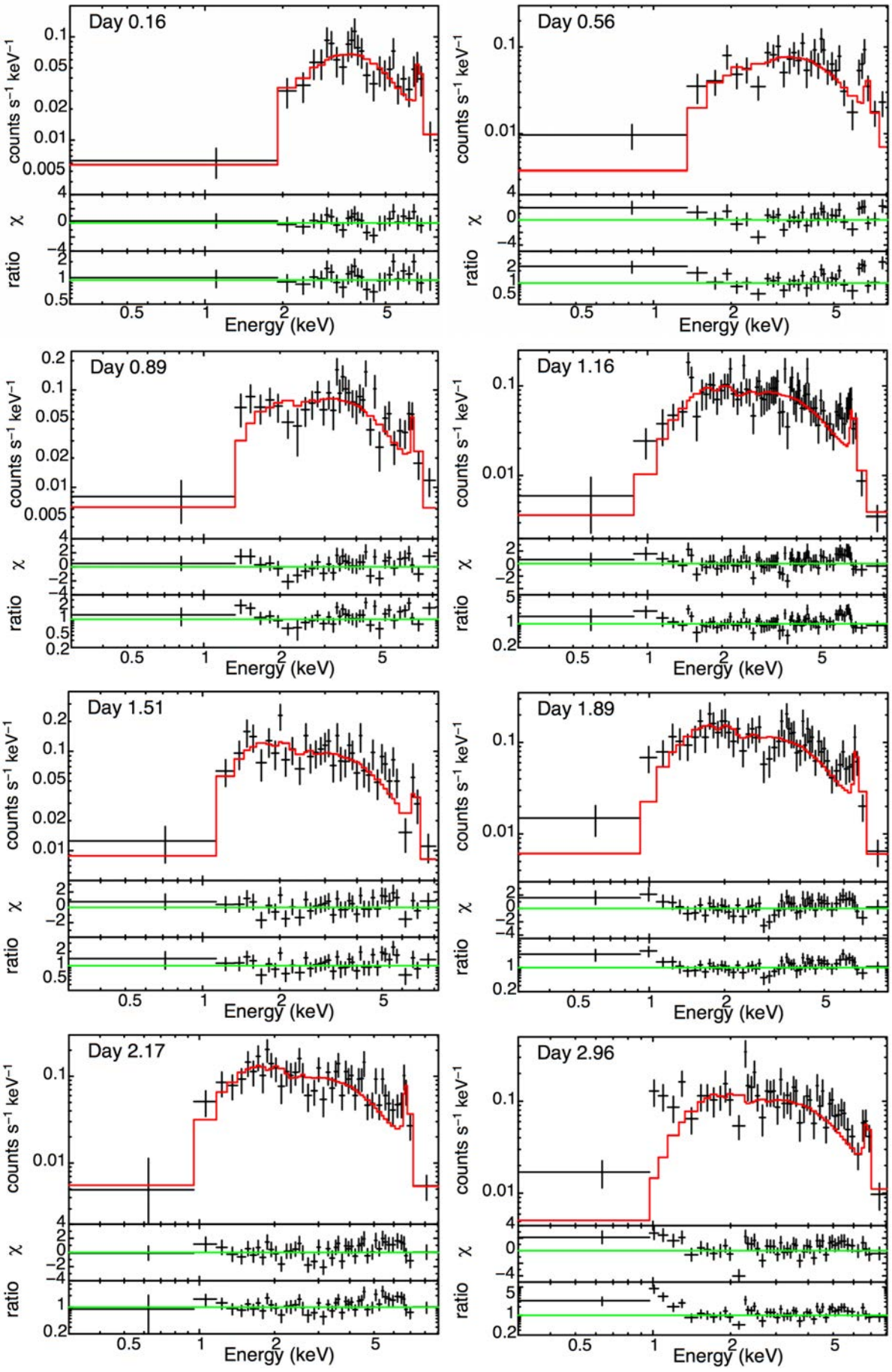

Figure 34: *Swift*/XRT observed spectra and best-fit models for V745 Sco at days 0.16, 0.56, 0.89, 1.16, 1.51, 1.89, 2.17 and 2.96. Residuals are plotted in the bottom panels.

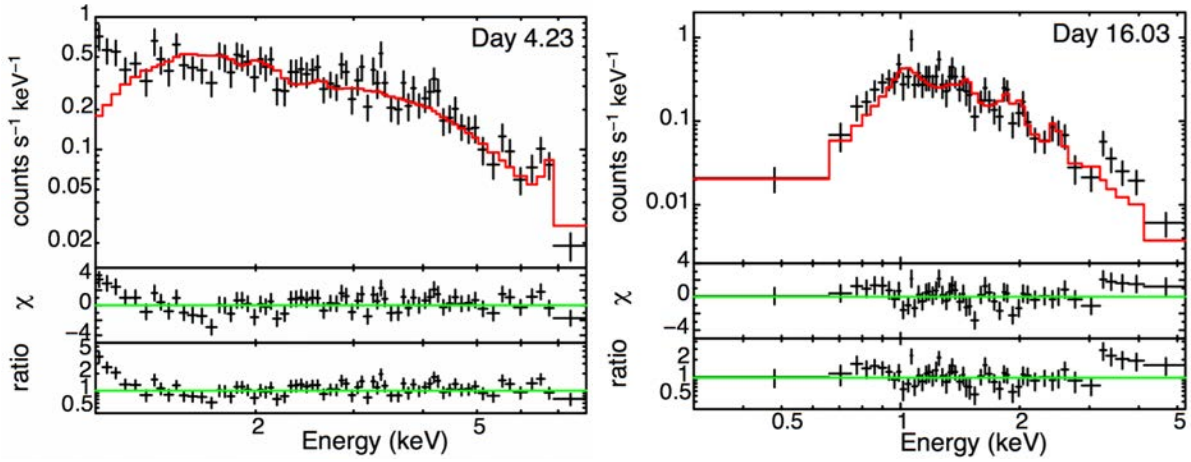

Figure 35: *Swift*/XRT observed spectra and best-fit models for V745 Sco at days 4.23 and 16.03. Residual, χ^2 and ratio, are plotted in the bottom panels.

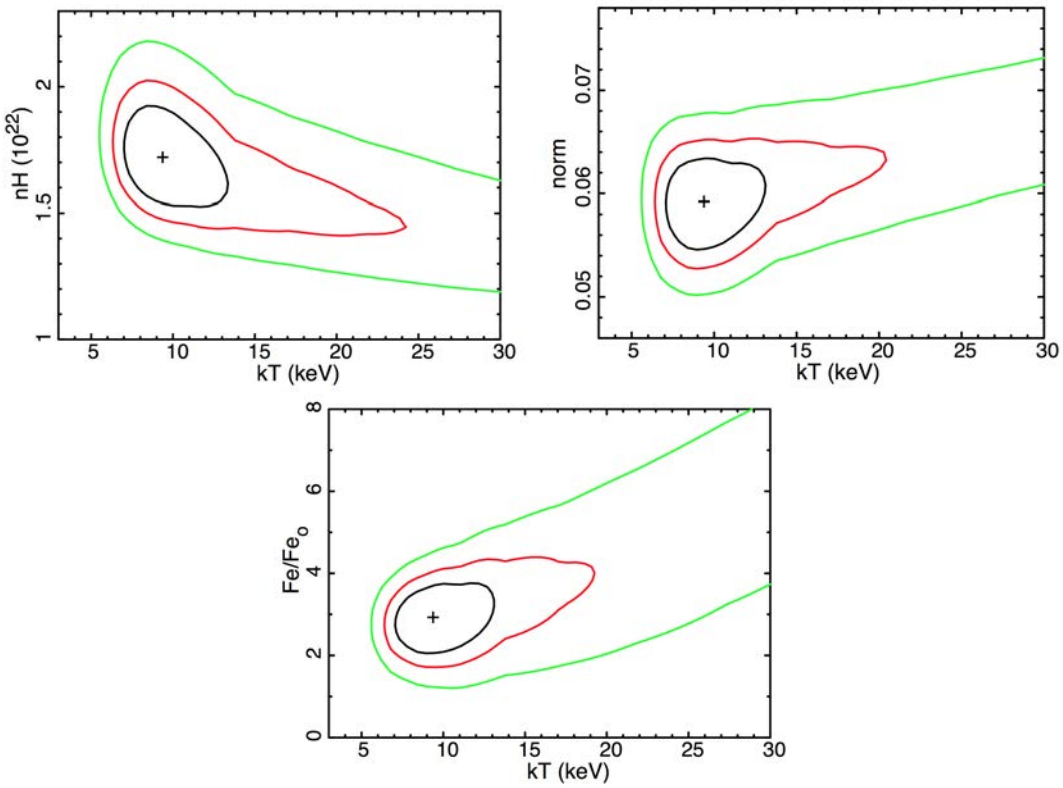

Figure 36: Confidence contours (1 (black line), 2 (red line), and 3 σ (green line)) of N_H-kT, normalization-kT and Fe/Fe$_\odot$-kT of VAPEC model fitting the *Swift*/XRT data 2.17 days after the outburst.

line. This excess can be interpreted as an additional line at 6.4 keV which is typical in a neutral gas spectrum, as in some magnetic CVs and that was also observed the first days of RS Oph *Swift* observations. In that case was considered as scattering in the red giant wind (Bode et al., 2006). In the *NuSTAR* observation, 10 days after outburst (Orio et al., 2015), a good fit was found with a Fe abundance of 0.51 $Fe/Fe_{\odot}$ for the energy range between 3 and 20 keV but the uncertainty in the abundance was not reported. Fe abundances should be the same every day, for this reason, we try to fit the observations with a VAPEC model with the Fe abundances fixed to the same value of the *NuSTAR* observation. Even with a good χ^2, the optimization procedures of XSPEC only found a good fit at high temperatures, at which it is not possible to have a Fe K line at 6.69 keV. These high temperatures were shown in the study of the first days by Page et al. (2015b, Table 1). The uncertainties of the Fe abundances of *NuSTAR* are very important to fit properly *Swift*/XRT data the first days after the outburst and to know the true nature of the excess in the iron line.

The high N_H during the first days of the nova outburst shows that there was not only the absorption of the ISM ($N_{H,ISM}=(5\pm1)\times10^{21}$ cm^{-2}, Page et al., 2015b). There was also absorption produced by the nova ejecta and the RG wind. As the measured N_H depends on the abundances used, we found discrepancies with Page et al. (2015b)'s N_H.

The fits include the whole XRT data range (0.3 - 10 keV) until the emergence of the super soft emission on day 4.23 after the outburst. This day, we only use the data at energies larger than 1.0 keV (Figure 34 and Figure 35). Table 15 shows the results of the model used to fit the spectra. Confidence contours for the total hydrogen column density (N_H), temperature, Fe abundance and normalization components are displayed in Figure 36 of day 2.17 after the outburst.

4.2.1.3 Post SSS phase X-ray observations with Chandra

V745 Sco was observed with the *Chandra* (Weisskopf et al., 2003) on 2014 February 22nd and 23rd (see Table 16). Its high spectral resolution is a powerful tool to understand the early blast wave. The SSS phase had already fainted out, and an optically thin plasma in collisional ionization equilibrium was detected between 0.9 and 6 keV, consistent with the spectrum obtained by *Swift*/XRT the same day. These spectra achieve energies lower than the spectra obtained the first days.

We focus on the observations obtained by HETG (E: 0.4 - 10 keV) on 2014 February 23rd, 16.9 days after the eruption (see Appendix A). The early appearance of the SSS emission and its fast turn off made impossible to observe this phase with LETG (E:0.007 - 0.2 keV) 16 days after the outburst. LETG gives information about the blast wave conditions but with a low resolution. A detailed analysis of the LETG observations is presented in Drake et al. (2016).

Table 16: Observations log of V745 Sco with *Chandra*

Observation Date	ID	Grating/ Detector	Exp.time (ks)	Energy grating	counts/s	Reference
2014 Feb 23	15737	HETG/ACIS-S	39.5	HEG MEG	0.218 0.539	This work and Drake et al. (2016)
2014 Feb 22	15738	LETG/HRC-S	32.2			Drake et al. (2016)
2014 Feb 23	16595		12.9			

4.2.1.3.1 Data reduction and analysis

We extract the spectra using the standard tools provided by the mission-specific software package, CIAO version 4.7 (Fruscione et al., 2006). We obtain the spectra for the high and medium energy grating (HEG and MEG). The grating data taken on day 16.9 are shown in Figure 37. All the details of the data reduction are shown in Appendix B.

The *Chandra* spectra show bright emission lines from H and He-like ions of Si, Mg, Ne and Fe, similar to those obtained in the 2006 RS Oph eruption (Drake et al., 2009) but less luminous than RS Oph 13 days after the outburst. This emission is also originated by the shock between the ejecta and the RG wind. We study the spectra from two different points of view: a global perspective, with the study of the continuum, that we compare with the *Swift*/XRT spectrum, and a more detailed view, with the study of the individual lines. These studies give us more information about the shock wave and its properties 16.9 days after the outburst. We have used XSPEC v.12.8.

Shocked plasma description using a plasma model and comparison with *Swift* spectra.

We study the HEG and MEG spectra globally in the same energy range between 2 and 13 Å, corresponding to 0.9 to 6 keV (Figure 37). To compare the analysis of the *Chandra* spectra with the analysis of *Swift*/XRT spectrum from day 16.03 after the outburst (see Table 15), we check that the same model fits correctly all the spectra. The spectra are fitted with an absorbed single-temperature VAPEC model (Smith et al., 2001), using the `tbabs` model (Wilms et al., 2000) for all the spectra. We modify the abundance of Ne, Mg, Si, S and Fe, which are the lines that appear in the spectra and assume solar abundances for the remaining elements (Anders & Grevesse, 1989). Recall that in the *Swift* spectrum we only saw the Fe K line at 6.69 keV, and we only modified the Fe abundance. Because of the range of the spectra, we can not see the Fe K line at 6.69 keV in these spectra, but thanks to the high spectral resolution of HETG, we know that this plasma is also composed of Ne, Mg, Si, S and Fe L lines. Without these spectra, we would not have this information. The values of the VAPEC model parameters obtained using XSPEC are given in Table 17. Figure 38 shows the confidence contours for the N_H, temperature, Fe abundance and normalization components.

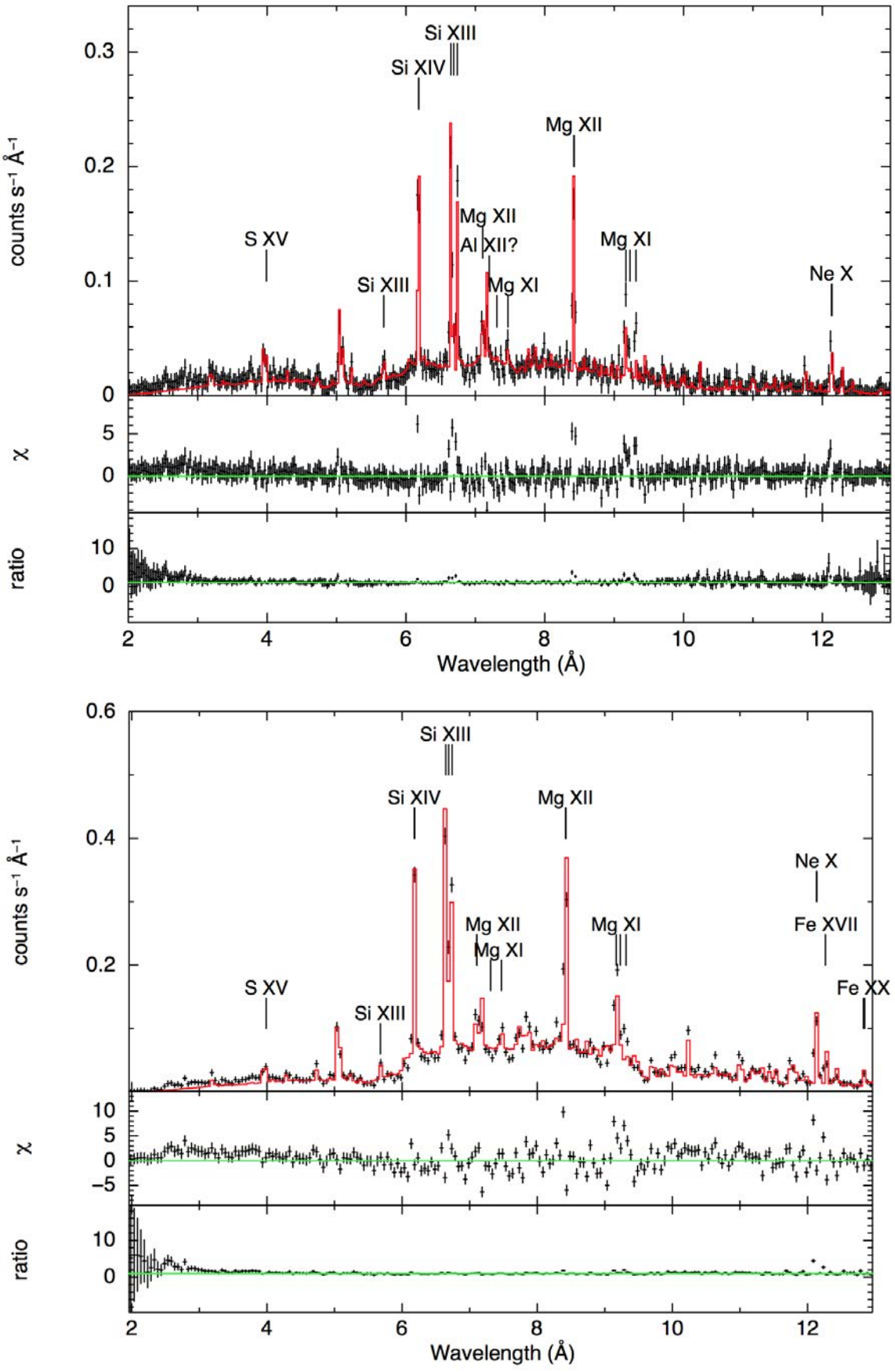

Figure 37: *Chandra*/HETG (HEG(top) and MEG (bottom)) observed spectra and best-fit models with the most representative lines for V745 Sco at day 16.9. Residual, χ^2 and ratio, are plotted in the bottom panels.

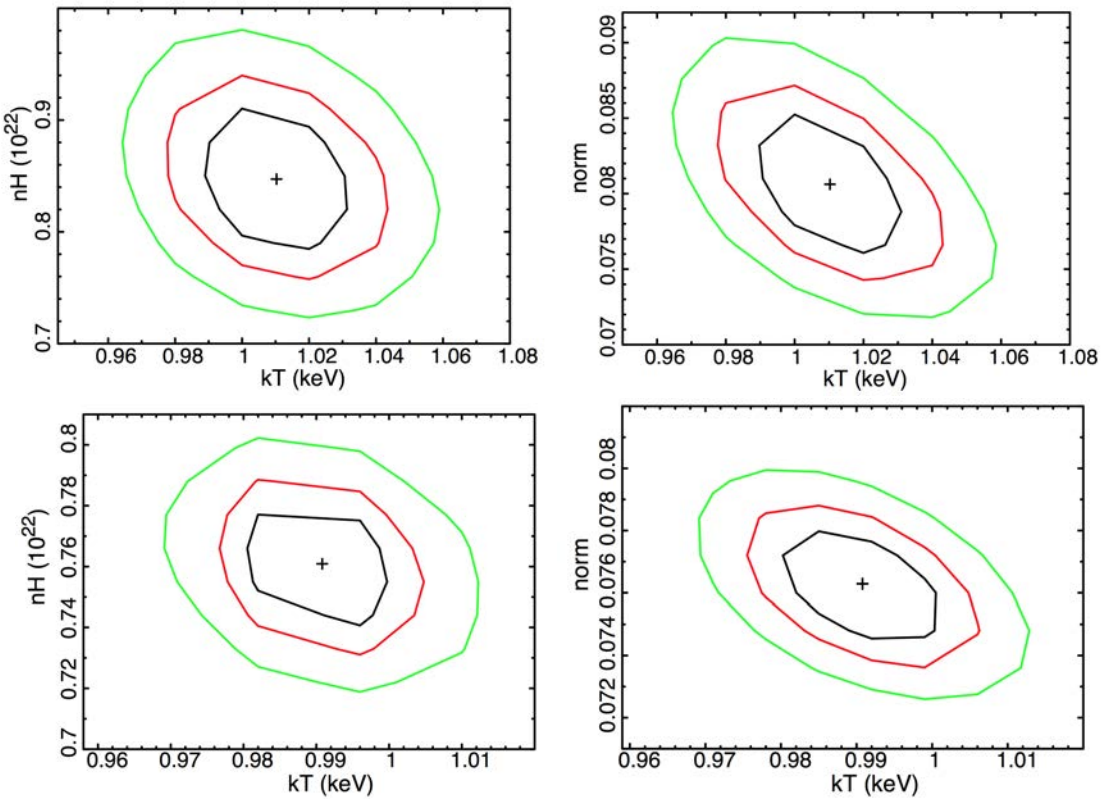

Figure 38: Confidence contours (1 (black line), 2 (red line), and 3 σ (green line)) of N_H-kT and normalization-kT of VAPEC model fitting the *Chandra*/HETG (HEG(top) and MEG (bottom)) data 16.9 days after the outburst.

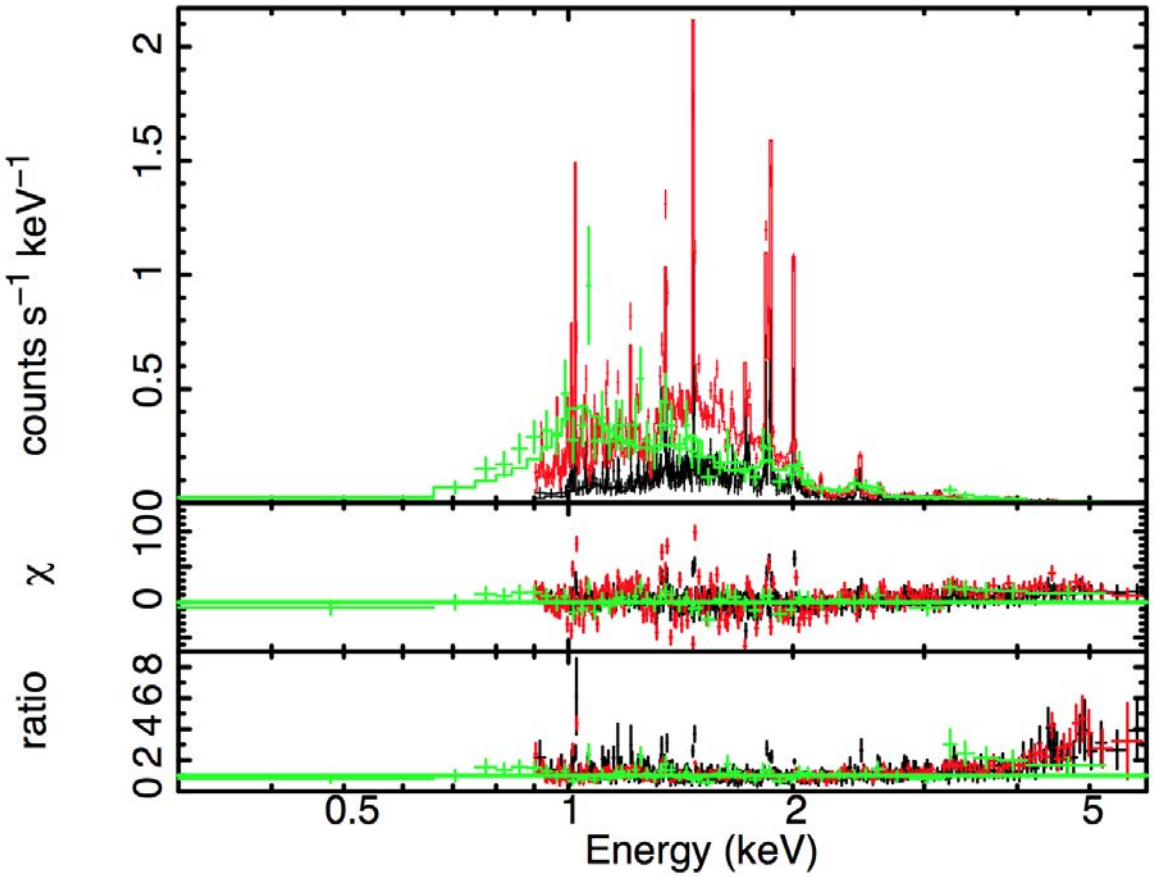

Figure 39: *Chandra*/HETG (HEG (black) and MEG (red)) at day 16.9 and *Swift*/XRT (green) at day 16.03 after the outburst observed spectra and best-fit models for V745 Sco. Residual, χ^2 and ratio, are plotted in the bottom panels.

Table 17: Parameters of the VAPEC Models of V745 Sco observed with *Chandra*

Parameters	HEG	MEG
N_H $^{(a)}$ ($\times 10^{22}$ cm^{-2})	0.8±0.1 [0.72-0.98]	0.76±0.04 [0.72-0.8]
kT $^{(a)}$ (keV)	$1.09^{+0.05}_{-0.04}$ [0.965-1.06]	0.99±0.02 [0.969-1.012]
EM$^{(a,d)}$ ($\times 10^{58}$cm^{-3})	5.8±0.6 [5.21- 6.51]	5.5±0.2 [5.269-5.79]
Ne$^{(c,b)}$	0.6±0.2	0.81±0.06
Mg$^{(c,b)}$	$0.33^{+0.05}_{-0.04}$	0.40±0.01
Si$^{(c,b)}$	0.35±0.03	0.49±0.01
S$^{(c,b)}$	0.41±0.09	0.61±0.04
Fe$^{(c,b)}$	$0.17^{+0.08}_{-0.06}$	0.21±0.02
F_{abs} $^{(c)}$ 0.9-6.0 keV($\times 10^{-11}$erg cm^{-2}s^{-1})	2.13±0.04	2.33±0.02
F_{unabs} $^{(c)}$ 0.9-6.0 keV($\times 10^{-11}$erg cm^{-2}s^{-1})	5.6±0.1	5.81±0.05
$\chi^2_{v,r}$(χ^2_v/dof)	1.1 (520/451)	5.2 (1103/211)

(a) Uncertainties correspond to 3σ.
(b) Uncertainties correspond to 1σ for the MEG data
(c) Uncertainties correspond to 2σ for the HEG data.
(d) norm$_{VAPEC}$=10^{-14}EM/(4πD^2), where EM is the emission measure and D the distance in cm. In this case V745 Sco is at a distance of 7.8±1.8 kpc ((2.4±0.5)×10^{22}cm) (Banerjee et al., 2014a).
Abundances are expressed as a fraction of the solar abundances of Anders & Grevesse (1989).

This observation was made after the SSS phase, and thus, we expected the N_H values to be similar to the interstellar column density ($N_{H,ISM}$=(5±1)×10^{21} cm^{-2}) as in the *Swift* observation, but as we see in Table 17, N_H is larger than $N_{H,ISM}$. This difference can be due to the fact that at low X-ray energies the absorption is measured better than at high X-ray energies.

In order to compare with the *Swift* observation 16.9 days after the outburst, we fit the spectra with a single temperature and we obtain the same temperature, but does not reproduce all the details of the spectra. The fit of the HEG spectrum reproduce correctly the data (χ^2=1.1) and the majority of the lines match the model. However, in the case of the MEG spectrum we obtain a poor fit ($\chi^2 > 5$) since the model underestimates the line width. The normalization factors give an X-ray EM around 5×$10^{58}$$cm^{-3}$ and an unabsorbed flux around 5×10^{-11}erg cm^{-2} s^{-1}. These are slightly larger than in the *Swift* observation. However, the absorbed flux is practically the same (2×10^{-11}erg cm^{-2} s^{-1}), because the N_H is larger than those of the *Swift* observation 16 days after the eruption. Figure 39 compares directly the *Chandra*/HETG and *Swift*/XRT spectra. We use the temperatures obtained on day 16 after the outburst to know the plasma temperature distribution. We conclude that we have a collisional ionized plasma with multiple temperatures: a dominant high temperature given by *Swift* (1.23±0.06 keV) and two low temperatures obtained through the study of individual lines ($0.4 - 0.6$ keV).

Analysis of spectral line profiles

One of the advantages of high spectral resolution is that we can use simultaneously the detection of both H and He-like ions of the same element and determine the range of temperatures required to produce the observed spectrum.

The extracted HEG and MEG spectra with the most important lines identified are shown in Figure 37. There are several emission lines that can be identified originated from H-like and He-like ions of *Si* and *Mg* (Si XV (3.99 Å), Si XV (5.06 Å), Si XIII (5.68 Å), Si XIV (6.18 Å), Si XIII (6.65 Å), Mg XII (7.11 Å), Mg XI (7.47 Å), Mg XII (8.42 Å) and Mg XI (9.2 Å)). The He-like triplets of *Si* and *Mg* show partial blending between the recombination (r), intercombination (i) and forbidden (f) lines. These elements are usually excited by the radiation emitted in the SSS phase. In addition, some lines of Al, Ne and Fe are identified (Al XII (7.17 Å), Ne X (12.1 Å), Fe XVII (12.26 Å) and Fe XX (12.84 Å).

Table 18 lists the line centre, FWHM and flux for the most prominent X-ray emission lines. We fit the lines with a gaussian profile and a bremsstrahlung continuum (see Appendix C). The bremsstrahlung temperature is the same as in the HEG and MEG best-fit models. We note that the intrinsic line shape is not a gaussian, but at this resolution it provides a good first order approximation. To obtain the line flux, we subtract the flux of the bremsstrahlung continuum to the flux of the gaussian profile. The errors correspond to 2σ. In the case of the He-like lines, we fit each of the three lines with a gaussian with the same line width (σ) and velocity shift (λ_{obs}-λ_{rest}) because we expect that the three lines come from the same ejecta material. The obtained uncertainties

Table 18: X-Ray Emission Lines of V745 Sco observed with *Chandra* spectra

Ion		λ^a_{rest} Å	λ^a_{obs} Å	FWHM km/s	Flux 10^{-14} erg cm^2 s^{-1}
S XVI		3.99	3.96±0.01	4000±1000	25±5
S XV		5.06	5.05±0.05	4000±1000	67±1
Si XIII		5.68	5.68±0.02	900±600	11±4
Si XIV		6.19	6.179±0.006	1300±700	56±4
	r	6.65	6.64±0.05		60±1
Si XIII	i	6.68	6.68±0.05	1200±200	16±3
	f	6.74	6.73±0.05		41±1
Mg XII		7.11	7.10±0.02	900±400	7.8±0.8
Al XII?		7.17	7.1±0.3	1600±800	10.1±0.7
Mg XI		7.47	7.4±0.2	1000±800	6.4±0.2
Mg XII		8.42	8.416±0.005	1200±200	45±3
	r	9.17	9.164±0.005		30.1±0.9
Mg XI	i	9.23	9.225±0.005	1200±300	7±3
	f	9.31	9.308±0.005		20.9±0.6
Ne X		12.13	12.125±0.005	1300±500	52±8
Fe XVII[b]		12.26	12.262±0.006	300±200	13.9±0.7
Fe XX[b]		12.84	12.84±0.02	1100±700	10.0±0.7

(a) Rest and observed wavelengths
(b) Observed wavelength and reported flux from the MEG spectrum; all other measurements are from the HEG spectrum.

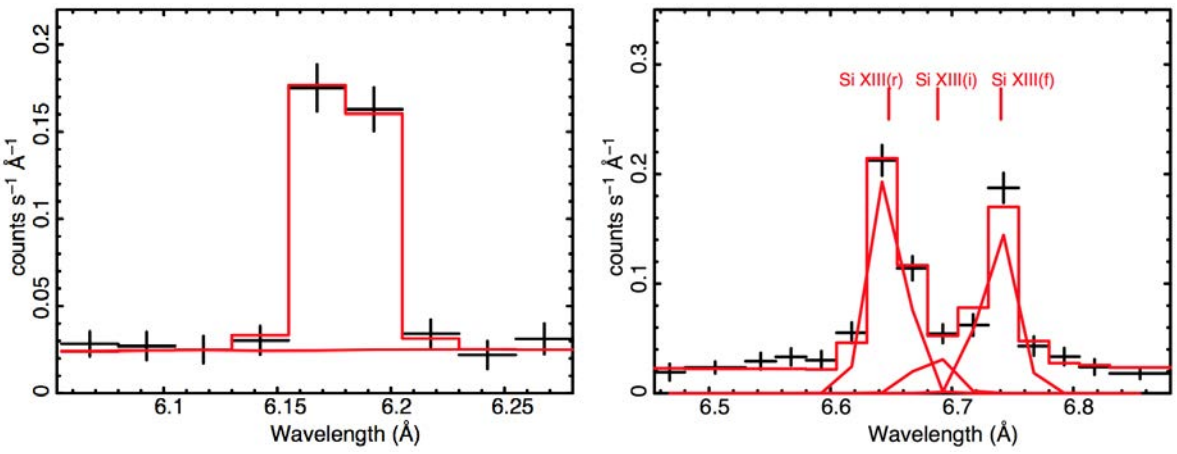

Figure 40: *Chandra*/HETG observed lines (Si XIV H-like (left) and Si XIII He-like (right)) and best-fit model for V745 Sco at day 16.9 after the outburst .

are only statistical and represent the precision of the values but not the exactitude of them.

In order to explain the mechanism related with the observed emission lines and to diagnose the electron temperature and density of the emitting material, we analyse the He-like triplet flux ratios of Si XIII (Figure 40) and Mg XI using diagnostics from Porquet et al. (2001). As in the case of RS Oph (§3.2.1.4.2), we calculate the ratio G=$(f+i)/r$ with the fluxes of the recombination, intercombination and forbidden lines. Once we have the G ratios, it is possible to obtain the temperature of the Si XIII and Mg XI lines by using Figure 7 of Porquet & Dubau (2000) that relates the G ratio with the corresponding temperature. From the Si XIII and Mg XI triplets, we obtained that G$\sim$1, so we have a plasma in collisional ionization equilibrium with a $T_e \sim$ 0.4-0.6 keV, lower than those obtained with the plasma model VAPEC ($\sim$ 1 keV). This means that this plasma does not have a single temperature, it has a distribution of temperatures as we also conclude with the several FWHM of the lines. Thanks to the G ratio, we know that the plasma must be at temperature of approximately 0.5 keV to observe these lines.

The ratio R=f/i is a sensitive diagnostic tool to measure electron densities, if the densities are in the range $n_e = 10^8 - 10^{13}$ cm^{-3} (Vink, 2012). Once we have the R ratio, it is possible to obtain the electron density of the Si XIII and Mg XI lines by using Figure 9 of Porquet & Dubau (2000) that relates the R ratio with the corresponding electron density between 10^9-10^{17} cm^{-3}. Just as in RS Oph (§3.2.1.4.2), the obtained n_e is orders of magnitude above the electron density that we obtain with the emission measure, $n_e \sim 10^7$ (see later in §4.3). Thus our diagnostic of electron densities would be wrong.

4.2.1.4 Global view of the X-ray observations

We analyse the evolution of the plasma properties, such as the temperature, flux, emission measure, and N_H to obtain a global view of the shocked plasma evolution in X-rays. We use the observations obtained by *Swift*, *Chandra* and *NuStar* the first two weeks after the outburst.

The temperature evolution is of great relevance in our study due to its relation with the study of particle acceleration. Figure 41 shows the result of the *Swift*, *NuStar* and *Chandra*/HETG-LETG observations. The temperature, as in RS Oph, is practically constant the first days after the outburst and later decays with time according to *NuSTAR* and *Chandra* observations. This decrease is faster than expected for an adiabatic shock due to radiative losses. In general, there is only one satellite observation at each epoch. However, the two temperatures obtained with *NuStar* and *Chandra*/HETG-LETG observations demonstrate the complexity of the plasma.

Figure 42 shows the evolution of N_H. The spectrum is strongly absorbed three hours after the outburst detecting hard X-ray counts from 2 keV (Figure 33). The absorption decreases very fast reaching the interstellar medium value 16 days after the eruption. Bode et al. (2006) stated that all N_H values greater than $N_{H,ISM}$ correspond to the ab-

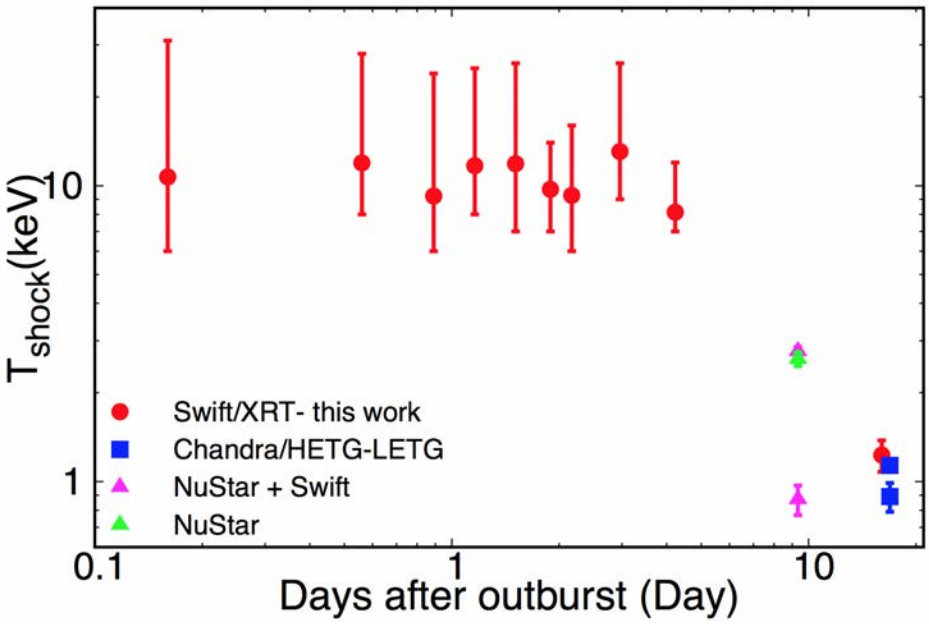

Figure 41: Post-shock plasma temperature evolution with time. Red dots correspond to *Swift*/XRT, blue boxes to *Chandra*/HETG-LETG (Drake et al., 2016), green triangle to *NuStar* and pink triangles to *NuStar* and *Swift* together (Orio et al., 2015). *Swift* measure have 1σ error bars (Only at 3σ are obtained lower limits). *NuStar* and *Chandra* values have 3σ error bars.

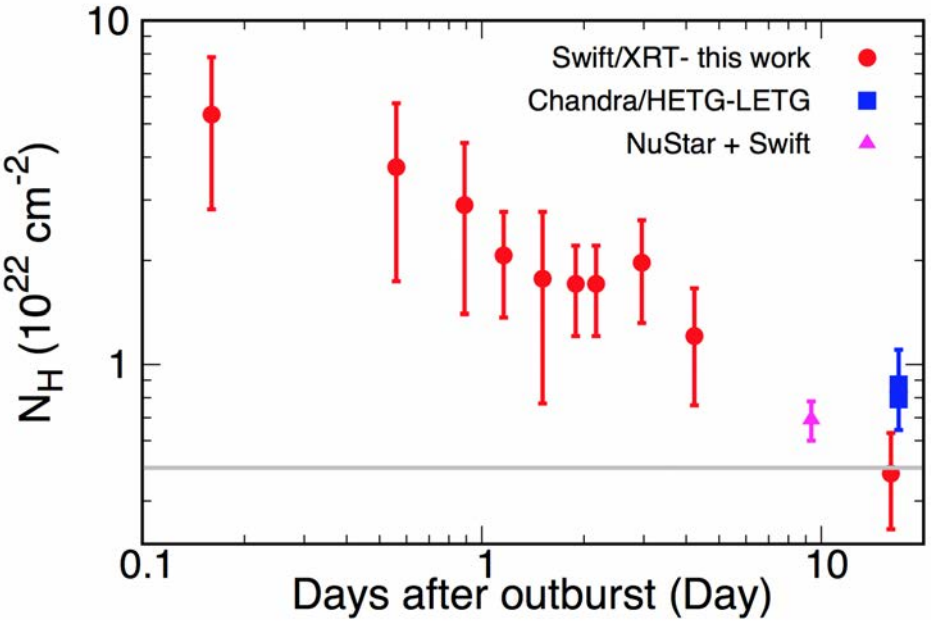

Figure 42: N_H evolution with time. Red dots correspond to *Swift*/XRT, blue boxes to *Chandra*/HETG-LETG (Drake et al., 2016) and pink triangle to *NuStar*+*Swift* (Orio et al., 2015). All measurements have 3σ error bars. Gray line corresponds to the ISM value.

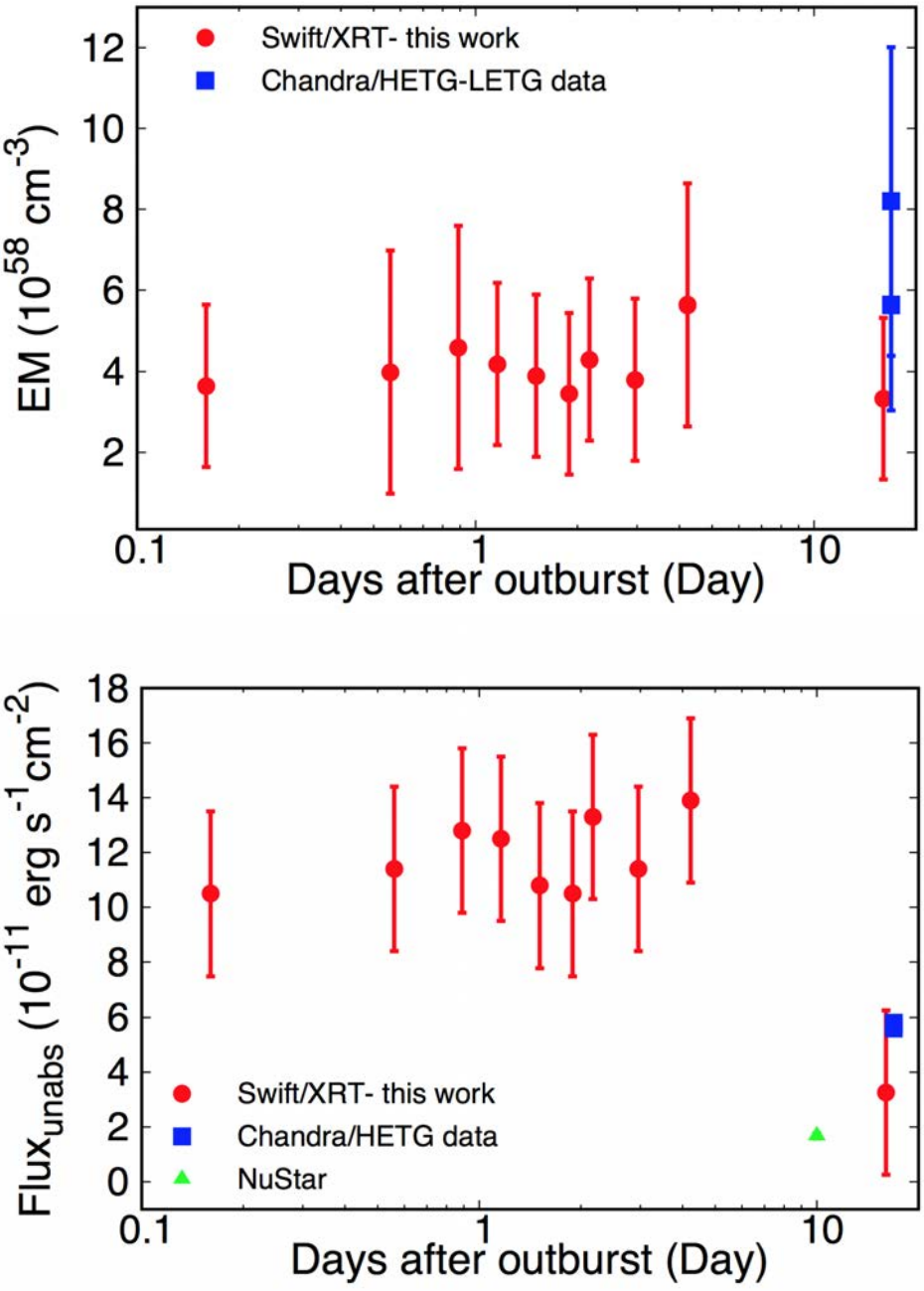

Figure 43: Top: Emission measure of the shock as a function of time. Bottom: Unabsorbed X-ray flux, F_{unabs}, as a function of time. Red dots correspond to *Swift*/XRT (3σ error bars), green triangle to *NuStar* (Orio et al., 2015) and blue boxes to *Chandra*/HETG-LETG(top) (Drake et al., 2016) and HETG(bottom) (this study).

sorption produced by the stellar wind of the RG ($N_{H,W}$), so $N_H = N_{H,W} + N_{H,ISM}$. In our case, we assume that this absorption is also related to the ejected material.

The emission measure gives information about the volume and electron (ion) densities of hot material that emits in X-rays. The EM obtained fitting the *Swift*/XRT spectra is practically constant, even up to day 16 after the outburst (Figure 43). However, the EMs obtained by *Chandra*/HETG-LETG are slightly higher. This can be due to the differences in the absorption or the sensitivities of the instruments, because the highest EM corresponds to *Chandra*/LETG (Drake et al., 2016). This instrument detects cooler materials than *Swift*/XRT and *Chandra*/HETG. This result agrees with the temperature evolution.

Finally, we study the evolution of the unabsorbed X-ray flux, F_{unabs}, comparing *Swift* F_{unabs} $[0.8-10$ keV$]$, *Chandra* F_{unabs} $[0.9-6.0$ keV$]$ and *NuStar* F_{unabs} $[3-10$ keV$]$ (Orio et al., 2015). F_{unabs} increased slightly during the first days, being practically constant until the SSS phase. During this phase, F_{unabs} obtained by *Swift* 10 days after the outburst shows that F_{unabs} increased two orders of magnitude (Orio et al., 2015, Table 2) but we only take into account the result of the hard X-ray emission obtained with *NuStar*. From day 16 after the outburst F_{unabs} decreased down to $\sim 4\times10^{-11}$ erg cm^{-2} s^{-1}.

4.2.2 *Radio and high energy γ-ray observations*

One of the most important observations was the detection of V745 Sco by *Fermi*/LAT in its last outburst (Cheung et al., 2014, 2016b). There were marginal observations (2 - 3σ) in 1-day intervals on February 6^{th} and 7^{th} with a F_γ(E>100 MeV)$\sim$ $(3\pm1)\times10^{-7}$ ph cm^{-2} s^{-1} and no significant emission was detected until the end of the observations four days after. From those days only upper limits for the flux ($F<(2$ - $3)\times10^{-7}$ ph cm^{-2} s^{-1} (95% confidence)) could be extracted. V745 Sco is the only recurrent symbiotic system with a RG companion detected by *Fermi*/LAT. The companion of V407 Cyg is a Mira-star and *Fermi* did not exist in the last outburst of RS Oph. This nova is far ($\sim$8 kpc) compared to the other novae detected by *Fermi*/LAT ($\sim$3 - 5 kpc) and is also close to the galactic center. These facts made its detection difficult. It was not possible to obtain a spectrum to know the nature of the very high energy emission (E>100 MeV). However, it is very important to have information about the flux to compare with the theoretical flux of RS Oph.

A related point to consider is the non-detection by *Swift*/BAT in the last outburst in contrast with the case of RS Oph. It is important to remember that this nova is at $\sim$8 kpc, a distance larger than that of RS Oph (1.6 kpc). In the detection of RS Oph only the light curve was measured, but no spectrum was obtained. Apparently, the non-detection by *Swift*/BAT indicated the non-emission of this nova in this energy range (15-150 keV). However, 10 days after the outburst, V745 Sco was detected by *NuStar* in an energy range between 3 and 20 keV. Therefore, the non-detection by *Swift*/BAT was due to the sensitivity of the instrument (0.8 mCrab in the 15-150 keV) and the distance

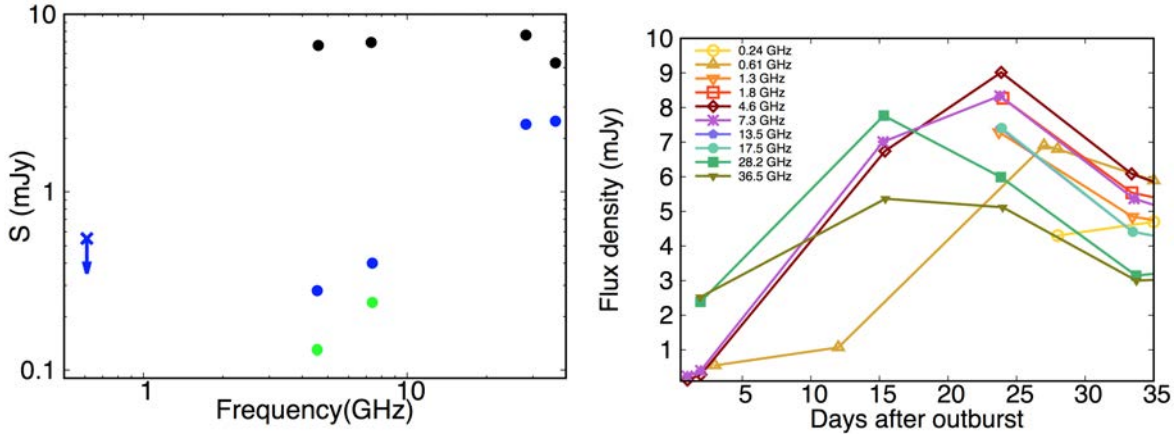

Figure 44: Left panel: Radio spectra the first days after the outburst on 2014 February 8 (green), 2014 February 9 (blue) and 2014 February 22 (black) (dots: Rupen et al. (2014), E-Nova[2] web site and crosses: Kantharia et al. (2016)). Right panel: Radio light curve using the data of Rupen et al. (2014), E-Nova[2] web site and Kantharia et al. (2016).

to V745 Sco.

Finally, it is also worth mentioning that the radio observations reveals the dual nature, thermal and non-thermal, of the plasma. Rupen et al. (2014) detected a rapid increase in radio flux density with the VLA two days after the optical maximum. They stated that this emission was consistent with an optically thick thermal plasma or with a self-absorbed synchrotron emission, similar to that obtained in RS Oph (see Appendix D). The brightness temperature obtained was 10^6 K. Kantharia et al. (2016) presented GMRT observations of V745 Sco. The energy range of this instrument allowed them to get information about the synchrotron emission of this nova. They interpreted the detection soon after the outburst as a decrease of circumstellar medium densities. They detected a clumpy material close to the white dwarf suggesting the existence of an accretion disc. The magnetic field of V745 Sco was estimated to be of 0.03 G, similar to that of RS Oph (0.04 G).

Thanks to this information and the light curve given by the E-Nova Project[3] web site, we build the radio spectra of the first days after the outburst (Figure 44). The radio spectra vary considerably over the course of the observations. We see the effects of the fast increase in flux at 4.56 GHz, which is interpreted as the appearance of the the nova within the dense circumstellar material. The second day after the eruption, the spectrum has a positive spectral index ($\alpha \sim 1$) ($S_\nu \propto \nu^\alpha$ convention (see Appendix D)), showing a thermal spectra. We must bear in mind that the first detection of GMRT took place the third day after the outburst. This detection provides us information about the synchrotron emission, but only as upper limits. This emission occurred sooner than expected because the circumstellar medium started being transparent, consistent with the appearance of the SSS phase. The spectrum of the third day shows a mix of synchrotron ($\alpha \sim$-0.3 between 0.61 to 4.56 GHz) and thermal ($\alpha \sim 1$ between 4.56 to 36.5 GHz) emission. On 2014 February 22^{nd} the spectrum becomes increasingly flat for

3 https://sites.google.com/site/enovacollab/data/v745-sco

E>4 GHz with an α ~0. This means that there is a mix of both emissions. Figure 44 shows the radio light curve of V745 Sco (Kantharia et al., 2016, E-Nova Project[1]). V745 Sco has a maximum 23 days after the outburst. However we do not know if two maxima occurred as in RS Oph because GMRT and VLA started to have good quality observations (synchrotron and thermal emission) 12 days after the outburst.

4.2.3 *IR observations*

V745 Sco was detected in IR by Banerjee et al. (2014a) the first days after the outburst. This observation started 1.3 days after the outburst as in RS Oph. The X-ray emission started before IR emission unlike in RS Oph, whose X-ray and IR emission started practically at the same time. Banerjee et al. (2014a) measured the profile of the H I Paschen β emission line between 1.3 to 15.3 days after the outburst, but they did not mention any uncertainties of their results. This line was chosen because it is not blent with other lines. They fit the IR line with two gaussians: a broad one that is related with the fast movement of the nova shell, and a narrow one that is related with the slow movement of wind material and is constant in time. These two components were also seen by Duerbeck (1989) in the previous eruption in 1989 and by Anupama et al. (2014) in optical in the 2014 eruption. We use the FWHM of the broad gaussian line component (Figure 45) as shock velocity (v_s) of V745 Sco. We see how v_s decreases very slowly during the first 4 days. After day 4, the slope becomes steeper and the velocity is drastically reduced, which indicates that the shocked plasma is now scattered by the circumstellar medium. Thanks to these observations, we estimate the v_s the first days after the outburst but with a certain uncertainty because we do not know the FWZI of the line as in RS Oph. In this case, we only know that the FWZI of Paβ was 9130 km/s when the FWHM was approximately 4000 km/s (Banerjee et al., 2014b). The shock velocity is approximately FWZI/2, slightly larger than the FWHM. For this reason we probably underestimate v_s.

Banerjee et al. (2014a) fitted the IR data with the power law associated to the adiabatic phase ($v \propto t^{-1/3}$) but as we see in Figure 45, it is clearly not a good fit to the data. Banerjee et al. (2014a) found that the best fit is a third degree polynomial. Nevertheless, this model does not correspond to any phase in the evolution of the shocked plasma (§2.4.1). We fit the data taking into account the different phases of the nova ejecta and the different behaviours of the speed. It is important to remember that we do not know the errors in the measure of the FWHM. For this reason, we fit the data directly knowing that the error in the measure could change the result.

4.2.3.1 **IR Data Analysis**

First of all, we try to fit the data with a single power law ($v \propto t^{\alpha}$), but as in Banerjee et al. (2014a), we did not find a good fit. However, we find several options using two power laws. We select the four best combinations (Figure 46).

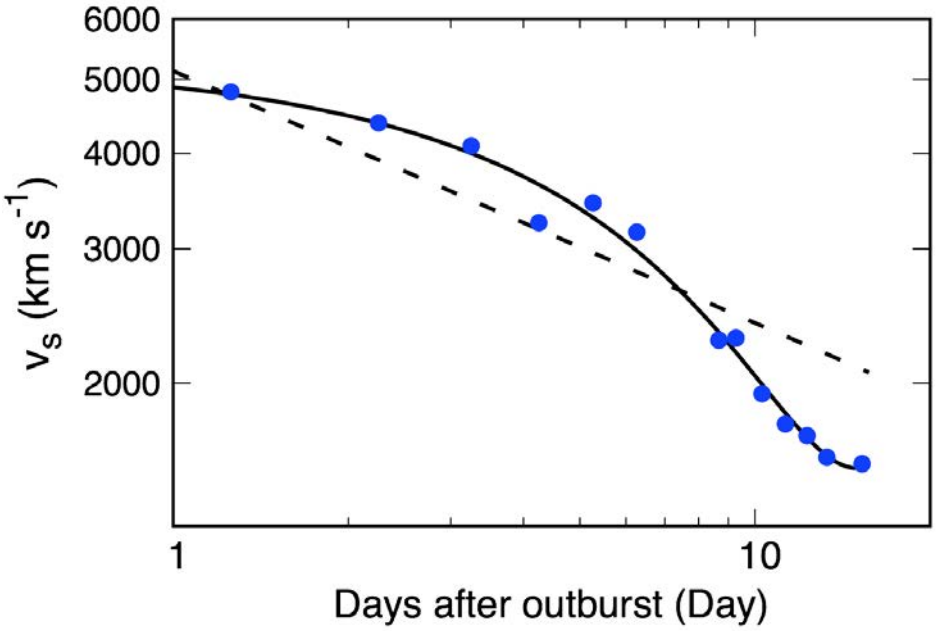

Figure 45: Temporal evolution of the broad gaussian line component FWHM of H I Paschen β emission line between 1.3 to 15.3 days after the outburst. The velocity is fitted by a $t^{-1/3}$ law (dash line) representative of the adiabatic phase and by a third degree polynomial (solid line) (Banerjee et al., 2014a, Figure 3).

- **First fit** (black dashed line). The first epoch starts on day 1.3 after the outburst with a constant velocity (α=0) and the second one starts on day 2 after the outburst with a power law index of α=-0.5. These indexes correspond to Phase I (v = const.) and Phase III (v $\propto t^{-1/2}$). The ejected mass expanded freely through the circumstellar medium until day 2, when it started to lose momentum by radiation, without going through the adiabatic phase, as in the case of RS Oph.

- **Second fit** (magenta dashed line). The first epoch began on day 1.3 after the outburst, which has a power law index of α=-0.33. On day 3 after the outburst started the second one that, as in the First fit, has a power law index of α=-0.5. This behaviour corresponds to Phase II (v $\propto t^{-1/3}$) and Phase III (v $\propto t^{-1/2}$). The model represents that the shocked material was in the adiabatic phase when the IR observations started and ended in the radiative phase, as in the classical case of the SNR.

- **Third fit** (red dashed line). In this model, the change in the slope also occurs on day 3 after the outburst. We fit the data with a power law index of α=-0.16 the first days after the outburst, and a power law index of α=-0.5 in the second time interval. This corresponds to Phase I→II (v $\propto t^{-1/(n-2)}$ where n=8) and Phase III (v $\propto t^{-1/2}$). This model would indicate that the shocked plasma was in a transition between the free expansion and the adiabatic phase and ended up losing momentum by radiation directly, without reaching the adiabatic phase.

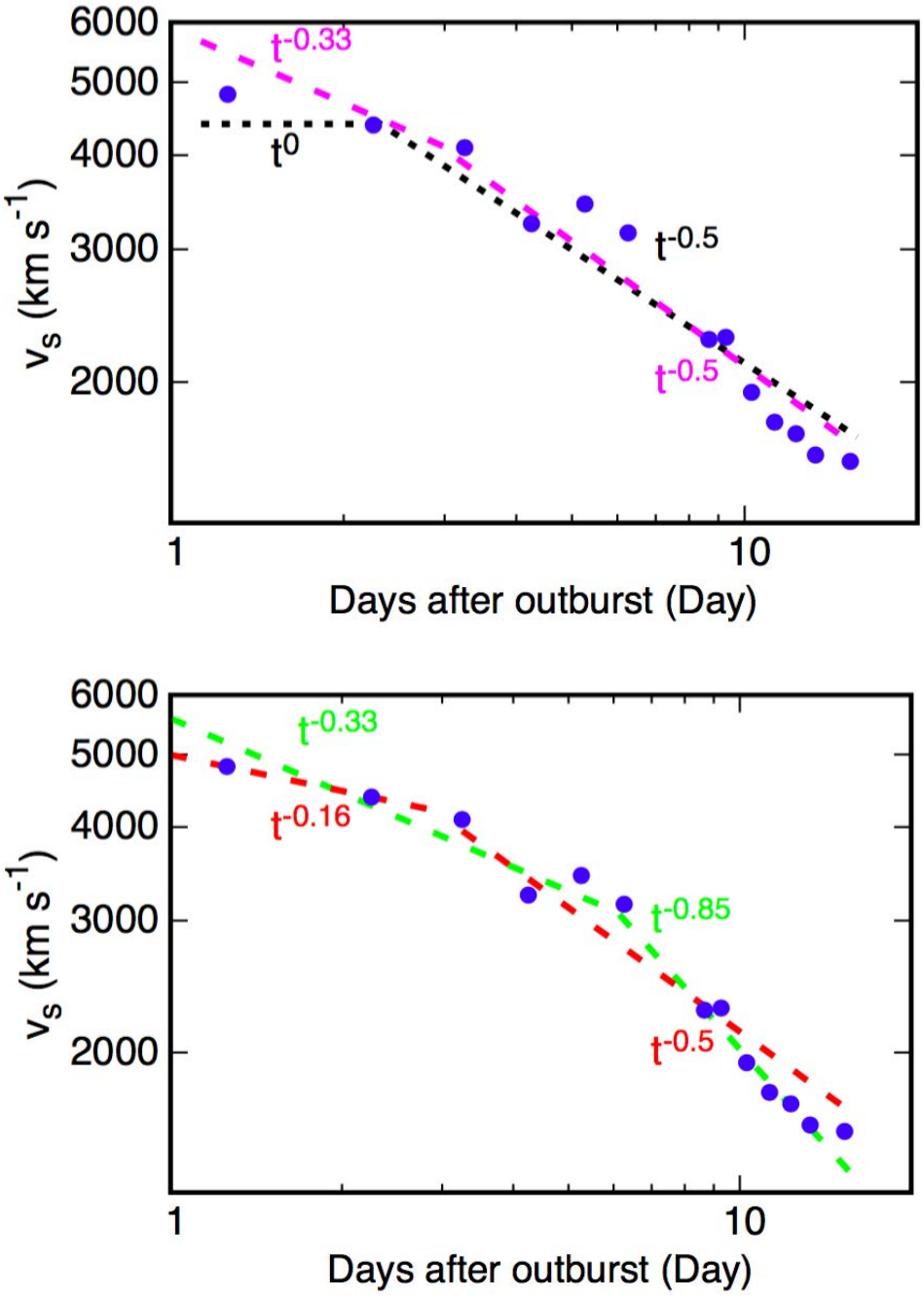

Figure 46: Data as in Figure 45. The velocity is fitted with four different models: In the first model, the shocked plasma passed from phase I on day 2 to phase III (black dash line) and in the second one, it passed from phase II on day 3 to phase III (magenta dash line) (top panel). Bottom: In the third model, the shocked plasma passed from phase I→II on day 3 to phase III (red dash line) and in the fourth model, it passed from phase II on day 6 to a combination of phases (green dash line) (bottom panel).

- **Fourth fit** (green dashed line). The change in the slope takes place 6 days after the outburst, later than in the other fits. The first power law has an index of α=-0.33. After day 6, the power law index is α=-0.85. Even though this power law corresponds to the best fit found between days 6 and 16, it does not correspond to any known SNR phase.

Other combinations are possible, but without the errors, we have many open questions such as when does the slope change take place, what is the state of the system in the first days, and also what is its state during the first hours, for which we do not have IR data. We conclude that the shocked plasma is in the radiative phase the last days. To understand better the first two weeks after the outburst, we combine IR data with data in other wavelengths to have a global picture of the V745 Sco evolution.

4.3 PROPERTIES AND EVOLUTION OF THE SHOCKED PLASMA OBTAINED FROM THE IR AND X-RAY OBSERVATIONS

As we showed in the last sections, we have obtained information about the shock wave expanding into the RG wind using several wavelengths. With the X-ray observations, we obtain the most representative temperature of the shock (T_s) and with IR observations we obtain the velocity of the shock (v_s). The relation for a test-particle strong shock (Equation 5) gives an estimation of the velocity at which the shock expands into the RG wind using T_s. However, this relationship underestimates the shock velocities when the shock is modified by the acceleration of particles. We compare the shock velocity obtained in IR with those deduced from the X-ray temperatures (Figure 47). A small difference between them is obtained. We must bear in mind that FWZI/2≥FWHM. Thus, the discrepancy between the FWHM and the v_s obtained with Equation 5 can be smaller than with the FWZI/2.

We use the v_s obtained with the IR data as the mean velocity of the shock. IR observations were not simultaneous to *Swift*/XRT observations. There is no information about the behaviour of the v_s during the first hours after the outburst. Besides, the X-ray observations have large uncertainties. Therefore, we assume different behaviours of the shock velocity when the X-ray observations took place. In Case A, we assume that the v_s is constant during the first hours as in a free expansion, and in Case B, we fit the data of the first three days to an exponential function and extrapolate to the first hours (Figure 48). For the remaining time instants, we interpolate the v_s corresponding to each X-ray measurement time. Another approach employed by some authors is to assume that the v_s is constant in time. However, it is more appropriate to derive the properties of the plasma taking into account the temporal evolution of the v_s as we will see in this section.

We calculate the shock radius (R_s) using Equation 9. There are some relevant radii in the geometry of the system. First of all, we have the separation between the WD

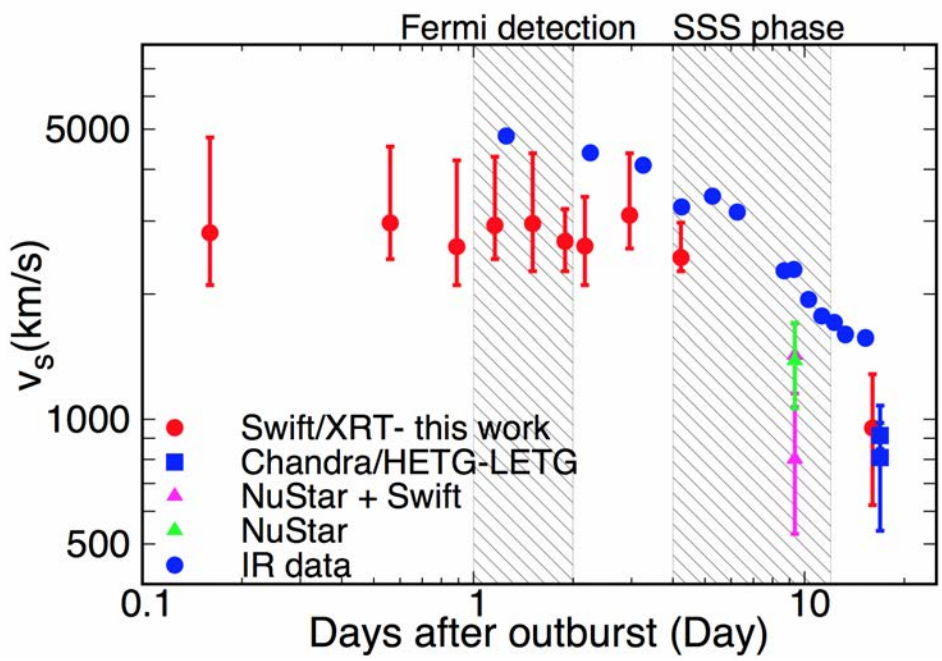

Figure 47: Temporal evolution of the velocity shock in IR (blue dots: (Banerjee et al., 2014a, low panel Figure 3) and X-ray (red dots: Swift/XRT to 1 σ; blue boxes: Chandra/HETG-LETG (Drake et al., 2016); green and pink triangles: *NuStar* and *NuStar+Swift* respectively (Orio et al., 2015). Patterns show the *Fermi* detection and the SSS phase duration.

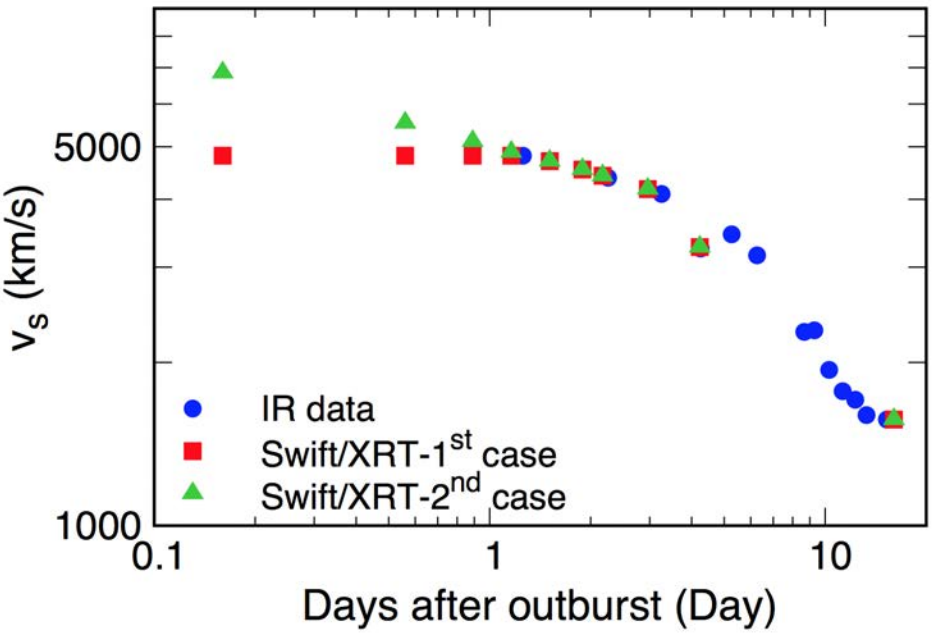

Figure 48: Comparison of the shock velocity as a function of time for cases A and B. Blue dots correspond to IR observations (Figure 45). In the Case A (red squares), we assume a constant velocity during the first hours, and in the Case B (green triangles), we fit the data of the first three days to an exponential function and extrapolate to the first hours.

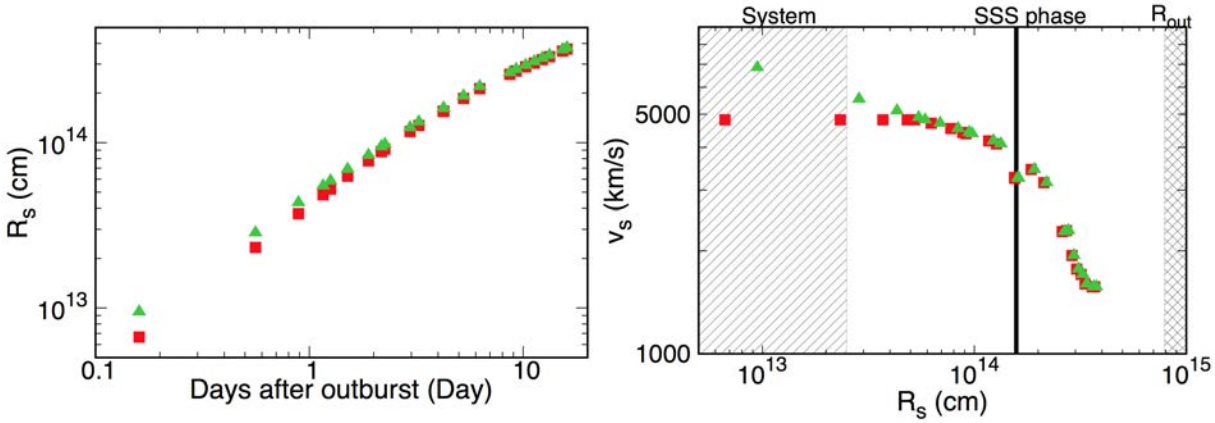

Figure 49: Top: Comparison shock radius as a function of time for cases A and B. Bottom: Comparison of shock velocity as a function of shock radius for cases A and B. Case A (red squares) and Case B (green triangles). Patterns show the system separation, the radius where the shock was the day the SSS began and r_{out}.

and the RG. Banerjee et al. (2014a) state that the M giants of S-type systems have a low-mass (<1 $M_\odot$). We assume M_{RG} ∼1 $M_\odot$. Since V745 Sco is a recurrent nova, we consider a massive WD (M_{WD} ∼1.2 -1.4 $M_\odot$). The separation of the system was obtained using Kepler's third law. As we explained in §4.1, the orbital period of the system is not clear. Therefore, the system distance is between ∼0.65 AU and ∼1.6 AU. Another important radius is the outer radius of the RG wind. The time between the last two outbursts is Δt =25 yr, so r_{out} was between 7.8×10^{14} cm and 1.6×10^{15} cm depending to u_{RG}(≅10-20 km s^{-1}).

Figure 49 shows the shock radius of the two v_s profiles, cases A and B, as a function of time. During the first hours, the radius of Case B is larger than the radius of Case A. However, the difference between them becomes smaller with time. When we compare the v_s and the R_s, we see that the shocked plasma crossed the system in the early hours before the first IR observation. We assume that the slope does not change during this time, but it is possible that during the first hours the ejecta expanded as an homologous expansion ($v_s \propto R_s$) before the free expansion. For future nova outbursts, it is important to have earlier IR observations to clarify the evolution of the shock radius and shock velocity during the first hours. We see a change in the slope of v_s simultaneous to the appearance of the SSS phase (R_{SSS} ∼1.55×10^{14} cm). It is noteworthy to mention that the R_s are smaller than r_{out} during the observations of our study. At r_{out}, it is assumed that N_H=$N_{H,ISM}$, but we obtain N_H=$N_{H,ISM}$ before reaching this radius.

We approximate the ejecta and the RG wind to an ideal spherical shell. With this simplification and Equation 10, we estimate the volume of the shock material (Vol_s). The evolution of the EM was obtained for the most representative temperatures of the shocked plasma. We do not know the EM for the times when the nova was detected in IR and not in X-rays. Thus, we extrapolate the EM for these times. Knowing the EM and the volume, we estimate the n_e. Figure 50 shows that the n_e decreases faster the

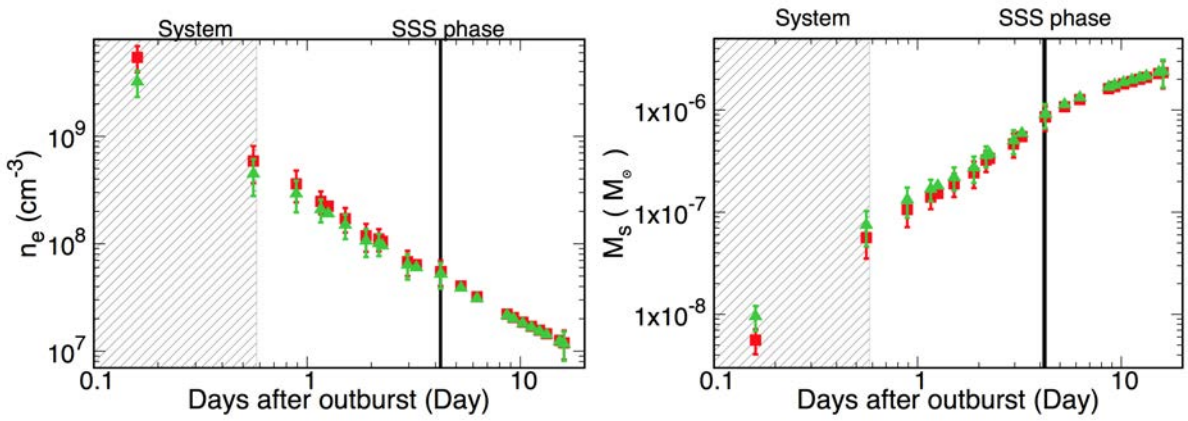

Figure 50: Sock electron density and shocked plasma mass evolution for the cases A (red squares) and B (green triangles). Patterns show the system separation and the R_{SSS}.

first four days and then slower, reaching to $\sim 10^7$ cm^{-3} 16 days after the outburst.

As we explained in §3.2.4, the mass density of the shock plasma is given by $\rho = n_e \times \mu_e / N_a$ where $\mu_e = 2/(X+1)$ and X is the fractional abundance of H. The mass density follows the same behaviour as the electron density, reaching values of $\sim 10^{-17}$ g/cm^{-3} 16 days after the outburst. The mass of the shock plasma is defined by $M_s = \rho \times Vol_s$, if the main element of our plasma is H. Figure 50 shows how the mass increases as a function of time. The M_s is composed by the ejected mass (M_{ej}) and the swept-up material (M_{sw}). We obtain three different behaviours for M_s: during the first hours, M_s rapidly increases reaching 10^{-7} $M_\odot$. After 1 day, M_s increases slower than in the first hours (8×10^{-7} $M_\odot$ on day 4 after the outburst), probably due to the increase of the M_{swe}. After the SSS phase M_s becomes practically constant, because the v_s drastically slows down. Finally, the M_s reached 2×10^{-6} $M_\odot$, 12 days after the beginning of the SSS phase.

The value of M_{ej} obtained by other authors is 10^{-7} $M_\odot$ (Banerjee et al., 2014a; Page et al., 2015b; Drake et al., 2016), that is the value that we obtain one day after the outburst. This means that the first day the shock mass is composed mainly of the ejected mass. They used different methods to derive it. For example, Page et al. (2015b) employed the following equation (Henze et al., 2014, Equation 2.):

$$N_H = \frac{M_{ej,H}}{(4/3)\pi (v_s t)^2 m_H f'} \tag{13}$$

where $M_{ej,H}$ is the ejected hydrogen mass, $m_H = 1.673 \times 10^{-24}$ g is the mass of the hydrogen atom and $f' \sim 2.4$ is a geometric correction factor, assuming a spherically symmetric shell. The N_H and t correspond to the day that the SSS phase began. If we use the same equation, we obtain that $M_{ej} = 10^{-6}$ $M_\odot$. The disagreement with the other authors is due to the fact that they used a constant v_s ($\sim$4000 km s^{-1}), while we use the v_s corresponding to day 4th after outburst (3200 km s^{-1}). As we have shown in this section, the changes in the v_s strongly affect the plasma properties. Thus, considering a non-constant v_s allows us to determine M_{ej} more correctly than previous studies.

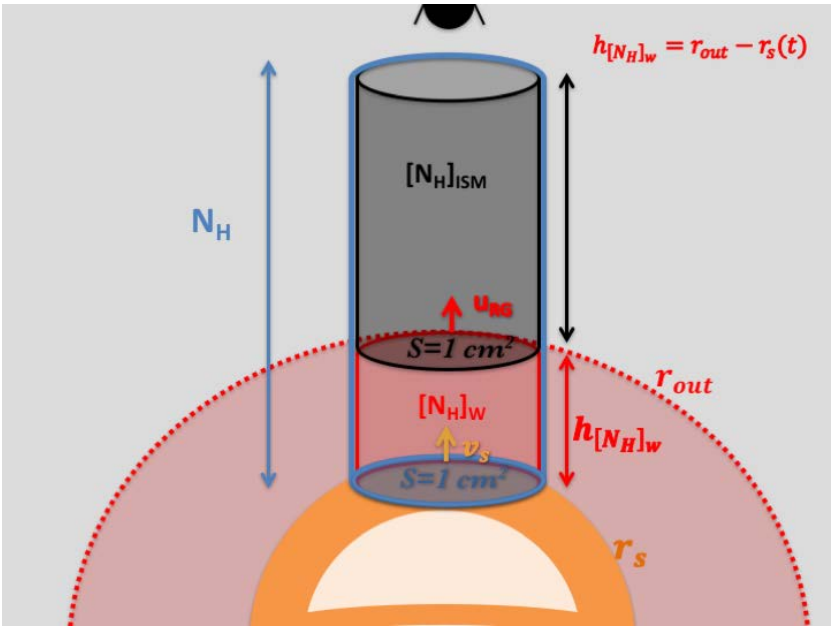

Figure 51: Schematic view of the N_H and its components.

4.3.1 *Characteristics of the red giant wind*

To obtain the magnetic field associated to the red giant wind (Equation 12) and to know if it was amplified by the particle acceleration, we need to find the density of the red giant wind (Equation 11). The density (ρ) is defined as:

$$\rho(t) = \frac{\dot{M}}{4\pi r^2 v} \rightarrow \rho_w = \frac{\dot{M}_{\rm RG}}{4\pi r^2 u_{\rm RG}} \tag{14}$$

where u_{RG} = 10-20 km s^{-1} and $\dot{M}_{RG}$ is the amount of wind mass per second to cross trough the sphere of radius r with a speed u_{RG}. In the case of V745 Sco, we do not know $\dot{M}_{RG}$. On the other hand, the average density can be obtained trough the N_H:

$$\overline{\rho}(t) = \frac{N_{\rm H} m_H}{hX} \tag{15}$$

where X is the mass fraction of hydrogen, h is the height of a cylinder of unitary base and m_H is the mass of a hydrogen atom. We will use X=0.7 which corresponds to a solar-like composition.

In a nova explosion, we observe three different components of N_H in X-rays, the N_H of the ejecta ($[N_H]_{ejecta}$), which is influential during the first few days, the N_H of the red giant wind ($[N_H]_w$) and the N_H of the interstellar medium ($[N_H]_{ISM}$). The material that we want to study is between two boundaries: the shocked plasma boundary that has radius R_s and speed v_s, and the interstellar medium boundary that has radius r_{out} and speed u_{RG}. Therefore, the height of a cylinder of unitary base h is not affected only by the red giant wind speed, but also by v_s. The absorption by the red giant wind is given by $[N_H]_w$= N_H-$[N_H]_{ISM}$, only when $[N_H]_{ejecta}$ is negligible.

To calculate $\overline{\rho_w}$, we need to convert Equation 14 into Equation 15 and to obtain the particle average between the borders R_s and r_{out} with v=u_{RG}.

$$\overline{\rho_w}(t)_{(r_s(t)\to r_{out})} = \frac{1}{r_{out}-r_s(t)}\int_{r_s(t)}^{r_{out}}\rho(r(t))dr = \frac{\dot{M}_{\rm RG}(t)}{4\pi r^2 u_{\rm RG}(t)}\frac{1}{r_{out}r_s(t)} \tag{16}$$

$$\overline{\rho_w}(t)_{(r_s(t)\to r_{out})} = \frac{[N_{\rm H}]_w(t)m_H}{h_{[N_{\rm H}]_w}X} = \frac{[N_{\rm H}]_w(t)m_H}{(r_{out}-r_s(t))X} \tag{17}$$

From Equation 16 and Equation 17, we obtain:

$$\overline{\rho_w}(t) = \frac{\dot{M}_{\rm RG}}{4\pi r^2 u_{\rm RG}}\frac{1}{r_{out}r_s(t)} = \frac{[N_{\rm H}]_w(t)m_H}{(r_{out}-r_s(t))X} \tag{18}$$

Then, we arrive at Bode et al. (2006, Equation 4) where $[N_H]_w(t)$ is given by

$$[N_{\rm H}]_w(t) = \frac{X}{4\pi m_H}\frac{\dot{M}_{\rm RG}}{u_{\rm RG}}\left(\frac{1}{r_s(t)}-\frac{1}{r_{out}}\right). \tag{19}$$

We do not know the mass-loss rate $\dot{M}_{RG}$ correspond to the RG of V745 Sco. We assume that the red giant wind has $\dot{M}_{RG}$= const. and u_{RG}= const. Therefore, Equation 19 is fitted to obtain $\dot{M}_{RG}/u_{RG}$.

Fitting the $[N_H]_w$ data to obtain $\dot{M}_{RG}/u_{RG}$, we find three problems: we do not know for what days Equation 19 is valid, N_H shows large uncertainties, and we need to determinate r_{out}. One of the parameters of Equation 19 is r_{out} in which N_H=$[N_H]_{ISM}$. Figure 52 shows that N_H=$[N_H]_{ISM}$ at R_s=3.7×10^{14} cm, that is smaller than r_{out} =7.8×10^{14} cm. However, according to the *Chandra* data, $N_H \neq [N_H]_{ISM}$ at R_s=3.7×10^{14} cm.

To tackle these problems we first carry out several tests. We fit N_H-$[N_H]_{ISM}$ extracting/adding one data point in each fit, to accurately identify the time at which Equation 19 is satisfied. We also use two different uncertainties, 3σ error bars and 1σ error bars. We perform two different fits using r_{out}=R_s=3.7×10^{14} cm and r_{out} =7.8×10^{14} cm. Figure 53 shows some of these test. Besides, we study some limiting cases to find the value of $\dot{M}_{RG}/u_{RG}$ and r_{out} that fit all the data. Finally, we retrieve directly $\dot{M}_{RG}/u_{RG}$ from the data that we have obtained in the observations for the cases of r_{out}=R_s=3.7×10^{14} cm and of r_{out} =7.8×10^{14} cm (Figure 54). All these tests have been carry out with the R_s obtained in Case A (Figure 49).

First, we find that we can not properly fit N_H-$[N_H]_{ISM}$ to Equation 19 with a single $\dot{M}_{RG}/u_{RG}$ or a single r_{out}. In most of the cases, we obtain a good fit of $[N_H]_w$ to Equation 19 from day 3 onwards (R_s >10^{14} cm) and r_{out}=R_s=3.7×10^{14} cm. Figure 54 shows that $\dot{M}_{RG}/u_{RG}$ is not constant. However, if we use r_{out}=R_s=3.7×10^{14} cm (left panel), $\dot{M}_{RG}/u_{RG}\sim$ turns out to be approximately constant after day 3. We conclude that the 3rd day after the outburst, the absorption of the red giant wind started to be dominant. Then, we obtain $\dot{M}_{RG}/u_{RG}$ = (5 ± 1)×10^{13} g cm^{-1} ($\dot{M}_{RG}$=[5 - 10]×$10^{-7}M_\odot$ $year^{-1}$), which is similar to the value estimated by Tatischeff & Hernanz (2007) for RS Oph.

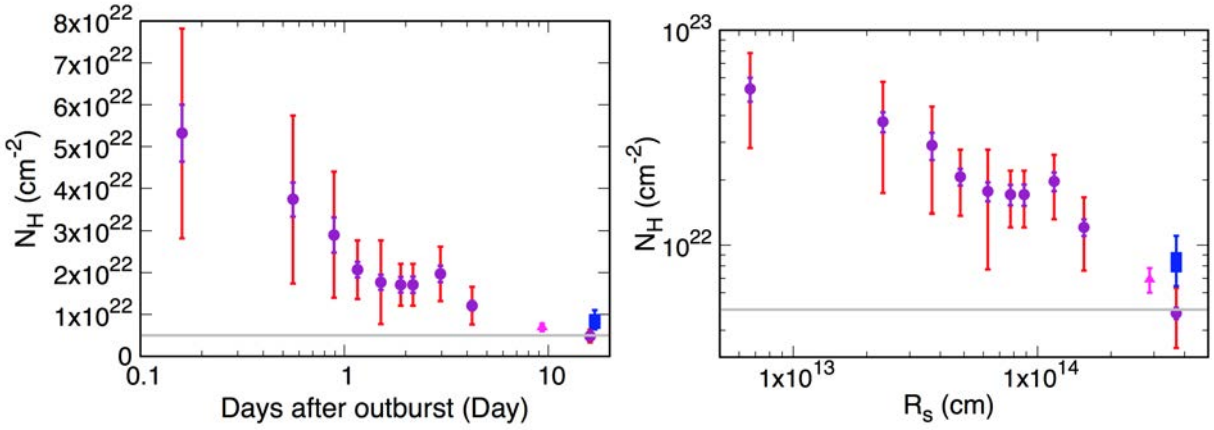

Figure 52: N_H evolution with time (left) and as a function of the shocked radius of Case A (right). Red dots correspond to *Swift*/XRT at 3σ error bars and purple dots at 1σ error bars, blue boxes to *Chandra*/HETG-LETG (Drake et al., 2016) and pink triangle to *NuStar*+*Swift* (Orio et al., 2015). The remaining measurements have 3σ error bars. Gray line corresponds to the ISM value.

One of the problems that we found in this nova is that N_H reached the value of $[N_H]_{ISM}$ earlier than expected. As a consequence of that, $r_{out} = R_s$ (day 16) works better in the models than $r_{out} = u_{RG}\Delta t$. We have three hypothesis to explain this fact. The first hypothesis, and the most likely, is that the circumstellar medium becomes transparent earlier than expected because of photoionization. Nielsen & Gilfanov (2015) stated that the photoionization of the wind material by the emission from the supersoft source can significantly reduce its opacity. In V745 Sco the SSS phase concluded 4 days before N_H reached the value for the ISM. The second hypothesis is the existence of a non-spherical symmetry explosion in V745 Sco. The asymmetries can cause the red giant wind to be swept-up faster than in other novae, since the binary separation causes an offset between the origin of the wind and the explosion. Drake et al. (2016) broadly discussed about the symmetry of the system. The third hypothesis is that the recurrence period of V745 Sco is smaller than expected. To obtain r_{out}, we need the time between the last two outbursts. But what if we have missed an intermediate outburst? We calculate the time between the last two outbursts necessary to have $r_{out}=R_s$(day 16). For u_{RG}=10 km s^{-1}, the time is $\sim$12 years, approximately half of the current recurrent period. For u_{RG}=20 km s^{-1}, the recurrent period is 6 years. This is the less probable hypothesis because nowadays the recurrent novae are practically monitored, but as this nova is very fast and faint, it is possible that we have missed some outbursts.

Once we have $\dot{M}_{RG}/u_{RG}$, we obtain ρ_w using Equation 11. Figure 55 compares ρ_w for cases A and B, where $\dot{M}_{RG}/u_{RG}=(5\pm1)\times10^{13}$ g cm^{-1}. We compare ρ and ρ_w and we obtain that ρ_w ($\sim10^{-13}$ g cm^{-3}) is larger than ρ ($\sim10^{-14}$ g cm^{-3}), but as time increases, they tend to be equal ($\sim10^{-17}$ g cm^{-3}). This means that on day 16, the red giant wind material dominates the shocked plasma.

To obtain the RG wind magnetic field (B_w), we use Equation 12. Figure 55 shows the RG wind magnetic field obtained using ρ_w for cases A and B. As we saw in RS Oph,

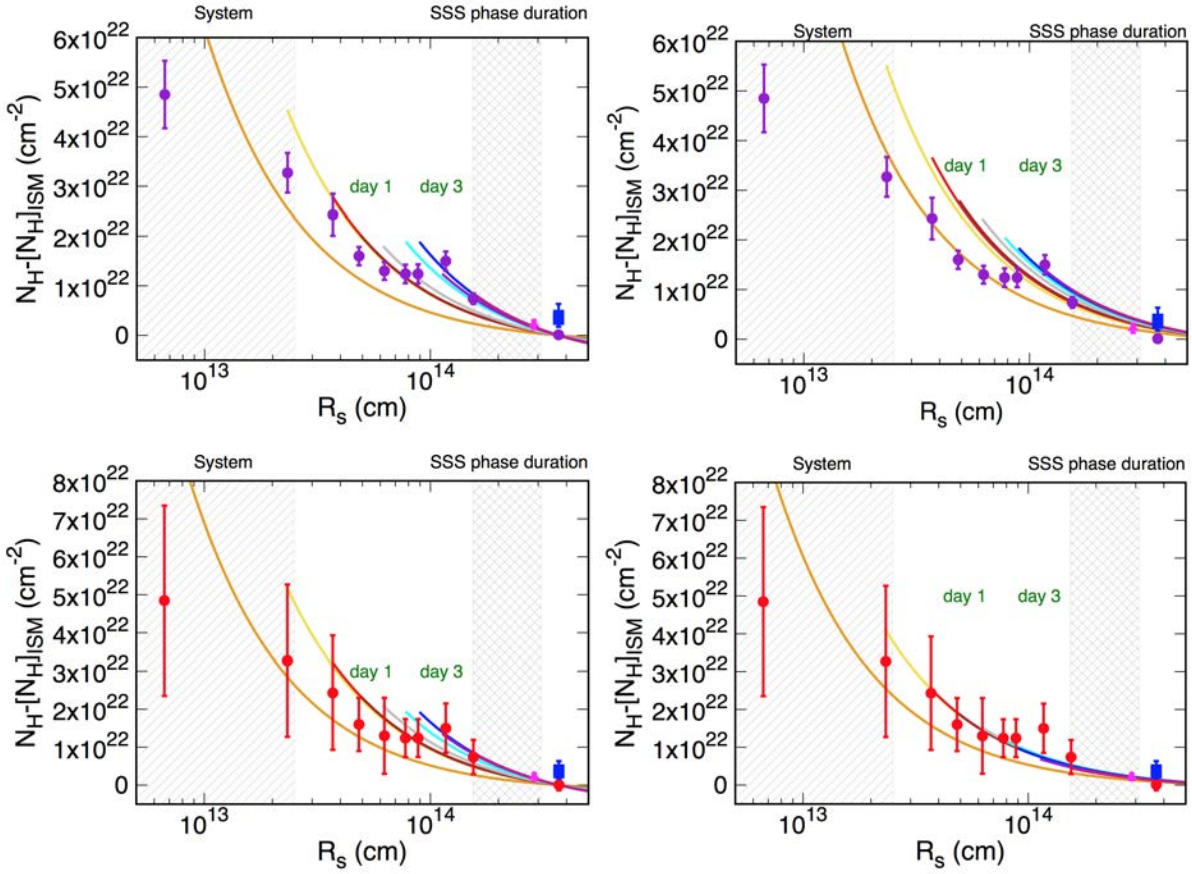

Figure 53: Some of the tests to obtain $\dot{M}_{RG}/u_{RG}$ through N_H=$[N_H]_{ISM}$ as a function of the shocked radius using Equation 19 with r_{out}=R_s=3.7×10^{14} cm (left panel) and r_{out} =7.8×10^{14} cm (right panel). Red dots correspond to *Swift*/XRT at 3σ error bars (bottom panels) and purple dots at 1σ error bars (top panels), blue boxes to *Chandra*/HETG-LETG (Drake et al., 2016) and pink triangle to *NuStar*+*Swift* (Orio et al., 2015). The remaining measurements have 3σ error bars. Colour lines correspond to the several fits using Equation 19. Patterns show the system separation and the SSS phase duration.

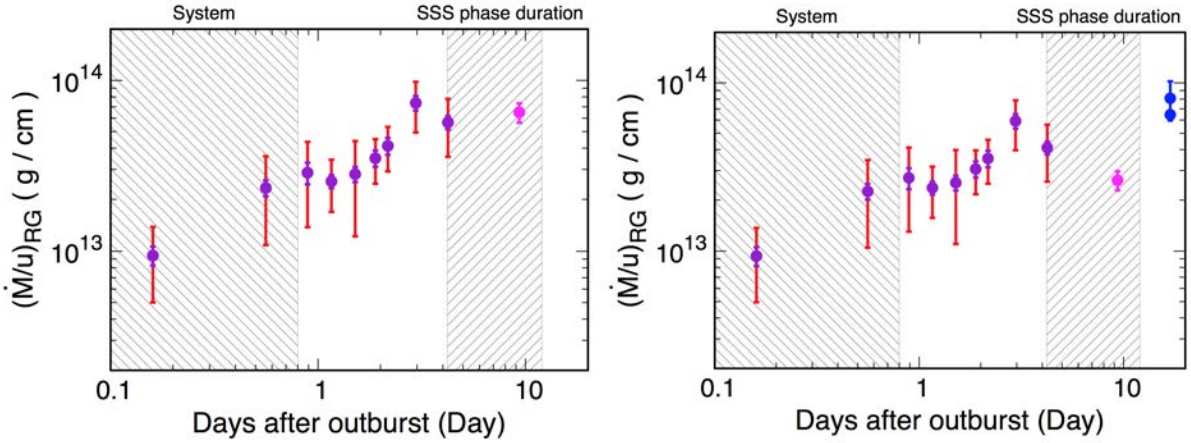

Figure 54: Temporal evolution of $\dot{M}_{RG}/u_{RG}$ obtained through Equation 19. Red dots correspond to *Swift*/XRT at 3σ error bars and purple dots at 1σ error bars, blue boxes to *Chandra*/HETG-LETG (Drake et al., 2016) and pink triangle to *NuStar*+*Swift* (Orio et al., 2015). The remaining measurements have 3σ error bars. Patterns show the system separation and the SSS phase duration.

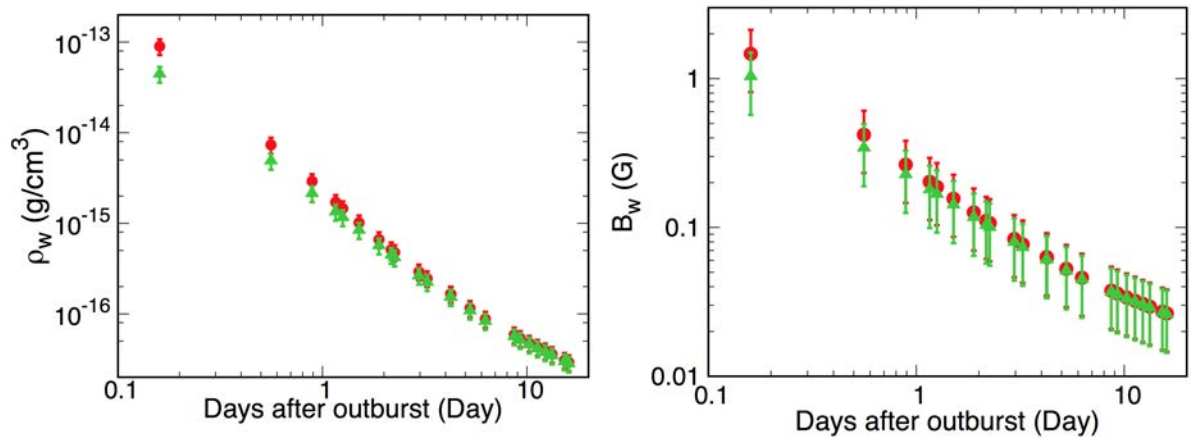

Figure 55: The density of the RG wind as a function of time (ρ_w) on the left and the magnetic field of the RG wind as a function of time (B_w) on the right. Case A (red squares) and Case B (green triangles).

the magnetic field is expected to be amplified by the interactions between accelerated particles and the shocked plasma (Lucek & Bell, 2000). In V745 Sco, the magnetic field of the shock obtained by Kantharia et al. (2016) was B_0=0.03 G. This value is similar to the B_w value obtained in this study, and therefore, the magnetic field amplification (α_B) should have been small. To know if there was acceleration of particles or not, and in this case, amplification of the magnetic field, we have also studied the phases of the nova evolution.

4.3.2 *Phases of remnant evolution*

In RS Oph, Tatischeff & Hernanz (2007) showed that the particles decelerate faster than expected as a consequence of the acceleration of particles (see § 3.3). They compared the IR and X-ray shock velocities which are derived from the FWZI of IR emission lines and Equation 5, respectively. In the case of V745 Sco, as we mentioned in § 4.2.3, we only have information about the FWHM. Figure 47 shows the small differences between the IR and X-rays shock velocities. As we do not know the IR uncertainties and the X-ray data have large errors, the differences between them are not clear.

In contrast to RS Oph, we have hard X-ray observations of V745 Sco during the first hours after the outburst. This information allows us to know for the first time the behaviour of the shock during the first hours in a recurrent nova. We know that there was a marginal detection by *Fermi*/LAT, and therefore, there was acceleration of particles the first day after the outburst. With this information and taking into account all the uncertainties that we have found in this nova due to the lack of data or the large errors, we carry out a similar study as Tatischeff & Hernanz (2007) did for RS Oph (see § 3.3). We try to relate the evolution of the shock velocity of V745 Sco with the phase stages of the SNR (see § 2.4.1).

We fit the IR and X-ray velocities taking into account the phases of the SNR. We find three possible fits related with the previous sections. Two correspond to the Third fit of §4.2.3 and are the most similar to the Cases A and B of §4.3, and one corresponds to the First fit of §4.2.3 and is the most similar to RS Oph. We obtain the shock radius by integration of the v_s, assuming that the system is spherical. Recall that without IR errors, we can not do a proper fit. Figure 56 shows the different cases. The velocities deduced from the X-ray data have the same behaviour than the velocities obtained in IR.

We observe three epochs in all cases. The first epoch was before the 1st day, the second one corresponds to the *Fermi*/LAT marginal detection, and the third one started before the SSS phase appeared. All cases differ in the first days but in the third epoch, they follow the same behaviour. We explain the behaviour in the different epochs of the First case, which is the most complex, to use it as example for the rest of the cases.

First case (Top left panel in Figure 56). It corresponds to Case A in §4.3. During the first epoch the ejecta was moving at a constant velocity across the system composed of the WD and the RG ($R(t) \propto t$). During this time, M_{ej} was larger than the swept up

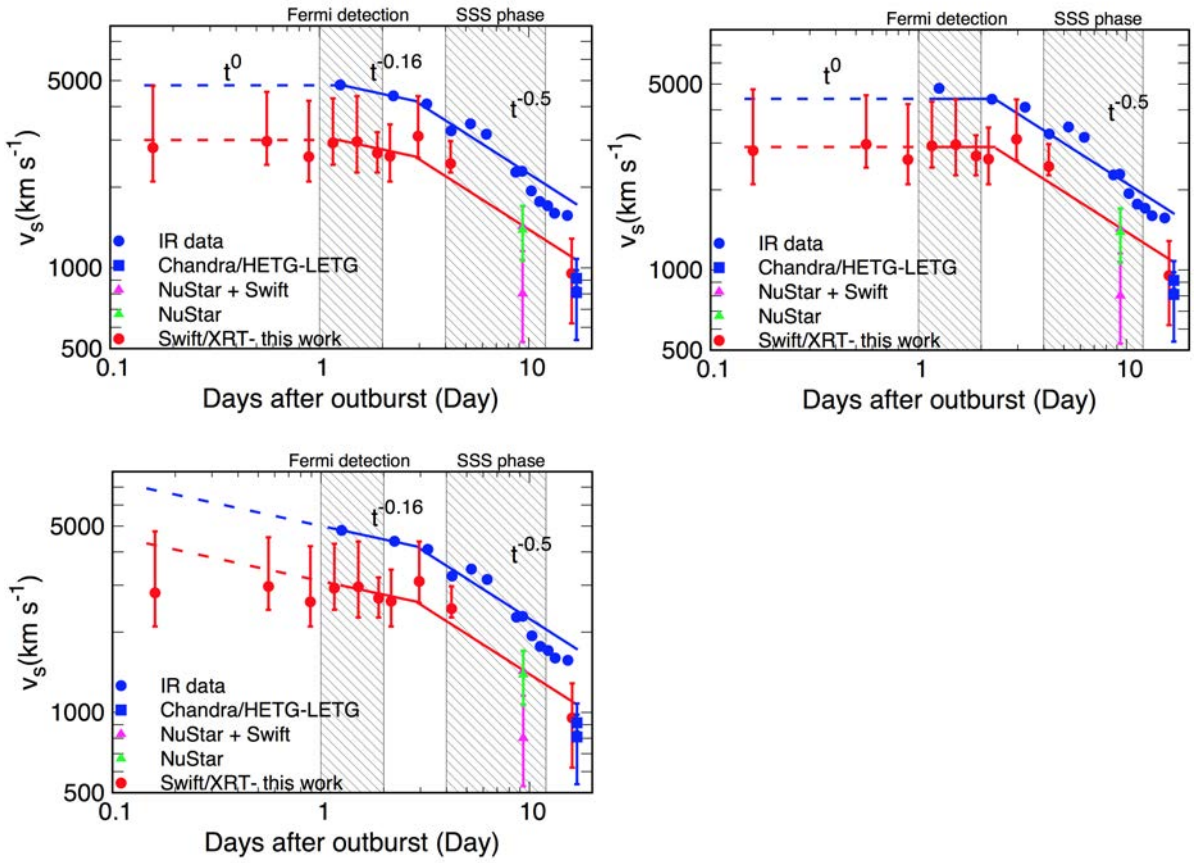

Figure 56: Temporal evolution of the shock velocity in IR and X-ray. Symbols as in Figure 47. Patterns show the *Fermi* detection and the SSS phase duration. Before 1st day after the outburst, v(t)= conts.(top) and v(t)=$t^{-0.16}$ (bottom). Between the 1st and the 3rd day after the outburst, v(t)= conts.(right) and v(t)=$t^{-0.16}$ (left). We use the same power law for the X-ray data.

mass ($M_{ej} \gg M_{sw}$) (Figure 50). The ejecta is in the free expansion stage (Phase I).

In the second epoch, between the 1st and the 3rd day after the outburst, we observe a slight decrease of the IR shock velocity, corresponding to $v_s(t) \propto t^{-0.16}$. In this phase M_{ej} is smaller than M_{sw} (Figure 50). This behaviour is characteristic of the self-similar driven wave of Chevalier (1982b) (phase I→II), where $v_s(t) \propto t^{\alpha}$ and $\alpha = \frac{-1}{n-2}$ with $n > 5$. For this days we fit the IR data with a power law index $\alpha = 0.16$ ($v_s(t) \propto t^{-0.16}$) which corresponds to $n = 8$.

The third epoch started approximately on day 3 after the outburst. v_s decreases abruptly compared with the second epoch ($v_s(t) \propto t^{-0.5}$). The shocked plasma is in the radiative snow-plough phase (Phase III). This phase is dominated by radiative losses and the radial expansion is governed by momentum conservation. The shocked mass is dominated by the mass of the RG wind ($M_{sw} \gg M_{ej}$). The fit of the IR v_s and its corresponding r_s give:

$$v_s(t) = \begin{cases} 4800 \text{ km s}^{-1} & t < 1 \text{ day} & \text{Phase I} \\ 5000\ t^{-0.16} \text{ km s}^{-1} & 1 < t < 3 \text{ day} & \text{Intermediate Phase I} \rightarrow \text{II} \\ 6700\ t^{-0.5} \text{ km s}^{-1} & t > 3 \text{ day} & \text{Phase III} \end{cases} \quad (20)$$

$$r_s(t) = \begin{cases} 4 \times 10^{13}\ t \text{ cm} & t < 1 \text{ day} & \text{Phase I} \\ 5 \times 10^{13}\ t^{0.84} - 10^{13} \text{ cm} & 1 < t < 3 \text{ day} & \text{Intermediate Phase I} \rightarrow \text{II} \\ 10^{14}\ t^{0.5} - 6 \times 10^{13} \text{ cm} & t > 3 \text{ day} & \text{Phase III} \end{cases} \quad (21)$$

Second case (Bottom left panel in Figure 56). It corresponds to Case B in §4.3. It has only two phases. The first days after the outburst, the power law index is α=-0.16 corresponding to Phase I→II ($v \propto t^{-1/(n-2)}$ where n=8). After day 3, the shock velocity behaves as in Phase III ($v \propto t^{-1/2}$). The shocked plasma is in a transition between the free expansion and the adiabatic phase, without reaching the adiabatic phase and passing directly to the radiative phase. v_s and r_s are given by

$$v_s(t) = \begin{cases} 5000\ t^{-0.16} \text{ km s}^{-1} & t < 3 \text{ day} & \text{Intermediate Phase I} \rightarrow \text{II} \\ 6700\ t^{-0.5} \text{ km s}^{-1} & t > 3 \text{ day} & \text{Phase III} \end{cases} \quad (22)$$

$$r_s(t) = \begin{cases} 5 \times 10^{13}\ t^{0.84} \text{ cm} & t < 3 \text{ day} & \text{Intermediate Phase I} \rightarrow \text{II} \\ 10^{14}\ t^{0.5} - 7 \times 10^{13} \text{ cm} & t > 3 \text{ day} & \text{Phase III} \end{cases} \quad (23)$$

Third case (Top right panel in Figure 56). This case is the most similar to RS Oph. It has two epochs, during the first epoch the ejecta is in a free expansion (Phase I) but after day 2, it decreases as expected for a well-cooled shock ($v_s \propto t^{-1/2}$).

$$v_s(t) = \begin{cases} 4400 \text{ km s}^{-1} & t < 2 \text{ day} & \text{Phase I} \\ 6700\ t^{-0.5} \text{ km s}^{-1} & t > 2 \text{ day} & \text{Phase III} \end{cases} \quad (24)$$

$$r_s(t) = \begin{cases} 4 \times 10^{13}\ t \text{ cm} & t < 2 \text{ day} \quad \text{Phase I} \\ 10^{14}\ t^{0.5} - 6 \times 10^{13} \text{ cm} & t > 2 \text{ day} \quad \text{Phase III} \end{cases} \tag{25}$$

All cases are possible as a consequence of the large X-ray error bars and compatible with the results of §4.3. In all of them, as in RS Oph, we show the skip or the very short duration of the adiabatic phase. The reason is that the nova cools faster than expected. According to Tatischeff & Hernanz (2007), this may be due to the diffusive acceleration of particles in a low power collision (Jones & Ellison, 1991).

Taking into account that $\dot{M}_{RG}/u_{RG} \sim 5{\times}10^{13}$ g cm^{-1}, we obtain the theoretical B_0 for each of the cases. As in § 4.3.1, we do not know α_w, but we know that it is smaller than in RS Oph (α_w <2):

$$B_0(t) = \alpha_w \left(\frac{4\dot{M}_{RG}}{u_{RG}} \frac{kT_w}{\mu m_H} \right)^{0.5} r^{-1} G = 1.4 \times 10^{13} \alpha_w r^{-1} G \tag{26}$$

With this information, in the future we will able to estimate the particle acceleration rate using a semianalytic model of nonlinear diffusive shock acceleration as employed by Tatischeff & Hernanz (2007).

4.3.3 *Acceleration of particles. Hadronic or leptonic process*

V745 Sco is a nova close to the galactic center at a distance of approximately 8 kpc. This means that it is the most distant nova of which *Fermi*/LAT has information. As we have only upper limits in γ-rays, we can not determine the nature of this emission, whether it is due to hadronic or leptonic processes, or due to both types of processes. Moreover, there is less information about V745 Sco, and with more uncertainties, than in the case of RS Oph. However, we can use the information that we showed in this chapter to understand the processes involved in the particle acceleration in V745 Sco and indicate what information about V745 Sco would be desirable to observe in its next nova explosions.

Martin & Dubus (2013) state that the low densities in novae are related with a low luminosity (V_{max} ∼9 mag), a short γ-ray emission and a less energetic spectrum. This fact can explain the short duration of the γ-ray emission (∼ 1 day), the short difference between the shock temperatures obtained in the X-ray observations and the shock velocities obtained from the IR observations, the similarities between the B_w and the B_0 obtained by Kantharia et al. (2016) and also the early appearance of the SSS.

In order to understand the nature of the particle acceleration, we build the SED of the shock material the second and third days after the outburst (Figure 57) with the radio emission information together with our work on *Swift*/XRT data (see § 4.2.1.2). Both X-ray and radio emission give us information about the mechanisms that produce the γ-rays. The radio, synchrotron (Kantharia et al., 2016) and thermal (Rupen et al.,

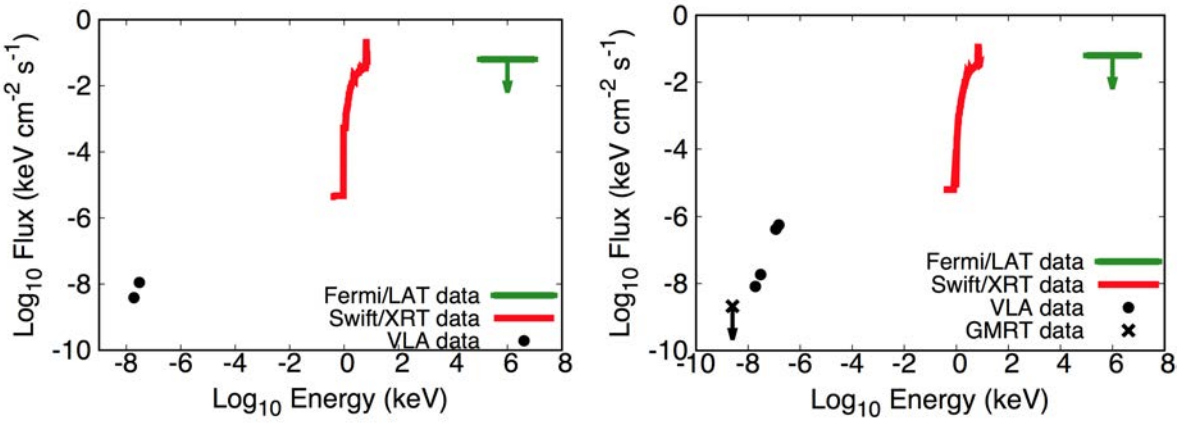

Figure 57: Broadband spectrum for V745 Sco on 2014 February 8 (left) and 2014 February 9 (right), 2 and 3 days after the outburst. Radio data: black dots (Rupen et al., 2014, E-Nova[2] web site) and black cross (Kantharia et al., 2016), X-ray data: red line and γ-ray data: green upper limit (Cheung et al., 2014)

2014) emissions were detected with similar fluxes. However, the thermal emission is predominant in X-rays. There is probably a non-thermal component related to the synchrotron emission. However, NuStar tried to observe this component, but the observation was very late and it was not possible to obtain the non-thermal emission tail. V745 Sco was also not detected with *Swift*/BAT nor *INTEGRAL* due to the sensitivity of their instruments. Finally, we state that both mechanisms, π^0 pion decay and Inverse Compton, are involved in the γ-ray emission. Taking into account the study by Hernanz & Tatischeff (2012) and that the ratio $\dot{M}_{RG}/u_{RG}$ of RS Oph and V745 Sco are similar, the hadronic process is more likely to be dominant.

4.4 SUMMARY AND OUTLOOK

Motivated by the study by Tatischeff & Hernanz (2007) and the marginal detection of *Fermi*/LAT of the symbiotic recurrent nova V745 Sco, we carried out a multiwavelength analysis of V745 Sco the first days after the outburst. We have focused on the reduction and the analysis of the X-ray observations obtained by *Swift* and *Chandra*. Based on this analysis we deduce the evolution of the properties of the shocked plasma the first two weeks after the outburst to understand better the shocked plasma and the acceleration of particles produced in it. Comparing with the case of RS Oph, the differences between the X-rays and the IR shock velocities could only be understood if a fraction of the shock energy went into cosmic rays (Decourchelle et al., 2000). Trying to relate the evolution of the shocked plasma with the very high energy emission of V745 Sco, we deduce that, as in the case of RS Oph, the fact that V745 Sco skipped Phase II indicates the acceleration of particles. From the the absorption produced from the RG wind and the expelled material therein, we deduce that the magnetic field amplification is very small and that the dominant process in the particle acceleration is most likely the hadronic one. In the future, it would be interesting to study the nature of the accelerated particles, as did by Tatischeff & Hernanz (2007) with RS Oph, using the

data shown in this chapter.

Some observations are missing in the energy range between 10 keV to E>100 MeV the first days after the outburst. In the next eruption of V745 Sco (∼2039?), it would be interesting to have early observations with the new generation of telescopes such as *ASTROGAM* in the MeV range. It will cover lower energies than *Fermi* (E:0.3-100 MeV) and with better sensitivity. This instrument will be able to discern between the π^0 pion decay and the Inverse Compton mechanisms. In addition, regarding the radio emission, it will be interesting to observe V745 Sco with the ngVLA and SKA (O'Brien et al., 2015) to obtain information about the thermal and the non-thermal emission the first days after the outburst and also to have enough resolution to resolve the structure of the ejecta.

5

RS OPH AND V745 SCO: SIMILARITIES AND DIFFERENCES

RS Oph and V745 Sco are very similar during the first days after the outburst, but they differ in some important properties. In this chapter, we will summarise the different nova features that we have studied in Chapter 3 and Chapter 4 to show their similarities and their differences.

5.1 THE SYSTEMS

RS Oph and V745 Sco belong to the group of long-orbital period novae, which also includes T CrB and V3890 Sgr (Anupama, 2008). They are symbiotic systems composed of a massive WD, close to the Chandrasekhar mass (∼1.4 $M_{\odot}$), orbiting a RG companion. The RGs of their systems are classified as M under the Harvard spectral classification (Russell, 1914, and references therein). The RG of RS Oph is an M0/2III (Bohigas et al., 1989; Anupama & Mikolajewska, 1999), and V745 Sco's RG is an M4/6 III (Duerbeck, 1989; Harrison et al., 1993). Their distances are very different and widely discussed in the literature. RS Oph seems to be close to us at 1.6 kpc, but there are different studies that place RS Oph closer (0.5 kpc (Monnier et al., 2006)) or further (4.2 kpc (Schaefer, 2010)) from us. In the case of V745 Sco, Sekiguchi et al. (1990) and Schaefer (2010) agree to place it in the galactic center at around 8 kpc. Because of this there are less observations of this nova.

The orbital period of RS Oph is accepted to be 455.7±0.8 days. Therefore, the separation between the WD and the RG is ∼ 1.5 AU (∼ 2.4×10^{13} cm) (Fekel et al., 2000). However, in the case of V745 Sco and because of its distance, the value of the orbital period is not clear. Mróz et al. (2014) and F. Walter (Page et al., 2015b) found semi-regular pulsations of the RG with sinusoidal variations at 136.5 days and 77.4 days, and because of that, the system separation is estimated to be of around 0.65 AU. However, Schaefer (2009, 2010) obtained an orbital period of 510 days, and this implies a system separation of ∼1.6 AU, similar to that of RS Oph.

Since V745 Sco decreases very fast and has a relatively faint peak, some outbursts were missed. Schaefer (2010) suggested a recurrence period of ∼25±1 years, which was confirmed in the last outburst in 2014. However, RS Oph has an irregular recurrence period being its outbursts separated by 9 to 26 years. Taking into account that the last

outburst was in 2006 and the shorter period is 9 years, we can state that at any moment from now an outburst of RS Oph can occur. It would be very interesting to determine the observational differences that produce these irregularities in the recurrence period.

5.2 THE FIRST WEEKS OF THE LAST OUTBURST

In the last outburst of RS Oph and V745 Sco, they were observed in practically all the wavelengths (Tables 3 and 13). There are two big differences between them. First, V745 Sco was marginally detected by *Fermi*/LAT, while in its last outburst, RS Oph could not have been detected because *Fermi* had not been launched, and second, the number of observations of RS Oph is larger than those of V745 Sco, the latter being less observed because of its distance and its speed.

5.2.1 *IR and radio observations*

IR emission is similar in both novae, it started being constant and changed its slope at the same time as the X-ray emission. Moreover, both novae began to be observed the first day after the explosion (Figure 58).

The FWHM and FWZI are good indicators of the shock velocity. FWZI is preferably used as FWHM as a measure of the expansion velocity. In RS Oph, we know both magnitudes, but in V745 Sco, we only know the FWHM. Figure 26 shows that FWZI/2 is larger than FWHM. Therefore, the difference between the v_s obtained with the FWHM and obtained with Equation 5 should be smaller in V745 Sco (Figure 47). In both systems some authors did not give uncertainties of the IR measures (Das et al., 2006; Banerjee et al., 2014a). In RS Oph, Das et al. (2006) gave the FWHM and the FWZI of two different lines that we use as lower and upper limits. This agrees with the uncertainties given by Evans et al. (2007). However, in the case of V745 Sco, Banerjee et al. (2014a) only gave the FWHM of the Paβ line.

Figure 58 shows the fit of half the FWZI of the O I and Paβ lines of RS Oph and FWHM of the Paβ line of V745 Sco. In RS Oph we see that before day 6 the FWZI is practically constant, but after day 6, a clear decrease in the velocity is observed. The power law index obtained was closer to 0.5 (Phase III) than to 0.3 (Phase II). In the case of V745 Sco, we propose different cases (§ 4.2.3.1) depending on the day that the v_s started to decrease (Figure 46). In this case, and because of the lack of uncertainties, it is difficult to determine the phases involved and the day on which the slope changes. For this reason, we proposed four different cases of which in three of them after day 3 the slope is 0.5 (Phase III). In Figure 58, we show the First fit that is the most similar to RS Oph. In both novae either Phase II was very short or it did not take place.

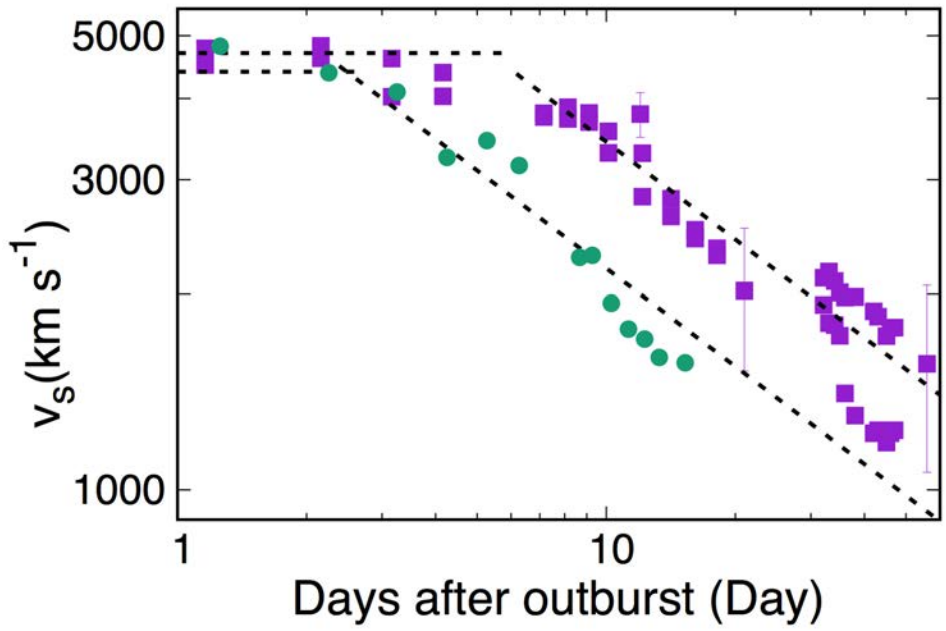

Figure 58: Shock velocity evolution for RS Oph (purple dots) and V745 Sco (turquoise squares). Same data than Figures 26 and 46.

The radio observations demonstrated the thermal and non-thermal nature of both systems the first weeks after the nova outburst (§ 3.2.2 and 4.2.2). These emissions are associated with the shock wave resulting from the outburst. Thanks to the high angular resolution of VLBA and its RS Oph radio images (Figure 59), we assume in the first epoch a spherical symmetry, similar to the remnant of a SN II. In both novae the spectra are dominated by the thermal component the first few days after the outburst. However, two weeks after the outburst both spectra are flat because their radio emissions are a combination between non-thermal and thermal emission.

An early fast rise in the radio emission the first days after the outburst was observed in RS Oph (4 days after the outburst) and V745 Sco (1-2 days after the outburst) related to the free expansion phase. They reached the maximum 13 and 23 days after the outburst respectively. However, in RS Oph a second maximum was observed 39 days after the outburst. The nature of the first maximum was mainly thermal and the second one a combination of both components (Eyres et al., 2009). For V745 Sco we only know a maximum with thermal and non-thermal emission. The lack of information about a first thermal peak in V745 Sco may be due to the rapid evolution of this nova and to the lack of more radio observations the first few days after the outburst. There were observations the first 3 days after the outburst, and the next observation was 12 days after the outburst (Rupen et al., 2014; Kantharia et al., 2016). For 10 days there were no radio observations. Taking into account the fast evolution of this nova, whose SSS phase appeared 4 days after the outburst, we probably missed the first maximum.

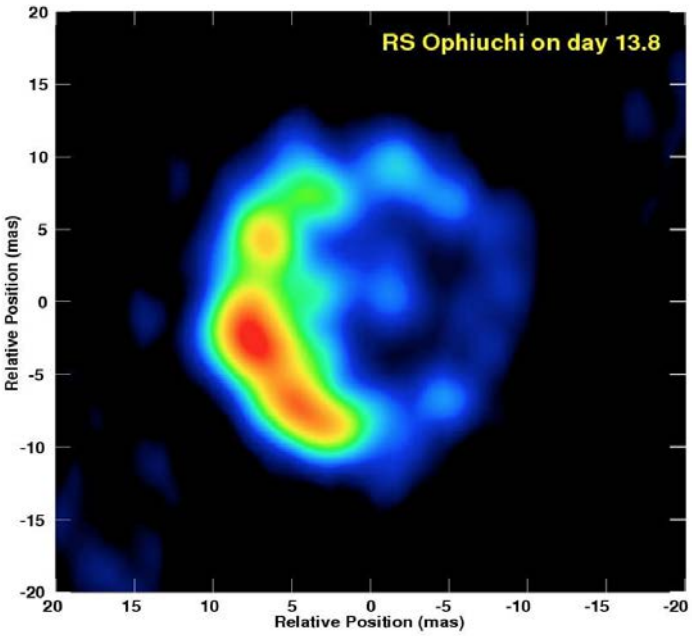

Figure 59: High-resolution radio image of RS Oph 13 days after the outburst at 5.0 GHz made with the VLBA and EVN (adapted from Evans et al., 2008).

5.2.2 *X-ray observations*

RS Oph was detected by *RXTE*, *Swift* (X-Ray Telescope (XRT) and Burst Alert Telescope (BAT)), *XMM-Newton* and *Chandra* (§3.2.1). The first observations of RS Oph took place 3 days after the outburst. However, and thanks to the fast repointing of *Swift* (Appendix A.2), V745 Sco was observed by the instrument XRT only 4 hours after the outburst. V745 Sco was also observed by *NuStar* and *Chandra*, but not by *Swift*/BAT (§ 4.2.1). One of the most notorious differences between these two novae is the time at which their corresponding SSS phase started to be visible. V745 Sco is until now, the nova for which the SSS phase appears soonest, only 4 days after the outburst. We observe three different epochs of V745 Sco: the early hard X-ray emission, the SSS phase and the post-SSS phase. However, we studied the X-ray emission of the first 26 days of RS Oph and we only observed the early hard X-ray emission and the first days of the SSS phase.

Comparing the lines observed with high spectral resolution instruments, we see that in RS Oph N, O, Ne, Mg, Si and Fe lines were visible before the SSS phase in an energy range between 5 and 30 Å (Figure 15). However, in V745 Sco the most representative lines are Ne, Mg and Si after the SSS phase between 2 and 13 Å (Figure 37). Because of its distance, the quality of the data is poor at energies larger than 13 Å. In both cases, we cannot determine the composition of the WD, because the Ne abundances are practically solar.

Furthermore, we compare the temperature, EM, flux and N_H of both novae obtained with the study of the X-ray thermal emission. The values of the temperature the first

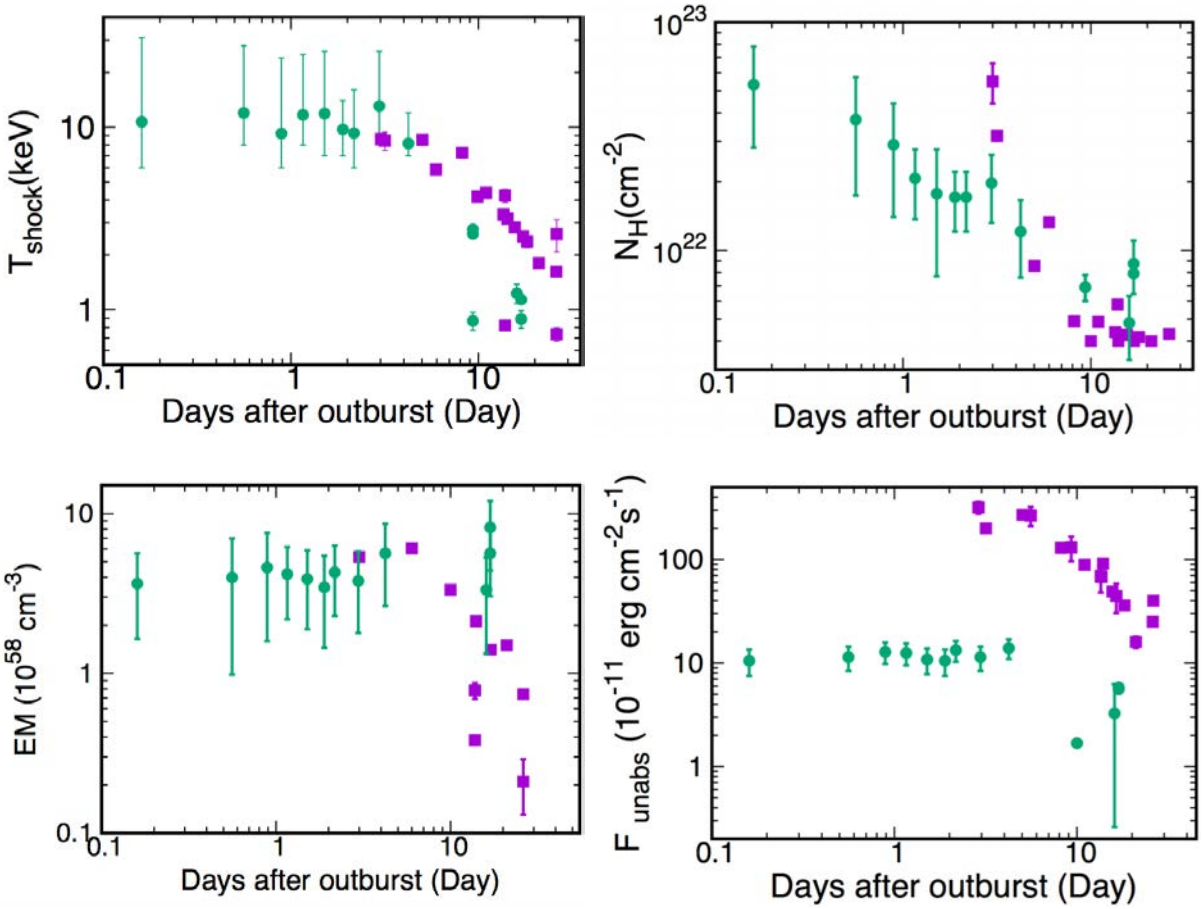

Figure 60: Temperature, N_H, EM and unabsorbed flux evolution with time for RS Oph (purple squares) and V745 Sco (turquoise dots). Same data than Figures 18 and 41, Figures 20 and 42, Figures 19 and 43, and Figures 21 and 43.

days are practically the same in both novae (Figure 60). In V745 Sco, the temperature is constant until the beginning of the SSS phase, 4 days after the outburst, while RS Oph's temperature was constant until day 6 after the outburst. In Figure 60, we deduce the temperature of RS Oph during the first hours, by comparison with the temperature of the first hours of V745 Sco. In the unabsorbed flux, we see a great difference due to the different distances. Their slopes change at the same time as their temperatures.

The EMs are very different between them. The EM of V745 Sco seems constant during the days of our study. Recall that the error bars of the EM obtained form *Swift*/XRT and *Chandra*/High Energy Transmission Grating (HETG) observations of V745 Sco are very large (Figure 43). However, the EM of RS Oph decreases with time. Figure 60 shows that both novae have the same behaviour during the first days. In RS Oph we obtain that more and more material was cooling with time (Figures 14 and 19).

The most relevant magnitude in the early appearance of the SSS phase in V745 Sco is the neutral hydrogen column density. The N_H of V745 Sco 4 hours after the outburst was practically the same as the N_H of RS Oph 3 days after the outburst. However, after day 3 both N_H follow the same behaviour. They have different $(N_H)_{ISM}$

($(N_H)_{ISM\ V745\ Sco}$ >$(N_H)_{ISM\ RS\ Oph}$). In the case of V745 Sco, N_H reaches $(N_H)_{ISM}$, but in RS Oph N_H remained constant before reaching $(N_H)_{ISM}$. As we mentioned N_H=$(N_H)_{ejecta}$+$(N_H)_w$+$(N_H)_{ISM}$. The RS Oph N_H on day 3 is larger than the V745 Sco N_H on day 3 (Figure 60). Taking into account that RS Oph $(N_H)_{ISM}$ is smaller than the V745 Sco $(N_H)_{ISM}$, then $(N_H)_{ejecta}$+$(N_H)_w$ of RS Oph will be larger than $(N_H)_{ejecta}$+$(N_H)_w$ of V745 Sco. Their companions seem also similar and their two last outbursts had practically the same period (21-25 years). We conclude that the mass ejected by V745 Sco is smaller than the ejected mass of RS Oph. This fact is related with the appearance of the soft X-ray emission in V745 Sco. Early X-ray monitoring as in V745 Sco is needed to properly know the N_H of RS Oph.

5.3 PLASMA PROPERTIES

As we mentioned before, the v_s obtained with the IR data can be used as the mean velocity of the shock between the ejecta and the RG wind. We compare the analyses carried out for both systems (§3.2.4 and §4.3).

We compare both shock velocities. The differences in speed account for the differences in the evolution of the two novae. In the case of RS Oph, as the IR observations started before the X-ray observations, we interpolated the shock velocity of the plasma for the days at which the X-ray observations were obtained. However, in the case of V745 Sco some X-ray observations took place before the IR observations, so we extrapolate its shock velocity taking into account two different behaviours, a constant velocity as in the free expansion phase or the velocity following the same slope as in the three first days that correspond to an intermediate phase between I and II.

We assume that RS Oph had a similar evolution to V745 Sco the first hours after the outburst. In the next outburst of RS Oph, it would be very interesting to have these early observations in X-rays and IR. After day 4 after the outburst, the velocity of V745 Sco changed its tendency and started to decrease very fast. Moreover, this day the SSS phase started which involves a decrease in the density of the surrounding material. In RS Oph, the change occurred 6 days after the explosion, but this day does not correspond with the beginning of the SSS phase that started 26 days after the outburst. In both cases this change drives the velocity the radiative phase that is dominated by radiative losses (Truelove & McKee, 1999).

The analytical study of the shock velocity of RS Oph and its properties was done by Tatischeff & Hernanz (2007) who showed these two different phases before and after day 6 after the outburst (§ 3.3). Carrying out an analytical study for V745 Sco was more complicated because of the quality of the data. However, we proposed 3 different possible cases (§ 4.3.2) in which we took into account the previous study of § 4.3.

By determining the radius, we can compare the evolution of the shock plasma in each moment and understand better its properties. Figure 61 shows the shock radius as a function of time and the shock velocity as a function of the radius. When we compare

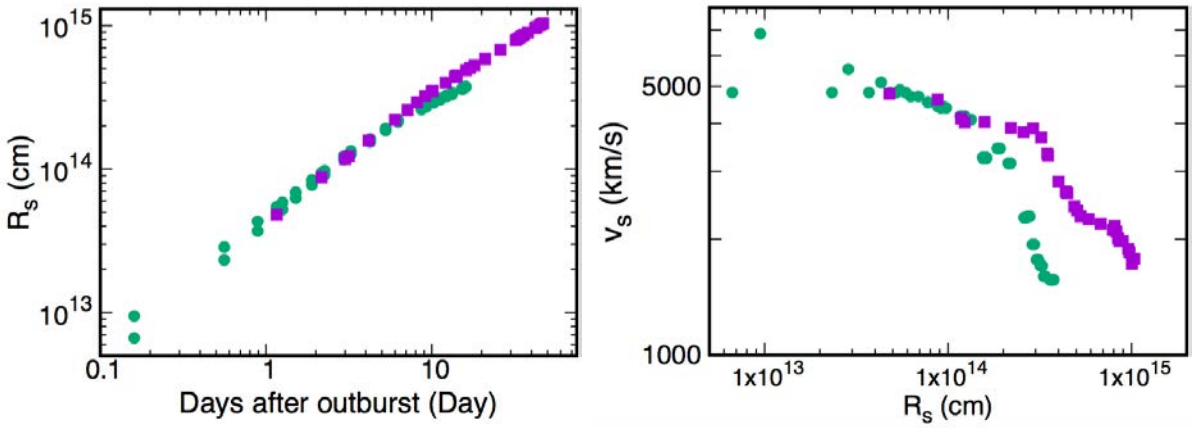

Figure 61: Left: Comparison shock radius as a function of time for RS Oph and V745 Sco. Right: Comparison of shock velocity as a function of shock radius for RS Oph and V745 Sco. RS Oph (purple squares) and V745 Sco (turquoise dots). Same data than Figures 27 and 49.

the v_s and the r_s, we can determine if there are changes in the v_s associated to the system separation, the radius of the beginning of the SSS phase, or the r_{out}.

In both novae, the radii increased rapidly the first week, and then, their increments were more moderate. The shock plasma crossed the system in the early hours before the first IR observation and we do not have any data on the slope change in the v_s at this time. We assume that there were no changes in the slope. However, for future outbursts, having IR observations in the first hours would useful for determining the radius of the nova. In the case of V745 Sco, the large change in the v_s slope appeared simultaneous to the appearance of the SSS phase at R_{SSS} $\sim$1.5$\times$10^{14}cm. However, the large change in RS Oph was on day 6 after the outburst at $R_s \sim 4 \times 10^{14}$ cm. On the other hand, in RS Oph, the radius corresponding to the day when the SSS phase appeared and the r_{out} are equal ($\sim$6$\times$10^{14} cm). The right panel in Figure 61 shows that there is a small plateau between 5- 8$\times$10^{14} cm, around day 30 after the outburst. In the case of V745 Sco, until day 16 after outburst, the radius is smaller than r_{out} ($\sim 8 \times 10^{14}$ cm). We do not have IR information after day 16. Thus, we do not know if V745 Sco has a plateau close to r_{out}.

We approximate the ejecta and the RG wind to an ideal spherical shell. With these simplifications, the volume of the shock material was obtained in both novae. The volume has the same behaviour as the radius. Both volumes increased faster the first week practically with the same slope, and after day 4, they began to differ because the volume of V745 Sco expanded slower than the volume of RS Oph.

With the EM we encounter the same problem as with v_s. We do not know the associated EM at the times of the IR observations. We interpolated their EMs for this times. The EM of both novae are very different taking into account the large uncertainties of V745 Sco. In V745 Sco, the EM was practically constant all the time and the volume increased as a function of time. Then, n_e should decrease faster the first four days

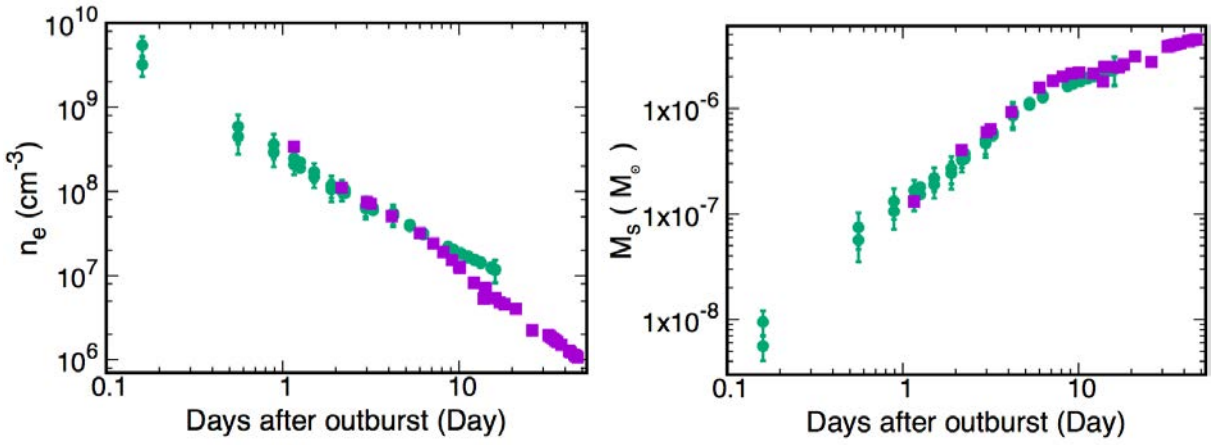

Figure 62: Evolution of the electron density and mass of the shocked plasma for the RS Oph (purple squares) and V745 Sco (turquoise dots). Same data than Figures 28 and 50.

and then slower to $\sim 10^7$ cm^{-3}. However, in RS Oph, the EM was practically constant before day 6 and after that it deceased with time, so n_e decreased faster after day 6. This implies that after day 6, n_e of RS Oph was lower than n_e of V745 Sco (Figure 62). As the mass density, ρ_H, is directly proportional to the electron density, then it followed the same behaviour over time.

The mass of the shock plasma has been defined by $M_s = \rho_H \times Vol_s$, for a hydrogen plasma. Therefore, the differences in the velocities (which propagate to the volume) and in the EMs (which propagate to the ρ_H) compensate each other making the M_s in both novae practically equal (Figure 62). The M_s detected before day 1 after the outburst was the same in both cases ($\sim 1\times10^{-7}$ $M_\odot$). We also assume that this M_s value is close to the M_{ej} in the case of V745 Sco, whose circumstellar material became transparent very soon. After this time, the shocked mass grew due to the RG wind sweeping, but slowly because of the decrease in the velocities. Around day 4 after the outburst, their M_s change slightly, but around day 10, they started to have practically the same behaviour again.

In addition to knowing the properties of the plasma through the X-ray observations, we can also get a better understanding of the properties of the RG wind as the density of the RG wind, as a function of the radius or the RG wind magnetic field. Tatischeff & Hernanz (2007) previously carried out a study on the RG wind density of RS Oph and its mass-loss rate ($(\dot{M}/u)_{RG\ RS\ Oph}=4\times10^{13}$ g cm^{-1}). We carry out the same kind of study in § 4.3.1 on the RG wind of V745 Sco obtaining a similar mass loss rate ($(\dot{M}/u)_{RG\ V745\ Sco}=(5\pm1)\times10^{13}$ g cm^{-1}). There is an important difference, in V745 Sco $N_H=[N_H]_{ISM}$ at $r_s=3.7\times10^{14}$ cm 16 days after the outburst and not when $r_{out}=7.8\times10^{14}$ cm. Equation 19 fits better the data if we use $r_{out}=r_s=3.7\times10^{14}$ cm. However, in RS Oph $N_H \geq [N_H]_{ISM}$ at r_{out}. To explain this difference between the novae, we propose different hypotheses. V745 Sco is the nova for which the SSS phase appeared earliest, 4 days after the outburst and it switched off 8 days later. As the SSS phase concluded 4 days before N_H reached the value of the interstellar medium,

then photoionization of the wind material by the super soft emission could significantly reduce its opacity.

Although the two novae are very similar, the beginning of the SSS phase is its main difference. Why this phase started so early in V745 Sco is something that is not clear. We expected some clear differences in the masses, but as we see in Figure 62, RS Oph and V745 Sco look very similar in practically all the magnitudes. This difference already hints that the ejected mass of RS Oph (10^{-6} $M_\odot$ (Das et al., 2006)) was larger than the ejected mass of V745 Sco (10^{-7} $M_\odot$ (Page et al., 2015b)) as we explained in § 5.2.2. Because they are in a symbiotic system and there is the RG wind around the system, the shocked mass obtained for the first day is not a good diagnosis of the ejected mass in the case of RS Oph. Otherwise their ejected masses would be the same (M_s=10^{-7} $M_\odot$ Figure 62). The influence of the RG wind material is more important than expected the first days after the outburst and it would be interesting to study its characteristics deeper. It can also be related to the geometry of the system, which in V745 Sco generates an irregular orbital period (§ 5.1) and can also be related to the fact that the v_s of V745 Sco decreased faster than the v_s of RS Oph. More information about the system is needed to know the reason of this difference between them.

5.4 HIGH ENERGIES γ-RAYS

A nova behaves as a miniature SN, whose whole evolution is observed in real time rather than only a portion of the evolution (Dubus, 2013). X-ray and γ-ray data are linked. The particle acceleration and heating are produce by the same source of energy, the kinetic energy of the shock, and the same source of particles, the swept-up material. The shock heats the material and radiates as thermal bremsstrahlung emission in X-rays. Accelerated particles (p and e^-) lose energy through inverse Compton emission and the p-p interactions. The combined study of thermal and non-thermal emission is a powerful tool to discriminate models. For example, γ-ray emission dominated by the pion decay needs high densities in order to accelerate a large number of protons and to produce a high number of p-p interactions. Thus, they tend to be less efficient than inverse Compton scattering. The γ-rays due to inverse Compton emission on the RG or nova light need less energy than in the case of the γ-rays due to pion decay, with a fraction of accelerated particles compatible with those derived from SNRs.

We obtain that ρ_w in both cases decreased over time. Figure 63 shows that the ρ_w of both novae are very similar until day 4, and after this day, they have different slopes. Moreover, we compare the magnetic field of the shock. They follow the same behaviour than the ρ_w. However, comparing the amplification produced by the interactions between accelerated particles and the shocked plasma, we state that the amplification of RS Oph was larger than in V745 Sco. A possible explanation for this difference is that in V745 Sco there was less material to produce the shock and therefore there were less interactions and less particles accelerated.

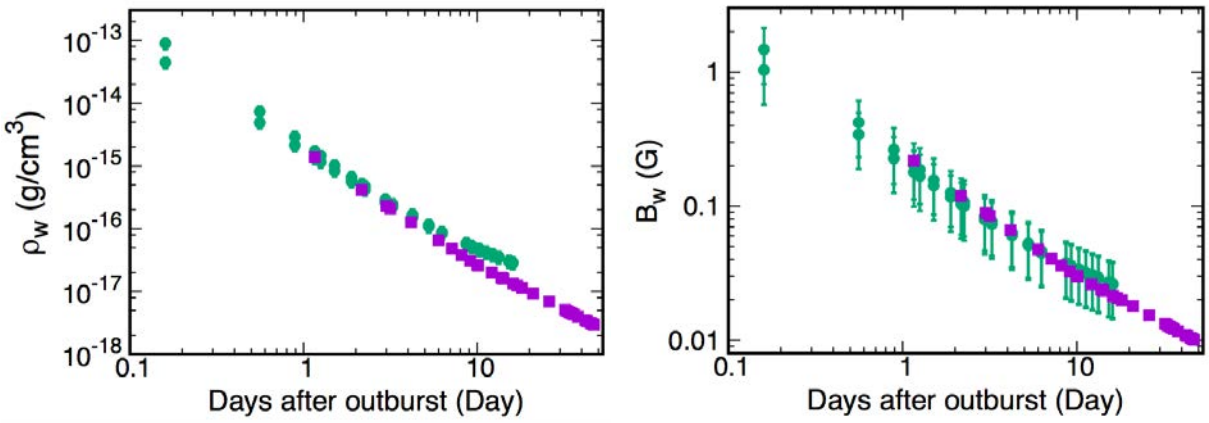

Figure 63: The density of the RG wind as a function of time (ρ_w) on the left and the magnetic field of the RG wind as a function of time (B_w) on the right. RS Oph (purple squares) and V745 Sco (turquoise dots).

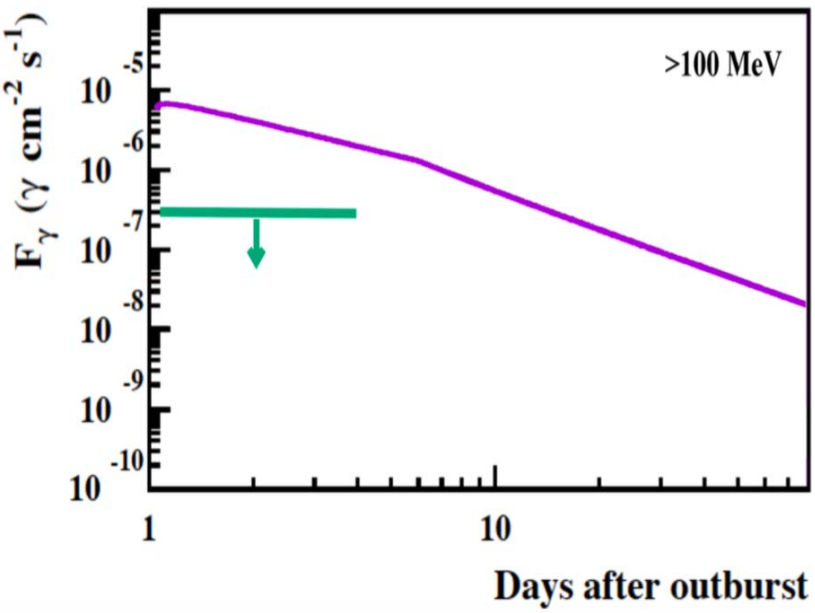

Figure 64: High energy γ-ray light curve expected for RS Oph (2006) (purple line) compared with marginal detection of Fermi/LAT for V745 Sco (turquoise line) (adapted from Hernanz & Tatischeff, 2012).

In RS Oph and V745 Sco, we have a RG wind magnetic field that was measured using synchrotron radio emission (Rupen et al., 2008; Kantharia et al., 2016) and can be related to the inverse Compton γ-ray emission. Moreover, we have a high density of particles in the shock that we have measured in X-rays. This high density of particles can also be related to the p-p interaction and therefore with the π^0 decay, because diffusive acceleration of particles can also be efficient in collisionless shocks (Tatischeff & Hernanz, 2007). In Figure 4, that represents the nova spectra detected by *Fermi*, we see that both mechanisms, hadronic and leptonic, fit correctly the data of the novae detected by *Fermi*. Taking into account that other wavelengths, as radio emission, show a mix of thermal and non-thermal emission, then γ-ray emission can be due to both hadronic and leptonic mechanisms.

The marginal (2 - 3σ) detection of V745 Sco by *Fermi*/LAT in its last outburst (Cheung et al., 2014, 2016b) does not provide us to with a spectrum to determine its nature. This nova is at $\sim$8 kpc that is the largest distance among all novae detected by *Fermi*/LAT (Table 1). However, in RS Oph, for which there was no detection at E>100 MeV, Tatischeff & Hernanz (2007) state that particle acceleration in a diffusive shock could explain the discrepancies between the shock velocity obtained from IR lines and from the X-ray temperatures. Because of the plethora of observations in the last outburst, Tatischeff & Hernanz (2007) could obtain the theoretical π^0 γ-ray spectra and its light curve. In V745 Sco, we have less information. Figure 64 shows the high energy γ-ray light curve predicted for RS Oph compared with the flux detected with *Fermi* for V745 Sco. The difference in the fluxes can be explained with the differences in their distances.

In the future, using our study and applying the model for plane-parallel steady state shocks used by Ellison et al. (2000) as Tatischeff & Hernanz (2007), it will be possible to build the γ-ray spectrum of V745 Sco and to know the nature of its high energy γ-ray emission. In any case, we can be sure that both mechanisms will play a role in it.

6

CONCLUSIONS

The aim of our thesis is to study the evolution of the symbiotic recurrent novae the first days after the outburst and the nature of their emission. The present thesis work has been aimed at performing a comprehensive multiwavelength study of the last outburst of RS Oph and V745 Sco. We have focused on the early X-ray observations by *XMM-Newton*, *RXTE*, *Swift*, and *Chandra*, but also radio, IR and γ-ray emissions in the first days after the outburst. Thanks to the fast action of the X-ray satellites, especially *Swift*, novae are detected in X-rays a few hours after the explosion. This fact together with the high resolution of some of the instruments on board of the satellites allow us to know the evolution of the shocked plasma from the early stages, improving the knowledge of the thermal plasma parameters, as the temperature and the EM, and its composition. Multiwavelength results concerning the shock between the ejecta and the RG wind the first weeks after the nova outburst, provide new insights into the evolution of the shocked plasma and the interaction with the circumstellar material. In addition, the combined study of X-ray, radio, IR and γ-ray emissions is a powerful tool to know the nature of the γ-ray emission. With the study of RS Oph and V745 Sco, and its comparison, we can extrapolate these results for all symbiotic recurrent novae.

In this chapter we summarize the main results that we have obtained in each of the chapters, as well as the work planned after this thesis.

RS Oph

We have carried out a new analysis of the early X-ray emission from RS Oph by *XMM-Newton*. The analysis of the EPIC/MOS1 data on day 13.8 has been realized for the first time. Moreover, we carry out a reanalysis of the EPIC/MOS1 observations on day 26.1 and the RGS data on both days. In addition, taking into account the previous study of the *RXTE*/PCA observations (Sokoloski et al., 2006), we have reanalysed them to obtain the evolution of the EM. With these two analyses together with the study of the *Swift* observations (Bode et al., 2006) and the previous studies of *XMM-Newton* and *Chandra* (Nelson et al., 2008; Ness et al., 2009; Drake et al., 2009), we have obtained a global picture of the evolution of the different properties of the plasma as the temperature, the N_H, the EM and the flux. Moreover, with the EM distribution, we know that the first days most of the material was hot, but over time, most of the material cooled down.

In our multiwavelength study, we took into account the radio and IR emission. The radio spectra revealed the double nature of the RS Oph radio emission, free-free and synchrotron emission, using the fluxes obtained by different radio telescopes in different

frequencies. Moreover, and thanks to the high angular resolution of the radio images, we know that the synchrotron emission was produced by the shock. The IR observations give us an appropriate measurement of the shock velocity. Therefore, we assume that the shock velocity was practically constant before day 6 after the outburst, and after this day, it decreased as expected for a well-cooled shock. The IR, X-ray and radio information give us the evolution of the properties of the shocked plasma and also the density and the magnetic field of the RG wind. We also showed the need for an amplification of the RG wind magnetic field to reach the magnetic field measured by Rupen et al. (2008), proving particle acceleration. The study of Tatischeff & Hernanz (2007) showed that the differences between IR and X-ray velocities are due to the escape of accelerated particles, and therefore, there was particle acceleration in RS Oph. With the information obtained with MOS1, we conclude that there was a slightly larger injection of particles than that obtained by Tatischeff & Hernanz (2007) to reproduce MOS1 temperatures.

V745 Sco

We have focused on the analysis of the X-ray observations of V745 Sco obtained by *Swift* and *Chandra*, deducing some shocked plasma parameters, as the temperature, the N_H, the EM and the flux, the first two weeks after the outburst, and also its composition after the SSS phase, thanks to the high spectral resolution of *Chandra*. A global view of the plasma evolution was obtained using the additional information given by *NuStar* (Orio et al., 2015).

We used the shock velocity obtained in IR together with the EM obtained in X-rays to determine the evolution of different parameters of the shocked plasma. Moreover, we showed the importance of the companion to understand the nature of the γ-ray emission. A good determination of the absorption produced by the RG wind would allow us to know density and the magnetic field of the RG wind, and therefore, the amplification produced by the particle acceleration. We have also studied the different phases of the evolution, and as in the case of RS Oph, V745 Sco skipped Phase II. This rapid cooling have also a relationship with the particle acceleration.

The marginal observation by *Fermi*/LAT, together with the differences between the shock velocity obtained in X-rays and in IR that, as in case of RS Oph, can be understood only if a fraction of the shock energy went into cosmic rays (Decourchelle et al., 2000), indicating that there was particle acceleration in V745 Sco. We could not prove the nature of the dominant process in the particle acceleration, but thanks to the multi-wavelength study we can state that both processes (hadronic and leptonic) were present.

Common characteristics and differences of the two systems

RS Oph and V745 Sco differ in some important aspects but other parameters are much more similar than on would expect.
IR emission is similar in both novae. The first days a constant shock velocity was observed. However, the big difference between them is the day at which the shock velocity

changes its slope. This affects other properties such as the radius or the volume. In radio both novae have the same flat spectra, therefore, we know that in both systems there was thermal and non-thermal emission. In RS Oph was observed two maxima. However, in V745 Sco, there was a period of time with no radio observations and the first maximum was probably missed.

Swift observations and their analysis allow us to deduce the possible behaviour of the temperature, the EM, and the flux the first hours after the outburst of RS Oph. The N_H is different between them, which is probably related, together with the low M_{eje}, to the rapid onset of the V745 Sco SSS phase. Moreover, we compare the properties of the plasma obtained with the IR shock velocity and the X-ray emission measure, and we show that the volume, the electron density and the mass density are similar before day 6, assuming that the behaviour of RS Oph was the same as V745 Sco's before day 3 after the outburst. The obtained shocked mass looks practically the same over time. The influence of the RG wind and the geometry of the system in the shocked mass is larger than expected, because otherwise, the ejected mass of V745 Sco and RS Oph would be the same, and we know that the ejected mass of RS Oph must have been larger. More information about the orbital period and the RG wind is needed.

Comparing the amplification in the RG wind magnetic field produced by the interactions between shocked plasma and accelerated particles, we state the amplification of the RS Oph RG wind magnetic field was larger than that of V745 Sco. V745 Sco has less ejected mass than RS Oph to shock with the RG wind, and therefore, there were less interactions and less particles accelerated. The RG wind magnetic field of both novae was measured in radio, yielding values that indicate inverse Compton γ-ray emission, and a high particle density related with the π^0 decay γ-ray emission. Taking into account all the information and the spectra detected by *Fermi* for other novae, we state that both mechanisms are involved in the γ-ray emission of novae. However, as $\dot{M}_{RG}/u_{RG}$ of V745 Sco is similar to the $\dot{M}_{RG}/u_{RG}$ of RS Oph obtained by Tatischeff & Hernanz (2007), and also its ρ_w, we conclude that the dominant process in both novae is the π^0 decay.

6.1 FUTURE WORK

The work presented in this thesis provides powerful tools to unveil the nature of the high energy γ-ray emission in the symbiotic recurrent novae. Using our study and applying the model to plane-parallel steady state shocks used by Ellison et al. (2000), it will be possible to build the γ-ray spectrum of the recurrent novae and to know their nature. As we mentioned in Chapter 3, this method was used by Tatischeff & Hernanz (2007) in the case of RS Oph. However, our new analysis can help to improve their study. Moreover, applying Ellison et al. (2000)'s model into our V745 Sco study will allow us to know better its high energy emission of which only an upper limit was measured.

With this work the shock evolution in the RS Oph-like novae is better understood. In the next outburst of RS Oph (2015-2032?) and V745 Sco (2039), and the other

members of their group, T CrB (2026) and V3890 Sgr (2018), we will be able to have a more complete study, if more observations are obtained.

- First of all, X-ray observations during the first hours after the outburst as in the case of V745 Sco are necessary to correctly characterize the plasma evolution. RS Oph and T CrB are at ∼1.6 and ∼1.3 kpc respectively, therefore, early X-ray observations will have a better resolution than those obtained in V745 Sco. With these observations, we expect to have a good determination of the free expansion phase in X-rays. But for that, it would be necessary to have a satellite that point as fast as *Swift*.

- Second, to have early IR observations simultaneous to the X-ray observations will allow us to have a better determination of the electron density and the mass of the shocked plasma, and to understand better their evolutions.

- Third, to have a good monitoring in radio will allow us do not lose any maxima and understand better its relationship with the free expansion phase. Moreover in the case of T CrB, that is close enough, to obtain good images will allows us to observe the evolution of the plasma in real time as in RS Oph.

- Finally, to observe with *Fermi* RS Oph, T CrB and V3890 Sgr in the next outburst will be very important to confirm our predictions. Moreover, to observe these novae with the new generation of telescopes as *ASTROGAM* that will have an energy range below the energy range of *Fermi*, will help us to know the true nature (hadronic and/or leptonic) of the emission at high energies.

These observations would be very useful, not only in recurrent symbiotic novae, but also in the next classical nova outbursts. These observations will allow us to understand better the shocked plasma in classical novae and to know the mechanisms that produce the particle acceleration in them.

APPENDIX

A

TELESCOPES

A.1 XMM-NEWTON SATELLITE

The X-ray Multi-Mirror Mission *XMM-Newton* (Jansen et al., 2001) was launch on Decembre 10th, 1999 and it is the second of ESA's four "cornerstone" missions defined in the Horizon 2000 Programme. It was launched with a highly elliptical orbit with an apogee of 144000 km and an orbital period of 48 hours. It has two different types of telescopes: three Wolter type-1 X-ray telescopes with different X-ray detectors and a 30-cm optical/UV telescope.The scientific payload of *XMM-Newton* is composed by three EPIC imaging X-ray cameras, two Reflection Grating Spectrometer (RGS) grating X-ray spectrometers (den Herder et al., 2001) and Optical/UV Monitor (OM) camera (Mason et al., 2001). The configuration of the spacecraft is shown in fig. 65. *XMM-Newton* allows us to have high sensitivity X-ray images and a moderate spectral resolution with the EPIC cameras and a high resolution X-ray spectra with the RGS of the same sources.

The three Wolter Type-I X-ray telescopes of *XMM-Newton*'s are composed by 58 thin nested mirrors shells, that makes *XMM-Newton* have the largest effective area, 4650 cm^2 in total. Its three X-ray telescopes are co-aligned with a relative astrometry between the three EPIC cameras calibrated to better than 1-2" across the Field of view (FOV). The EPIC cameras are at the focal plane of the telescope. The RGS are mounted in the light path of the EPIC Metal Oxide Semiconductor (MOS) cameras diffracting part ($\sim$ 40%) of the incoming radiation onto their secondary focus. Nevertheless, the OM has its own telescope (Longinotti, 2013).

The most important characteristics of *XMM-Newton* are:

- The simultaneous operation of all scientific instruments. It gives simultaneous information on two widows of the electromagnetic spectrum: X-ray and optical/UV. They can be operated independently and in different modes of data acquisition.
- High sensitivity. It is one of the most sensitive X-ray observatories, with a mirror effective area at 1 keV more than 5 times larger than *Chandra* and 11 times larger than ROSAT.
- Good angular resolution. The point-spread function (PSF) has a FWHM around 6", while *Swift* is 8.8" and *NuStar* 18".
- Moderate (EPIC cameras) and high (RGSs) spectral resolution.

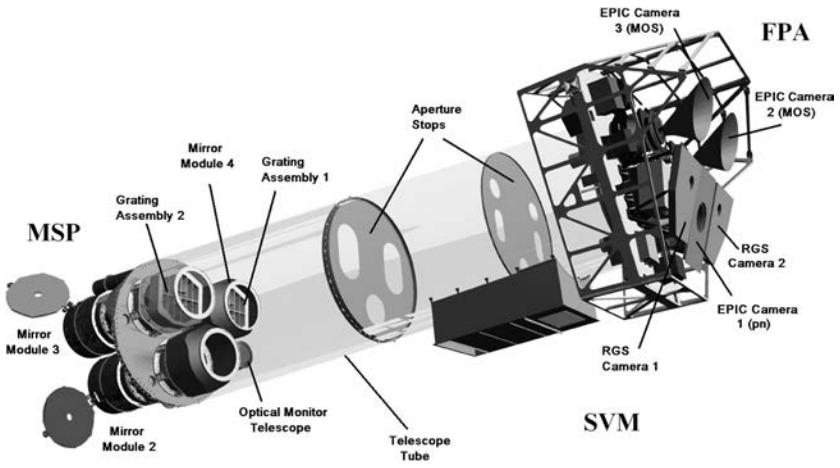

Figure 65: View of the *XMM-Newton* spacecraft subsystems, with external shrouds and structure removed for clarity (from Lumb et al., 2012).

- Long continuous target visibility. Its elliptical orbit allows of the order of 40 hour of visibility per orbit.

A.1.1 *European photon imaging camera (EPIC)*

In *XMM-Newton*, two of the three X-ray telescopes use EPIC MOS CCD arrays and the other uses EPIC pn CCDs. These CCDs give the possibility to perform extremely sensitive imaging observations over a FOV of 30' in the energy range from 0.2 to 12 keV. Moreover, they have a moderate angular resolution ($\sim$ 6" FWHM;$\sim$ 15" HEW (Half Energy Width)) and spectral resolution (E/Δ E$\sim$20-50). The intrinsic energy resolution of the pixels allows for the simultaneous acquisition of an image and a spectrum. For all the cameras, the sensitive area of the detector is about 30' across.

All EPIC CCDs operate in photon counting mode that produce a readout frequency-dependent event list. This event list contains a list of all photons with their time of arrival, position on the camera and energy. Thanks to that, we can extract images, light curves and spectra. The CCDs have different data acquisition modes: Full frame, extended full frame, large window, small window, timing and burst mode. Furthermore, the CCD cameras are also sensitive to IR, optical and UV photons, for this reason, filters are needed to block these wavelengths in order to obtain X-ray images without contamination. One of the three filters is needed (thin, medium or thick) depending on the X-ray flux of the object. The two types of EPIC cameras are different, not only in their chip geometry, but also in other properties such as a their readout times or how they are illuminated. We will focus in the EPIC MOS camera.

EPIC MOS camera The EPIC MOS camera are formed by 7 individual identical front illuminated MOS chip arrays. As we mentioned before, the MOS cameras are in the same X-ray telescope as the RGS instrument, and as a consequence of that, they only receive 44% of the reflected light. The individual CCDs are not in the same plane, but

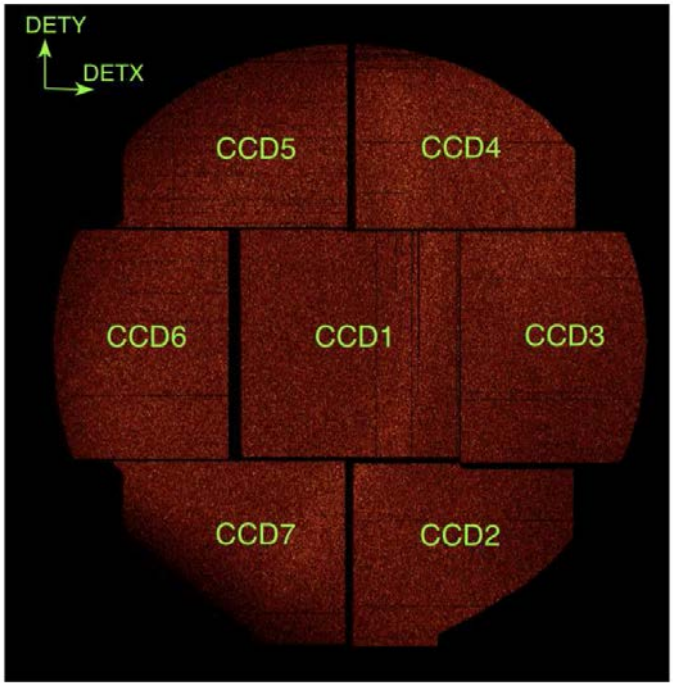

Figure 66: View of the MOS1 camera with the number of the CCD of the calibrated event list files (from Longinotti, 2013).

have a small curvature similar to that of the focal surface of the telescope, so that the central chip is behind the ring formed by the other 6 chips. The MOS chips have a frame store region that is used as a data buffer for storage, while the other chips are ready for a new exposure.

A.1.2 *Reflection grating spectrometer (RGS)*

The Reflexion Grating Spectrometers consists of the Reflection Grating Assembly (RGA) mounted behind the mirror module. As two of the three X-ray telescopes have the RGA in their paths, only a 40% of the X-ray photons are diffracted to RGS Focal Camera (RFC). RFC is a linear array composed by 9 MOS CCD chips. These chips are back-illuminated to increase the soft energy response and they are aluminium-coated on the exposed side to minimize the effect of optical/UV light. Both spectrometers cover the same FOV and when they are in the dispersion direction, the aperture of RGS covers the entire FOV of the mirrors while the effective area declines significantly for off-axis sources. The zero-order image of RGS is not visible on the detector for an on-axis source.

RGS have high X-ray spectral resolution (from 100 to 500, FWHM) and spectrophotometry, in the energy range 0.33 - 2.5 keV (5 - 38 Å). There are H-like and He-like transitions of light elements like C, N, O, Ne, Mg and Si, and also the L-shell transitions of heavier elements as Fe and Ni.

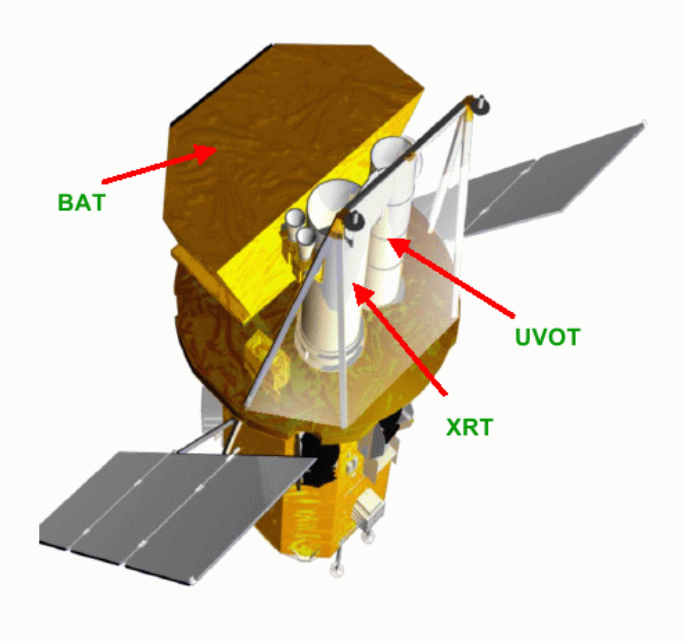

Figure 67: *Swift* Satellite (Adapted from Gehrels et al., 2004).

A.2 SWIFT SATELLITE

The *Swift* satellite (See Gehrels et al. (2004) for a general description) is a multi-wavelength mission designed to detect Gamma-Ray Bursts (GRBs). It was launched on November 20, 2004 and is part of NASA's Medium Explorer program. It has three instruments, BAT, XRT and UV/Optical Telescope (UVOT), to observe GRBs simultaneously. Thanks to that we have observations in the γ-ray, X-ray, UV and optical bands. *Swift* is continuously monitoring the sky with the wide-field hard X-ray BAT (Barthelmy et al. (2005)). It is used for the detection of GRBs and XRT (Burrows et al. (2005)) for their follow-up. *Swift* is available for other scientific investigations, as novae, in the time between GRB events. *Swift* has two important characteristics: its fast re-point when it discovers a GRBs and its flexibility. These two characteristics allow us to have observations only some hours after the outburst.

A.2.1 *Burst alert telescope (BAT)*

The BAT was designed to make an all-sky hard X-ray survey and monitor the hard X-ray transients. BAT detects GRBs, it obtains its position in the sky and, finally, it sends the position to the ground telescopes that can quickly follow-up them. BAT runs in two modes: burst mode, which finds the position of the burst, and survey mode, which produces hard X-ray survey data and is the mode it spends most of the time in.

BAT telescope has an energy range between 15 to 150 keV for imaging with a noncoded response up to 500 keV. It has a large FOV instrument created to obtain critical GRB triggers and 4' positions. BAT is composed of a coded-mask with a 1.4 sr FOV and a large-area solid state detector array. The FOV of BAT includes the XRT and UVOT

FOVs. These make that BAT can study many different sources and simultaneous with XRT and UVOT telescopes. BAT has a FWHM of 17' for individual images when corrected to infinite distance, a background event range of 17,000 events/s, a sensitivity of $\sim 10^{-8}$ ergs cm^{-2} s^{-1} and an instrumental angular resolution of 20' FWHM.

A.2.2 *X-ray telescope (XRT)*

XRT telescope was created to measure the fluxes, spectra and light curves of GRBs and afterglows. It uses a grazing incidence Wolter 1 telescope to focus X-rays onto the the CCD detector that is the same than the EPIC MOS instrument of *XMM-Newton*. It has an energy range between 0.2-10 keV, a 110 cm^2 effective area, a 23' FOV and a 18" resolution. XRT supports three readout modes necessary to cover a dynamic range and fast variability of GRB afterglows. These are imaging mode, windowed timing mode and photon-counting mode.

- The Imaging Mode (IM) mode produces an integrated image but does not permit spectroscopy. It is only to position bright sources $>7 \times 10^{-7}$ ergs cm^{-2} s^{-1}.
- Windowed Timing (WT) mode does not give information about the position but has a high time resolution (2.2 ms) and spectroscopy through fast CCD readouts. It is useful for sources $\sim 7 \times 10^{-7}$ ergs cm^{-2} s^{-1}. WT mode data should not be affected by pile-up if the intensity is below 100 count s^{-1}.
- Photon-Counting (PC) mode uses subarray windows to permit full spectral and spatial information about sources with fluxes between 2×10^{-14} to 2×10^{-11} ergs cm^{-2} s^{-1}. PC mode data should have pile-up if the count rate is larger than 0.5 count s^{-1}.

A.3 CHANDRA SATELLITE

The *Chandra* X-Ray Observatory was designed to detect X-ray emission from very hot regions of the Universe (Weisskopf et al., 2003). It was launched on July 23, 1999 as one of NASA's "Great Observatories". It was launched with a highly elliptical orbit with an apogee of 134527 km and allows to observe continuously for up to 55 hours of its 64-hour orbital period. The Wolter Type-I X-ray telescopes of *Chandra* is composed by 4 pairs of nested mirrors with diameters of 65 cm, 87 cm, 99 cm and 123 cm together with their supporting structure, the High Resolution Mirror Assembly (HRMA). They have a thick substrate of 2 cm thick glass with a reflecting iridium surface of 33 nm. The thick substrate makes that the $\sim$90% of the X-ray photons is focused into a 1 arcsec circle, but at the same time, the thick substrate makes that *Chandra* has a low collecting area compared to *XMM-Newton*. *Chandra* has an angular resolution of 0.5 arcsec that is 1000 times better than the resolution of the first orbiting X-ray telescope.

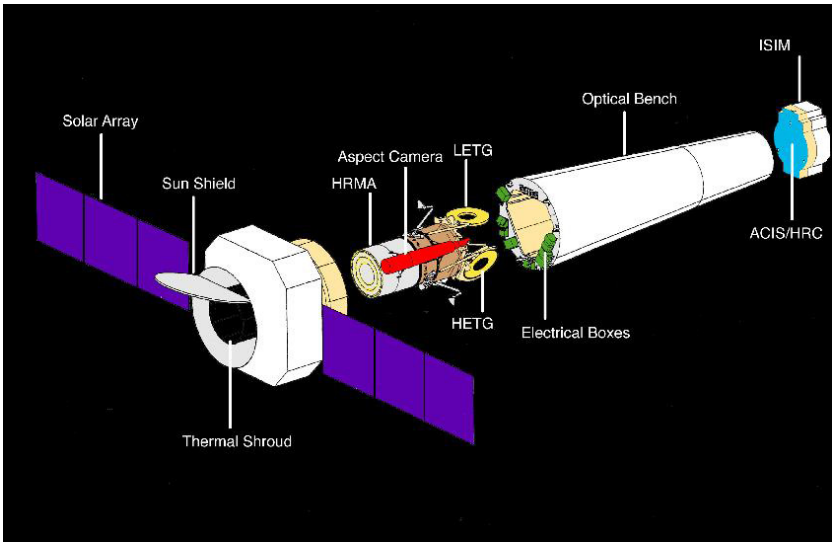

Figure 68: Schematic of the *Chandra* spacecraft with an exploded view of the science instruments. Image credit: NASA[1].

Chandra has four scientific instruments (Figure 68)[1]. In the science instrument module (SIM) at the focal plane there are two of them, Advanced CCD Imaging Spectrometer (ACIS) and High Resolution Camera (HRC). In the optical path behind the mirrors, the two grating spectrometers are located: Low Energy Transmission Grating (LETG) (Brinkman et al., 2000) and HETG (Canizares et al., 2000). The HRMA can only focus onto one of the two instruments ACIS or HRC, because only one detector can be on the focal plane at the same time. We will focus in the high resolution spectrometers.

A.3.1 *The high resolution spectrometers*

As we mentioned before, there are two instruments used to obtain high resolution spectra HETG and LETG. They do not work simultaneously, because only one of them can be behind the mirrors. They are made up of hundreds of gold transmission gratings. These gratings diffract the X-rays and one of the cameras in the focal plane (ACIS or HRC) detects them. The gratings are located into a toroidal ring structure matched to the mirrors. The high resolution spectrometers help us to study individually the lines and have information about the temperature, ionization or the chemical composition of the sources.

The LETG have a gold grating period, or spacing, of $1\mu m$. It is optimized for the energy band between 0.007 to 0.2 keV and its resolving power is >1000. In general LETG is combined with HRC-S to obtain high spectral resolution data.

The HETG have two periods, $0.2\mu m$ for the HEG and $0.4\mu m$ for the MEG. The X-ray are diffracted in a "X" pattern at the focal plane to be able to distinguish between

1 http://chandra.harvard.edu/about/science_instruments.html

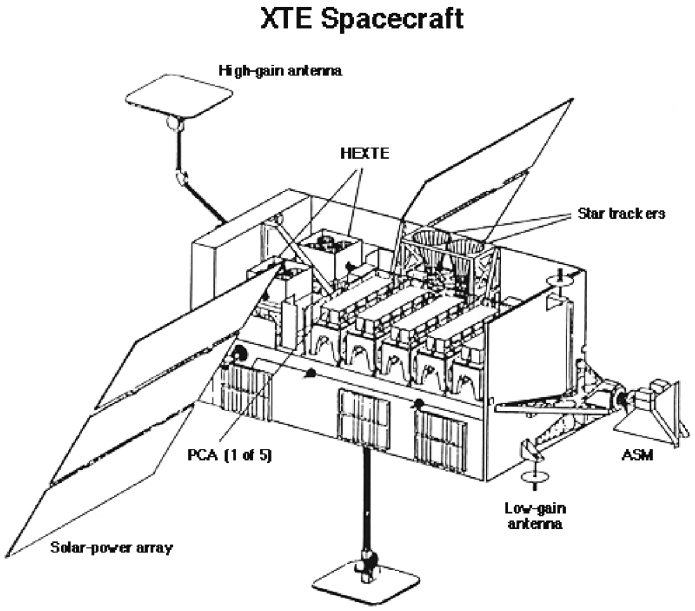

Figure 69: Diagram of the *RXTE* spacecraft, with instruments labelled. Image credit: NASA[3].

the two types. It is optimized for the energy band between 0.4 to 10 keV and is usually used with ACIS-S, which was developed as a readout for the HETG. The resolving power ($E/\Delta E$) can vary from 800 at 1.5 keV to 200 at 6 keV.

A.4 RXTE SATELLITE

Rossi X-ray Timing Explorer (RXTE)[2] was designed to observe the time variation of astronomical X-ray sources (Jahoda et al., 1996). It was launched on 30 December 1995 as part of the Explorer program of NASA and ceased their scientific operations on 3 January 2012. Its circular orbit at 382 km allowed to have a period of 92'. RXTE had three instruments (Figure 69)[3], the All Sky Monitor (ASM), the PCA and the High-Energy X-ray Timing Experiment (HEXTE).

The ASM[4] had three wide-angle shadow cameras with Xenon proportional counters which were sensitive to the position. It had a total collecting area of 90 cm^2 and its time resolution allowed us to observe 80% of the sky every 90'. Its energy range was between 2 to 12 keV.

The PCA[5] was an array of five proportional counters with an energy range between 2 to 60 keV. Its energy resolution was less than 18% at 6 keV and its time resolution was $1\mu s$ which allowed us to observe the time variation of the X-ray sources. It had a collecting area of 6500 cm^2.

2 https://heasarc.gsfc.nasa.gov/docs/xte/XTE.html
3 http://cass.ucsd.edu/hexte/hexte/hexte_pictures.html
4 https://heasarc.gsfc.nasa.gov/docs/xte/ASM.html
5 https://heasarc.gsfc.nasa.gov/docs/xte/PCA.html

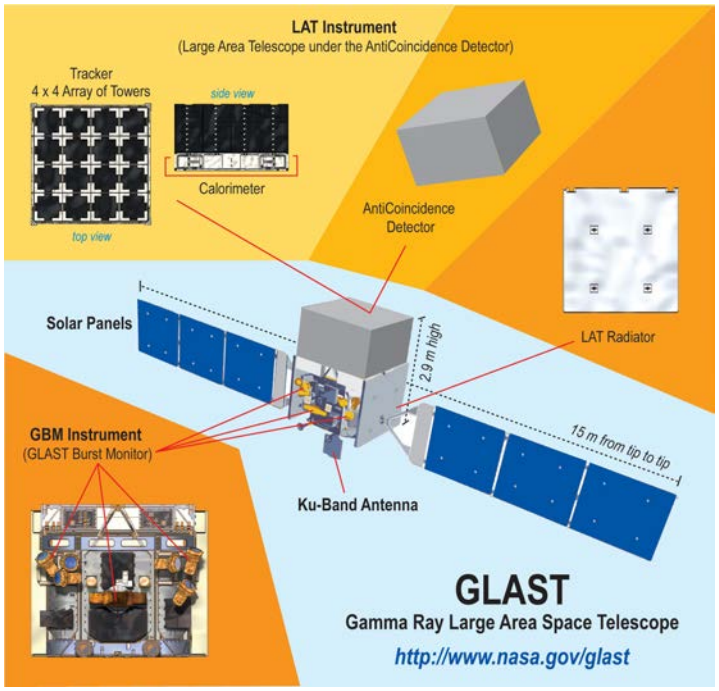

Figure 70: Diagram of the *Fermi* spacecraft, with instruments labelled. Image credit: NASA/Sonoma State University/Aurore Simonnet

The HEXTE[6] was composed of two clusters containing four phoswich scintillation detectors. The clusters provided an observation every 8 μs to detect time variability in the sources. It had an energy resolution of 15% at 60 keV. Its energy range was between 15 to 250 keV and its sensitivity was around 360 count/s per cluster.

A.5 FERMI

The *Fermi* satellite, previously called Gamma-ray Large Area Space Telescope (GLAST), was launched on 2008 by NASA. It was named in honour of professor Enrico Fermi who was a pioneer in high-energy physics. *Fermi* is a multi-agency space mission that studies the cosmos between 10 keV - 300 GeV and improves other missions at high energies as the Compton Gamma Ray Observatory (CGRO). It is a γ-ray observatory whose aim is to explore the most extreme environments in the Universe, explain the mysteries of the dark matter and the GRBs and also give an answer about how black holes accelerate immense jets of material or the origin of the cosmic rays. *Fermi* is in a low-Earth circular orbit at 550 km and at an inclination of 28.5 degrees. It has 2 instruments, the Large Area Telescope (LAT) and the Gamma-ray Burst Monitor (GBM) (Figure 70).

LAT is composed of a 4 x 4 array of identical towers. Each tower is formed by a tracker, a calorimeter and a data acquisition module (Atwood et al., 2009). The tracking detector have 18 xy layers of silicon strip detectors. The calorimeter was built with 8 layers of 12 CsI bars and permits to measure the three-dimensional profiles of showers.

6 https://heasarc.gsfc.nasa.gov/docs/xte/HEXTE.html

It has an energy range between 20 MeV and 300 GeV. Its angular resolution is less than 3.5^o around 100 MeV and less than 0.15^o at energies larger than 10 GeV.

GBM has two detectors composed of two different types of scintillators. One has 12 sodium iodide (NaI) scintillators and is sensitive between a few keV and about 1 MeV. The other detector has 2 cylindrical bismuth germanate (BGO) scintillators and cover the energies from 150 keV to 30 MeV, giving a good overlap with the NaI detector and LAT. Its FOV is all the sky except the part occulted by the Earth and the final GRB location is around 3^o.

B

DATA REDUCTION

B.1 XMM-NEWTON DATA REDUCTION (SAS)

The *XMM-Newton* data were reduced with Standard Analysis System (SAS) (v 13.5.0). We did two different processes depending on the instrument. First, the data reduction of EPIC/MOS camera which was quite complex due to the pile-up and second, the data reduction of RGS.

B.1.1 *EPIC/MOS camera*

We are focused on the observations made by the EPIC/MOS1 whose image was made using the small window mode (Figure 71). We processed the original Observation Data Files (ODFs) and used standard SAS routines for the extraction of MOS spectra for point-like sources.

The background in the EPIC cameras can be of two types: a cosmic X-ray background (CXB), and instrumental background. The spectra is filtered of intervals with flaring particle background, creating a Good Time Interval (GTI) filter table. To have this GTI, we need a count rate lower than 0.1 counts/sec.

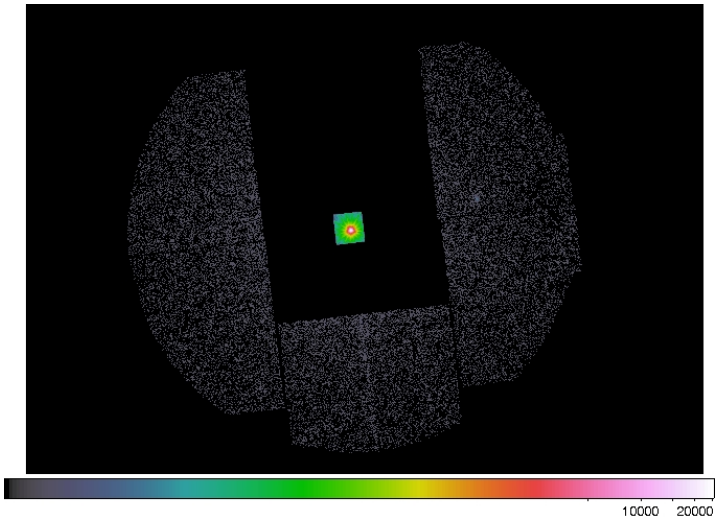

Figure 71: EPIC/MOS1 camera image of RS Oph on day 13.8 after the outburst, using the small window mode.

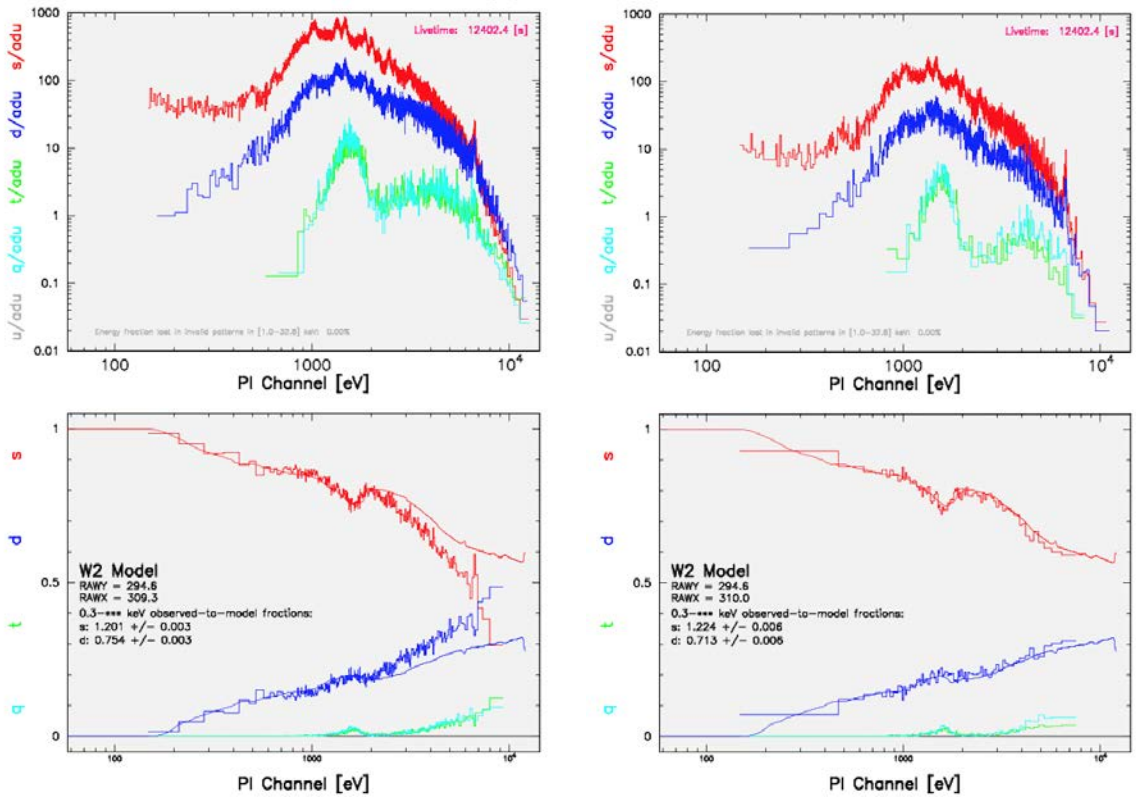

Figure 72: `epatplot` output file. The left panels indicate the presence of pile-up and the right panels indicate a negligible pile-up fraction using an annular extraction region with an inner radius of 350 pix on day 13.8 after the outburst. The upper panels show a spectrum distribution for each event pattern class. The lower panels show the expected pattern distribution functions (smooth solid lines) superimposed on the observed ones (histogram) for single (red), double (blue), triple (green) and quadruple (cyan) events.

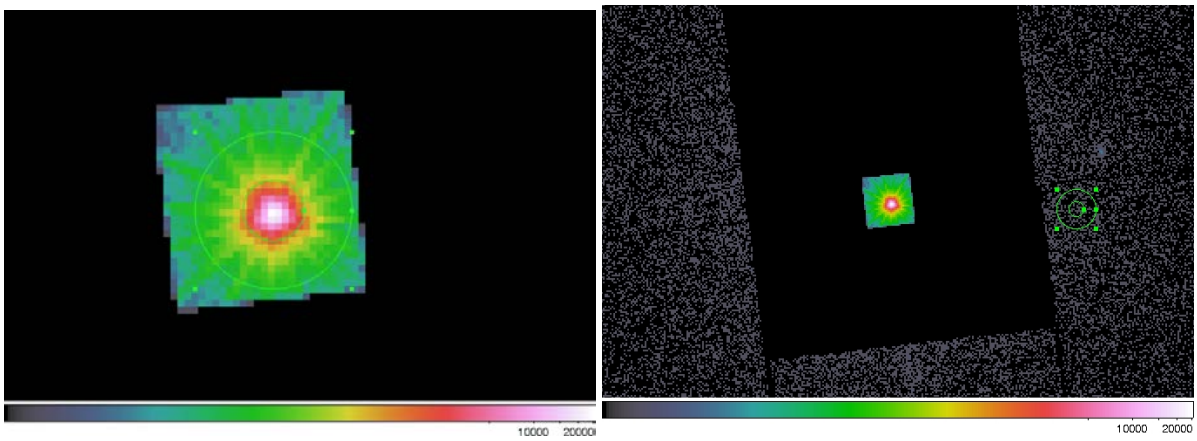

Figure 73: An annulus region (green circle) around the source, eliminating the central part to avoid the pile-up (left) and the same area to extract the background (right).

If the source is very bright, as is the case of the EPIC/MOS1 image of RS Oph in the last outburst, we can have pile-up in the MOS observations and some additional reduction steps are. Photon pile-up is the arrival of more than one X-ray photon in one camera pixel or in adjacent pixels before it is read out. It can affect the PSF and the spectral response of EPIC. The PSF is modified by pile-up because many photons arrive at the same time to the core of the PSF. These photons create multi-pixel photon patterns and are rejected by the onboard event reconstruction software. The problem in the case of the spectral response is that the charge deposited is larger than one photon and it creates artificial "hard" photons where there have been two or more "soft" photons. To extract the spectrum, we use the `emproc` command and only selected events with pattern 0 to help to avoid the pile-up.

The Standard Analysis System (SAS 13.5.0) has the `epatplot` command that can be used as a diagnostic tool for estimating the level of pile-up. With this tool, we can compare the observed and expected distributions of event lists and quantify the pile-up of the observation. First of all, we estimate the pile-up using a circle region that includes the whole source. The left bottom panel of Figure 72 shows the big differences between the expected and the observed pattern distribution function at PI Channels larger than 2 keV. To correct more efficiently the pile-up, we did different tests using annular extraction regions. This annular extraction allows to extract photons from the inner regions of the PSF even if we lose information. The right bottom panel of Figure 72 shows that the expected and the observed pattern distribution function are the same on day 13.8, using an inner radius of 350 pix and an external radius of 900 pix. For the image of day 26.1 after the outburst an inner radius of 300 pix was used. The same area was extracted away fromthe source to obtain a background spectrum (Figure 73).

For spectral analysis, we generate a redistribution matrix (`rmfgen` command) and an ancillary file (`arfgen` command). Finally, the spectrum was binned using the `specgroup` command to include 30 counts per bin and link the spectrum with the associated files.

B.1.2 *RGS*

In the case of RGS observations, we have extracted the spectra with the SAS task `rgsproc`. We have filtered the RGS observations affected by periods with a high particle background. It is unusual that this instrument has pile-up but when the spectrum is very bright (flux $\sim 1.5 - 3 \times 10^{-10}$ erg cm^{-2} s-1), as in the SSS phase, it can be possible. This is the case of the RGS observations of RS Oph during the SSS phase of its last outburst (Ness et al., 2007b).

The effects of pile-up on RGS spectra are the migration of photons from first to second order. If some individual CCD has a total count rate of 12 counts s^{-1} in RGS 1 and 6 counts s^{-1} in RGS 2, then this observation is affected by 2% of pile-up. There is no analogous tool to `epatplot` in SAS for this instrument to estimated the pile-up. For this reason, in Table 11 of Longinotti (2013), there is an estimation of the fluxes in the individual RGS1 and RGS2 CCDs for which a 2% of pile-up is expected in point

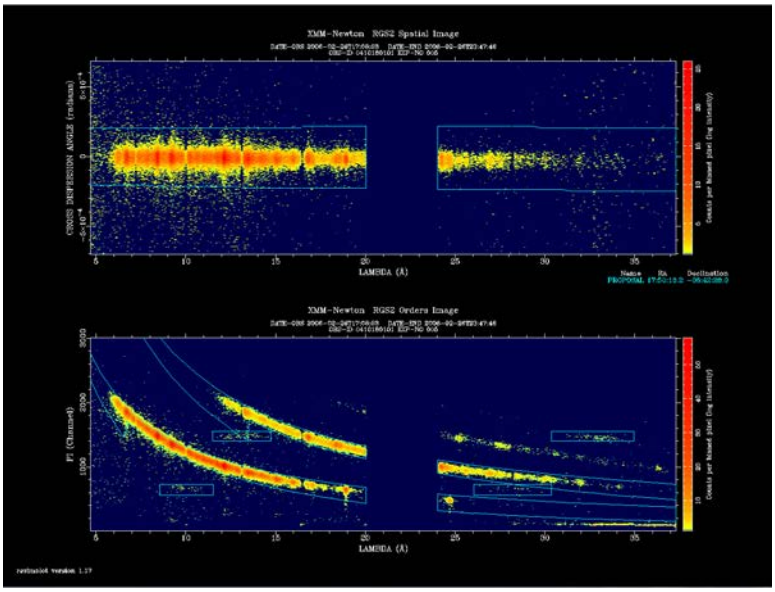

Figure 74: RGS2 data for a calibration observation of RS Oph 13.8 days after outburst. The top panel shows the image of the dispersed light in the detector. The bottom panel shows the order selection plane, with the energy, PI, on the ordinate. Standard data selections are indicated by blue curves.

sources with a smooth continuum.

In our case the observations were taken during the first days after the outburst. However, we checked the pile-up of RGS as Ness et al. (2007b) and we confirmed that these spectra did not have pile-up. Finally, we combine the RGS source spectrum, the background spectrum and the response matrices with the `rgscombine` command. To combine correctly the spectra of the RGSs 1 and 2, they must belong to the same spectral order.

B.2 SWIFT/XRT DATA REDUCTION (FTOOLS)

Data were reduced using High Energy Astrophysics Software (HEASoft) (version 6.15). We used standard routines for the extraction of spectra from the cleaned PC event list (FITS-based software Tools developed at Goddard Space Flight Center (FTOOLs) `xselect`). If we have a count rate higher than 0.6 count s^{-1} in PC mode, we need to use an annular extraction region around the source to reduce the pile-up. To estimate the level of pile-up, it is necessary to know the deviation between the observed PSF and the un-piled-up PSF. The *Swift* PSF can be modelled by a King function without pile-up (Moretti et al., 2005). The FTOOL `XIMAGE` with the command `psf` allows to fit the PSF data with a King function using an interactive plot window with two plots: the encircled energy fraction and the PSF as a function of radius. Once we know at what radio the King function is deviated from XRT PSF, we can determine the inner radius

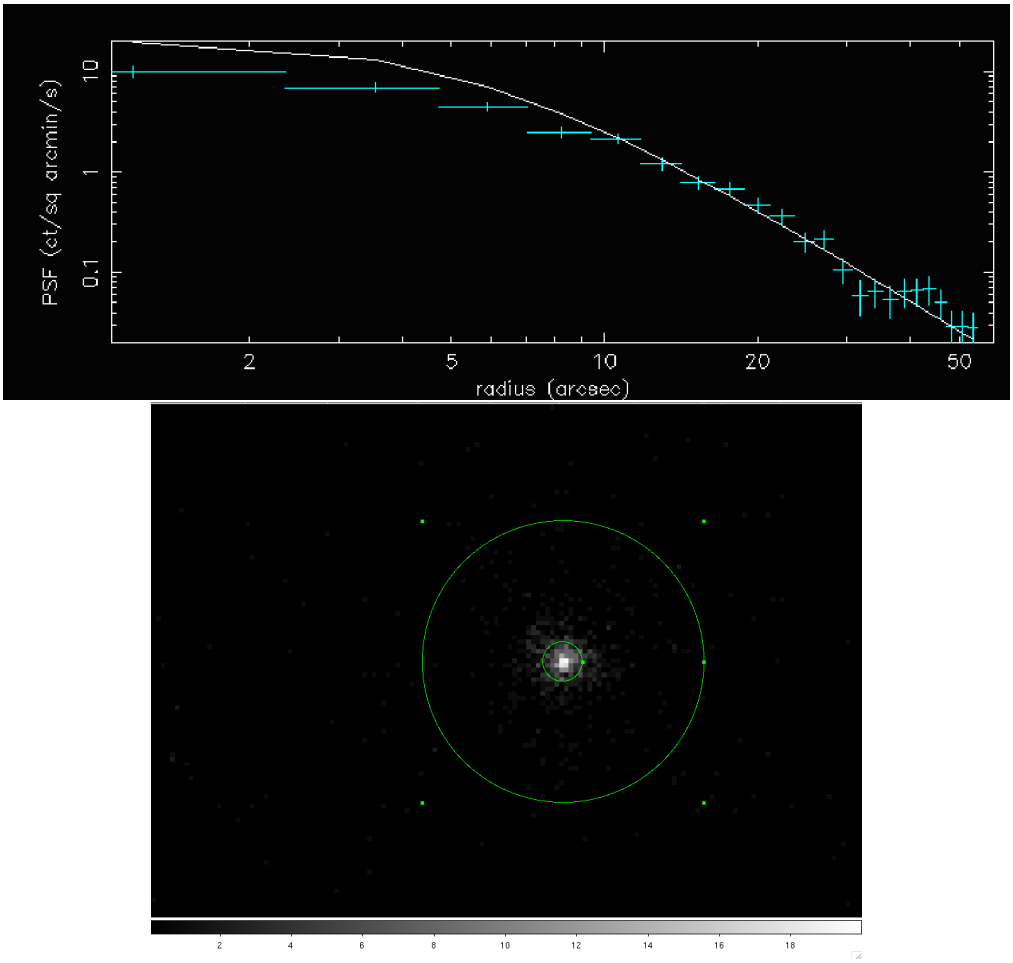

Figure 75: Top panel: XRT PSF as a function of radius modelled by a King function 2.17 days after the outburst. Bottom panel: XRT image using an annulus region (green circle) with and inner radius of 10 arcsec around the source.

of the annular region. Figure 75 shows PSF data fitted with the King function for V745 Sco on day 2.17 after the outburst. This day, the King function fit properly the XRT PSF at radios smaller than 10 arcsec. Knowing the inner radius needed to avoid the pile-up, we can extract this region around the source (Figure 75). In the case of V745 Sco, we used an annular extraction region with an inner radius between 2.5 to 5 pixels (1 pixel = 2.36")(See Table 19). The same area is extracted away from the source to obtain a background spectrum.

WT mode is the best mode to reduce the effects produced by the pile-up because in this mode, pile-up only appears for count rates higher than 100 count s^{-1}. In the case of V745 Sco, the SSS emission was first detected on day 4.23 after the outburst. Therefore, the source began to be observed with WT mode. As the count rate is small for this day, we did not need the annular extraction region. Instead, we used a circular region.

For the spectral analysis, we chose grade 0-12 events for PC and 0-2 events for WT. The ancillary response files were created by the FTOOL `xrtmkarf`. This tool give also

Table 19: Inner Radios of the Annulus Extraction in V745 Sco Swift/XRT observations

Observation Date	Time after discovery	Segment	Inner Radio arcsec	pixel
2014 Feb 06	0.16	001	8	3.38
2014 Feb 07	0.56	002	8	3.38
2014 Feb 07	0.89	003	10	4.23
2014 Feb 07	1.16	004	11.8	5
2014 Feb 08	1.51	005	8	3.38
2014 Feb 08	1.89	006	6	2.54
2014 Feb 08	2.17	007	10	4.23
2014 Feb 09	2.96	012	6	2.54
2014 Feb 10	4.23	017	WT mode	
2014 Feb 12	16.03	056	9.5	4

the corresponding Redistribution Matrix File (RMF) as an output. All spectra were grouped to a minimum of 10 counts per bin with the FTOOL `grppha`, to have enough bins but also to be able to use the χ^2 statistics in XSPEC.

B.3 CHANDRA/HETG DATA REDUCTION (CIAO)

We obtained the spectra for the high and medium energy grating (HEG and MEG) directly from the CHANDRA_REPRO script. The script reads data from the standard data distribution and creates a new bad pixel file, a new level=2 event file, and a new level=2 Type II PHA file. Also, this script creates the appropriate Auxiliary Response File (ARF) and RMF for each grating order in the spectrum. By default, each of the ACIS HETG file contains 12 different spectra, giving the positive and negative first, second, and third orders for each the MEG and HEG spectra. The information of each RMF and ARF for each spectrum was associated and automatically combined with the `combine_grating_spectra` subroutine taking into account the positive and negative orders for HEG and MEG spectra.

In order to use Gaussian statistics to fit a model, it is necessary to combine the data until the spectrum has enough counts. Because it is not possible to group all the rows in a spectrum file at once, the individual spectra first need to be split from the file with the `dmtype2split` subroutine, and then, the different spectra were grouped to a minimum of 10 counts per bin using the `dmgroup` subroutine.

C

SPECTRAL ANALYSIS

In our analysis, we use some models included in the X-ray fitting package X-Ray Spectral Analysis Package (XSPEC) version 12.8 (Arnaud et al., 2012). For this reason, we will explain what is XSPEC and what commands are important to obtain different magnitudes as errors or fluxes; and we will describe the different models that we use in this document and their physical meaning.

C.1 XSPEC

XSPEC is a program that allows to fit spectra in X-rays. It can be used for any spectrometer because it was designed to be completely detector-independent. We use XSPEC to analyse data from *XMM-Newton*, *Chandra*, *Swift* and *RXTE*.

XSPEC allows to fit the data obtained by the spectrometer using a model spectrum described with some parameters. The spectrometer does not obtain the spectrum of the source, it obtains photon counts within specific instrument channels related to the instrumental response at each energy. For each model, it calculates a theoretical count spectrum ($C_p(I)$) and it compares it to the observational one ($C(I)$) to find the model that best fit the data obtained by the spectrometer. Once we define a model, XSPEC finds the best-fit values of the model parameters, varying the different parameters of the model. Once XSPEC has fitted the spectrum, it gives the best-fit parameter value and a confidence interval at 1σ. The statistic that we use to find the best-fit model is χ^2:

$$\chi^2 = \sum \frac{(C(I) - C_p(I))^2}{(\sigma(I))^2} \tag{27}$$

where $\sigma(I)$ is the standard deviation for channel I. Given a number of degrees of freedom (dof), χ^2 proves the goodness of the fit. The dof is calculated as the number of channels minus the number of model parameters. In this thesis, we used the reduced χ^2 ($\chi^2_{red} \sim \chi^2 / dof$). When $\chi^2_{red} \sim 1$, this means that $\chi^2 \sim dof$ and we have a good fit. We have a poor fit if $\chi^2_{red} < 1$, and we over-estimated the errors of the data when $\chi^2_{red} > 1$.

XSPEC provides us with several commands to know the range of the most significant values of the different parameters. To derive the confidence intervals for a parameter, XSPEC fixes the parameter at a particular value and varies the remaining parameters. The command `steppar` gives confidence contours at 3σ (99% of confidence level), 2σ (90% of confidence level) and 1σ (68% of confidence level) around the best-fit model

for two parameters. In some cases, we also use the command `error`. This command gives uncertainties corresponding to the 90% confidence region for one degree of freedom. The command `error` can not be used to calculate uncertainties when χ^2_{red} >2, while the command `steppar` can always be used.

Besides obtaining the values of the parameters of the best-fit model, we can also derive other magnitudes as the flux. The best-fit model is an estimation of the true spectrum emitted by the source. In XSPEC, the model is defined in physical units independent of the instrument. The command `flux` gives the model integrated in a specific energy range. In our case, we used the command `flux` to obtain the flux of the lines, absorbed or unabsorbed (N_H =0), plus the bremsstrahlung. To obtain the line flux, we subtracted the flux of the bremsstrahlung continuum to the flux of the Gaussian profile (See §3.2.1.4.2 and § 4.2.1.3).

Furthermore, we can vary the abundances with the command `abund` together with the abundances model that we chose. As we studied the first days after the outburst, we assume that the absorption comes from the ejecta and the red giant wind. Therefore, we adopt the solar abundances of Anders & Grevesse (1989) using `abund angr`.

C.2 SPECTRAL MODELS

Throughout the thesis we have used X-ray models related to different emission mechanisms. We will describe briefly the models used in this work.

There are several spectral codes to model hot plasmas. We use collisionally-ionized plasma models as Astrophysical Plasma Emission Code (APEC), when we study the spectrum globally. However, when we analyse the individual lines, we use a bremsstrahlung model to fit the continuum and a Gaussian model for the individual lines.

- **APEC models (apec, vapec, bvapec)**Astrophysical Plasma Emission Code (APEC) calculates both line and continuum emissivities for a hot, optically thin plasma that is in collisional ionisation equilibrium (Smith et al., 2001). APEC is a collisional-radiative plasma code that use the ATOMDB code v2.0.2. This code is based on Raymond & Smith (1977) code and its main goal is to calculate the emissivity and cooling curve properly. The fitting parameters are the plasma temperature in keV, the metal abundances and normalisation constant:

$$norm = \frac{10^{-14}}{4\pi[D_A(1+z)]^2} EM \tag{28}$$

  where D_A is the angular distance to the source in cm, z is the redshift, and EM is the emission measure. We used two variants of APEC:

  - VAPEC allows to vary the abundances of some elements, He, C, N, O, Ne, Mg, Al, Si, S, Ar, Ca, Fe and Ni, individually.

  - BVAPEC takes into account the velocity- and thermal-broadening. This model has the same parameters as VAPEC and, in addition, it has the gaussian sigma for velocity broadening (km/s).

- **Bremsstrahlung model (bremss)** A thermal bremsstrahlung continuum is produced by a transition of a free plasma electron between two continuum states with an energy spectrum $\propto T^{-\frac{1}{2}} e^{-E/kT}$. In XSPEC, it is described by the Kellogg et al. (1975) polynomial fit to the Karzas & Latter (1961) numerical values. The He abundance is 8.5% of H by number. At low temperature a different routine was used. The parameters are the plasma temperature in keV and normalisation constant

$$norm = \frac{3.02 \times 10^{-15}}{4\pi D_A^2} EM \tag{29}$$

  where D_A is the distance to the source in cm and EM is the emission measure.

- **Gaussian model (gaussian)** XSPEC also provides a simple gaussian line profile. In this model the parameters are the line energy and the line width (σ) in keV, and the normalisation constant that is the total photons in the line in cm^{-2} s^{-1}.

When the residual nuclear burning shell on top of the WD becomes visible, we can model it with a white dwarf atmosphere model. However, as our data do not have a lot of details, we can approximate the hot photosphere of the WD to a black body model.

- **Black body model (bbody)** The intensity of the radiation for a temperature T and at energy E is given by $I(E,T) = 2E^2/h^2c^2(e^{E/kT} - 1)$. In the case of XSPEC, a black body spectrum is given by

$$A(E) = \frac{K \times 8.0525 E^2 dE}{(kT^4)\left[e^{E/kT} - 1\right]} \tag{30}$$

  where the normalization constant ($K = L_{39}/D_{10}^2$) is related to the source luminosity (L_{39}) in units of 10^{39} erg^{-1} using the distance to the source in units of 10 kpc (D_{10}). The temperature is given in keV.

When we interpret the X-ray data, we need to know how the X-ray spectrum is modified by the material that it crosses until arriving at the detectors. To evaluate this absorption, a multiplicative model for the photoelectric-absorption is employed on top of all the models previously presented.

- **Tuebingen-Boulder absorption model (tbabs)** The Tuebingen-Boulder ISM absorption model is an improved model for the absorption of X-rays in the ISM (Wilms et al. (2000)). tbabs allows to vary the hydrogen column density in XSPEC measurements in units of 10^{22} atom/cm^{-2}. The total hydrogen column density (N_H) consists of a normalization of the gas cross-section (σ). The observed X-ray spectrum (I_{obs}) is given by

$$I_{obs}(E) = I_{source}(E) \times e^{-\sigma(E) \times N_H} \tag{31}$$

  where I_{source} is the X-ray spectrum of the source.

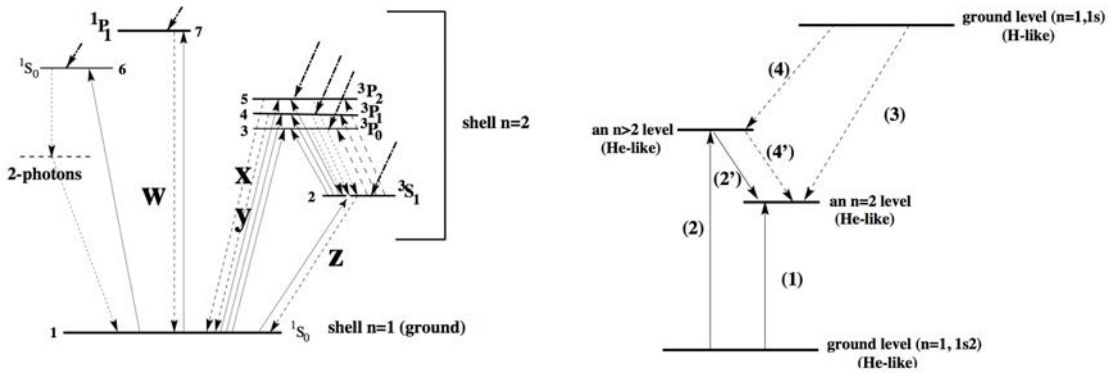

Figure 76: Left panel: diagram of the energy levels for He-like ions (from Porquet & Dubau, 2000). Right panel: Simplified diagram showing the different contributions to the population of a given n=2 shell level. 1 is the the collisional excitation contribution from the ground level ($1s^2$) of He-like ions. 2 and 2' are the collisional excitation and the upper-level radiative cascade contributions respectively. 3 is the radiative recombination from H-like ions. And 4 and 4' are the radiative recombination and the upper-level radiative cascade contributions respectively (from Porquet & Dubau, 2000).

C.3 LINE EMISSION DIAGNOSTIC

The other relevant process in thermal plasmas is the emission lines. Line emissions in novae come from excitation and recombination of electrons in ions (Mewe, 1999). There are three relevant types of lines in the collisional plasmas that allow to carry out some diagnostic of the plasma properties. They are the H-like, the He-like and the Fe lines.

C.3.1 *H- and He-like transitions*

With the new X-ray telescopes, it is possible to observe and to resolve the three most intense lines of He-like ions: the resonance line (w: $1s^2\ ^1S_0$ - $1s2p\ ^1P_1$), the intercombination lines ($x+y$: $1s^2\ ^1S_0$ - $1s2p\ ^3P_{2,1}$ respectively), and the forbidden line (z: $1s^2\ ^1S_0$ - $1s2s\ ^3S_1$) (Figure 76). The He-like ions have only K-shell electrons. The lines correspond to transitions between the n=2 shell and the n=1 ground state shell. The H-like ions have a single electron. This transition is usually quite bright (Porquet & Dubau, 2000, and references therein).

These lines are a powerful tool to diagnose the electron temperature and the electron density (Gabriel & Jordan, 1969). These following ratios characterize the 'triplet' emission lines from He-like ions. The G ratio, $G \equiv (z+x+y)/w = (f+i)/r$, which is sensitive to the temperature. The relative intensity of the resonance line compared with the others, contains information about the ionization processes that occur, e.g. a wide resonance line corresponds to a photo-ionized plasma (G>4); while a strong resonance line corresponds to a collisional plasma (G∼1) (Mewe, 1999; Liedahl, 1999). The R ratio, $R \equiv z/(x+y) = f/i$, is a sensitive diagnostic tool to measure electron densities (Porquet & Dubau, 2000). In the case of an intense UV radiation field, the

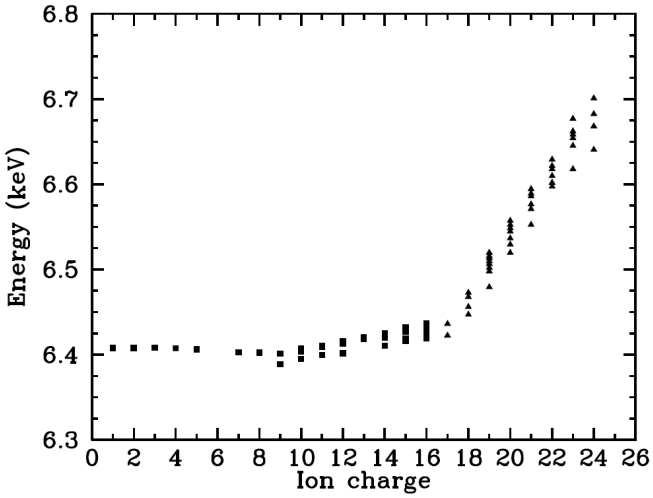

Figure 77: Fe-K shell line emission energies as a function of the ionization state (Vink, 2012, from).

photo-excitation between the ^{3}S term and the ^{3}P term has the same effect as the collisional coupling. This may appear to have high densities because the obtained R ratio is small, but is actually the effect of intense UV radiation. This diagnostic tool is valid only when the electron densities are in the range $n_e = 10^8 - 10^{13}$ cm^{-3}, which is much higher than that encountered in some SNRs and novae (Vink, 2012, and references therein).

C.3.2 *Fe lines*

Fe emission lines can be used to characterize the state of the plasma. At electron temperatures $kT_e \geq 2$keV, Fe-K shell (n=2) emission can be observed for all ionization states of Fe. X-ray spectra can present a prominent line around 6.7 keV that indicates the existence of H- and He-like Fe lines (Fe XXV and Fe XXVI) at 6.96 keV (Figure 77). For low ionization states, between Fe I and Fe XVII, the Fe-K shell line is close to 6.4 keV. Moreover, in the case of non-thermal bremsstrahlung, the production of the non-thermal Fe K line (6.4 keV) and a continuum appears due to the interaction of accelerated electrons, protons and α-particles with a neutral ambient gas (Vink, 2012, and references therein).

In X-ray spectra it is also easy to see the Fe-L shell transitions in the energy range between 0.7-1.12 keV. These transitions appear in the spectrum when there are electrons present in the L-shell ($n = 2$) for ionisation states. Fe-L emission lines (Fe XVII to Fe XXIV) appear in the spectrum at lower temperatures than Fe K emission lines (kT$\geq$0.15 keV). The presence of Fe L- and K-lines serve as a tool to determine the ionisation state of the plasma and can help to determine the nature of the plasma. For example, the Fe-K line at 6.4 keV could be originated by Fe XVII-XIX at $\sim$ 1 keV or by lower ionisation states. However, in the latter case, Fe-L lines should not be present in the spectrum.

D

RADIO EMISSION

In most of the novae the radio emission is dominated by the thermal bremsstrahlung (free-free emission). However, in some cases, synchrotron (non-thermal emission) is also observed. In order to have synchrotron emission, a significant population of relativistic electrons which have been accelerated in the shocks is needed in addition to a magnetic field. Therefore, radio observations can play a crucial role in the interpretation of particle acceleration in novae. In radio astronomy, the Jansky (Jy) unit [Jy$\equiv 10^{-26}$W m^{-2} Hz^{-1} $\equiv$ 10 $^{-23}$erg s^{-1}cm^{-2} Hz^{-1}] is employed, which is a measure of the strength of the radiation from a source.

Thermal emission corresponds to a thermal bremsstrahlung free-free absorption. It is typically characterized by a brightness temperature ($\sim 10^4$ K) assuming a steady-state for a spherically symmetric system. In novae, it is observed as a diffuse emission. In a cloud of ionized gas, the strength and spectrum of radio emission depends on the distribution of the electron velocities, v, that depends on the electron temperature, T, and collision impact parameters, b, that depends on n$_e$ (cm^{-3}) and n$_i$ (cm^{-3}). We assume that the plasma is macroscopically neutral (n$_i$ =n$_e$) and we consider only collisions with small relative energy changes, ΔE/E, for the electrons. The changes in their velocity are very small during the collision, so we can adopt a Maxwell-Boltzmann distribution for the distribution function (Rybicki & Lightman, 1979; Wilson et al., 2013, and references therein):

$$f(v) = \frac{4v^2}{\sqrt{\pi}} \left(\frac{m}{2kT}\right)^{3/2} e^{-\frac{mv^2}{2kT}} \tag{32}$$

where m is the electron mass and k is the Boltzmann constant. The free-free emission coefficient is given by

$$\varepsilon_v = \frac{8}{3}\frac{Z^2e^6}{c^3}\frac{n_in_e}{m^2}\sqrt{\frac{2m}{\pi kT}} ln\frac{b_2}{b_1} \tag{33}$$

where Z is the electron charge, $b_2/b_1 = (2kT/\gamma m)^{3/2}m/\pi\gamma Ze^2\nu$, $\gamma = e^C = 1.781$ and C is Euler's constant (=0.577) which T>20 K and $\nu_{max} > 30$ GHz (Oster, 1961).

Knowing the free-free emission coefficient and the blackbody brightness (B$_\nu$(T)), Kirchhoff's law yields the absorption coefficient $\kappa = \varepsilon_v/B_\nu(T)$. Using the Rayleigh-Jeans approximation, where B$_\nu$(T)=$2\nu^2kT/c^2$, then

$$\kappa = \frac{4Z^2e^6}{3c}\frac{n_en_i}{\nu^2}\frac{1}{\sqrt{2\pi(mkT)^3}} ln\frac{b_2}{b_1} \tag{34}$$

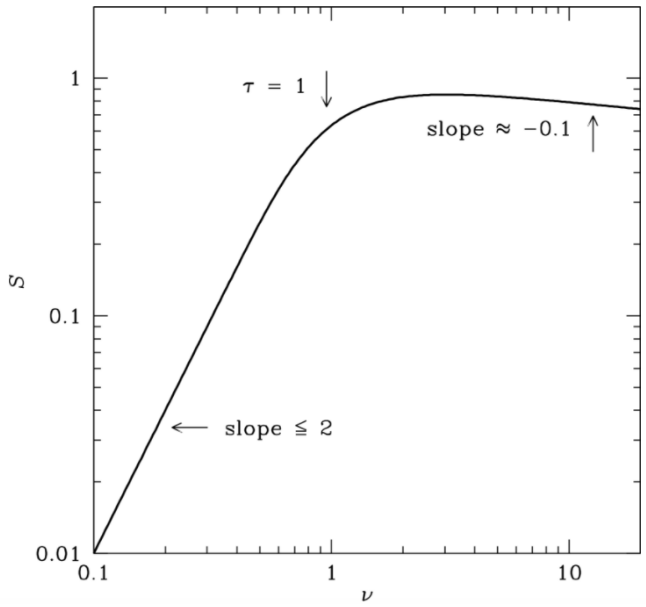

Figure 78: The radio spectrum of a cloud of ionized gas from NRAO web site[1]. At low frequencies it behaves as a black body with $\alpha = 2$, while at frequencies close to $\tau \approx 1$ or higher frequencies $\alpha = -0.1$.

The κ is not exactly proportional to ν^{-2}, $\kappa \propto \nu^{-2.1}$, because the limit b_2 also depend on ν. The integral of $-\kappa$ along the line of sight is the total opacity τ of the cloud of ionized gas. τ is given by

$$\tau = -\int_0^s \kappa ds \propto \int \frac{n_e n_i}{\nu^{2.1} T^{3/2}} ds \tag{35}$$

The cloud of ionized gas becomes opaque at low enough frequencies so that $\tau \gg 1$. Its spectrum can be approximated to a blackbody with a brightness temperature of T$\sim 10^4$ K, and its flux density follows the Rayleigh-Jeans approximation.

$$S(\nu) \propto \nu^2, \tag{36}$$

and the cloud of ionized gas becomes practically transparent at very high frequencies ($\tau \ll 1$) (Figure 78)[1]

$$S(\nu) \propto \frac{2kT\nu^2}{c^2} \tau(\nu) \propto \nu^{-0.1}. \tag{37}$$

At low frequencies, the brightness depends only on T. However, at high frequencies the brightness depends also on the EM.

Synchrotron radiation requires a population of relativistic and ultra-relativistic electrons gyrating in a magnetic field. The spectrum of synchrotron emission results from summing the emission of individual electrons. As the electron rotates around the magnetic field, it emits radiation over a range of frequencies that is determined by the speed of the electron at that instant (Rybicki & Lightman, 1979). The power per unit

1 https://www.cv.nrao.edu/course/astr534/FreeFreeEmission.html

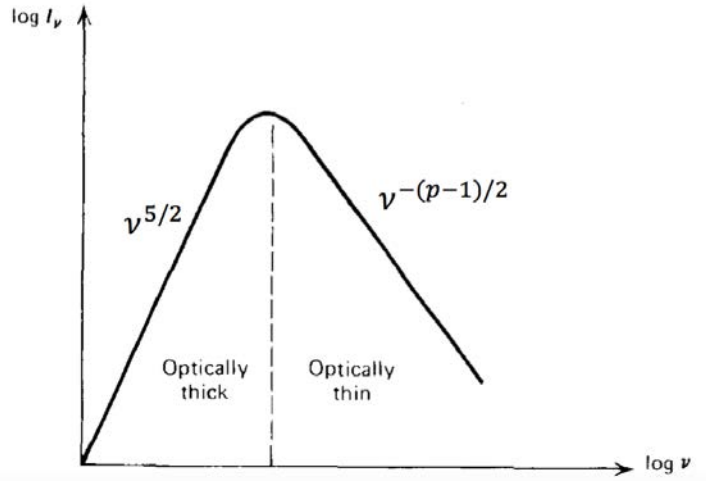

Figure 79: Synchrotron spectrum from a power-law distribution of electrons (adapted from Rybicki & Lightman, 1979). At low frequencies is synchrotron self-absorption with $\alpha = 5/2$, while at high frequencies $\alpha = -(p-1)/2$.

frequency $P(\nu)$ emitted by each electron can be approximated by a power law over a limited range of frequency

$$P(\nu) = C_1 F\left(\frac{\nu}{\nu_c}\right) \propto \nu^{-s} \tag{38}$$

where F is a dimensionless function and C_1 is a constant. The emitted spectrum of electrons of energy E peaks near the critical frequency $\nu \approx \nu_c \propto \gamma^2$. The energy distribution of electrons radiating in synchrotron sources with energies between E and $E + dE$ (or γ and $\gamma + d\gamma$) is given by

$$N(E)dE = CE^{-p}dE, \quad E_1 < E < E_2 \quad \text{or} \quad N(\gamma)d\gamma = C\gamma^{-p}d\gamma, \quad \gamma_1 < \gamma < \gamma_2, \tag{39}$$

where C can vary with the angle and p is the particle distribution index. The total power radiated as a function of frequency by a distribution of relativistic electrons is given by the integral of $N(\gamma)d\gamma$ times the radiation formula for the single particle over all energies or γ

$$P_{tot}(\nu) = C\int_{\gamma_1}^{\gamma_2} P_\nu \gamma^{-p} d\gamma \propto \int_{\gamma_1}^{\gamma_2} F\left(\frac{\nu}{\nu_c}\right)\gamma^{-p}d\gamma \tag{40}$$

if we change $x \equiv \nu/\nu_c$, taking into account that $\nu_c \propto \gamma^2$, then the total power is given by

$$P_{tot}(\nu) \propto \nu^{-(p-1)/2}\int_{x_1}^{x_2} F(x)x^{(p-3)/2}dx \tag{41}$$

The limits x_1 and x_2 depend on ν. However, if the energy range is broad enough, $x_1 \approx 0$ and $x_2 \approx \infty$. As the flux density is proportional to the total power, we obtain that

$$P_{tot}(\nu) \propto S(\nu) \propto \nu^{-(p-1)/2} \tag{42}$$

Synchrotron emission shows a high brightness temperature ($\gg 10^6$ K) and a negative radio spectral index. The spectral index s and the particle distribution p are related by $s{=}(p-1)/2$.

The synchrotron mechanism can also be an absorption mechanism (Rybicki & Lightman, 1979; Longair, 1999). This process is called *synchrotron self-absorption*. The flux density of a synchrotron radio source could increase without limit at low frequencies. However, the electrons begin to reabsorb the low-energy photons when the intensity of the synchrotron radiation becomes sufficiently large, so they become optically thick at lower frequencies. This can occur in sources that are compact and have very high synchrotron electron densities. For ultra-relativistic electrons, we can associate a temperature with electrons of a given energy through $E = \gamma mc^2 = 3kT_e$. As $\nu \approx \nu_c \propto \gamma^2$ and the effective temperature of the particles becomes a function of their energies, so

$$kT_e \approx \frac{mc^2}{3}(\nu/\nu_c)^{1/2} \propto \nu^{1/2}. \tag{43}$$

The effective temperature of the particle, T_e, is equal to the brightness temperature of the radiation. Taking into account the blackbody brightness in the Rayleigh-Jeans approximation, then

$$S(\nu) \propto \nu^2 kT_e \propto \nu^2 \nu^{1/2} \propto \nu^{5/2} \tag{44}$$

the power law index will be $\alpha = 5/2$, independent of the value of p.

E

SNR PHASES

The supernova remnants go through different phases over time. These phases can last millions of years. For nova explosions, if these phases occur, they only last for short periods of time (Sedov, 1959; Colgate & McKee, 1969; Woltjer, 1972; Chevalier, 1981, 1982b,a,c; Truelove & McKee, 1999; Vink, 2012).

Phase I: Free expansion ($M_{ej} \gg M_{sw}$). This phase is the irruption of the ejecta moving at constant velocity ($v_s \sim cont$) into the circumstellar medium (Woltjer, 1972). The ejecta dominates this phase because the ejected mass is larger than the swept-up matter (M_{sw}). The duration of this phase will depend on the amount of matter swept by the shock. When the swept matter is larger than the ejected mass, the remnant will move to the phase II.

Phase I $\rightarrow$ II: Self-similar driven wave ($M_{ej} \geq M_{sw}$). This phase is an intermediate phase between the free expansion (Phase I) and the Sedov-Taylor phase (Phase II). It occurs when the shock starts to slow down, the expanding ejecta runs into the swept-up circumstellar medium and a reverse shock appears. In this intermediate phase the supernova remnant develops a characteristic structure from the center outwards: ejecta, reverse shock into the ejecta, shocked ejecta, contact discontinuity, shocked circumstellar medium and forward shock into the circumstellar medium. The expanding medium and the stationary circumstellar medium have a power law density profile ($\rho \propto r^{-n}$ and $\rho \propto r^{-s}$ respectively) (Chevalier, 1982b).

The motion of the supernova remnant during this phase is usually described in terms of the Sedov solution (Sedov, 1959). The energy of the explosion, E, and the density of the circumstellar medium, ρ, are the free parameters in the self-similar solution in the case of the evolution of the adiabatic blast wave in uniform circumstellar media. Using the Euler equations of hydrodynamics, the equations of state of an ideal mono-atomic gas ($\gamma = 5/3$) with spherical symmetry are (Colgate & McKee, 1969; Truelove & McKee, 1999):

$$\begin{aligned} \frac{\partial r}{\partial t} &= v & \frac{\partial v}{\partial t} &= -4\pi r^2 \frac{\partial P}{\partial M} \\ \frac{\partial}{\partial t}\left(\frac{P}{\rho^{5/3}}\right) &= 0 & \frac{\partial}{\partial M}\left(\tfrac{4}{3}\pi r^3\right) &= \frac{1}{\rho} \end{aligned} \tag{45}$$

where M is defined as $M(R,t) = \int_0^R 4\pi R'^2 \rho(R', t')dt$. The initial conditions to describe a remnant using the Euler equations of hydrodynamics (Equation 45) corresponding to the state of the gas in the limit t$\rightarrow$ 0 are given by

$$\rho(r,t) = \begin{cases} \rho_2(v,t) \equiv \dfrac{M_{ej}}{v_s^3} f(\dfrac{v}{v_s}) t^{-3} & r < R \\ \\ \rho_1 \equiv q r^{-s} & r > R \end{cases} \tag{46}$$

$$v(r,t) = \begin{cases} \dfrac{r}{t} & r < R \\ \\ 0 & r > R \end{cases} \tag{47}$$

$$P(r,t) = 0 \tag{48}$$

where q is constant, and the expanding ejecta surface has a radius $R \equiv v_s t$. At this time the ejecta expands freely with a general density distribution into a stationary, cold uniform ambient medium. The initial condition of the pressure is $P = 0$ everywhere because the pressures generated by the shocks greatly exceed any preexisting pressure in the ejecta or ambient medium. The initial ejecta density distribution is separated into time-independent and time-dependent terms. The term t^{-3} is derived from the free expansion of the ejecta before its interaction with the circumstellar medium and the structure function $f(v/v_s)$ describes the time-independent shape distribution. If we expand ρ_2[1], we arrive at the initial conditions describe by Chevalier (1982b)

$$\rho(r,t) = \begin{cases} \rho_2 \equiv \dfrac{M_{eje}}{v_s^3} f\left(\dfrac{v}{v_s}\right) t^{-3} = \left(\dfrac{r}{gt}\right)^{-n} t^{-3} & r < R \\ \\ \rho_1 \equiv q r^{-s} & r > R \end{cases} \tag{49}$$

where $(1/g) = \left(M_{ej} f_n / v_s^{(3-n)}\right)^{(1/-n)}$. The ejecta and the circumstellar medium are separated by a contact discontinuity at $r = R$. Comparing both densities at this distance, we obtain

$$R = \left(\frac{g^n}{q}\right)^{1/(n-s)} t^{(n-3)/(n-s)} \propto t^{(n-3)/(n-s)} \tag{50}$$

1

$$\rho_2 \equiv \frac{M_{ej}}{v_s^3} f\left(\frac{v}{v_s}\right) t^{-3} = \frac{M_{ej}}{v_s^3} f_n \left(\frac{v}{v_s}\right)^{-n} t^{-3} = \frac{M_{ej}}{v_s^{(3-n)}} f_n \left(\frac{r}{t}\right)^{-n} t^{-3} =$$
$$= \left(\frac{M_{ej} f_n}{v_s^{(3-n)}}\right) \left(\frac{r}{t}\right)^{-n} t^{-3} = \left(\left(\frac{M_{ej} f_n}{v_s^{(3-n)}}\right)^{\frac{1}{-n}} \frac{r}{t}\right)^{-n} t^{-3} = \left(\frac{r}{gt}\right)^{-n} t^{-3}$$

There are different constraints to s and n. First, s must be < 3 because the contact discontinuity can not be accelerated while the ejecta has a constant velocity. Second, n must be > 5 because $n = 5$ represents the expansion law for the shock wave in a point explosion (Phase II) and $n < 5$ corresponds to a steady separation between the outer region and the contact discontinuity (Chevalier, 1982b).

Different values of s and n describe the density profiles of Type I and Type II supernova (Chevalier, 1982b). Type I supernovae expand with a density profile $\rho \propto r^{-n}$ with $n = 7$ (Colgate & McKee, 1969), into a uniform medium ($s = 0$) with $R \propto t^{4/7}$ (Chevalier, 1981). In Type II supernovae, unlike in Type I supernovae, the progenitor is surrounded by a circumstellar density distribution of matter ($\rho \propto r^{-s}$ with $s = 2$). Therefore, $R \propto t^{(n-3)/(n-2)}$ because the ejected matter density profile is $\rho \propto r^{-n}$ where n>5 (Chevalier, 1982c) (see Table 2). This case is similar to symbiotic nova systems because the RG wind matter is around the WD. The density distribution of the RG wind is $\rho_w = \dot{M}_{RG}/4\pi r^2 v_w$, where $v_w \sim 10 - 20$ km s^{-1}.

Phase II: Adiabatic phase or Sedov-Taylor phase ($M_{ej} \ll M_{sw}$). In this phase the swept-up mass dominates over the ejecta and the remnant forgets its early history. The total energy is about the same as the explosion energy because the radiative losses are negligible. According to Sedov (1959), this occurs when a large amount of energy is released into a uniform ambient medium, creating a strong explosion characterized by a strong shock wave emanating from the point where the energy was released. The mass of the swept-up material is of the order of $M(t) \sim \rho R^3(t)$ and the velocity of the expanding ejecta, $v_s(t) \sim R/t$. Using Equation 8 and solving for the radius R of the expanding ejecta, we obtain:

$$R \propto \left(\frac{E}{\rho}\right)^{1/5} t^{2/5} \tag{51}$$

If we compare Equation 51 and Equation 50, we obtain the radius for a point explosion ($n = 5$) in a uniform ambient medium ($s = 0$) as in the case of the Type I Supernova. However, if the ambient medium has a density profile $\rho \propto R^{-s}$ where $s \neq 0$ (Chevalier, 1982a), the energy is given by

$$E \propto \rho R^{-s} \frac{R^5}{t^2} \tag{52}$$

As a consequence of that, the radius and the shock velocity are given by

$$R \propto \left(\frac{E}{\rho}\right)^{1/(5-s)} t^{(2/(5-s))} \tag{53}$$

$$v_s \propto \frac{2}{5-s} \left(\frac{E}{\rho}\right)^{1/5-s} t^{(s-3)/(5-s)} \tag{54}$$

In the case of a nova remnant where the ejecta shocks with the RG wind whose density profile is $\rho_W(R) \propto R^{-2}$ ($s = 2$), R becomes:

$$R \propto \left(\frac{E}{\rho}\right)^{1/3} t^{2/3} \tag{55}$$

$$v_s \propto \frac{2}{3}\left(\frac{E}{\rho}\right)^{1/3} t^{-1/3} \tag{56}$$

Note that these equations assume ρ =const., which is not true since the remnant expands. Nevertheless, it is a good approximation. In supernova remnants, this phase lasts up to $\sim$ 1000 years after the outburst. In novae, it can last up to few months.

Phase III: Radiative snow-plow ($t > t_{rad}$) This phase is dominated by radiative losses. The radial expansion is governed by momentum conservation, $Mv = 4\pi/3R^3\rho\ dR/dt$. According to Truelove & McKee (1999, Appendix A), $\rho = M_{ej}/(4\pi/3)\ R^{(3-s)}$ in this phase. Therefore, we can relate the time t and radius R of the remnant at any future moment to the time $t_{\rm rad}$, radius $R_{\rm rad}$ and expansion velocity $v_{\rm rad}$ at the transition. At the time for which radiative losses become important, t_{rad}, the transition from the Sedov-Taylor phase to the radiative snow-plow phase occurs. After this time, the remnant passes through the radiative evolutionary phase. This phase is dominated by momentum conservation, as a consequence of that, this conservation law is given by

$$\frac{dp}{dt} = \frac{d}{dt}\left(\left(\frac{4\pi}{3}\rho R^{(3-s)}\dot{r}\right)\right) = 0 \tag{57}$$

Integrating the momentum conservation for the time, t, as a function of the radius, we obtain

$$t = t_{\rm rad} + \frac{R_{\rm rad}^{(1-s)}}{(4-s)v_{\rm rad}}\left[\left(\frac{R}{R_{\rm rad}}\right)^{(4-s)} - 1\right] \tag{58}$$

$R_{\rm rad}$ and $v_{\rm rad}$ can be obtained from the Sedov self-similar solution where $v_s = v_{\rm rad}$ and $t_{\rm rad} = R_{\rm rad}/v_{\rm rad}$ (Vink, 2012). At this time, the remnant will have a radius, R, which is the observed radius.

$$R = R_{\rm rad}\left[\frac{(4-s)v_{\rm rad}\ t_{\rm rad}}{R_{\rm rad}^{(1-s)}}\left(\frac{t}{t_{\rm rad}} - 1\right) + 1\right]^{\frac{1}{(4-s)}} \propto t^{1/(4-s)} \tag{59}$$

Thus, velocity will be $v \propto t^{(s-3)/(4-s)}$

Phase IV: Merging with the ISM. Finally, the shock wave slows, cools and becomes subsonic. The expansion velocity of the remnant becomes comparable to that of interstellar gas ($\sim$10 km/s). As a consequence of that, the shock wave loses its identity and merges into the interstellar medium (Woltjer, 1972).

BIBLIOGRAPHY

Abdo, A. A., Ackermann, M., Ajello, M., et al. 2010, Science, 329, 817

Ackermann, M., Ajello, M., Albert, A., et al. 2014, Science, 345, 554

Anders, E., & Grevesse, N. 1989, Geochim. Cosmochim. Acta, 53, 197

Anupama, G. C. 2008, RS Ophiuchi (2006) , the Recurrent Nova Phenomenon, 401, 31

Anupama, G. C., & Mikolajewska, J. 1999, A&A, 344, 177

Anupama, G. C., Selvakumar, G., Moorthy, V., Velu, C., & Dinakaran, N. 2014, The Astronomer's Telegram, 5871, 1

Arnaud, K., Dorman, B., & Gordon, C. 2012, XSPEC: An X-Ray Spectral Fitting Package, User's Guide for Version 12.9.x (Greenbelt, MD:GSFC)

Atwood, W. B., Abdo, A. A., Ackermann, M., et al. 2009, ApJ, 697, 1071

Baade, W., & Zwicky, F. 1934, Proceedings of the National Academy of Science, 20, 254

Balman, S., & Krautter, J. 2001, MNRAS, 326, 1441

Balman, S., Krautter, J., & Oegelman, H. 1998, ApJ, 499, 395

Banerjee, D. P. K., Das, R. K., & Ashok, N. M. 2009, MNRAS, 399, 357

Banerjee, D. P. K., Joshi, V., Venkataraman, V., et al. 2014a, ApJL, 785, L11

Banerjee, D. P. K., Venkataraman, V., Joshi, V., Raj, A., & Ashok, N. M. 2014b, The Astronomer's Telegram, 5865

Barry, R. K., Mukai, K., Sokoloski, J. L., et al. 2008, in Astronomical Society of the Pacific Conference Series, Vol. 401, RS Ophiuchi (2006) and the Recurrent Nova Phenomenon, ed. A. Evans, M. F. Bode, T. J. O'Brien, & M. J. Darnley, 52

Barthelmy, S. D., Barbier, L. M., Cummings, J. R., et al. 2005, Space Sci. Rev., 120, 143

Beals, C. S. 1936, MNRAS, 96, 661

Berezhko, E. G., & Ellison, D. C. 1999, ApJ, 526, 385

Bode, M. F., & Evans, A. 2008, Classical Novae (Cambridge University Press)

Bode, M. F., Harman, D. J., O'Brien, T. J., et al. 2007, ApJL, 665, L63

Bode, M. F., & Kopal, Z. 1987, Ap&SS, 134, 419

Bode, M. F., O'Brien, T. J., Osborne, J. P., et al. 2006, ApJ, 652, 629

Bohigas, J., Echevarria, J., Diego, F., & Sarmiento, J. A. 1989, MNRAS, 238, 1395

Brinkman, B. C., Gunsing, T., Kaastra, J. S., et al. 2000, in Proc. SPIE, Vol. 4012, X-Ray Optics, Instruments, and Missions III, ed. J. E. Truemper & B. Aschenbach, 81–90

Buil, C. 2006, Cent. Bur. Electron. Tel., 403, 1

Burrows, D. N., Hill, J. E., Nousek, J. A., et al. 2005, Space Sci. Rev., 120, 165

Burwitz, V., Starrfield, S., Krautter, J., & Ness, J.-U. 2002, in American Institute of Physics Conference Series, Vol. 637, Classical Nova Explosions, ed. M. Hernanz & J. José, 377–380

Canizares, C. R., Huenemoerder, D. P., Davis, D. S., et al. 2000, ApJL, 539, L41

Cheung, C. C., Donato, D., Wallace, E., et al. 2010, The Astronomer's Telegram, 2487

Cheung, C. C., Glanzman, T., & Hill, A. B. 2012a, The Astronomer Telegram, 4284, 1

Cheung, C. C., Hays, E., & on behalf of the Fermi-LAT collaboration. 2013a, ATel, 5342, 1

Cheung, C. C., Hays, E., Venters, T., Donato, D., & Corbet, R. H. D. 2012b, The Astronomer Telegram, 4224, 1

Cheung, C. C., Jean, P., Collaboration, F. L. A. T., & Shore, S. N. 2015, The Astronomer's Telegram, 7283

Cheung, C. C., Jean, P., & Shore, S. N. 2014, The Astronomer's Telegram, 5879, 1

Cheung, C. C., Jean, P., Shore, S. N., & Fermi Large Area Telescope Collaboration. 2013b, ATel, 5649, 1

—. 2016a, The Astronomer's Telegram, 9594

Cheung, C. C., Jean, P., Shore, S. N., et al. 2016b, ApJ, 826, 142

Chevalier, R. A. 1981, ApJ, 246, 267

—. 1982a, ApJL, 259, L85

—. 1982b, ApJ, 258, 790

—. 1982c, ApJ, 259, 302

Chomiuk, L., Linford, J. D., Yang, J., et al. 2014a, Nature, 514, 339

Chomiuk, L., Nelson, T., Mukai, K., et al. 2014b, ApJ, 788, 130

Colgate, S. A., & McKee, C. 1969, ApJ, 157, 623

Darnley, M. J., Henze, M., Bode, M. F., et al. 2016, ApJ, 833, 149

Das, R., Banerjee, D. P. K., & Ashok, N. M. 2006, ApJL, 653, L141

Decourchelle, A., Ellison, D. C., & Ballet, J. 2000, ApJl, 543, L57

den Herder, J. W., Brinkman, A. C., Kahn, S. M., et al. 2001, A&A, 365, L7

Dere, K. P., Landi, E., Mason, H. E., Monsignori Fossi, B. C., & Young, P. R. 1997, A&A, 125, 149

Dobrzycka, D., & Kenyon, S. J. 1994, Aj, 108, 2259

Drake, J. J., Wagner, R. M., Starrfield, S., et al. 2003, ApJ, 584, 448

Drake, J. J., Laming, J. M., Ness, J.-U., et al. 2009, ApJ, 691, 418

Drake, J. J., Delgado, L., Laming, J. M., et al. 2016, ApJ, 825, 95

Dubus, G. 2013, A&AR, 21, 64

Duerbeck, H. W. 1989, The Messenger, 58, 34

Ellison, D. C. 2013, Acceleration Processes II (Fermi II and Monte Carlo), http://www.issibern.ch/cargese2013/index.php/File:Cargese_1_and_2_Ellison.pdf

Ellison, D. C., Berezhko, E. G., & Baring, M. G. 2000, ApJ, 540, 292

Ellison, D. C., Patnaude, D. J., Slane, P., Blasi, P., & Gabici, S. 2007, ApJ, 661, 879

Evans, A., Bode, M. F., O'Brien, T. J., & Darnley, M. J., eds. 2008, Astronomical Society of the Pacific Conference Series, Vol. 401, RS Ophiuchi (2006) and the Recurrent Nova Phenomenon (Astronomical Society of the Pacific Conference Series)

Evans, A., Kerr, T., Yang, B., et al. 2007, MNRAS, 374, L1

Eyres, S. P. S., O'Brien, T. J., Beswick, R., et al. 2009, MNRAS, 395, 1533

Fekel, F. C., Joyce, R. R., Hinkle, K. H., & Skrutskie, M. F. 2000, Aj, 119, 1375

Fruscione, A., McDowell, J. C., Allen, G. E., et al. 2006, in Society of Photo-Optical Instrumentation Engineers (SPIE) Conference Series, Vol. 6270, 62701V

Gabriel, A. H., & Jordan, C. 1969, MNRAS, 145, 241

Gehrels, N., Chincarini, G., Giommi, P., et al. 2004, ApJ, 611, 1005

Grevesse, N., & Sauval, A. J. 1998, Space Sci. Rev., 85, 161

Hachisu, I., & Kato, M. 2000, ApJL, 536, L93

—. 2001, ApJ, 558, 323

Harris, M. J., Leising, M. D., & Share, G. H. 1991, ApJ, 375, 216

Harrison, T. E., Johnson, J. J., & Spyromilio, J. 1993, Aj, 105, 320

Henze, M., Pietsch, W., Haberl, F., et al. 2010, A&A, 523, A89

—. 2011, A&A, 533, A52

—. 2014, A&A, 563, A2

Hernanz, M. 2015, Nature, 518, 307

Hernanz, M., & Sala, G. 2002a, Science, 298, 393

Hernanz, M., & Sala, G. 2002b, in American Institute of Physics Conference Series, Vol. 637, Classical Nova Explosions, ed. M. Hernanz & J. José, 381–385

Hernanz, M., & Tatischeff, V. 2012, Baltic Astronomy, 21, 62

Hirosawa, K., Narumi, H., Kanai, K., & Renz, W. 2006, Cent. Bur. Electron. Tel., 399, 1

Hjellming, R. M., van Gorkom, J. H., Taylor, A. R., et al. 1986, ApJL, 305, L71

Ibarra, A., Kuulkers, E., Osborne, J. P., et al. 2009, A&A, 497, L5

Iijima, T. 2006, IAU Circ., 8675, 1

Iyudin, A. F., Bennett, K., Bloemen, H., et al. 1995, A&A, 300, 422

Izzo, L., Della Valle, M., Mason, E., et al. 2015, ApJL, 808, L14

Jahoda, K., Swank, J. H., Giles, A. B., et al. 1996, in Proc. SPIE, Vol. 2808, EUV, X-Ray, and Gamma-Ray Instrumentation for Astronomy VII, ed. O. H. Siegmund & M. A. Gummin, 59–70

Jansen, F., Lumb, D., Altieri, B., et al. 2001, A&A, 365, L1

Jones, F. C., & Ellison, D. C. 1991, Space Sci. Rev., 58, 259

José, J. 2016, Stellar Explosions: Hydrodynamics and Nucleosynthesis (CRC Press/Taylor and Francis), doi:10.1201/b19165

José, J., & Hernanz, M. 1998, ApJ, 494, 680

Kantharia, N. G., Anupama, G. C., Prabhu, T. P., et al. 2007, ApJL, 667, L171

Kantharia, N. G., Dutta, P., Roy, N., et al. 2016, MNRAS, 456, L49

Karzas, W. J., & Latter, R. 1961, ApJS, 6, 167

Kashyap, V., & Drake, J. J. 2000, Bulletin of the Astronomical Society of India, 28, 475

Kellogg, E., Baldwin, J. R., & Koch, D. 1975, ApJ, 199, 299

Kolotilov, E. A., Munari, U., Popova, A. A., et al. 1998, Astronomy Letters, 24, 451

Krautter, J., Oegelman, H., Starrfield, S., Wichmann, R., & Pfeffermann, E. 1996, ApJ, 456, 788

Landau, L. D., & Lifshitz, E. M. 1987, FLuid mechanics, Vol. 6, Course of theoretical physics (Oxford: Pergamon Press)

Landi, E., Del Zanna, G., Young, P. R., et al. 2006, ApJS, 162, 261

Li, K.-L., & Chomiuk, L. 2016, The Astronomer's Telegram, 9699

Li, K.-L., Chomiuk, L., & Strader, J. 2016, The Astronomer's Telegram, 9736

Liedahl, D. A. 1999, in Lecture Notes in Physics, Berlin Springer Verlag, Vol. 520, X-Ray Spectroscopy in Astrophysics, ed. J. van Paradijs & J. A. M. Bleeker, 189

Lloyd, H. M., Bode, M. F., O'Brien, T. J., & Kahn, F. D. 1993, MNRAS, 265, 457

Lloyd, H. M., O'Brien, T. J., Bode, M. F., et al. 1992, Nature, 356, 222

Longair, M. S. 1984, Theoretical concepts in physics (Cambridge: University Press)

Longair, M. S. 1999, in Lecture Notes in Physics, Berlin Springer Verlag, Vol. 520, X-Ray Spectroscopy in Astrophysics, ed. J. van Paradijs & J. A. M. Bleeker, 1

Longinotti, A. L. 2013, XXMM-Newton Users Handbook, Issue 2.11 (ESA:XMM-Newton SOC)

Lucek, S. G., & Bell, A. R. 2000, MNRAS, 314, 65

Lumb, D. H., Schartel, N., & Jansen, F. A. 2012, Optical Engineering, 51, 011009

Luna, G. J. M., Pillitteri, I., Mukai, K., & Sokoloski, J. L. 2014, The Astronomer's Telegram, 5881, 1

Lundmark, K. 1920, Kungl. Svenska Vetenskapsakademiens Handlingar, 60, 1

MacDonald, J., & Vennes, S. 1991, ApJL, 373, L51

Martin, P., & Dubus, G. 2013, A&A, 551, A37

Mason, K. O., Córdova, F. A., Bode, M. F., & Barr, P. 1987, in RS Ophiuchi (1985) and the Recurrent Nova Phenomenon, ed. M. F. Bode, 167

Mason, K. O., Breeveld, A., Much, R., et al. 2001, A&A, 365, L36

Mauche, C. W. 2002, in Astronomical Society of the Pacific Conference Series, Vol. 261, The Physics of Cataclysmic Variables and Related Objects, ed. B. T. Gänsicke, K. Beuermann, & K. Reinsch, 113

Mewe, R. 1999, in Lecture Notes in Physics, Berlin Springer Verlag, Vol. 520, X-Ray Spectroscopy in Astrophysics, ed. J. van Paradijs & J. A. M. Bleeker, 109

Mewe, R., Gronenschild, E. H. B. M., & van den Oord, G. H. J. 1985, A&A, 62, 197

Molaro, P., Izzo, L., Mason, E., Bonifacio, P., & Della Valle, M. 2016, MNRAS, 463, L117

Monnier, J. D., Barry, R. K., Traub, W. A., et al. 2006, ApJL, 647, L127

Moretti, A., Campana, S., Mineo, T., et al. 2005, in Proc. SPIE, Vol. 5898, UV, X-Ray, and Gamma-Ray Space Instrumentation for Astronomy XIV, ed. O. H. W. Siegmund, 360–368

Mróz, P., Poleski, R., Udalski, A., et al. 2014, MNRAS, 443, 784

Mukai, K., & Ishida, M. 2001, ApJ, 551, 1024

Mukai, K., Nelson, T., Chomiuk, L., et al. 2014, in Astronomical Society of the Pacific Conference Series, Vol. 490, Stellar Novae: Past and Future Decades, ed. P. A. Woudt & V. A. R. M. Ribeiro, 327

Munari, U., Margoni, R., & Stagni, R. 1990, MNRAS, 242, 653

Nelson, T., Donato, D., Mukai, K., Sokoloski, J., & Chomiuk, L. 2012a, ApJ, 748, 43

Nelson, T., Mukai, K., Chomiuk, L., & Sokoloski, J. 2013, The Astronomer's Telegram, 5593

Nelson, T., Mukai, K., Chomiuk, L., et al. 2012b, The Astronomer Telegram, 4321, 1

Nelson, T., Orio, M., Cassinelli, J. P., et al. 2008, ApJ, 673, 1067

Nelson, T., Chomiuk, L., Roy, N., et al. 2014, ApJ, 785, 78

Ness, J.-U., Schwarz, G., Starrfield, S., et al. 2008, AJ, 135, 1328

Ness, J.-U., Schwarz, G. J., Retter, A., et al. 2007a, ApJ, 663, 505

Ness, J.-U., Shore, S. N., Drake, J. J., et al. 2012a, The Astronomer Telegram, 4569, 1

Ness, J.-U., Starrfield, S., Jordan, C., Krautter, J., & Schmitt, J. H. M. M. 2005, MNRAS, 364, 1015

Ness, J.-U., Starrfield, S., Burwitz, V., et al. 2003, ApJL, 594, L127

Ness, J.-U., Starrfield, S., Beardmore, A. P., et al. 2007b, ApJ, 665, 1334

Ness, J.-U., Drake, J. J., Starrfield, S., et al. 2009, Aj, 137, 3414

Ness, J.-U., Osborne, J. P., Dobrotka, A., et al. 2011, ApJ, 733, 70

Ness, J.-U., Schaefer, B. E., Dobrotka, A., et al. 2012b, ApJ, 745, 43

Ness, J. U., Schwarz, G. J., Page, K. L., et al. 2013, The Astronomer's Telegram, 5626

Nielsen, M. T. B., & Gilfanov, M. 2015, MNRAS, 453, 2927

Nomoto, K., Thielemann, F.-K., & Yokoi, K. 1984, ApJ, 286, 644

O'Brien, T., Rupen, M., Chomiuk, L., et al. 2015, Advancing Astrophysics with the Square Kilometre Array (AASKA14), 62

O'Brien, T. J., Bode, M. F., & Kahn, F. D. 1992, MNRAS, 255, 683

O'Brien, T. J., Bode, M. F., Porcas, R. W., et al. 2006, Nature, 442, 279

O'Brien, T. J., Beswick, R. J., Bode, M. F., et al. 2008, RS Ophiuchi (2006) , the Recurrent Nova Phenomenon, 401, 239

Ögelman, H., Beuermann, K., & Krautter, J. 1984, ApJL, 287, L31

Ögelman, H., Orio, M., Krautter, J., & Starrfield, S. 1993, Nature, 361, 331

Oppenheimer, B., & Mattei, J. A. 1993, in Bulletin of the American Astronomical Society, Vol. 25, American Astronomical Society Meeting Abstracts, 1378

Orio, M., Balman, S., della Valle, M., Gallagher, J., & Oegelman, H. 1996, ApJ, 466, 410

Orio, M., Covington, J., & Ögelman, H. 2001a, A&A, 373, 542

Orio, M., della Valle, M., Massone, G., & Oegelman, H. 1997, A&A, 325, L1

Orio, M., & Greiner, J. 1999, A&A, 344, L13

Orio, M., Hartmann, W., Still, M., & Greiner, J. 2003, ApJ, 594, 435

Orio, M., & Pa, B. T. 2012, The Astronomer Telegram, 4633, 1

Orio, M., Parmar, A. N., Greiner, J., et al. 2002, MNRAS, 333, L11

Orio, M., Rana, V., Page, K. L., Sokoloski, J., & Harrison, F. 2015, MNRAS, 448, L35

Orio, M., Parmar, A. N., Amati, L., et al. 2001b, X-ray Astronomy: Stellar Endpoints, AGN, and the Diffuse X-ray Background, 599, 466

Orio, M., Behar, E., Gallagher, J., et al. 2013, MNRAS, 429, 1342

Osborne, J. P., Page, K. L., Beardmore, A. P., et al. 2011, ApJ, 727, 124

Oster, L. 1961, ApJ, 134, 1010

Page, K. L., & Beardmore, A. P. 2013, The Astronomer's Telegram, 5429

Page, K. L., Beardmore, A. P., Osborne, J. P., & Schwarz, G. J. 2014, The Astronomer's Telegram, 5966, 1

Page, K. L., Kuin, N. P. M., Osborne, J. P., & Schwarz, G. J. 2015a, The Astronomer's Telegram, 7953

Page, K. L., Osborne, J. P., Wagner, R. M., et al. 2013, ApJL, 768, L26

Page, K. L., Osborne, J. P., Evans, P. A., et al. 2010, MNRAS, 401, 121

Page, K. L., Osborne, J. P., Kuin, N. P. M., et al. 2015b, MNRAS, 454, 3108

Patterson, J., & Raymond, J. C. 1985a, ApJ, 292, 550

—. 1985b, ApJ, 292, 535

Pinto, C., Ness, J.-U., Verbunt, F., et al. 2012, A&A, 543, A134

Plaut, L. 1958, Annalen van de Sterrewacht te Leiden, 21, 217

Plinius, C. 1855, The Natural History of Pliny (transl. and ed. J. Bostock, and H. T. Riley. London H. G. Bohn.)

Porquet, D., & Dubau, J. 2000, A&AS, 143, 495

Porquet, D., Mewe, R., Dubau, J., Raassen, A. J. J., & Kaastra, J. S. 2001, A&A, 376, 1113

Rauch, T. 1997, A&A, 320, 237

Rauch, T., Orio, M., Gonzales-Riestra, R., et al. 2010, ApJ, 717, 363

Raymond, J. C., & Smith, B. W. 1977, ApJS, 35, 419

Ribeiro, V. A. R. M., Bode, M. F., Darnley, M. J., et al. 2009, ApJ, 703, 1955

Rosino, L. 1987, in RS Ophiuchi (1985) and the Recurrent Nova Phenomenon, ed. M. F. Bode, 1

Rosino, L., & Iijima, T. 1987, in RS Ophiuchi (1985) and the Recurrent Nova Phenomenon, ed. M. F. Bode, 27

Rupen, M. P., Mioduszewski, A. J., Chomiuk, L., et al. 2014, The Astronomers Telegram, 5884, 1

Rupen, M. P., Mioduszewski, A. J., & Sokoloski, J. L. 2008, ApJ, 688, 559

Russell, H. N. 1914, Popular Astronomy, 22, 275

Rybicki, G. B., & Lightman, A. P. 1979, Radiative processes in astrophysics (Die Deutsche Bibliothek)

Sala, G., Hernanz, M., & Ferri, C. 2007, The Astronomer's Telegram, 1184

Sala, G., Hernanz, M., Ferri, C., & Greiner, J. 2008, ApJL, 675, L93

Sala, G., Ness, J. U., Hernanz, M., & Greiner, J. 2017, A&A, 601, A93

Schaefer, B. E. 2004, IAU Circ., 8396, 2

—. 2009, ApJ, 697, 721

—. 2010, ApJS, 187, 275

Schlegel, E. M., Shipley, H. V., Rana, V. R., Barrett, P. E., & Singh, K. P. 2014, ApJ, 797, 38

Schwarz, G. J., Ness, J.-U., Osborne, J. P., et al. 2011, ApJs, 197, 31

Sedov, L. I. 1959, Similarity and Dimensional Methods in Mechanics (New York: Academic Press)

Sekiguchi, K., Whitelock, P. A., Feast, M. W., et al. 1990, MNRAS, 246, 78

Shafter, A. W. 2017, ApJ, 834, 196

Shafter, A. W., Henze, M., Rector, T. A., et al. 2015, ApJS, 216, 34

Shanley, L., Ogelman, H., Gallagher, J. S., Orio, M., & Krautter, J. 1995, ApJL, 438, L95

Shore, S. N., Kenyon, S. J., Starrfield, S., & Sonneborn, G. 1996, ApJ, 456, 717

Shull, J. M., & Draine, B. T. 1987, in Astrophysics and Space Science Library, Vol. 134, Interstellar Processes, ed. D. J. Hollenbach & H. A. Thronson, Jr., 283–319

Smith, R. K., Brickhouse, N. S., Liedahl, D. A., & Raymond, J. C. 2001, ApJ, 556, L91

Snijders, M. A. J. 1987, in RS Ophiuchi (1985) and the Recurrent Nova Phenomenon, ed. M. F. Bode, 51

Sokoloski, J. L., Luna, G. J. M., Mukai, K., & Kenyon, S. J. 2006, Nature, 442, 276

Sokoloski, J. L., Rupen, M. P., & Mioduszewski, A. J. 2008, ApJL, 685, L137

Starrfield, S., Shore, S. N., Butt, Y., et al. 2000, in Bulletin of the American Astronomical Society, Vol. 32, AASHigh Energy Astrophysics Division, 1253

Stephenson, F. R., & Green, D. A. 2002, Historical supernovae and their remnants, by F. Richard Stephenson and David A. Green. International series in astronomy and astrophysics, vol. 5. Oxford: Clarendon Press, 2002, ISBN 0198507666, 5

Surina, F., Hounsell, R. A., Bode, M. F., et al. 2014, AJ, 147, 107

Tajitsu, A., Sadakane, K., Naito, H., Arai, A., & Aoki, W. 2015, Nature, 518, 381

Tajitsu, A., Sadakane, K., Naito, H., et al. 2016, ApJ, 818, 191

Takei, D., Ness, J.-U., Tsujimoto, M., et al. 2011, PASJ, 63, S729

Takei, D., Tsujimoto, M., Kitamoto, S., et al. 2009, ApJL, 697, L54

Tatischeff, V., & Hernanz, M. 2007, ApJL, 663, L101

Tatischeff, V., & Hernanz, M. 2008, in Astronomical Society of the Pacific Conference Series, Vol. 401, RS Ophiuchi (2006) and the Recurrent Nova Phenomenon, ed. A. Evans, M. F. Bode, T. J. O'Brien, & M. J. Darnley, 328

Taylor, A. R., Davis, R. J., Porcas, R. W., & Bode, M. F. 1989, MNRAS, 237, 81

Tofflemire, B. M., Orio, M., Page, K. L., et al. 2013, ApJ, 779, 22

Truelove, J. K., & McKee, C. F. 1999, ApJS, 120, 299

van Rossum, D. R., & Ness, J.-U. 2010, Astronomische Nachrichten, 331, 175

Vink, J. 2012, A&ARv, 20, 49

Vlasov, A., Vurm, I., & Metzger, B. D. 2016, MNRAS, 463, 394

Waagen, E. O., & Pearce, A. 2014, Central Bureau Electronic Telegrams, 3803

Weisskopf, M. C., Aldcroft, T. L., Bautz, M., et al. 2003, Experimental Astronomy, 16, 1

Wilms, J., Allen, A., & McCray, R. 2000, ApJ, 542, 914

Wilson, T. L., Rohlfs, K., & Hüttemeister, S. 2013, Tools of Radio Astronomy (Springer-Verlag Berlin Heidelberg), doi:10.1007/978-3-642-39950-3

Woltjer, L. 1972, ARA&A, 10, 129

Worters, H. L., Eyres, S. P. S., Bromage, G. E., & Osborne, J. P. 2007, MNRAS, 379, 1557

Wynn, G. 2008, in Astronomical Society of the Pacific Conference Series, Vol. 401, RS Ophiuchi (2006) and the Recurrent Nova Phenomenon, ed. A. Evans, M. F. Bode, T. J. O'Brien, & M. J. Darnley, 73

Zeldovich, Y. B., & Raizer, Y. P. 1967, Physics of shock waves and high-temperature hydrodynamic phenomena (New York: Academic Press)